

**Synthesis, characterisation and in vitro investigation of  
bioactive nanoparticles**

Dissertation

Zur Erlangung des akademischen Grades eines Doktors der

Naturwissenschaften

- Dr. rer. nat. -

vorgelegt von

**Shabnam Hosseini**

geboren in Iran

Fakultät für Chemie

Institut für Anorganische Chemie

Universität Duisburg-Essen

**2021**

# DuEPublico

Duisburg-Essen Publications online

UNIVERSITÄT  
DUISBURG  
ESSEN

*Offen im Denken*

ub | universitäts  
bibliothek

Diese Dissertation wird via DuEPublico, dem Dokumenten- und Publikationsserver der Universität Duisburg-Essen, zur Verfügung gestellt und liegt auch als Print-Version vor.

**DOI:** 10.17185/duepublico/75320

**URN:** urn:nbn:de:hbz:464-20220215-114340-4

Alle Rechte vorbehalten.

Die vorliegende Dissertation wurde im Zeitraum von Oktober 2017 bis Oktober 2021 am Institut der Anorganischen Chemie der Universität Duisburg-Essen unter der Anleitung von Prof. Dr. Matthias Epple angefertigt.

1. Gutachter: Prof. Dr. Matthias Epple

2. Gutachter: Prof Dr. Christian Mayer

Vorsitzender: Prof. Dr. Oliver J. Schmitz

Tag der Disputation 21.12.2021



## Table of contents

1. Introduction .....	1
2. Theoretical Background .....	3
2.1 Nanoparticles .....	3
2.2 Nanoparticles in biology and medicine .....	4
2.3 Biomaterials.....	4
2.3.1 Smart biomaterials.....	4
2.4 Calcium phosphate .....	5
2.5 Biological background .....	6
2.5.1 Endocytosis .....	6
2.5.2 Transfection.....	8
2.5.3 Gene silencing .....	9
2.6 Oral and rectal administration .....	10
2.6.1 Colon drug delivery .....	10
2.6.2 Enteric coating.....	11
2.6.3 Enteric coating polymers.....	11
2.6.4 Suppositories .....	13
2.7 Strontium, magnesium and their influence on bone health .....	14
3. Material and methods .....	17
3.1 Dynamic light scattering (DLS) and zeta potential .....	17
3.2 Scanning electron microscopy (SEM).....	18
3.3 Disc Centrifuge System (DCS) .....	19
3.4 Energy dispersive X-ray spectrometry (EDX) .....	20
3.5 Transmission electron microscopy (TEM).....	21
3.6 Nuclear magnetic resonance spectroscopy (NMR) .....	21
3.7 Thermogravimetric analysis (TGA) .....	22

3.8 UV/Vis spectrometry.....	23
3.9 Fluorescence spectroscopy (Fluorimetry or Spectrofluorometry).....	23
3.10 Atomic absorption spectrometry (AAS).....	24
3.11 Freeze drying.....	24
3.13 Cell biological analysis methods.....	25
3.13.1 MTT test.....	25
3.13.2 Confocal laser scanning microscopy (CLSM).....	26
3.13.3 Alkaline Phosphatase Assay (ALP).....	27
4 Experimental.....	28
4.1 Synthesis and characterization of the nanoparticles.....	28
4.1.1 Synthesis of CaP-PEI.....	28
4.1.2 Synthesis of CaP-CMC.....	28
4.1.3 Synthesis of CaP-PEI-pcDNA-CaP-PEI.....	29
4.1.4 Synthesis of CaP-PEI-siRNA-CaP-PEI.....	29
4.1.5 Synthesis of labeled calcium phosphate-Rhodamine-PLGA nanoparticles.....	30
4.1.6 Synthesis of calcium phosphate-DNA-PLGA-nanoparticles.....	31
4.1.7 Synthesis of calcium phosphate-siRNA-PLGA nanoparticles.....	31
4.1.8 Synthesis of labeled strontium-doped calcium phosphate-fluorescent dye nanoparticles.....	32
4.1.9 Synthesis of labeled magnesium-doped calcium phosphate-fluorescent dye nanoparticles.....	33
4.2 Synthesis of gold nanoparticles.....	34
4.2.1 Synthesis of ultrasmall gold-glutathione-FITC nanoparticles.....	34
4.2.2 Synthesis of ultra-small gold-BSA and gold-BSA-AF555 nanoclusters.....	34
4.3 Freeze drying.....	35
4.4 Cell culture experiments.....	35
4.4.1 Seeding the cells.....	35
4.4.2 MTT test.....	36

4.4.3 Uptake of nanoparticles in cells .....	36
4.4.4 Transfection of cells .....	36
4.4.5 Gene silencing .....	37
4.4.6 Fixing and dyeing the cells.....	38
4.4.7 ALP test.....	38
4.5 Creating the transport vehicle.....	40
4.5.1 Filling and coating the capsule .....	40
4.5.2 Making the suppositories.....	42
5 Results and discussion.....	43
5.1 Calcium Phosphate nanoparticles.....	43
5.1.1 Characterization of the CaP-nanoparticles for uptake and transfection studies .	43
5.1.2 Uptake of calcium phosphate nanoparticles by different cells.....	45
5.1.3 Calcium phosphate nanoparticle transfection by different cells .....	47
5.1.4 Characterization of calcium phosphate nanoparticles for gene silencing .....	51
5.1.4 Silencing the EGFP in HeLa EGFP cells .....	53
5.2 Transport of nanoparticles into the intestine .....	57
5.2.1 Characterization of the transport vehicle (capsules) .....	58
5.2.2 Release rate of the nanoparticle filled capsules after being in stomach and intestine simulation medium .....	62
5.2.3 Colloid-chemical analysis of the particle release from the gelatin capsule .....	63
5.2.4 In vitro investigations of the transport vehicles .....	66
5.3 Calcium phosphate PLGA nanoparticles for drug delivery .....	87
5.3.1 Characterization of the nanoparticles .....	88
5.3.2 MTT test.....	90
5.3.3 Uptake of nanoparticles in HeLa cells .....	91
5.3.4 Transfection of nanoparticles in HeLa cells.....	93
5.3.5 Gene silencing of nanoparticles in HeLa cells .....	95
5.3.6 Conclusion.....	97

5.4 Strontium and magnesium-doped calcium phosphate nanoparticles .....	97
5.4.1 Characterization of strontium-doped calcium phosphate nanoparticles.....	99
5.4.2 Cell-biological characterization of strontium-doped nanoparticles in different cells.....	102
5.4.3 Characterization of magnesium-doped calcium phosphate nanoparticles .....	107
5.5 Incorporation of ultra-small gold nanoparticles and gold nanoclusters in capsules and suppositories.....	128
5.5.1 Characterization of ultra-small gold nanoparticles .....	129
5.5.2 Capsule and suppository loading.....	133
5.5.3 Particle release from capsules and suppositories .....	134
5.5.4 In vitro studies of the transport vehicles contain ultra-small gold nanoparticles .....	136
5.5.5 Uptake of particle released from capsules and suppositories by cells .....	137
5.5.6 Conclusions .....	140
6. Summary and conclusions.....	142
7. Zusammenfassung .....	145
8. References .....	148
9. Appendix .....	164
9.1 List of abbreviations used.....	164
9.2 List of devices used .....	166
9.3 List of chemicals used .....	167
9.4 List of publications .....	169
9.6 CV .....	171
9.7 Eidesstattliche Erklärungen .....	175
9.8 Acknowledgments .....	176

### 1. Introduction

Due to their small size, nanoparticles can be taken up by cells. At the same time, they can be loaded with functional molecules and transported across the cell membrane. Calcium phosphate nanoparticles offer several advantages for these applications. Calcium phosphate is biocompatible, biodegradable and easy to stabilize nanoparticulate along with having a high affinity for nucleic acids. In this thesis, functionalized calcium phosphate nanoparticles should first be synthesized and characterized. The nanoparticles should be loaded with different nucleic acids in order to influence the protein synthesis of cells *in vitro*. Afterward, the nanoparticles served as a transport vehicle for the nucleic acids across the cell membrane. Both DNA and RNA should be used to influence protein biosynthesis. For example, plasmid DNA (pDNA) should stimulate the synthesis of proteins foreign to the cell, while siRNA should down-regulate the expression of specific proteins. Both the transfection and the muting of specific genes offer the possibility of treating chronic inflammatory bowel disorders. Therefore, both DNA- and RNA-loaded particles should be tested *in vitro* in different cell lines. In addition to the effects of the functionalized nanoparticles on protein biosynthesis, options for applying the particles in the intestine should also be investigated. In this way, nanoparticles can enter the intestine rectally and orally. However, since calcium phosphate dissolves in an acidic environment, the particles must be protected from gastric acid when administered orally. Transport vehicles should be developed and investigated for both routes of administration. Achieving this goal, soft gelatin mini capsules were developed which were covered with five different enteric coating polymers as well as suppositories [1-9].

In the second segment of this thesis, encapsulation of calcium phosphate nanoparticles and bioactive calcium phosphate nanoparticles was studied. The aim of this work was to determine the *in vitro* performance of the PLGA encapsulated calcium phosphate nanoparticles as well as PLGA encapsulated bioactive calcium phosphate nanoparticles.

The use of nanoparticles in biomedicine is a steadily growing area of research. Drug delivery is always in particular interest. Systems based on nanoparticles offer many advantages over conventional therapeutics such as a high surface area in relation to volume and different shapes. The nanoparticles to be used in medicine must meet criteria such as low cell toxicity and high efficiency. Both are fulfilled by calcium phosphate (CaP) nanoparticles, in addition to the ability to bind biomolecules. Calcium phosphate nanoparticles are also used as material for bone replacement [8, 10-12]. Properties of calcium phosphate nanoparticles can be improved by substituting various ions such as strontium and magnesium [13]. In order to

study the use of trace elements such as strontium and magnesium in calcium phosphate biomaterials, strontium and magnesium-doped calcium phosphate nanoparticles were synthesised, characterized and *in vitro* studies in three different cell lines were completed.

Among nanoparticles, ultrasmall gold nanoparticles have gained particular interest due to their small size. Ultrasmall gold nanoparticles with a diameter less than 2 nm have a fascinating potential to cross the cell barrier [14-17].

In the last part of the work, we studied the transportation of ultrasmall gold nanoparticles and nanoclusters into various cell types. Again, the polymer coated soft gelatin capsules and suppositories were used in order to investigate the *in vitro* behavior of nanoparticles and nanoclusters after releasing from the capsules and suppositories.

## 2. Theoretical Background

### 2.1 Nanoparticles

The term '*nano*' originates from the Greek word for 'dwarf, nanos' which means the factor  $10^{-9}$  for SI units. Nanoparticles are particles that have broadening in  $1-100 \cdot 10^{-9}$  m in all spatial directions [18]. However, since this definition is not taken too strictly, sub-microparticles are also generally referred to as nanoparticles. The small size of the nanoparticles, high surface-to-volume ratio and the physicochemical properties of the particles such as optics or electrical conductivity, are the factors that make the particles suitable in catalysis, for energy storage or in the medical field [19-24].

The synthesis of the nanoparticles can be achieved in two ways: the top-down or bottom-up method. These synthesis routes are shown schematically in Figure 1.

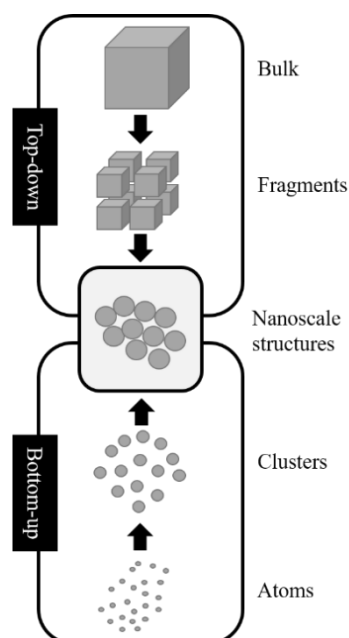


Figure 1: Schematic representation of the top-down and bottom-up syntheses for nanoparticles [25].

The top-down approach turns around fabrication of nanomaterials with wearing bulk material away to achieve the required smaller materials or substances. Top-down synthesis consists of particle size declination of large particles into smaller particles. This process is comparable to sculpting a block of stone to the required image. Whereas the bottom-up approach contains the structures being constructed from the smaller units such as atoms or molecules through covalent or supramolecular interactions. This process is also similar to building a house brick by brick [26-29].

### **2.2 Nanoparticles in biology and medicine**

In nanomedicine, the particles are used as contrast media for imaging methods or as carrier systems for drugs or biomolecules. Controlling the particle size, surface properties and release of drug agents in order to achieve the site and time specific drug release is the main aim in designing nanoparticles as a delivery system [30-33].

Improvements in nanotechnology have encouraged innovative applications in biomedicine where nanoparticles are developed for drug delivery and photodynamic therapy. Owing to their small size, nanoparticles can be efficiently directed and internalized by tumor cells where these tiny particles offer the effective approach for specific targeting of tumor cells [34, 35]. Nanoparticles have also been manipulated in several biomedical applications such as bioimaging and biosensing for example, gold nanoparticles are capable of detecting small proteins. To design the nanoparticle-based agents, understanding the fundamental mechanisms that control the transmembrane transport and study about nanoparticles in biological cells, is significant [36-40].

Nanomaterials and nanoparticles are being acquired to advance the diagnosis and therapy of diseases with beneficial effects in drug delivery system and biopharmaceutical molecules to control site and time of drug delivery. These therapeutic nanomaterials and techniques are called ‘nanomedicines’ which employ multiple pathways for cellular entry [16].

### **2.3 Biomaterials**

According to the American National Institute of Health a biomaterial is defined as “Substance or combination of active ingredients which can be synthetic or natural and they should be suitable for supporting a tissue, organ or body function” [41].

Biomaterials should replace or support corporal functions in the body, which are impaired in their function. Therefore, a biomaterial specific chemical, mechanical and biological depending on the application requirements. The biocompatibility results from these requirements of a biomaterial and includes the functional similarity to the body's own structures as well as biological compatibility [42].

#### **2.3.1 Smart biomaterials**

Biomaterials which are capable to respond to changes in their nearby environment, are attractive because these changes affect the control parameters such as drug release and cell adhesiveness. Numerous studies have been researched about the changes in parameters such

as pH value [43, 44], temperature [45, 46], and light [47, 48]. The body uses changes in pH to simplify a range of different processes. Food is broken down into nutritive substances in the stomach under acidic pH around 2 and later absorbed in the small intestine having pH about 7 to 8. Drug delivery along the gastrointestinal track by oral administration is desirable for patients who require routine, periodic delivery of drugs. However, effective drug delivery for the patient with intestinal issues achieves with survival of drugs in the acidic pH of the stomach. For this purpose, pH-sensitive materials are developed to take advantages of pH changes in the gastrointestinal tract and carry drugs through the stomach for successful delivery in the small intestine [49].

### 2.4 Calcium phosphate

Calcium phosphates (CaP) are the inorganic components in human hard tissue [50]. Calcium phosphate can be produced as a solid in different phases and characterized by the molar ratio of calcium to phosphate. Most calcium phosphates are sparingly soluble or insoluble in water at neutral or basic pH values. However, calcium phosphates are water-soluble in acidic medium. Stoichiometric ratio of calcium to phosphate for calcium phosphates is between 0.5 and 2.0. Typically, calcium phosphates with a higher Ca/P ratio are less soluble in water. In biology, calcium phosphates are mainly known as inorganic components of hard tissues such as teeth and bones which occur in mammals as hydroxyapatite (HAP). The stoichiometric composition of hydroxyapatite is  $\text{Ca}_{10}(\text{PO}_4)_6(\text{OH})_2$ . However, since non-stoichiometric apatites are present in biological systems, the Ca/P ratio is between 1.5 and 1.67 [42, 50]. Calcium phosphate mainly occurs in nanoparticles which are considered to be very biocompatible [51]. The synthesis of calcium phosphate nanoparticles is fascinating because of the capability of them to be functionalized with different biomolecules such as nucleic acids and proteins. Calcium phosphate nanoparticles have an ability of transporting the active substances due to their small size and absorbing by the cells [7, 51-53]. Synthesis of calcium phosphate nanoparticles is easy and quick and many factors including the pH value, the Ca/P ratio used in the synthesis and the temperature play critical roles. The most predominant phase of calcium phosphate is amorphous calcium phosphate (ACP), however, hydroxyapatite (HAP) may be formed from ACP by spontaneous transformation [10, 42, 51]. A phase of calcium phosphates which gets involved in a biological environment as ACP stimulates bone growth better than crystalline calcium phosphates. Nevertheless, in the transfection of mammalian cells, the difference between brushite and HAP nanoparticles was only marginal [54, 55]. The functionalization of calcium phosphate nanoparticles with

biomolecules makes it possible to transport active substances into cells. Organic molecules, proteins or nucleic acids are taken up desirably on the surface of calcium phosphate [51, 56-61]. The adsorption process on “bare” calcium phosphate surfaces is described by the replacement of ions on the surface of the calcium phosphate crystals with charged or polar groups of the adsorbing molecules. Negatively charged groups such as nucleic acids are more likely to interact with calcium ions, while positively charged groups can interact with phosphate ions [51, 52]. The adsorption of proteins and small molecules depend on the crystal phase of the calcium phosphate [51].

The cell transfection process with DNA loaded calcium phosphate nanoparticles is shown schematically in Figure 2. Nanoparticles with DNA are given to the cell culture medium and incorporated into the cells by endocytosis. The nanoparticles reach the nucleus and insert the DNA inside the cytoplasm and finally into the nucleus [62]. Controlling the size and morphology of the calcium phosphate loaded nucleic acid nanoparticles led to improved transfection efficiency by the cells. The development of multi-shell calcium phosphate nanoparticles enabled the nucleic acids to be protected from enzymatic degradation. Furthermore, positively charged calcium phosphates were better absorbed by cells due to a PEI shell [54, 63-66].

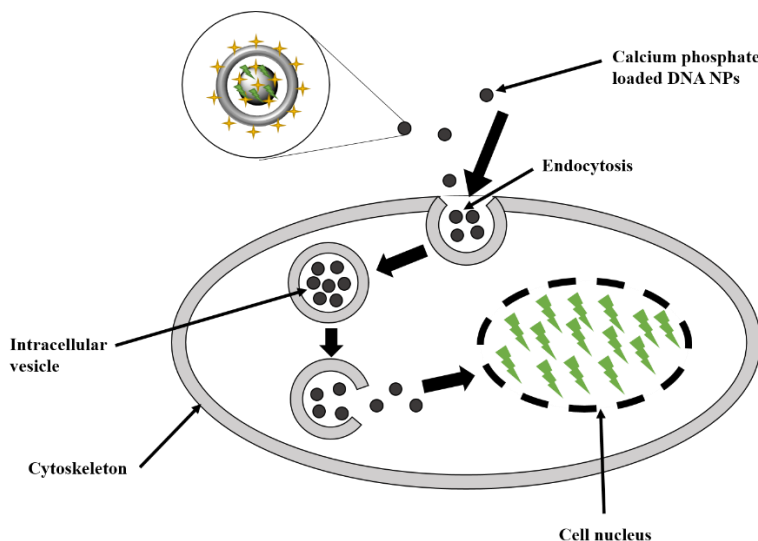


Figure 2: Schematic representation of the transfection mechanism [62].

## 2.5 Biological background

### 2.5.1 Endocytosis

Mammalian cells take up extracellular material by a variety of different mechanisms that are cooperatively named endocytosis. Endocytosis consists of several extracellular material

uptake methods by cells, including phagocytosis (cell eating), pinocytosis (cell drinking) clathrin-dependent receptor-mediated endocytosis (requiring the coat protein clathrin), and clathrin-independent endocytosis (do not require clathrin). Moreover, endocytic mechanisms provide many important cellular functions such as uptake of extracellular nutrients, regulation of cell-surface receptor expression, maintenance of cell polarity and antigen presentation. Endocytic pathways are also utilized by viruses, toxins, and symbiotic microorganisms to enter the cells [67].

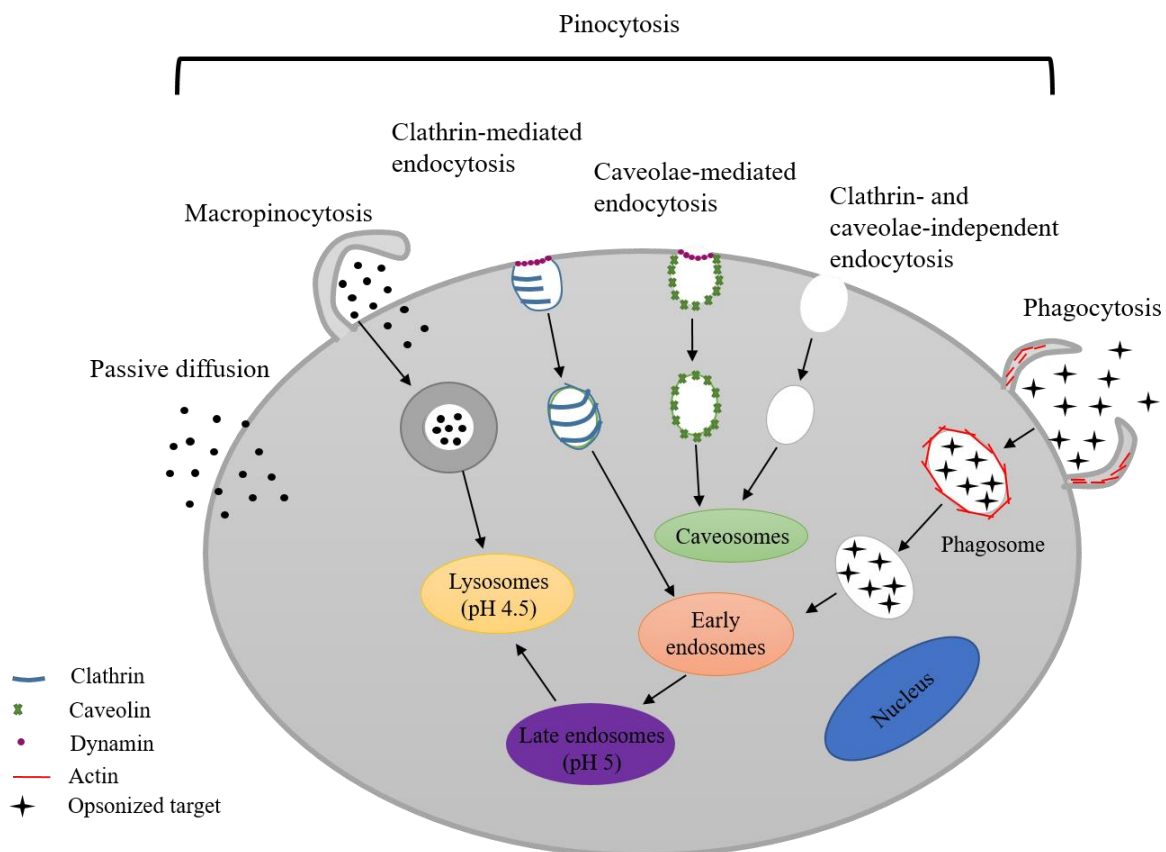


Figure 3: Summary of pathways of cellular uptake [68].

To destroy pathogens such as bacteria or to remove dead cells, cells need to bring large particles into the cell interior. This procedure, called phagocytosis which comes from the Greek words for ‘eating’ and ‘cell’. Phagocytosis consists transporting particles through the cell membrane. Cells accomplish this mechanism by wrapping themselves around the target particle and creating a new internal membrane-bound section called phagosome [69-72].

Drug carriers in the form of nanoparticles are promising routes for preventing ranges of diseases, like the human immunodeficiency viruses (HIV), tuberculosis (TC), and cancer. Probable advantages of these drug carriers consist of protecting drugs from degradation, smaller amount of side effects on vital tissues, smaller doses of loaded drugs and targeting

drugs directly to where they are needed. One problem with this method is that microparticle drug carriers are repeatedly recognized as foreign particles by the immune system and removed via phagocytosis [69, 73-81].

The name of pinocytosis comes from the Greek words for ‘drink’ and ‘cell’ [82]. In pinocytosis, fluids are absorbed from the extracellular matrix with the dissolved substances and ingredients in it. Pinocytosis is further subdivided into clathrin-mediated and clathrin-independent pinocytosis. Clathrin-mediated pinocytosis is the most studied pinocytosis mechanism in which many macromolecules and nanoparticles such as PLGA nanoparticles, gold nanoparticles or silica nanoparticles are taken up. Receptor proteins are gathered in the cell membrane, which then form the protein clathrin and forms a hollow or scoop of the cell membrane around the nanoparticle and absorb them into the interior of the cell. A vesicle forms that strips off the clathrin in the cytosol and then transforms into an endosome [16, 83-90]. Vesicles grow from the cell surface (such as clathrin-coated vesicles), take up solute and become fluid-phase pinocytosis. Several biochemical investigations in baby hamster kidney cells indicate that clathrin-mediated endocytosis can account for all fluid-phase uptake [91-95]. The endocytosis of many cargoes is relatively unaffected by inhibition of the pathway. Moreover, these cargo molecules are assumed in a cholesterol-dependent manner, differ to clathrin-mediated endocytosis cargo molecules. Clathrin-independent endocytosis is an independent of clathrin endocytic pathway [96].

The clathrin-independent endocytosis mechanism is comparable to phagocytosis so that the cell membrane is reverted and the surrounding extracellular medium is enclosed. These swellings form macropinosomes with the cell membrane, which then mature into endosomes [16, 96-100]. A cell can have various forms of clathrin-independent endocytic mechanisms and they can be responsible for the major fraction of membrane and fluid taken into the cell. The uptake of calcium phosphate nanoparticles could also be assigned to this endocytosis mechanism [101, 102].

### **2.5.2 Transfection**

Transport of nucleic acids into the interior of cells is called transfection. This includes both the transport of DNA and RNA [52, 103]. In this work, however, transfection refers to the introduction of nucleic acids into cells with the aim of expressing certain genes. If RNA is channeled into cells with the aim of reducing the expression of certain proteins, this is known as gene silencing [104].

Process of transfection introduces foreign nucleic acids into cells to produce genetically modified cells. Studying the function of genes or gene products by improving or reducing specific gene expression in cells, is the main aim of transfection [105-107].

Chemical transfection methods are the most extensively used transfection ways in modern researches [108]. Cationic polymers, calcium phosphates, cationic lipids, and cationic amino acids are the most generally used materials in chemical transfection methods. Positively charged chemical substances can easily attach to negatively charged nucleic acids in order to make the chemical complexes such as positive foundation and nucleic acids [108-110]. These positively charged chemical complexes will be attracted to the cell membrane with negative charge. Transported nucleic acids to the cells require to be delivered to the nucleus to be expressed. Once the nucleic acid has reached the nucleus, it can be transcribed into mRNA by RNA polymerases. After exiting the nucleus, protein biosynthesis can then take place in the ribosomes by translation of the mRNA. The transfection efficiency of chemical methods dependent basically on the ratio of nucleic acid to chemical substances, pH, cell membrane conditions, and cell type [106, 111-114].

### 2.5.3 Gene silencing

A specific inhibition of unwanted gene expression by blocking mRNA activity is generally called gene silencing. Gene silencing is the perfect tactic to control the new genomic knowledge for drug discovery [115]. Disease-associated genes can be targeted and silenced by synthetic short interfering RNA (siRNA) which offers respectable prospects as a novel therapeutic strategy. siRNA consists of a double-stranded RNA duplexes which silence or mute the target gene expression among the process of RNA interference (RNAi) [116].

In contrast to transfection with DNA, the nucleic acid no longer has to get into the cell nucleus in order to perform its function. Rather, when genes are silenced, RNA is brought into the cytosol of the cell. After exiting the endo-/lysosome, sequence-specific interaction with the mRNA of a certain protein leads to the inhibition of the synthesis of the corresponding protein. This process can reduce the level of expression of certain proteins [15, 117-119].

Similar to DNA, siRNA alone cannot permeate the cell membrane due to its negative charge. [8, 120] Calcium phosphate nanoparticles were discussed as carriers for nucleic acids for genetic vaccination [121-123].

### 2.6 Oral and rectal administration

#### 2.6.1 Colon drug delivery

Oral drug delivery to the colon achieved an increasing attention. Colon targeting is distinguished for having several therapeutic and medicinal advantages, such as the oral delivery of drugs which are normally destroyed by acidic medium and conditions of stomach. Local treatment of colonic diseases, such as ulcerative colitis, colorectal cancer and Crohn's disease, is more efficient with the delivery of drugs to the involved area. Moreover, smaller amount of drugs or doses of medicaments is required for treatment of colonic infections with colon drug delivery system [124]. There has been an increased interest in using the colon and intestine as sites for oral peptide drug delivery [125, 126].

Colonic delivery can not only be accomplished by oral but also by rectal administration. Rectal delivery forms, suppositories, are the typical dosage form designed to deliver drugs via rectal and vaginal routes of administration. Suppositories prevent the complications associated with oral drug delivery like first pass effect, degradation of drugs by gastric acid, and the need for enteric coating polymers. Suppositories also show a faster drug release compared to capsules or tablets that are administered by oral administration [127-131].

For having a satisfactory colon targeting drug delivery, there are two considerable physiological factors including pH and the transit time in the GI tract. Absence or presence of food in the stomach changes gastric pH range from 1.4-2.1 in the empty state, to 3-7 in the full state [6]. Luminal pH in the proximal small bowel ranges from 5.5 to 7.0 and gradually rises to 6.5-7.5 in the distal ileum. In almost every recording published there has been a fall in luminal pH from the terminal ileum to the caecum (range 5.5-7.5); pH then rises in the colon and rectum to 6.1-7.5 [132].

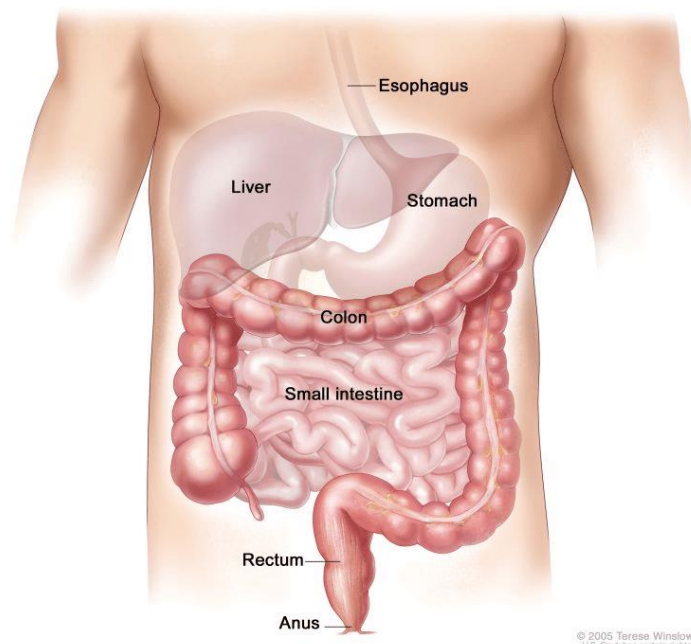


Figure 4: Schematic view of the intestine and colon [133].

The gastrointestinal transit time of drugs shows that in humans, it would be expected to be of the order of 1.5 to 2 hours [134, 135].

### 2.6.2 Enteric coating

An enteric coating is a polymer barrier employed to the drug or medication in oral administration. These enteric coatings prevent dissolution or disintegration of drugs through the way of delivery to the destination. The word ‘enteric’ reveals small intestine; hence enteric coating avoids drug release before reaching in small intestine. Helping by enteric protecting drug from being released in the acidic medium of stomach, is the major advantage of using enteric coatings in colon drug delivery system. Enteric coating is also an effective method to achieve drug targeting with site and time specific delivery [136-139].

### 2.6.3 Enteric coating polymers

The pH of the stomach is low but increases in the small and large intestine. For targeting drugs to the colon, it is critical to coat the tablets, capsules or pellets with a pH-dependent or pH-sensitive polymer which is insoluble at low pH and soluble at neutral or marginally basic pH. This capability of polymers to react to different pH, leads to release of drugs in the small intestine or in the colon. The enteric coated polymers stay unchanged and insoluble at low pH. Nevertheless, as the pH increases in the gastrointestinal track, the acidic functional

groups of these enteric coating polymers will be active and capable of ionization. Therefore, the polymers expand or become soluble in the intestinal fluid. Widely used polymers which use for enteric coatings in colon drug delivery include EUDRAGIT, cellulose acetate phthalate (CAP), poly(methacrylic acid-co-methyl methacrylate) cellulose acetate trimellitate (CAT), poly(vinyl acetate phthalate) (PVAP), hydroxypropyl methylcellulose phthalate (HPMCP), fatty acids, waxes, shellac, plastics and plant fibers [139, 140].

EUDRAGIT is the brand name for various ranges of polymethacrylate-based copolymers [141]. Different types of EUDRAGIT, whether water insoluble or water soluble, apply for colon targeting. EUDRAGIT L is soluble at pH more than 6, EUDRAGIT S dissolves at pH more than 7 because of its higher ratio of esterified groups to carboxylic groups. Combination of EUDRAGIT L and S can also develop in tablet coatings in order to achieving proper results in colon targeting [142, 143]. EUDRAGIT S and L have been commonly used, alone or in combination with other polymers to coat tablets, capsules, microspheres, micro particles, and micro capsules [144-151]. Along with EUDRAGIT, other pH-dependent polymer enteric coatings such as hydroxypropyl methylcellulose (HPMC), cellulose acetate phthalate (CAP), poly-vinyl acetate phthalate (PVAP), or using the blend of these polymers have been also studied as delayed coatings for colon and intestine targeting drug delivery [152-154]. These polymers have acidic ionizable carboxylic acid groups on their structure, which are insoluble at low gastric pH but soluble at higher pH of the intestine [155, 156]. Cellulose ester polymers such as cellulose acetate (CA), cellulose acetate butyrate (CAB) and cellulose acetate phthalate (CAP) are widely used for various pharmaceutical applications. [157] CAP is a well-known enteric coating polymer and dissolves only at higher pH than 6. *In-vivo* studies on the CAP-coated tablets and capsules show that CAP is an adequate enteric polymer [158, 159].

Hydroxypropyl methylcellulose (HPMC) is regularly used as a pre-coating polymer for enteric coating, it is expected that the application of enteric coated capsules with HPMC and then with another polymer such as EUDRAGIT or CAP, results in appropriate polymer to polymer adhesion and compatibility [160-164].

HPMC as a capsule pre-coating agent enhances properties such as toughness, elasticity and tensile strength. Hydrophilic materials such as chitosan, HPMC, and poly (vinyl) alcohol can leak from mixed enteric coatings in gastrointestinal fluids and affect the particles or drugs as they navigate the gastrointestinal tract. The leaching of hydrophilic materials in enteric coating systems happens as a rapid leaching process or a rate-controlling one. Hydrophilic materials and polymers play roles as the drug release managers in mixed polymer coatings.

Therefore, some dosage form of the drugs will release in the upper GIT, and the rest in the colon. This can be invaluable in a range of therapeutic areas [165-170].

As an example, for such capsule coatings is the work of Gazzaniga and colleagues which developed two-layered polymer coatings in order to have an oral time-based drug release system for colonic specific delivery. This colon targeting system coated with two polymeric layers consisted of hydroxypropyl methylcellulose (HPMC) as an inner layer, which was used to give a system a determined drug release time, and acrylic resins as the outer layer that dissolved at pH more than 5 and worked as enteric coating of a core. The thickness of the inner layer controlled the drug release time and site of the action and treatment [171-173].

### 2.6.4 Suppositories

A constructive alternative route of administration to the oral route is drug delivery via the rectum specifically for patients who cannot swallow or have a stomach problem after taking the capsules or pills [174]. Suppositories are a dosage form designed to deliver drugs through rectal and vaginal routes of administration. Suppositories as drug delivery vehicles are not new dosage forms. Rectal drug delivery is one of the world's oldest strategies for drug dosing and rectally applied products have existed for hundreds of years [175, 176]. The main rectal administration form of medications is the suppository. The rapidity release of drugs in the rectal fluid depends essentially on the physicochemical properties of the suppositories [177, 178].

Several drug formulations can be applied rectally by developing transport agents such as suppositories and enemas [179]. Site of absorption and direction of blood flow are two important factors in rectal drug delivery with respect to the blood system of the rectum and transport of absorbed drug into the systemic circulation. If drugs absorb in the upper part of the rectum, they will transport to the portal system and circulates through the liver, on the other hand, by absorption in the lower rectum, the drugs will transport immediately to the systemic circulation. By using the hard fat based suppositories, the drugs receive the second transport way and will take advantages of being in the systemic passage [179-182].

Suppositories have been classified in different shapes include bullet or torpedo, round oval, elongated oval, tampon and teardrop (Figure 5). However, suppositories are typically cylindrical in geometry, longer than wide, with the most general shape being the 'bullet' or 'torpedo' shape [176, 183].

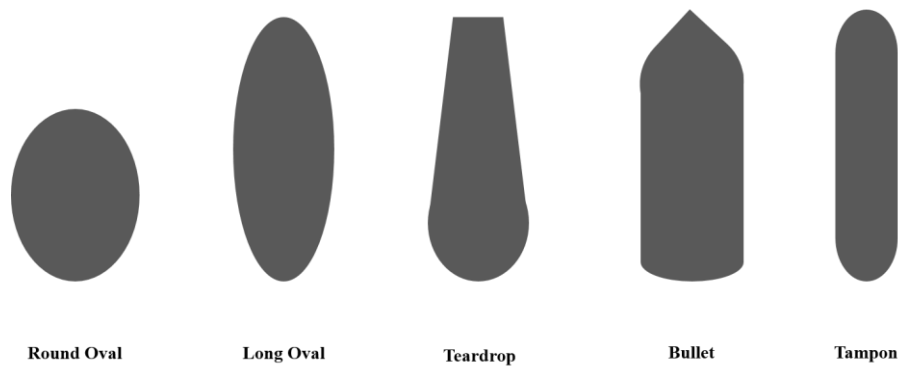


Figure 5: Typical suppository shapes

## 2.7 Strontium, magnesium and their influence on bone health

A fundamental understanding of the physical, chemical, biological, and mechanical processes surrounding the use of materials of a biocompatible nature is required to develop bone graft substitute materials. Bone is a highly dynamic, complex and vascularized tissue, which is able to heal and remodel throughout life [184].

The mineral component of human bone consists of non-stoichiometric carbonated hydroxyapatite (HA) with trace amounts of other ions ( $\text{CO}_3^{2-}$ ,  $\text{Na}^+$ ,  $\text{Mg}^{2+}$ ,  $\text{Fe}^{2+}$ ,  $\text{F}^-$ ,  $\text{Zn}^{2+}$ , and silicate) [185, 186].

During the past decades, much research has demonstrated that a variety of ionic substituents can be incorporated into synthetic HA to produce a mineral composition more akin to that of natural bone tissue. Substitutions in the HA lattice have significant effects on the physical properties, that is, lattice parameters, crystal structure, morphology, solubility, and thermal stability relative to unsubstituted HA. Significant research has been carried out on zinc, magnesium, strontium, silicon, fluoride, and carbonate substituted HAs and some of these substituted HAs are now commercially available for bone repair, bone augmentation and as a coating material for orthopedic implants [187, 188].

HA is categorized as a bioactive ceramic of importance due to its close analogy to the mineral portion of human bone and teeth. HA is an inorganic mineral exhibiting a typical apatite lattice structure namely  $(\text{A}_{10}(\text{BO}_4)_6\text{X}_2)$  where A, B and X are represented by  $\text{Ca}^{2+}$ ,  $\text{PO}_4^{3-}$ , and  $\text{OH}^-$  respectively. Pure HA contains 39.68 wt % calcium and 18 wt % phosphorus giving rise to a Ca/P ratio of 1.67. Thermal stability of this compound is critically important as it affects the mechanical properties, biocompatibility, solubility, and morphology of HA [185, 186, 189].

Synthetic HA bone grafts prepared through chemical routes tend to possess a higher dissolution rate in physiological environments, which has a susceptibility to elicit an immune reaction in the body [187, 190-192].

HA is regarded as a bioactive, nontoxic, and osteoconductive material that is able to form direct chemical bonds with living tissues. Hence, it is widely used as an implantable material in dentistry, maxillofacial surgery and orthopedic surgery to repair bone defects and as a coating material for metallic implants [193, 194].

Magnesium is an important trace element in biological apatite where it exists in weight percentages of 0.72, 0.44, and 1.23 % in bone, enamel, and dentin, respectively.<sup>[195]</sup> Magnesium ions are known to play a vital role in bone metabolism as they stimulate osteoblast proliferation during the early stages of osteogenesis. All stages of skeletal metabolism are adversely affected by the deficiencies in Mg so causing impaired bone growth, decrease in osteoblast activity, osteopenia, and bone fragility [196]. The Mg intake is related to bone mass or rate of bone loss and hence has a strong link with osteoporosis.

Various research has been conducted into substituting magnesium ions into the HA lattice. The main objective of these investigations was to retain the desired stoichiometry and phase purity of HA but at the same time allowing the maximum degree of magnesium ion substitution. Magnesium has a known inhibitory effect on the crystallization of HA. This is mainly due to the smaller ionic radius of  $Mg^{2+}$  with respect to that of  $Ca^{2+}$  (~0.28 Å difference in radius according to the Pauling scale) which eventually introduces more defects and gives rise to strains in the HA lattice structure [197, 198].

Although numerous spectroscopic techniques have confirmed that  $Mg^{2+}$  enters the HA lattice, the exact position of  $Mg^{2+}$  in the HA lattice is still a controversy. Several authors stated that  $Mg^{2+}$  occupies the Ca (I) site [199, 200].

Recently, with the aid of complex analytical techniques such as X-ray absorption spectroscopy (XAS), multinuclear nuclear magnetic resonance, and computer modeling, it was clearly demonstrated that the  $Mg^{2+}$  ion substitutes into the Ca(II) site in the HA structure [201].

Strontium is a trace element present (0.00044 % of body mass) in the mineral component of bone and plays a vital role in bone mineralization [202, 203]. Incorporating strontium into the HA lattice is of paramount interest due its biological role in bone where it enhances the activity of osteoblasts and inhibits the activity of osteoclasts [202, 204]. In addition, *in-vitro* studies have shown that Sr has a direct influence on the stimulatory effect on DNA and bone collagen synthesis [203]. In recent years, a strontium compound known as *strontium ranelate*

has attracted attention since it is used as a successful treatment for osteoporosis. Both *in-vitro* and *in-vivo* studies have shown that *strontium ranelate* increases bone formation and decreases bone resorption [202, 205].

Incorporation of  $\text{Sr}^{2+}$  ions into the HA lattice has a strong influence on the crystallinity and lattice parameters depending on the level of strontium substitution.<sup>[204]</sup> Many studies have shown that incorporation of strontium ion reduces the crystallinity and crystal size of HA although recent research conducted by Curran et al. showed that low concentrations of strontium (<1.5 wt %) do not affect the crystallinity of HA [206].

$\text{Sr}^{2+}$  substitutes to the calcium ion in the HA lattice and prefers the Ca (II) site at high concentrations. However, Bigi et al. showed that Ca (I) sites can also be occupied at relatively low strontium concentrations [202]. Sr-HA has a higher solubility than HA thus increasing bioactivity from the release of  $\text{Sr}^{2+}$  that makes it extremely desirable to use in *in-vivo*. In addition, Sr-HA releases a  $\text{Ca}^{2+}$  ion, which activates calcium channels thus stimulating cell response [204-206]. Although both *in-vitro* and *in-vivo* results were promising, further *in-vivo* studies would be required to affirm the therapeutic benefit of using Sr-HA in clinical applications for treating defects related to osteoporosis.

### 3. Material and methods

#### 3.1 Dynamic light scattering (DLS) and zeta potential

Dynamic light scattering can be used to characterize colloidal dispersions. Statements can be made about the average particle size distribution, the polydispersity and the colloidal stability of the dispersion. If the zeta potential is also determined, statements can be made about the properties of the surface of the particles and their charge. If electromagnetic radiation hits matter, it can be scattered, among other things. In addition to the scattered light, the dynamic light scattering takes advantage of the fact that the position of colloidal particles is constantly changing due to Brown's molecular movement. To determine the size distribution of particles in a colloidal dispersion using DLS, monochromatic light from a laser is radiated into the sample. The intensity of the scattered light is measured by a detector at a certain angle. Since there are very many particles in the irradiated volume, all of which scatter the incident light, constructive and destructive interference occurs. The interference leads to spatial fluctuations in the scattered light intensity, which are perceived on the detector as light and dark points [207-210]. Furthermore, due to the movement of the particles, there are temporal fluctuations in the scattered light intensity. This is the actual measured variable at DLS. The correlation of the scattered light decreases as a function of time. This is described by the autocorrelation function. If the particles move faster, the correlation of the scattered light intensity also decreases faster. Typically, the DLS measurement intervals are microseconds to nanoseconds. The diffusion coefficient can be calculated using the autocorrelation function. The diffusion coefficient  $D$  is in turn related to the hydrodynamic diameter  $R_h$  of the particles via the Stokes-Einstein equation:

$$D = \frac{kT}{6\pi\eta R_h}$$

Here  $D$  is the diffusion coefficient,  $k$  the Boltzmann constant,  $T$  the temperature,  $\eta$  the dynamic viscosity and  $R_h$  the hydrodynamic radius. Strictly speaking, this relationship only applies to spherical particles. Since there are often different particle sizes in a dispersion (polydispersity), suitable algorithms are necessary to obtain the particle size distribution from the autocorrelation function. The most widespread is the cumulative method. The sizes given in this work according to DLS always relate to the  $z$ -average, which indicates the mean size of the particles [207, 208]. DLS measurements offer many advantages. The measurement is very quick and the size of the particles in dispersion is measured.

Furthermore, compared to microscopic methods, a large number of particles are taken into account in the result. On the other hand, the data from DLS measurements are difficult to interpret. Large particles scatter the light with a much higher intensity than small ones. Assuming Rayleigh scattering, which applies to very small particles ( $d < \lambda / 20$ ;  $\lambda =$  wavelength of the incident light), the scattered light intensity is  $I \sim d^6$  [211].

This relationship shows that large particles have a much stronger influence on the particle size distribution than smaller particles have. The PDI (polydispersity index) allows conclusions to be drawn about the polydispersity of a sample. This value results from the breadth of the particle size distribution. Since the value shows whether the sizes of different particles differ significantly within a sample, it also allows an assessment of the measurement result. For example, size distributions determined by DLS can only be compared with size distributions from other methods if the PDI is  $< 0.1$ . For PDIs between 0.1 and 0.5, the size distributions of dispersions determined using DLS are comparable with one another [207, 208].

On the one hand, the scattering of light on particles allows conclusions to be drawn about their size. On the other hand, the scattering of charged particles moving in an applied electric field can be used to determine the speed of the particles. This is done using the so-called LDV technique (laser doppler velocimetry). The speed of the particles allows conclusions to be drawn about their electrophoretic mobility. This, in turn, is linked to its zeta potential via the Henry equation:

$$U_E = \frac{2\varepsilon z f (Ka)}{3\eta}$$

$U_E$  is the electrophoretic mobility,  $\varepsilon$  denotes the dielectric constant,  $\eta$  is the dynamic viscosity,  $f(Ka)$  is the Henry function and  $z$  is the zeta potential. To measure the particle size distribution of colloidal dispersions, a Nano ZS Zetasizer from Malvern was used in this work. In addition to the particle size distribution, this device can also measure the zeta potential. The "Zetasizer Software" from Malvern was used for the evaluation [7].

### **3.2 Scanning electron microscopy (SEM)**

Additionally to DLS, scanning electron microscopy (SEM) can also be used to determine the size of particles. In contrast to DLS, the samples have to be dried beforehand so that the particles cannot be measured in dispersion. It is advantageous that the result is not disproportionately influenced by a few large particles. If agglomeration occurs in the dispersion, the primary particles can still be observed through the scanning electron

microscope. It is also possible to describe the morphology of particles. This is just some of the information that is easily obtained from a sample using scanning electron microscopy. In addition to the fact that particles cannot be examined in dispersion, a further disadvantage is that only a small section of a sample can be examined. The maximum resolution of microscopes is limited by the wavelength. Depending on the energy of the electron beam, the wavelength can be up to 100,000-fold smaller than the wavelength of visible light. Commercial electron microscopes achieve resolutions of around 2-5 nm and are therefore suitable for examining nanomaterials. [212-214]

First of all, an electron beam is required for electron microscopy. This is generated at the electron gun and electrons with an energy of 1 keV to 40 keV are produced. Electron beams can be generated with tungsten wires or LaB<sub>6</sub> crystals (lanthanum hexaboride crystals). In the next step, the electron beam can be focused using magnetic lenses. After the electron beam has been focused, it can be guided over the sample in a specific grid, whereby an image can be generated with the aid of a detector. The electrons can interact with the irradiated matter in various ways, generating different signals that are detected by detectors. On the one hand, electrons can be detected whose energy roughly corresponds to that of the electron beam. These electrons are known as BSE (back scattered electrons) and are caused by Rutherford scattering near the atomic nucleus. On the other hand, electrons with lower energy than that of the electron beam can be detected. These result from the interaction of the electron beam with the electron shell of the atoms in the sample. These include SE (secondary electrons) [213]. In order to prevent the interaction of the electron beam with atoms in gases, SEM is carried out under vacuum conditions. Furthermore, irradiating non-conductive samples with the electron beam would lead to charging of the sample. To prevent this, the sample can be coated with a very thin layer (10 nm to 20 nm) of a noble metal. This process is known as sputtering. In this work gold-palladium (80:20) was used for all samples. The images from this work were taken with an ESEM Quanta 400 from FEI. After the synthesis, the particle dispersions were dropped onto a silicon wafer which was fixated to the aluminum carrier by means of a self-adhesive carbon pad.

### 3.3 Disc Centrifuge System (DCS)

The analytical disc centrifuge (Differential Centrifugal Sedimentation, DCS) enables the determination of the particle size distributions of colloids. This is based on the fact that the sedimentation of very small particles in an artificially created gravity field occurs faster than the Brownian molecular movement. Under these conditions, small particles sediment within

a few hours. The measuring instrument consists of an optically transparent disc with an injection point in the middle. A light source and a photomultiplier detector are also attached to the outer edge of the pane. A laser is used as the light source. A density gradient is built up in the rotating disk chamber with sucrose solutions of different densities and as soon as this is stable, the time from the point of injection until the particles are reached at the detector is measured using a standard (PVC particles with known size distribution). The subsequent measurement is calibrated with this value. Then 100  $\mu\text{L}$  of the sample are injected into the disk chamber, the sample dispersion initially spreads radially to the surface of the gradient and the sedimentation of the individual particles begins. Since the injection of the sample is fast ( $\sim 50$  ms), the start time and therefore the sedimentation time  $t$  can be defined. Taking into account the dynamic viscosity of the medium  $/\eta/$ , the density of the particles  $/\rho_P/$  and the medium  $/\rho_M/$ , the angular velocity of the rotating disk  $\omega$ , the radius of the disk at the injection point  $/R_0/$  and the detector location  $/R_f/$ , the Stokes law is modified so that the diameter  $/d/$  is derived from the Sedimentation time can be calculated. Assuming constant speed and temperature, the following relationship results for the diameter: [215, 216]

$$d = \sqrt{\frac{18 \cdot \eta \cdot \ln\left(\frac{R_f}{R_0}\right)}{(\rho_P - \rho_M) \cdot \omega^2 \cdot t}}$$

With the help of the Mie theory, which describes the behavior of the absorption of small particles, the measured intensity distribution is ultimately represented by the device software in a mass, number and volume distribution depending on the diameter of the particles.

### 3.4 Energy dispersive X-ray spectrometry (EDX)

The energy dispersive X-ray spectroscopy (EDX) is an analytical method to determine the elementary composition of a sample, in terms of apparatus, it is often coupled with a SEM. When the generated electron beam hits the atoms of the sample, element specific X-rays are emitted [42]. When the electrons hit the sample with high energy, electrons are knocked out of the inner shells of the sample atoms. The X-ray emission is explained by the filling in of the gaps that have arisen more energetic electrons from outer shells. The energy released in the process is given off in the form of X-ray quanta. Since the diameter of the electron beam is very small, the elemental composition of the sample can be analyzed with high spatial resolution [42]. By detecting the characteristic X-rays and the subsequent comparison with a database, the X-ray emission can be assigned to a corresponding element. The intensity of the signals is proportional to the contained relative Amount of atoms.

### 3.5 Transmission electron microscopy (TEM)

The transmission electron microscope is a special electron microscope in which the very thin sample (<100 nm) is irradiated with an electron beam with a constant current density and this passes through the sample. An electromagnetic lens system behind the sample ensures that the electron intensity distribution is mapped onto a fluorescent screen, which is coupled to a CCD camera. The primary electrons of the electron beam are high-energy electrons that ideally pass through the sample. A multitude of events that can happen to the electrons must be taken into account. These include elastic and inelastic scattering, which in turn can be more precisely characterized by Rutherford scattering or phonon production. It should also be noted that when the primary electron passes through the sample, it usually scatters multiple times. If the electron interacts with the atomic nucleus or with the entire electrostatic field of the atom, it is an elastic scattering effect. Inelastic scattering effects of the electrons are in most cases due to electron-electron interactions. The average distance that an electron travels between interactions through the cross-sectional area  $\sigma$  of the scattering unit with the number of atoms  $N_V$  per unit volume is expressed as the mean free path  $\Lambda$ : [217]

$$\Lambda = \frac{1}{N_V \cdot \sigma}$$

In high-resolution transmission electron microscopy (HRTEM), the phase of the diffracted wave is obtained, which influences the phase of the transmitted wave constructively or destructively. Ultimately, this leads to the generation of a phase contrast, which is noticeable in an HRTEM image through the imaging of atomic positions. The Fast Fourier Transformation (FFT) from a certain area of the sample provides diffraction information from which the crystal system and the spatial orientation of the system in the selected area of the HRTEM image result. In addition, this information can be used to determine the lattice parameters [216, 218].

### 3.6 Nuclear magnetic resonance spectroscopy (NMR)

Nuclear magnetic resonance spectroscopy has proven to be very helpful for determining chemical structures for many years. To resolve the chemical structure of a substance, the substance to be examined is exposed to a homogeneous, static magnetic field  $B_0$ . The atomic nuclei of the sample align themselves in the magnetic field and can be excited by means of a radio frequency pulse. The nuclei can have multiple excited states depending on the nuclear spin number  $I$ . In the case of Protons  $^1\text{H}$  with a spin of  $I = \frac{1}{2}$  two energy level exist. One is aligned parallel to the magnetic field and one antiparallel. The Energy gap increases with

higher magnetic fields resulting in the so called Zeeman splitting. After the excitation with a radio frequency pulse the nuclei fall back to the ground state causing a loss of magnetization. The Fourier transformation of this free induction decay (FID) results in structure-dependent signals which are distinguished by a specific chemical shift (in ppm) and by an optical appearance. In the whole of NMR spectroscopy there are many influences of nuclei, chemical properties of the functional groups, charge distributions and positions of substituents that characterize the spectrum. This is expressed, among other things, by the chemical shift. It depends on the electronegativity and the charge density distribution of the surrounding atoms. In the spectrum, this results in a stronger or weaker deshielding or shielding of a core in the electric field, which leads to an increase or decrease in the ppm value in the spectrum. There are a variety of different 2 dimensional NMR Spectroscopy methods, which provide a deeper insight of structural properties of molecules. In this work however only  $^1\text{H}$ -NMR was performed [219-226].

The  $^1\text{H}$ -NMR spectra in this work were recorded with an Avance III 600 MHz spectrometer (Bruker, Rheinstetten, Germany) equipped with a Prodigy cryoprobe head. The spectra were recorded with simultaneous suppression of the water signal by excitation sculpting due to the low ligand concentration in the aqueous dispersions. The excited spectral range had a width of approximately 0.6 ppm.

### 3.7 Thermogravimetric analysis (TGA)

Thermogravimetric analysis (TGA) is based on the measurement of changes in the mass of a sample as a function of temperature. These changes in mass can be based on physical or chemical processes such as drying, surface reactions, dehydration, decomposition or oxidation. A defined amount of the sample to be analyzed is heated in a corundum crucible in an oven under an argon or oxygen atmosphere at a constant heating rate. Due to the increase in temperature, changes in the mass of the sample occur, which can be recorded with the aid of a microbalance. These changes in mass are shown in a thermogram and allow conclusions to be drawn about the composition of the sample [227].

The TGA analysis was performed with a Netzsch STA-449 F3 Jupiter device. The sample was heated from 20 °C to 1000 °C with a rate of 3 °C min<sup>-1</sup> under an oxidative atmosphere of 254 mL min<sup>-1</sup> O<sub>2</sub> flow. A mass of 15-25 mg was placed in an Al<sub>2</sub>O<sub>3</sub> crucible holder.

### 3.8 UV/Vis spectrometry

UV/Vis spectrometry makes it possible to determine the concentration of molecules in solutions. A prerequisite for this is that the molecule absorbs light in the UV to Vis range. In this work the concentration of nucleic acids was determined in order to obtain their concentration in the colloidal dispersions. The intensity of a light beam that is passed through a sample can be reduced by absorption, scattering or reflection. During the measurement, the contributions from scattering and reflection are determined by measuring a blank sample. The decrease in intensity of a light beam is then due to the absorption by dissolved molecules. Depending on their electronic structure, molecules dissolved in the sample absorb light with certain wavelengths. The concentration of the dissolved molecules is related to the absorption for dilute solutions with the Lambert-Beer law [225, 228, 229]:

$$A = \log \frac{I_0}{I} = \varepsilon cd$$

$A$  is the absorption at a certain wavelength,  $\varepsilon$  is the molar absorption coefficient and  $d$  is the thickness of the layer through which the light beam penetrates. The molar absorption coefficient is a substance-specific quantity that can be determined, for example, with a calibration line. Concentrations with a range of  $2 \mu\text{g mL}^{-1}$  to  $50 \mu\text{g mL}^{-1}$  can be detected for DNA [229]. A Varian Cary Bio 300 spectrophotometer was used for this work. All measurements were carried out in a quartz cuvette with a path length  $d=1$  cm.

### 3.9 Fluorescence spectroscopy (Fluorimetry or Spectrofluorometry)

The spontaneous emission of photons a few nanoseconds after the excitation of a molecule is known as fluorescence. This applies provided that the radiative deactivation takes place between the states of the same multiplicity. These are transitions from the excited singlet state ( $S_1$ ) to different vibrational states of the electronic ground state of a molecule. Since the electronic transitions occur faster than a core oscillation period, a change in the dynamic state of the nuclei during excitation can be excluded. In addition, according to the Franck-Condon principle, the transition to an electronically excited state runs vertically. After excitation of an electron from the electronic ground state into a vibrational state of the electronically excited state, various relaxation processes are in competition with one another. The excited system mostly loses the amount of energy up to the basic vibration state of the electronically excited state through radiation less deactivation. The energy is released in the form of relaxation processes with other molecules. This loss of energy to the environment becomes noticeable in the form of a so-called Stokes shift, which describes the bathochromic

shift of the emission maximum relative to the absorption maximum. The loss of the amount of energy from S1 to the electronic ground state can also be lost by the molecule through collisions or through the emission of photons [230, 231].

The emission spectrum is recorded at a constant excitation wavelength at a 90 ° angle to the excitation in order to exclude stray light and interference. A photomultiplier serves as a detector and translates the emitted photons into an electrical signal [216, 232].

Fluorescence spectra were measured with an Agilent Cary Eclipse spectrophotometer in a quartz cuvette.

### 3.10 Atomic absorption spectrometry (AAS)

Atomic absorption spectrometry (AAS) can be used to obtain the concentration of certain elements in a sample. Free atoms absorb the light that is specific to them. In this work the AAS was used to determine the calcium content in colloidal dispersions. From this, the number of particles per milliliter could be calculated. For atomic absorption spectrometry, the sample to be examined must be atomized so that the element to be examined is present as a gas. In the simplest case, this atomization can be achieved with a flame. The absorption of monochromatic light of a specific wavelength can then be measured. The concentration of the desired element can then be calculated using the Lambert-Beer law [233, 234]. The detection limit for calcium in atomic absorption spectrometry is 0.1 mg L<sup>-1</sup>. In this work, the calcium determinations were carried out with an M series atomic absorption spectrometer from Thermo Electron. Before the measurements, the calcium phosphate nanoparticles were dissolved in acid. The analyses were carried out in the laboratory for microanalysis of the AK Epple.

### 3.11 Freeze drying

Freeze drying is also known as lyophilization and is a gentle process for drying aqueous solutions and dispersions. In this work, freeze-drying was used to increase the stability of a colloidal dispersion. Furthermore, freeze-dried nanoparticles were used to load capsules and suppositories, which were supposed to transport the active ingredients in the body to the necessary tissues. Lyophilization is based on the sublimation and resublimation of water. This describes the direct phase transitions from the solid state to the gaseous state and vice versa. The conditions under which water sublimates and resublimates can be taken from the phase diagram of water. These phase transitions only take place at pressures below 6 mbar and temperatures below 0 °C. The addition of suitable cryoprotectants before freezing, such

as trehalose, can protect the sample from stress during freezing and drying. The protection is usually based on the immobilization of a substance through the formation of a matrix by the cryoprotectant [235]. In this work an Alpha 2-4 LSC freeze dryer from Martin Christ was used. Samples were first snap frozen in liquid nitrogen. The water was then sublimed at 0.32 mbar and  $-10^{\circ}\text{C}$ . The temperature of condenser was  $-85^{\circ}\text{C}$ . Part of the strontium and magnesium-doped calcium phosphate nanoparticles was dried without addition of trehalose for characterizing with XRD and TG, with all other dispersions  $20\text{ mg mL}^{-1}$  trehalose was used as a cryoprotectant.

### 3.13 Cell biological analysis methods

This section describes the most important methods used for the analysis of cell culture experiments and *in vivo* experiments. The effects and interactions of nanoparticles with cells and nanomaterials were mainly investigated. In addition to the methods described here, other techniques such as light and fluorescence microscopy were used.

#### 3.13.1 MTT test

The MTT test offers the possibility to quickly determine the cytotoxicity of substances. Using a colorimetric method, the proliferation of untreated control cells can be compared with the proliferation of cells treated with a substance. In this work the MTT test was used to investigate the cytotoxic properties of the nanoparticles. First, the cells are incubated with the water-soluble dye MTT (3-(4,5-dimethylthiazol-2-yl)-2,5-diphenyltetrazolium bromide). This is reduced intracellularly and enzymatically by living cells to the water-insoluble formazan ((E, Z)-5-(4,5-dimethylthiazol-2-yl)-1,3-diphenylformazan). The dye changes its color from yellow to blue. Due to the solubility of formazan, the blue dye also accumulates in living cells. The formazan can then be dissolved in DMSO and examined photometrically at a wavelength of 570 nm. The absorption of the dye is proportional to the number of cells [236]. Figure 6 shows the conversion of the dye. The reduction of the MTT takes place in the mitochondria by means of succinate dehydrogenase. In the cytosol, MTT is reduced by NADH- and NADPH-dependent enzymes [237].

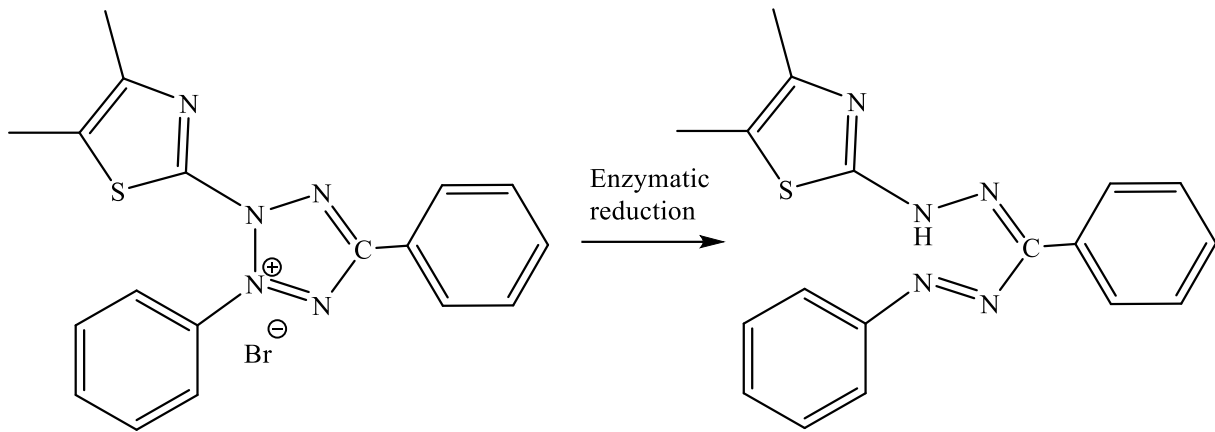


Figure 6: The water-soluble, yellow dye MTT is enzymatically reduced intracellularly to the water-insoluble formazan.

### 3.13.2 Confocal laser scanning microscopy (CLSM)

Confocal laser scanning microscopy (CLSM) attains the optical breakdown of a biological sample into individual, precisely focusable levels and can be understood as an optical microtome. The meeting (con) of the illumination and observation focal point (focal) enables both points to be focused at the same time. When using a laser as the light source, high light yields are obtained. The beam, which is a few millimeters in diameter, has to be widened afterwards with beam expansion optics in order to produce uniform illumination of the diffraction-limited spot. The highest intensity of the light is in the focal point, above and below the focal plane the intensity decreases with the square of the distance from the focal point. As a result, however, fluorescent molecules are also excited in the defocus regions, the emission takes place in all spatial directions and is superimposed with the light from the focal plane. Adding the signals of the focal plane and the extrafocal signals results in a reduction in the contrast and the expense of generating a diffraction-limited spot is not yet justified. But through a pinhole, which is centered on the optical axis in the intermediate image plane and thus confocal to the specimen, the signal reaches the detector from the focus. The signals of the extrafocal planes are filtered here. For this reason the pinhole is also referred to as a spatial filter [238]. Due to the necessity of the diffraction-limited spot, the specimen has to be scanned line by line in order to generate an image in two dimensions. The thickness of these optical sections in the  $z$ -direction  $/d_{z0}/$  depends on the excitation wavelength  $/\lambda/$ , the refractive index  $/n/$  and the numerical aperture  $/NA/$ :

$$d_{z0} = \frac{n \cdot \lambda}{NA^2}$$

The numerical aperture /NA/ is determined by the diameter of the pinhole, which cannot be reduced as desired, since diffraction effects dominate from a certain diameter. As a rule, the cuts cannot be made smaller than 500 nm ( $n = 1$ ,  $NA = 1$  and  $\lambda = 500$  nm), which is roughly twice the lateral resolution. The lateral resolution of a CLSM according to the equation is ~ 200 nm, as with a light microscope with, for example, an NA of 1.4 (oil immersion objective) and a wavelength of 500 nm [216, 238].

### 3.13.3 Alkaline Phosphatase Assay (ALP)

The most widely recognized biochemical marker of the osteoblast is alkaline phosphatase (ALP). ALP is an abundant enzyme which catalyses the hydrolysis of phosphate esters at an alkaline pH [239].

In these biochemical techniques, ALP at alkaline pH catalyses the reaction of p-nitrophenyl phosphate with water. In this reaction, p-nitrophenyl phosphate is colourless in basic conditions and after reacting with water, p-nitrophenol and P are the yield of the reaction with changing the colour to yellow in basic conditions [240].

The Alkaline Phosphatase Assay Kit is a highly sensitive and simple colorimetric assay which designed to measure ALP activity in serum and biological samples. The kit uses p-nitrophenyl phosphate (pNPP) as a phosphatase substrate which turns yellow ( $\lambda_{max} = 405$  nm) when dephosphorylated by ALP [241].

## 4 Experimental

### 4.1 Synthesis and characterization of the nanoparticles

#### 4.1.1 Synthesis of CaP-PEI [65]

In order to synthesize model particles for the coating with positive zeta potential, calcium nitrate (6.25 mM, pH 9.0), diammonium hydrogen phosphate (3.74 mM, pH 9.0) and PEI solution (2 g L<sup>-1</sup>) were pumped together using a peristaltic pump at 5 mLmin<sup>-1</sup> for the calcium and phosphate solution and 2 mLmin<sup>-1</sup> for the PEI solution and stirred for 10 min at 600 rpm. Afterwards, the dispersion was centrifuged for 15 minutes at 14,800 rpm and the particles were redispersed in the desired medium. These particles are referred to below as CaP-PEI or single-shell particles.

In order to label the nanoparticles with fluorescent dyes, FITC-labeled PEI (PEI<sup>FITC</sup>) or rhodamine-labeled PEI (PEI<sup>Rh</sup>) from Surflay Nanotec GmbH was used. The labeled PEI were diluted 1:10 to 1:20 with unlabeled PEI. The synthesis is shown schematically in Figure 7.

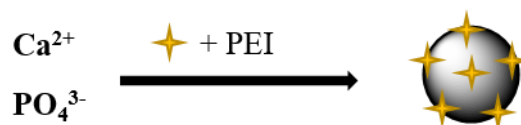


Figure 7: Schematic of the synthesis of CaP-PEI.

#### 4.1.2 Synthesis of CaP-CMC [242]

Model particles with negative zeta potential were synthesized by pumping together calcium nitrate (6.25 mM, pH 9.0), diammonium hydrogen phosphate (3.74 mM, pH 9.0) and carboxymethyl cellulose solution (CMC, 2 g L<sup>-1</sup>) with a peristaltic pump in a ratio of 5:5:2 and stirred for 10 min at 600 rpm. The dispersion was then centrifuged for 15 min at 21,100 g and the particles were redispersed in the desired medium. These particles are referred to as CaP-CMC. The synthesis is shown schematically in Figure 8. In order to mark the nanoparticles with fluorescent dye, FITC-labeled CMC (CMC<sup>FITC</sup>) was used. The labeled CMC were used diluted 1:10 with unlabeled CMC.

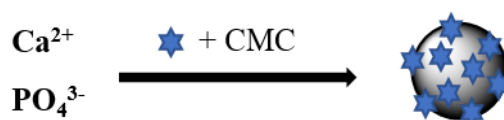


Figure 8: Schematic of the synthesis of CaP-CMC.

### 4.1.3 Synthesis of CaP-PEI-pcDNA-CaP-PEI [243]

To synthesize the triple-shell calcium phosphate nanoparticles, 3.5 mL of calcium nitrate (6.25 mM, pH 9.0), 3.5 mL of diammonium hydrogen phosphate solution (3.74 mM, pH 9.0) and 1.5 mL of PEI solution (2 g L<sup>-1</sup>) were pumped together with a peristaltic pump in a ratio of 5:5:2 and stirred for 10 min at 500 rpm. The dispersion was then centrifuged for 15 minutes at 21,100 g and the particles were redispersed in ultrapure water. With stirring about 600 rpm, 350 μL plasmid DNA (850 mg L<sup>-1</sup>) was added and the mixture was stirred for 10 min. Then 3.5 mL calcium nitrate solution and 3.5 mL diammonium hydrogen phosphate solution were added to the previous dispersion in order to form a second calcium phosphate shell and thus protect the DNA. An additional volume of 2.8 mL PEI (2 g L<sup>-1</sup>) per mL of the stock dispersion was added to these two-shell particles, to stabilize the system. The dispersion was centrifuged for 15 min at 14,800 rpm and then redispersed in ultra-pure water. In the following scheme, these particles are represented as triple-shell particles (CaP-PEI-pcDNA-CaP-PEI). In order to store the samples with long-term stability, 10-20 mg trehalose as a cryoprotectant was added per 1 mL of the solution and aliquoted into 1.5 mL centrifuge tubes. The samples were snap frozen with liquid nitrogen and dried in the lyophilizer. The dried samples were stored at -20 ° C.

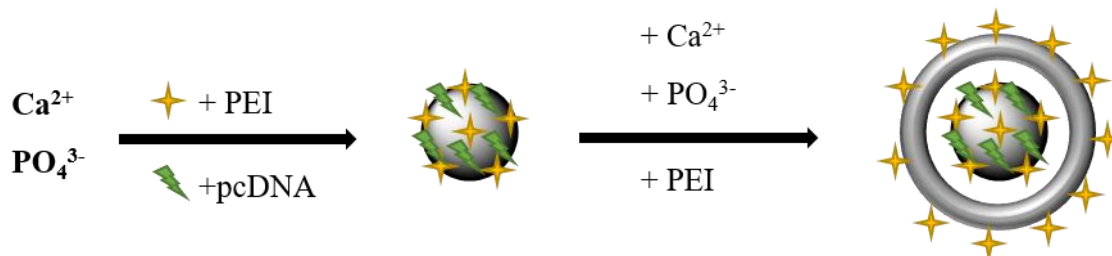


Figure 9: Schematic of the synthesis of single-shell and triple-shell of bioactive calcium phosphate nanoparticles and plasmid DNA.

### 4.1.4 Synthesis of CaP-PEI-siRNA-CaP-PEI [244, 245]

In order to synthesize the CaP/PEI/siRNA-EGFP/CaP/PEI, 1.57 mL of each solution: calcium-L-lactate (6.25 mM, pH 9) and diammonium hydrogen phosphate (3.74 mM, pH 9) were pumped together in an empty 50 mL beaker and stirred for 5 min at room temperature, allowing the nanoparticles to precipitate. The calcium phosphate nanoparticle dispersion (3.14 mL) was added to 630 μL PEI (2 g L<sup>-1</sup> in water) and stirred for 10 min. After purification by centrifugation (14,800 rpm, 15 min) and redispersion, 133 μg siRNA-EGFP (10 nmol) were added to the nanoparticles and stirred again for 10 min. Finally, 1.57 mL of each calcium-L-lactate and diammonium hydrogen phosphate solutions and 1.26 mL of PEI

solution were added subsequently to the above mentioned CaP-PEI/siRNA-EGFP and stirred for 15 min to obtain triple shell calcium phosphate nanoparticles. This product was centrifuged and purified once with ultra-pure water by 21,100 g for 15 min. The samples were dried in the lyophilizer together with 10-15 mg trehalose as a cryoprotectant per 1 mL of the solution. The dried samples were stored at -20 ° C.

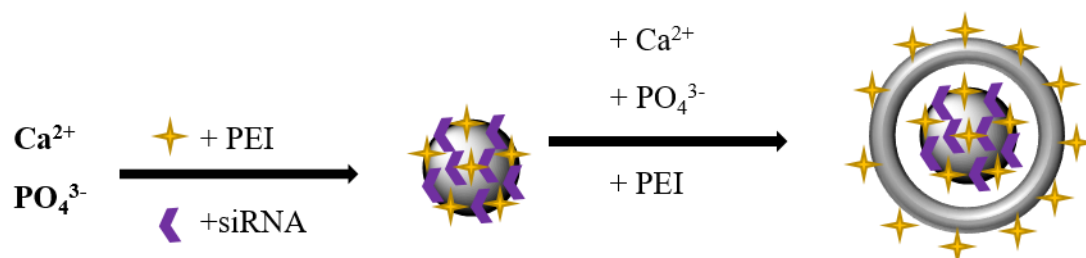


Figure 10: Schematic of the synthesis of single-shell and triple-shell of bioactive calcium phosphate nanoparticles with siRNA.

#### 4.1.5 Synthesis of labeled calcium phosphate-Rhodamine-PLGA nanoparticles [246]

The encapsulation of the labeled calcium phosphate-FITC-PLGA nanoparticles was carried out using a water-in-oil-in-water emulsion technique (Figure 11). For this purpose, calcium-L-lactate (6.25 mM, pH 9) and diammonium hydrogen phosphate (3.74 mM, pH 9) were pumped together in an empty 50 mL beaker and stirred for 5 min at room temperature. 40  $\mu\text{L}$  diluted PEI<sup>Rh</sup> was added to 210  $\mu\text{L}$  calcium phosphate solution and stirred for 5 min. In another beaker, 10 mg PLGA were dissolved in 750  $\mu\text{L}$  dichloromethane and mixed with 250  $\mu\text{L}$  of the labeled calcium phosphate PEI<sup>Rh</sup> nanoparticle dispersion (Figure 11 A). The two-phase system was emulsified with an ultrasonic disperser for 20 s (Figure 11 B) and the emulsion was then quickly inserted into a reservoir containing ice pieces. In the next step, resulting dispersion of B was added to an aqueous PVA solution (10  $\text{mg mL}^{-1}$ ) and emulsified for 20 s at the same settings (Figure 11 C). The emulsion was initially stirred for 3 h to clear out the dichloromethane completely. Figure 11 shows schematically the synthetic route of the polymer nanoparticles. The individual steps are named according to the previously assigned letters.

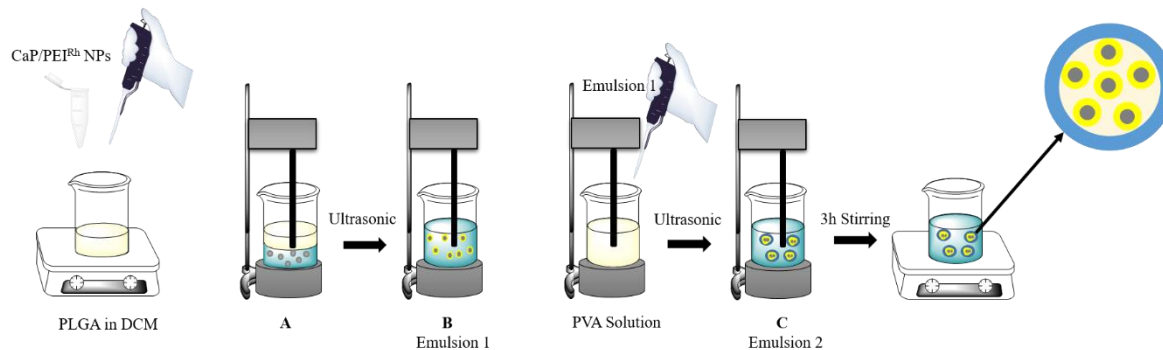


Figure 11: Schematic representation of the synthesis of the PLGA capsules with nanoparticles using a water-in-oil-in-water emulsion and the structure of a finished capsule. A: The PLGA solution is present alongside the dispersion of calcium phosphate particles. B: The particle dispersion is emulsified in the PLGA solution. C: PLGA capsules filled with the particle dispersion are in an aqueous PVA solution.

#### 4.1.6 Synthesis of calcium phosphate-DNA-PLGA-nanoparticles [246]

CaP-nucleic acid-PLGA nanoparticles were functionalized with pcDNA3-EGFP. The synthesis was the same as for the nucleic acids and was carried out as described above. First, 105  $\mu\text{L}$  of a calcium L-lactate solution (6.25 mM, pH 9) and 105  $\mu\text{L}$  of a diammonium hydrogen phosphate solution (3.74 mM, pH 9) were added to 40  $\mu\text{L}$  of a nucleic acid solution (4  $\text{mg mL}^{-1}$ ). This led to the precipitation of functionalized calcium phosphate nanoparticles with DNA after rotating for 5 min. This colloidal dispersion was then added to the 750  $\mu\text{L}$  of PLGA solution (13.3  $\text{mg mL}^{-1}$ ) dissolved in dichloromethane, which was cooled with ice before and emulsified with an ultrasonic sonotrode (MS3, pulse 0.8, amplitude 70 %) for 20s. This emulsion 1 (E1) was immediately emulsified in 3 ml of 1 % polyvinyl alcohol solution while cooling with ice and emulsified again with ultrasonic sonotrode for 20s. This emulsion 2 (E2) was stirred at room temperature until the evaporation of the dichloromethane led to the precipitation of the CaP nucleic acid PLGA particles (approx. 3 h). The dispersion was purified by centrifugation (30 min, 14,800 rpm). After redispersion, the particles were lyophilized (0.32 mbar, 10 °C).

#### 4.1.7 Synthesis of calcium phosphate-siRNA-PLGA nanoparticles [246]

Encapsulation of CaP-siRNA-PLGA was synthesized with RNA tumor necrosis factor- $\alpha$  (siRNA-TNF- $\alpha$ , 5'-GCCGAUGG-GUUGUACCUUG-3', Dharmacon). 105  $\mu\text{L}$  of a calcium L-lactate solution (6.25 mM, pH 9) and 105  $\mu\text{L}$  of a diammonium hydrogen phosphate solution (3.74 mM, pH 9) were added dropwise to 40  $\mu\text{L}$  of a siRNA solution (66.5  $\mu\text{g}$

siRNA) and stirred for 5 min. After precipitation of functionalized calcium phosphate nanoparticles with siRNA, this colloidal dispersion was added to 750  $\mu\text{L}$  of ice-cooled PLGA solution ( $13.3 \text{ mg mL}^{-1}$ ) in dichloromethane and emulsified with an ultrasonic sonotrode (MS3, pulse 0.8, amplitude 70 %) for 20s. This water in oil solution, then was added directly to 3 mL of ice-cooled 1 % poly (vinyl) alcohol solution and emulsified with ultrasonic for 20s and stirred 3h to dispose of excess dichloromethane. The w/o/w dispersion was purified by centrifugation (30 min, 14.800 rpm). After redispersion the particles were lyophilized (0.32 mbar,  $10 \text{ }^\circ\text{C}$ ).

### **4.1.8 Synthesis of labeled strontium-doped calcium phosphate-fluorescent dye nanoparticles [65]**

Strontium-doped calcium phosphate nanoparticles were synthesized according to Kozlova et al. [65], and strontium in concentrations of 5 %, 10 %, 15 %, and 20 % molar ratio were used. Calcium phosphate and strontium phosphate nanoparticles were also used as control. As an example for strontium-doped calcium phosphate nanoparticles, synthesis of 5 % strontium-doped calcium phosphate nanoparticles is explained at this point. To begin with, 1.75 mL calcium lactate pentahydrate ( $\text{C}_6\text{H}_{10}\text{CaO}\cdot 5 \text{ H}_2\text{O}$ ) (4.54 mM, pH 10.0), 1.75 mL strontium nitrate (0.24 mM, pH 10.0), and 3.5 mL diammonium hydrogen phosphate solution (2.77 mM, pH 10.0) were pumped together using a peristaltic pump at  $5 \text{ mL min}^{-1}$  and stirred for 5 min. To stabilize the particles, 7 mL of solution was added to 1.5 mL of PEI solution ( $2 \text{ g L}^{-1}$ ), stirred for 20 min at 600 rpm. The dispersion was then centrifuged for 15 minutes at 21,100 g and the particles were redispersed in the desired medium.

In order to mark the nanoparticles with fluorescent dye, Rhodamine-labeled PEI (PEI<sup>Rh</sup>) from Surflay Nanotec GmbH was used. The labeled PEI was used diluted 1:10 to 1:20 with unlabeled PEI.

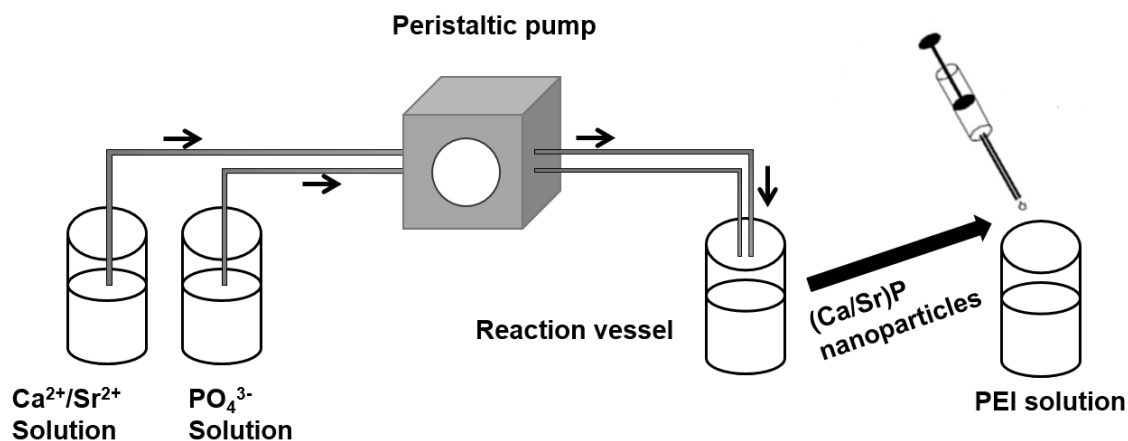


Figure 12: Schematic representation of the synthesis of the strontium-doped calcium phosphate nanoparticles

#### 4.1.9 Synthesis of labeled magnesium-doped calcium phosphate-fluorescent dye nanoparticles [65]

Comparable to the synthesis of strontium-doped calcium phosphate nanoparticles, magnesium was also used in concentration of 5 %, 10 %, 15 %, and 20 % molar ratio. Calcium phosphate and magnesium phosphate nanoparticles were correspondingly developed as control. Synthesis of 5% magnesium-doped calcium phosphate nanoparticles was attained with pumping a volume of 1.75 mL calcium lactate pentahydrate solution ( $C_6H_{10}CaO \cdot 5 H_2O$ ) (4.54 mM, pH 10.0), 1.75 mL magnesium sulphate solution (0.24 mM, pH 10.0), and 3.5 mL diammonium hydrogen phosphate solution (2.77 mM, pH 10.0) together using a peristaltic pump at  $5 \text{ mLmin}^{-1}$  and stirring for 5 min. Stabilization of the particles was achieved with adding 7 mL of the particle dispersion to 1.5 mL of PEI or CMC solution ( $2 \text{ g L}^{-1}$ ), and stirring for 20 min at 600 rpm. Finally, the resulting dispersion was centrifuged for 15 minutes at 21,100 g and the particles were redispersed in the desired medium. 10 %, 15 %, and 20 % doped magnesium-doped calcium phosphate nanoparticles were similarly synthesized. In order to mark the nanoparticles with fluorescent dye, Rhodamine-labeled PEI (PEI<sup>Rh</sup>) from Surflay Nanotec GmbH was used for positive nanoparticles and FITC-labeled CMC (CMC<sup>FITC</sup>) was developed for negative nanoparticles.

## 4.2 Synthesis of gold nanoparticles

### 4.2.1 Synthesis of ultrasmall gold-glutathione-FITC nanoparticles [247, 248]

For the synthesis of glutathione-protected ultrasmall gold nanoparticles (denoted as Au-GSH in the following) in an adapted Brust-Schiffrin synthesis [247, 248], 2.5 mL tetrachloroauric (III) acid (20 mM, 50  $\mu\text{mol}$ ) and 46 mg glutathione (150  $\mu\text{mol}$ ) were dissolved in 30 mL degassed water. After 30 min stirring time, 2 mL of a freshly prepared solution of sodium borohydride (250 mM, 500  $\mu\text{mol}$ ) was added to the mixture and stirred further for 30 min. The product was purified by spin filtration (3 kDa molecular weight cutoff; Amicon; Merck) for 40 min at 4000 rpm (2500 g). The gold nanoparticles precipitated at low pH (ca. 3). The precipitated product was redispersed in 15 ml 0.1 mM NaOH and centrifuge filtrated twice. Fluorescein isothiocyanate (FITC) was used for reactive amino labelling of Au-GSH nanoparticles. 10 mg of NHS-Fluorescein was dissolved in 100  $\mu\text{L}$  dimethylformamide (DMF) and added to a solution of 1 mg freeze-dried particles dissolved in 5 mL borate buffer (pH = 8.5). The mixture was stored in the fridge for 48 h at 8  $^{\circ}\text{C}$  and then centrifuged filtrated several times for 40 min at 4000 rpm (2500 g) to remove the nonreacted NHS-fluorescein until the filtrate was colorless. These particles are denoted as Au-GSH-FITC in the following.

### 4.2.2 Synthesis of ultra-small gold-BSA and gold-BSA-AF555 nanoclusters [249]

Synthesis of gold BSA nanoclusters (denoted as Au-BSA in the following) was accomplished according to Xie et al.,[249] aqueous  $\text{HAuCl}_4$  solution (5 mL, 10 mM, and 37  $^{\circ}\text{C}$ ) was added to BSA solution (5 mL, 50  $\text{mg mL}^{-1}$ , 37  $^{\circ}\text{C}$ ) under vigorous stirring. NaOH solution (0.5 mL, 2 M) was added 2 min later, and the reaction was allowed to proceed under stirring at 37  $^{\circ}\text{C}$  for 16 h. The product was purified by ultracentrifugation at 66.000 g for 12 hours.

BSA in the nanoclusters was additionally functionalized with Alexa Fluor™ 555 (AF555, C2 Maleimide). 200  $\mu\text{L}$  AF555-C2-maleimide was added to a BSA (10 mL, 50  $\text{mg mL}^{-1}$ , and 37  $^{\circ}\text{C}$ ), stirred for 5 minutes and remained for 1 hour in room temperature to react completely. Then the labelled Au-BSA-AF555 was centrifuged three times at 14,000 g for 15 min with 500  $\mu\text{L}$  spin filter tube and then used for the synthesis of gold-BSA-AF555 nanoclusters.

### 4.3 Freeze drying

Freeze drying is also known as lyophilization and is a gentle process for drying aqueous solutions and dispersions. In this work freeze drying was used to increase the stability of the colloidal dispersions. Furthermore, freeze-dried nanoparticles were used to load capsules and suppositories, which were supposed to transport the active ingredients in the body to the necessary tissues. The addition of suitable cryoprotectants before freezing, such as trehalose, can protect the sample from stress during freezing and drying. The protection is usually based on the immobilization of a substance through the formation of a matrix by the cryoprotectant [235].

In this work an Alpha 2-4 LSC freeze dryer was used. Samples were first shock frozen in liquid nitrogen. The water was then sublimed at 0.32 mbar and -10 °C. The condenser had a temperature of -85 °C. Functionalized calcium phosphate dispersions contained 10-20 mgmL<sup>-1</sup> trehalose as a cryoprotectant. For the gold nanoparticle and nanocluster dispersions, trehalose was also added as a cryoprotectant to the colloidal particles in the weight ratio of 100 to 1 gold. Afterwards the dried mixtures were analyzed with UV-Vis to calculate the amount of dyes and percentages of elements such as calcium (in samples containing calcium) and gold (in the samples containing gold) in the whole dried sample by using a calibration curve together with AAS results.

### 4.4 Cell culture experiments

In this work, HeLa (human cervical epithelial carcinoma) cell line, HeLa-EGFP cell line, Caco-2 (colon carcinoma), MG-63 (Human osteosarcoma), and MC3T3 (mouse osteoblast precursor) were studied. HeLa, MG-63 and Caco-2 were cultivated in Dulbecco's Modified Eagle's medium (DMEM) supplemented with 10 % fetal bovine serum (FBS), 100 U mL<sup>-1</sup> penicillin, 100 U mL<sup>-1</sup> streptomycin, and 1 mM sodium pyruvate at 37 °C in 5 % CO<sub>2</sub> atmosphere. HeLa-EGFP cell line was cultivated in DMEM with 10 % FBS, 100 U mL<sup>-1</sup> penicillin, and 50 µg mL<sup>-1</sup> Geneticin. MC3T3 cell line was cultivated in Minimum Essential Medium Eagle alpha modification ( $\alpha$ -MEM) with 10 % FBS and 100 U mL<sup>-1</sup> penicillin.

#### 4.4.1 Seeding the cells

In order to seed the cells for the investigations, cells were washed 2 to 3 times in the culture flask with 5 mL PBS and then incubated with 500 µL trypsin at 37 °C for 3 to 5 min and then rinsed with 5 mL DMEM to stop the trypsin. The cells were detached from the bottle

and suspended by rinsing the culture bottle several times with the medium. The cell suspension was transferred to 15 mL centrifuge tubes and centrifuged for 3 min at 900 rpm. The supernatant was discarded and the cells redispersed in 5 mL medium.

### 4.4.2 MTT test

Cytotoxicity of the samples was determined after treating the cells with nanoparticles for 24 hours. The freeze-dried nanoparticles with trehalose were redispersed in DMEM or  $\alpha$ -MEM in the corresponding concentrations. The cells were then washed two to three times with 500  $\mu$ L PBS and covered with 500  $\mu$ L of redispersed nanoparticles in cell medium. The cells were incubated for 24 h at 37 °C in a humid atmosphere and 5 % CO<sub>2</sub>. To prepare the reagent for staining living cells, 8 mg (3-(4, 5-dimethylthiazol2-yl)-2, 5-diphenyltetrazolium bromide (MTT)) were first dissolved in 1.6 mL PBS and diluted with 6.4 mL cell medium. The cells were washed three times with 500  $\mu$ L PBS and incubated with 300  $\mu$ L of the MTT reagent for 1 h in the incubator. The supernatant was then aspirated and the cells covered with 300  $\mu$ L DMSO. After 30 min at room temperature, the supernatant was added in triplets 100  $\mu$ L each was transferred to a 96-well plate and the absorbance at 570 nm was determined using a Multiskan FC from Thermo Fisher Scientific Inc. Untreated cells and DMSO without the cells were used as controls.

### 4.4.3 Uptake of nanoparticles in cells

To ensure that nanoparticles can be absorbed by cells, cell uptake studies were performed using confocal laser scanning microscopy (CLSM) and digital microscope on HeLa, Caco-2, MG-63, and MC3T3 cells with the green fluorescent particles dyed with FITC or the red fluorescent nanoparticles dyed with rhodamine (Rh). For this purpose, HeLa cells were first seeded in an 8-well  $\mu$ -Slide plate ( $2 \cdot 10^4$  cells per well) and for 24 h at 37 °C and 5 % CO<sub>2</sub> atmosphere in cell culture for 24 h cultivated. The nanoparticle dispersion in cell culture then were given to the cells and incubated for 24 h. Subsequently, the cells were washed two to three times with 200  $\mu$ L PBS, fixated, colored and the nanoparticle uptake by the cells were analyzed by CLSM.

### 4.4.4 Transfection of cells

HeLa and Caco-2 cells were used for transfection by DNA-EGFP loaded calcium phosphate nanoparticles. To do the transfection studies, 20.000 cells per well were seeded in 200  $\mu$ L in  $\mu$ -Slide 8 wells and allowed to adhere for 24 h. The cells were washed three times with

200  $\mu$ L PBS each and incubated in 200  $\mu$ L samples dissolved in DMEM, corresponding to at least 1  $\mu$ g DNA per well. In order to remove non-absorbed nanoparticles from the cells, the cells were washed three times after 24 h with 200  $\mu$ L PBS and cultivated in DMEM for a further 48 h. As a positive control, the cells were treated with Lipofectamine and the plasmid pcDNA3.3EGFP. For this purpose, 1  $\mu$ g of the plasmid and 2  $\mu$ L Lipofectamine<sup>TM</sup>2000 were diluted in 50  $\mu$ L DMEM without additives and the solutions were combined by vigorous shaking before the mixture was incubated for 15 min. The mixture was then added to the cells and incubated for 6 h. The cells were then washed three times with 200  $\mu$ L PBS and cultivated further for 66 h. After the cultivation of the cells had been completed, they were fixated, stained and examined on a Leica SP8 Falcon.

For the microscopic evaluation, the cells were seeded in 24-well plates about 24 h before the addition of the nanoparticles. 25,000 cells were plated out per well and the protocol was done as above. The cells were then examined with a Keyence BZ900 microscope. For this purpose, images were recorded both in the transmitted light channel and in the fluorescence channel. The cells on the images were counted, and the transfection efficiency (TE (%)) could be calculated by the following formula.

$$TE(\%) = \frac{N(\text{fluorescent cells})}{N(\text{whole cells})} \cdot 100$$

### 4.4.5 Gene silencing

In order to silence EGFP in HeLa-EGFP cells with nanoparticles, HeLa-EGFP cells were seeded in 8-well plates 24 h before the addition of the nanoparticles. Colloidal dispersions of the nanoparticles were diluted with cell culture medium in order to obtain the desired concentration of siRNA. 200  $\mu$ L of the nanoparticles dispersed in DMEM was given to the cells and incubated for about 24 h. After incubation, the cells were washed and cell culture medium was exchanged. The cells were cultured for an additional 48 hours before gene silencing efficiency and microscopy were performed.

As a control, the cells were preserved with the commercially available transfection agent Lipofectamine and siRNA-EGFP. 0.28  $\mu$ g of siRNA-EGFP was mixed with 50  $\mu$ L cell culture medium without FBS. In a separate vessel, 1  $\mu$ L Lipofectamine reagent was mixed with 50  $\mu$ L cell culture medium without FBS. After incubation for 5 min, the two solutions were mixed together and incubated again for 20 min at room temperature. The mixture was then added to the cells and incubated for 6 h. The cells were subsequently washed three times

with 200  $\mu$ L PBS and cultivated further for 66 h. After the cultivation of the cells had been completed, they were fixated, stained and examined on a Leica SP8 Falcon.

For the microscopic evaluation, the cells were examined using a Keyence BZ900 microscope. For this purpose, images were recorded both in the transmitted light channel and in the fluorescence channel. The cells on both images were counted and the gene silencing efficiency (GS (%)) could be calculated by following Formula.

$$GS(\%) = \frac{(\text{nonfluorescent cells } [\%]) - (\text{nonfluorescent cells of the control } [\%])}{(\text{fluorescent cells of the control } [\%])} \cdot 100$$

### 4.4.6 Fixing and dyeing the cells

To study the cells with CLSM, the cells were fixated and their core and cytoskelett were dyed. For this purpose,  $\mu$ -slides with working volume of 150-200  $\mu$ L were used. After finishing the cells cultivation for uptake, transfection or gene silencing, the cells were washed three times with 200  $\mu$ L PBS and fixated with 150  $\mu$ L 4 % formaldehyde (PFA) at room temperature. After 20 minutes, the cells were washed three times with 200  $\mu$ L PBS each time and permeabilized with 150  $\mu$ L 0.1 % Triton-X100 for 5 minutes at room temperature before the actin staining. The actin staining was done with AlexaFluor<sup>TM</sup>647-Phalloidin or AlexaFluor<sup>TM</sup>488-Phalloidin depends on the dyes used in samples. To dye the cytoskelett, the cells were incubated in 150  $\mu$ L PBS with 2.5  $\mu$ L dye per well for 1 h at room temperature. The cells were then washed three times with 200  $\mu$ L PBS and the nucleus was stained with a 0.1 gL HOECHST33342 solution in PBS for 10 minutes. Finally, the cells were washed three times with 200  $\mu$ L PBS and stored in 200  $\mu$ L PBS.

### 4.4.7 ALP test

The alkaline phosphatase test of the strontium- and magnesium-doped calcium phosphate nanoparticles was performed as described in the protocol of the ALP kit from Alkaline Phosphatase Assay Kit (Colorimetric) (ab83369). HeLa cells were seeded into the 24-well plate at a density of 10,000 cells/well and incubated for 24 h. After removing the culture medium (DMEM), cells were treated with 500  $\mu$ L of DMEM medium containing strontium- or magnesium-doped calcium phosphate nanoparticles. Strontium- and magnesium-doped calcium phosphate nanoparticles were first freeze-dried with the cryoprotectant and then

redispersed in the cell culture. ALP activity was measured by a colorimetric method using Alkaline Phosphatase Assay kit following the manufacturer's protocol on days 7, 14, and 21. In order to perform the ALP test,  $10 \cdot 10^3$  HeLa cells were harvested in 24 well plate and incubated for 24 h. The cells were then washed with cold PBS. The nanoparticles were given to the cells and the cells were then incubated with the nanoparticles. The cells were incubated for further 7, 14, and 21 days. Every two to three days, the cell medium of the cells was changed.

To prepare the cells for ALP reaction, 96 well microplate was used. To begin, the 1 mM pNPP standard solution was prepared by diluting 40  $\mu$ L pNPP. 5 mM Standard was diluted in 160  $\mu$ L of Assay Buffer. Using 1 mM standard in 0, 10, 20, 30, 40, 50  $\mu$ L per well, prepare standard curve dilution.

Then, 20  $\mu$ L Stop Solution was added to the sample background control wells to terminate ALP activity in these samples and mixed well by pipetting up and down. 50  $\mu$ L of 5 mM pNPP solution was added to each well containing sample and background sample controls (Mock). Then 10  $\mu$ L of ALP enzyme solution was added to each pNPP standard well and mixed by pipetting up and down. The microplate was then incubated at 25 °C for 60 min protected from light. The enzyme will convert pNPP substrate to an equal amount of colored p-nitrophenol (pNP). The reaction was stopped in sample wells and standard wells by adding 20  $\mu$ L Stop Solution. The measurements were done by gently shaking the plate and measuring output at OD 405 nm on a microplate reader.

For calculating the ALP activity of the samples a standard curve was plotted and the line of the best fit to construct the standard curve was drawn. Then, the average of the duplicate reading for each sample was calculated. ALP activity ( $\mu\text{mol min}^{-1} \text{mL}^{-1}$  or  $\text{U mL}^{-1}$ ) in the test samples is calculated as:

$$\text{ALP activity (U mL}^{-1}\text{)} = \frac{A}{V \cdot T}$$

With:

A = amount of pNP in sample well calculated from standard curve ( $\mu\text{mol}$ ).

V = original sample volume added into the reaction well (mL).

T = reaction time (min).

## 4.5 Creating the transport vehicle

### 4.5.1 Filling and coating the capsule

Size "M" gelatine capsules for delivery into mice were obtained from Torpac Inc. (Fairfield, USA; volume 4  $\mu$ L; external diameter 1.27 mm; maximum length after closing 8.4 mm; capsule surface 31 mm<sup>2</sup>; weight about 2 mg; disintegration time in the stomach about 10 min; all data according to Torpac Inc.). To fill the capsules with solid, a funnel, a stand for the capsules, and a piston were all obtained from Torpac Inc. (Figures 13A and 13B). The capsules consist of a longer capsule body, and a slightly shorter cap. The capsule body was placed in the capsule stand with the funnel on top. Now, the capsule was filled with the cargo (freeze-dried nanoparticles and trehalose) with the help of the piston. Subsequently, the capsule was closed with the cap. The amount of the cargo was determined gravimetrically. The filled capsules were coated with polymers by dip-coating. For coating, the capsules were fixated in a custom-made PTFE capsule holder, consisting of a frame with a silicone mat (2 mm) attached to it (Figures 13). The silicone mat contained holes with a diameter of 1.2 mm. The capsules were fixated with one side in these holes, so that the major part of the capsule protruded from the holder. Now the capsule was immersed in the polymer solutions by dip-coating as explained below. After each coating step, the capsule was dried for 20 min at room temperature to remove the solvent.

To coat the capsules with EUDRAGIT L100, solution A: 8 g EUDRAGIT L100, 76 g acetone, 114 g isopropanol, and 2 g propylene glycol, and solution B: 42 g EUDRAGIT L100, 58 g acetone, 87 g isopropanol, and 13 g of propylene glycol, were prepared. For the coating, the capsule was immersed subsequently in solutions A and B twice from each side. After each coating step, the capsule was dried for 20 min at room temperature to remove the solvent.

For coating with EUDRAGIT-chitosan, solution C was prepared with 10 g ethanol, 0.8 g Eudragit L100, and 0.4 g chitosan. The capsules were immersed once in solution C and then solution B. In between, the capsule was dried for 20 min at room temperature.

For coating with cellulose acetate phthalate (CAP), solution D: 1 g CAP and 20 g acetone and solution E: 32 % solution of CAP with 47 g CAP and 100 g acetone, were prepared. For the coating, the capsules were dipped subsequently in solutions D and E twice from each side.

For coating with hydroxypropyl methylcellulose (HPMC) and EUDRAGIT, solution F: 5.6 g HPMC and 48.5 g ethanol/water (10:1=v:v) was prepared. The capsules were immersed first in solution F and then in solution B.

For coating with HPMC/poly (vinyl) alcohol (PVA)-EUDRAGIT, solution G was prepared: 2.5 g HPMC, 2.5 g PVA, and 45 g ethanol/water (10:1=v:v). The capsules were immersed first in solution G and then in solution B.

The final weight of each capsule was taken to determine the amount of coating polymer [124].

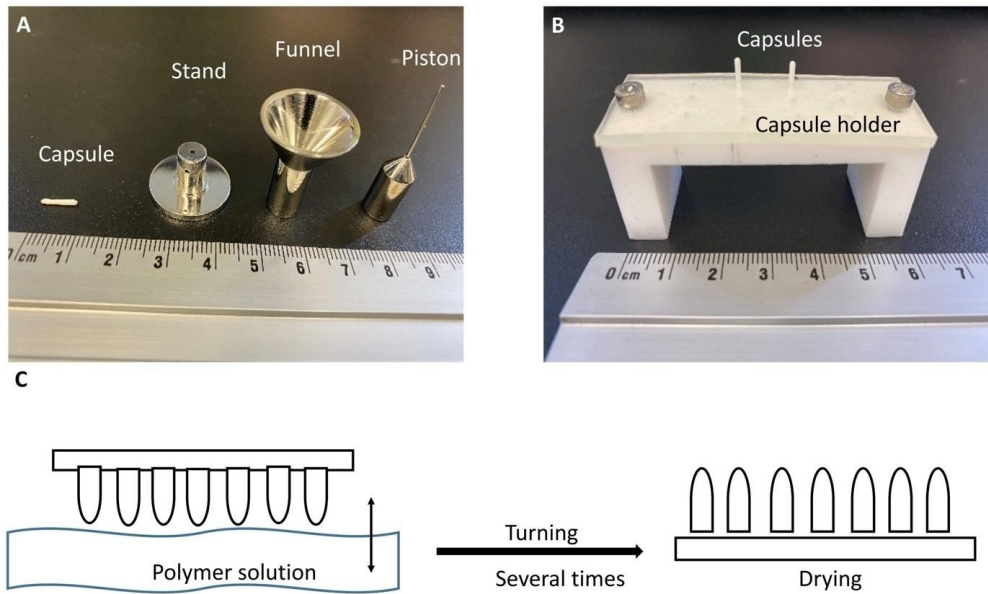


Figure 13. A: Capsule, stand, funnel, and piston to fill the gelatin capsule with freeze-dried calcium phosphate nanoparticles/trehalose; B: Capsule holder for dip-coating with enteric polymers; C: Schematic representation of the dip-coating process (C) [124].

#### 4.5.2 Making the suppositories

A PTFE mold (polytetrafluoroethylene) was used to prepare the hard-fat suppositories loaded with freeze-dried nanoparticles. The mold contained cylindrical holes of 2 mm diameter and 1.6 cm length. Hard fat was first melted in a syringe at 37 °C and mixed with the freeze-dried nanoparticles (about 0.25 mg of freeze-dried particles/trehalose per mg of hard fat). One end of the closed suppository mold was sealed with a gas-permeable membrane. The molten hard fat was then introduced with the syringe and then solidified at 4 °C in the refrigerator. The contents of nucleic acid, dye, and calcium phosphate, respectively, were computed from the mixing ratios and the mass of the suppository [127].

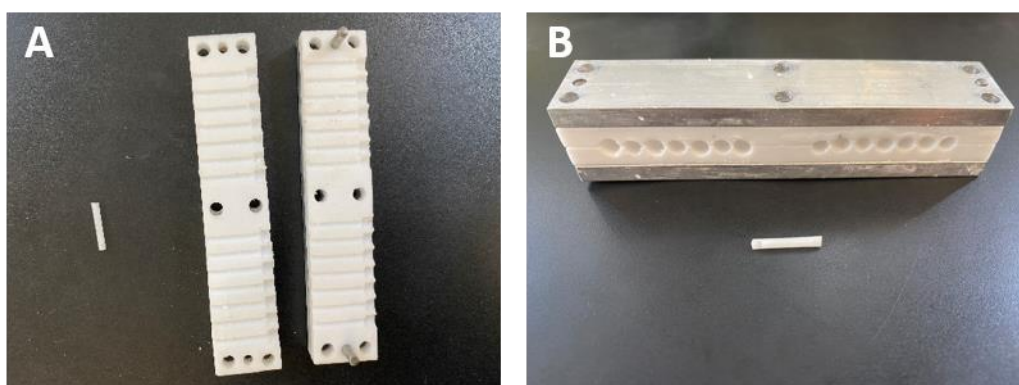


Figure 14. (A) Opened suppository former casting system and a suppository (15 mm·2 mm). (B) Closed suppository mold and a suppository

## **5 Results and discussion**

### **5.1 Calcium Phosphate nanoparticles**

In this chapter calcium phosphate nanoparticles were synthesized in order to fill them in gelatin capsules and suppositories for oral and rectal application methods. First the nanoparticles were characterized by SEM, DLS, UV/Vis spectroscopy and AAS. Afterwards the biological properties were characterized by cell uptake, transfection and gene silencing studies. To be able to track the particles in the cells, the particles were dye-labeled with FITC. The particles for transfection were loaded with EGFP and protected with a second shell of CaP and PEI. For gene silencing studies siRNA was introduced in the nanoparticles.

#### **5.1.1 Characterization of the CaP-nanoparticles for uptake and transfection studies**

Calcium phosphate nanoparticles, i.e. CaP/PEI-FITC and CaP/PEI/cEGFP-DNA/CaP/PEI were characterized by SEM, DLS, UV/Vis spectroscopy, and AAS. Figure 15 shows representative SEM images and DLS data of all particle types. The primary particles had a diameter around 50-60 nm (SEM) with a low degree of agglomeration in dispersion (diameter by DLS around 200 nm). The composition was estimated by taking the calcium content from AAS and converting it to calcium phosphate. Particles had a positive zeta potential due to the presence of the cationic polyelectrolyte PEI, whose positive charge was obviously not compensated by the presence of negatively charged nucleic acid. The properties of the three particle types are summarized in Table 1.

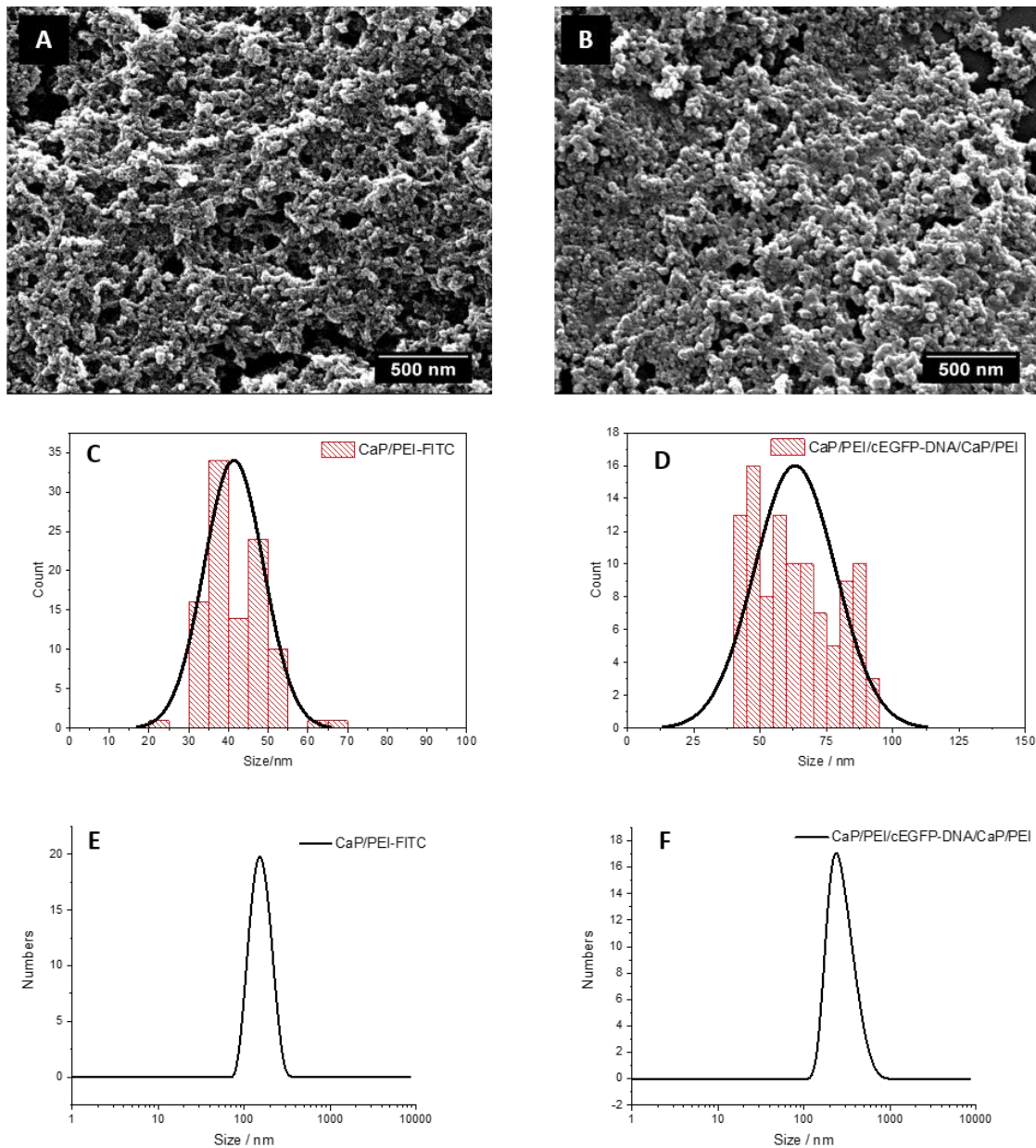


Figure 15. Scanning electron micrograph of CaP/PEI-FITC nanoparticles A) and CaP/PEI/cEGFP-DNA/CaP/PEI B), particle size distribution (C and D), and dynamic light scattering of calcium phosphate nanoparticles (E and F).

The content of nucleic acid was measured with UV/Vis (DeNovix DX11+). The DNA concentration measurement was carried out from the supernatants after centrifugation and the remaining mass of DNA on the particles was determined in the solution. The contents of nucleic acids and PEI-FITC were obtained by UV/Vis spectroscopy. And the content of calcium and therefore calcium phosphate was measured with AAS. After drying the nanoparticles with a certain amount of trehalose, the content of Ca, Nucleic acid, and dye could be measured in the whole dried sample. The content of each element is summarized in Table 1.

Table 1. Characterization of the functionalized calcium phosphate nanoparticles (mean  $\pm$  standard deviation). The contents of calcium, calcium phosphate (CaP), nucleic acid, and PEI-FITC were computed from the dispersion before mixing with trehalose and lyophilization.

Particle type	Size (SEM) / nm	Size (DLS) / nm	PDI	Zeta potential / mV	Ca content / wt %	CaP content / wt %	Nucleic acid content / wt %	PEI-FITC content / wt %
CaP/PEI-FITC	45 $\pm$ 8	150	0.16	18 $\pm$ 4	0.37	0.93	-	0.15
CaP/PEI/cEGFP-DNA/CaP/PEI	65 $\pm$ 23	230	0.33	16 $\pm$ 4	0.21	0.53	0.07	-

### 5.1.2 Uptake of calcium phosphate nanoparticles by different cells

Figure 16 shows the digital microscope images of the cells (HeLa, and Caco-2) after the incubation with calcium phosphate nanoparticles. A green fluorescence signal for FITC in the calcium phosphate nanoparticles could be detected in both cell lines indicating a successful uptake. Particle uptake by cells was similarly performed with confocal microscopy (Figure 17).

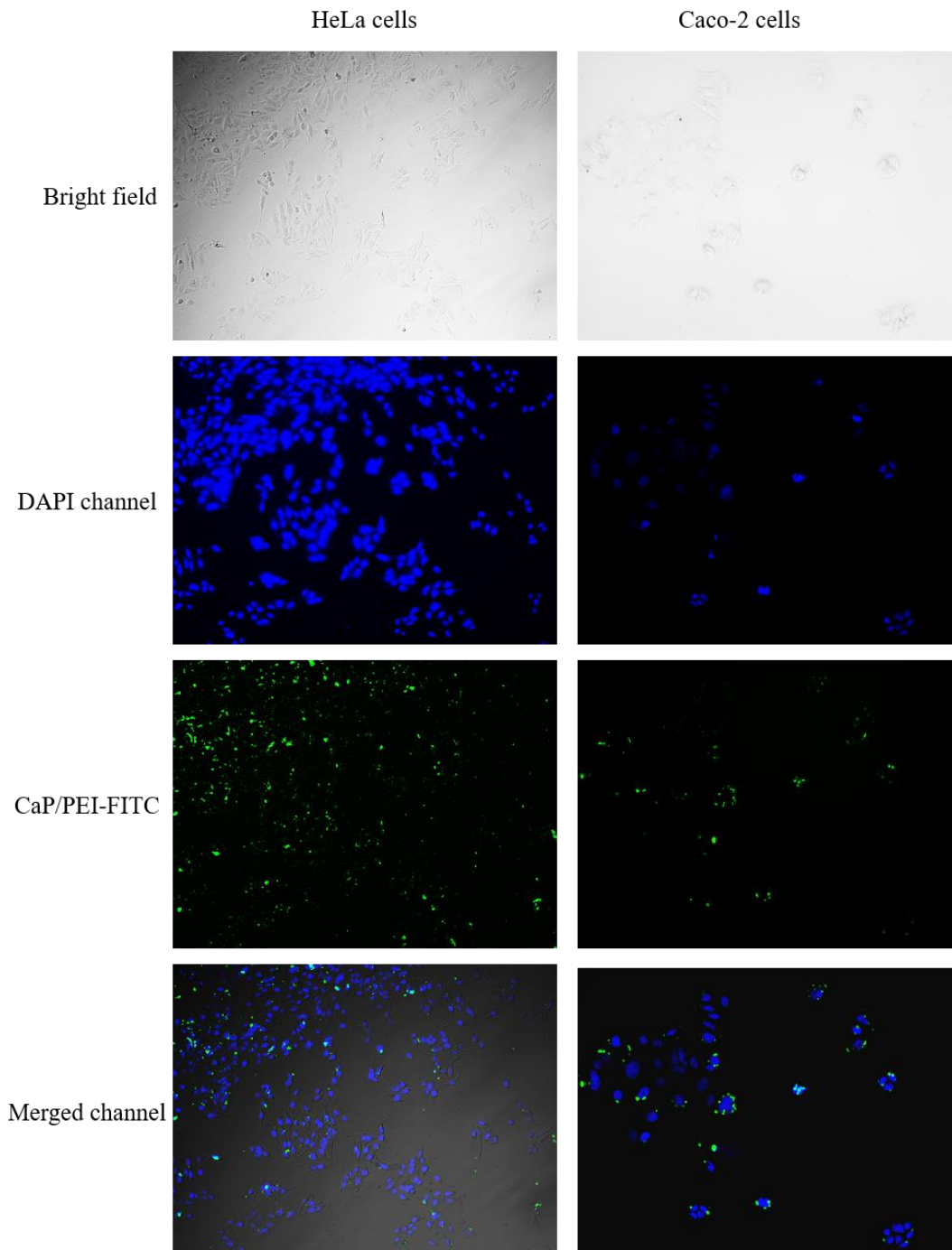


Figure 16: Microscopic images of cells after 24h uptake with CaP/PEI-FITC particles. The scale corresponds to 100  $\mu\text{m}$ , magnification: 10x.

Figure 17 shows the confocal microscopic images for the cells (HeLa, and Caco-2) after the incubation with calcium phosphate nanoparticles and a sample of untreated cells (Mock) as a control. No fluorescence in the wavelength range for FITC could be found in the Mock group. The fluorescence in this area came exclusively from the labeled nanoparticles. For CaP/PEI-FITC, a signal for FITC was detected in the cells for all types of particles. In order to be able to examine the distribution of the nanoparticles in the cell more precisely, images

were taken with a zoom factor (10x). These results clearly show that PEI-stabilized calcium phosphate nanoparticles are taken up in both cell lines. The concentration of nanoparticles in this study was  $3 \text{ mg mL}^{-1}$ .

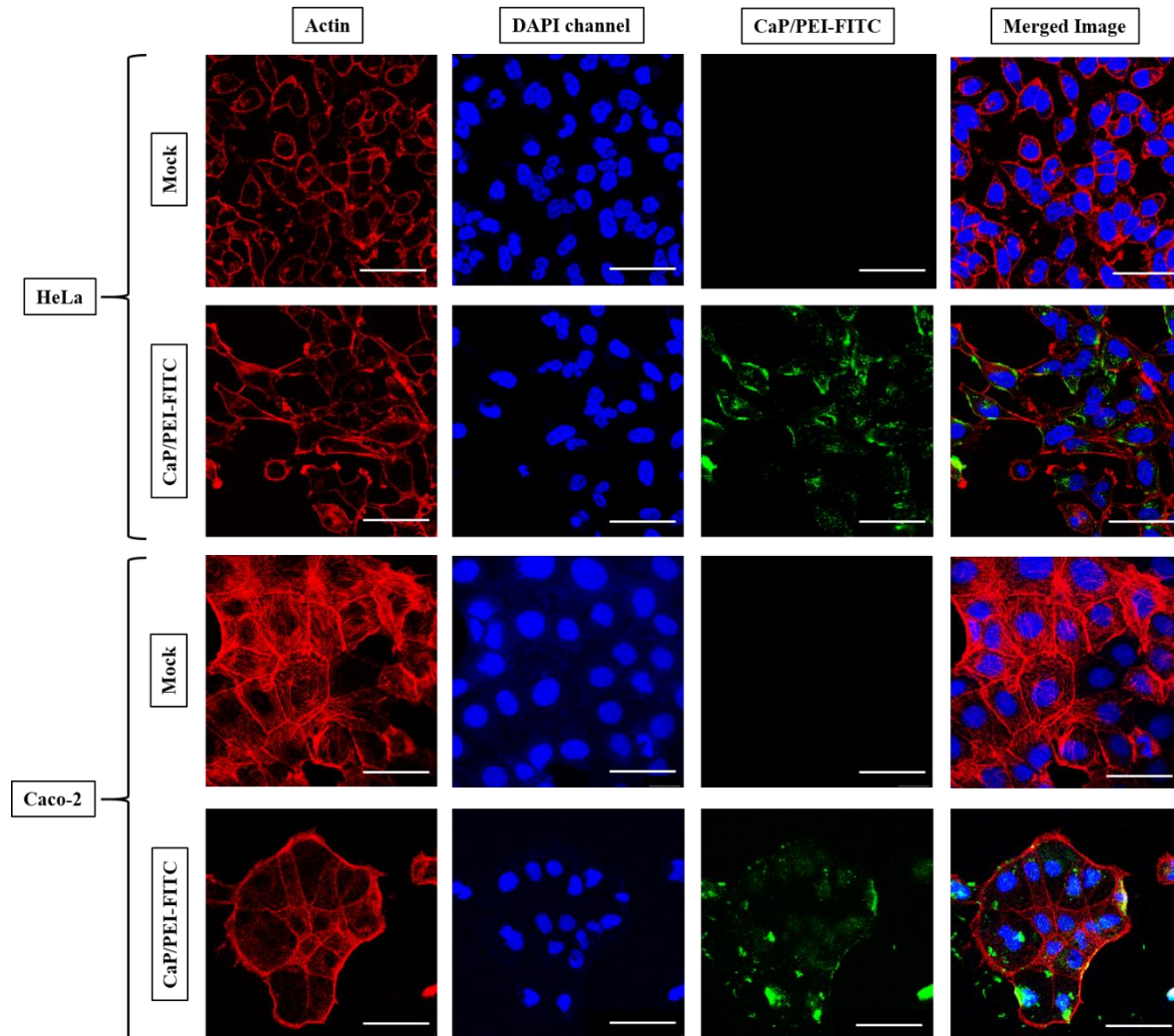


Figure 17: Confocal laser scanning microscopy images of HeLa cells and Caco-2 cells incubated for 24 h with dispersed CaP/PEI-FITC nanoparticles. Red: Actin; Blue: Nucleus; Green: CaP/PEI-FITC nanoparticles. Scale bar  $20 \mu\text{m}$ .

### 5.1.3 Calcium phosphate nanoparticle transfection by different cells

Figure 18 shows pictures of HeLa and Caco-2 cells which were incubated for 72 h with lipofectamine or calcium phosphate nanoparticles. Lipofectamine was used as a positive control due to its well-known transfection efficiency [250]. As indicated in the pictures below, the nanoparticles could penetrate the cell membranes of both cell lines for both particle types and release plasmid DNA into the cells. The green fluorescence of the cells confirms a

successful transfection process. To ensure the successful transfection process, confocal microscopy was also performed (Figure 20 and 21).

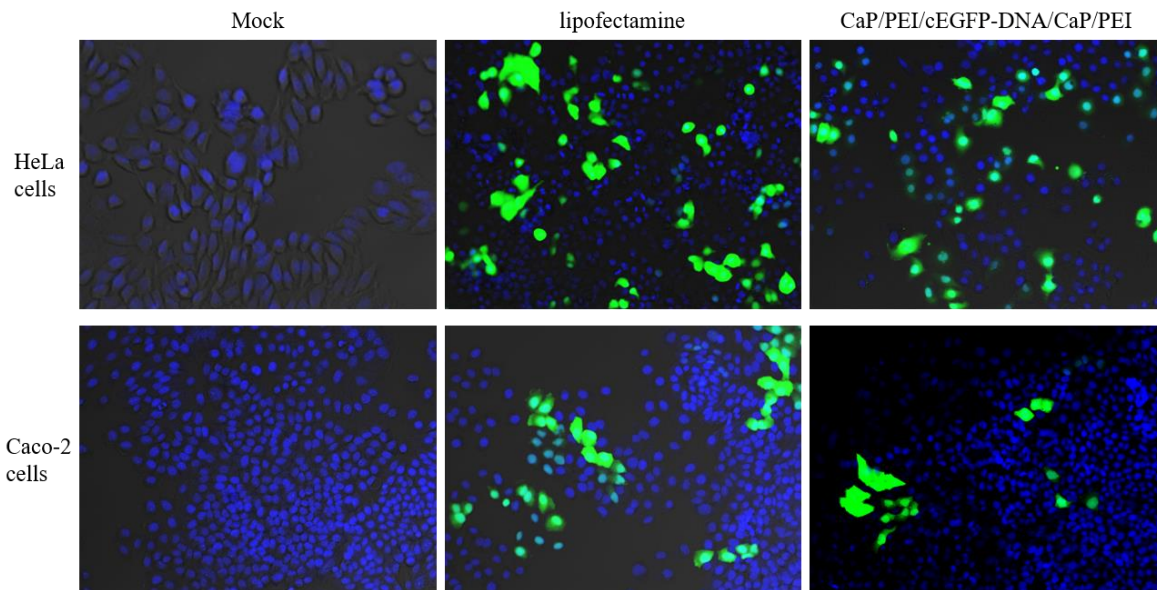


Figure 18: Light and fluorescence microscopic images of HeLa and Caco-2 cells after 72 h incubation with CaP/PEI/cEGFP-DNA/CaP/PEI nanoparticles. In comparison an untreated control group (Mock) and a positive lipofectamine control is also shown. Magnification 20x.

Transfection efficiency of the calcium phosphate nanoparticles was calculated by relating the green fluorescent cells to the total number of cells in the digital microscope images. Figure 19 shows the transfection efficiency graph of lipofectamine and the calcium phosphate nanoparticles by two different cell lines. Transfection efficiency of both lipofectamine and the nanoparticles is higher for the HeLa cells than the Caco-2 cells. Lipofectamine showed 21 % transfection efficiency by HeLa cells while DNA loaded calcium phosphate nanoparticles had 15 % transfection efficiency by HeLa cells. On the other hand, transfection efficiency of lipofectamine and DNA loaded calcium phosphate nanoparticles in Caco-2 cells were 11 % and 8 % respectively. According to these efficiencies, transfection in both cell lines occurred and efficiency showed appropriate expression percentage for both cell lines.

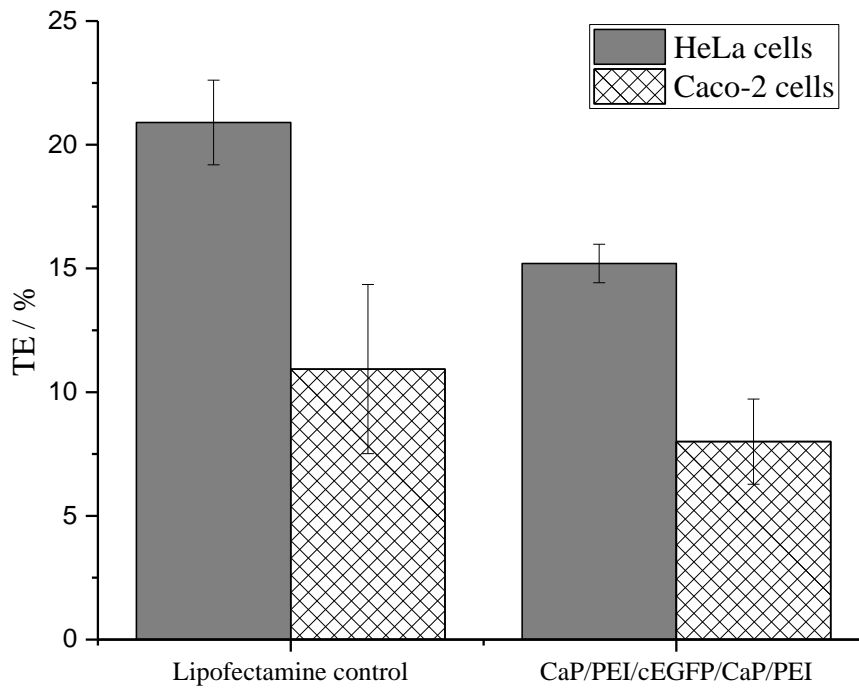


Figure 19: Evaluation of expression percentage of EGFP after the transfection. ( $\pm$  Standard error)

Biocompatible nanoparticles like calcium phosphate represent a non-cytotoxic carrier. Therefore, calcium phosphate nanoparticles were functionalized with the plasmid cEGFP-DNA and used in transfections of HeLa and Caco-2 cells to show general genetic activity. Figures 20 and 21 show the confocal microscopy images of HeLa and Caco-2 cells after 72 h incubation with nanoparticles. Cell morphology and EGFP fluorescence after transfection by HeLa and Caco-2 cells are recognized in these images. It was observed that in both cell lines the transfection occurred. Concentration of CaP/PEI/cEGFP-DNA/CaP/PEI used in these studies, was  $3 \text{ mg mL}^{-1}$ .

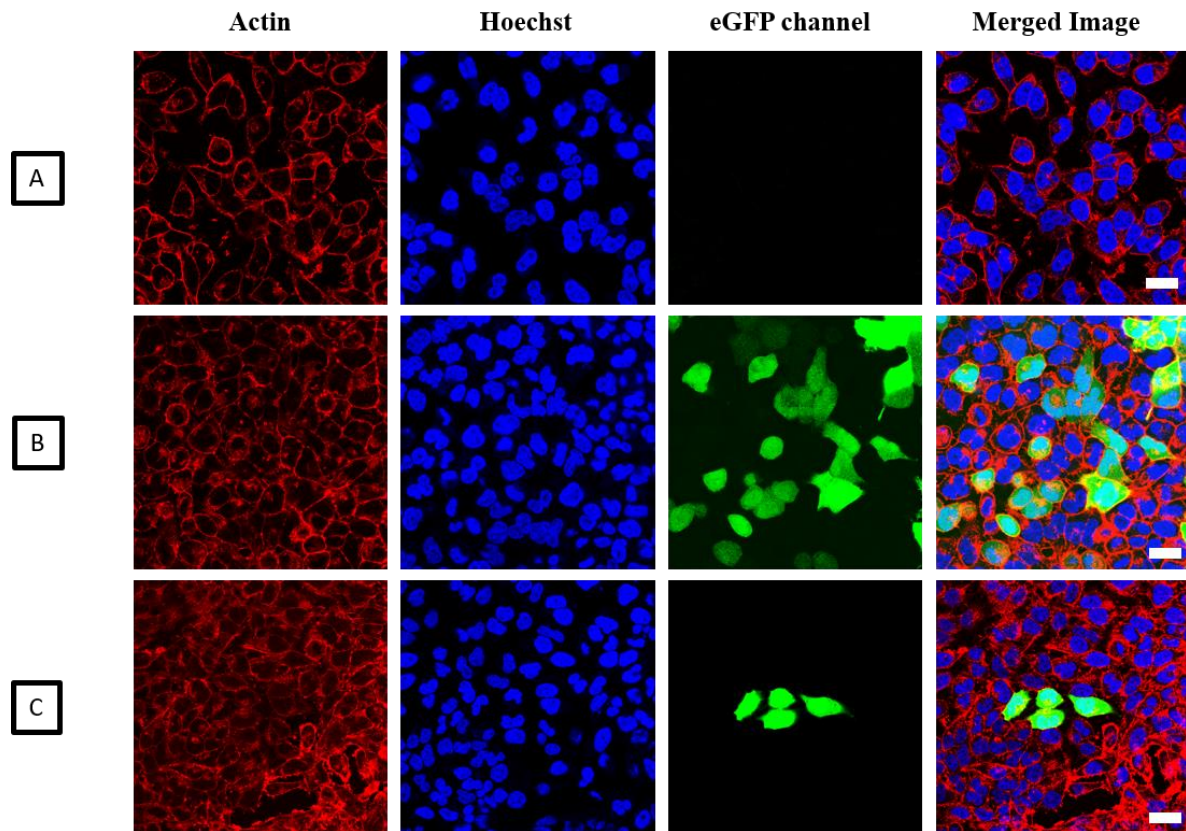


Figure 20: Confocal laser scanning microscopy images of HeLa cells after transfection for 72 h. Untreated cells (A); Lipofectamine control (B); and dispersed CaP/PEI/cEGFP-DNA/CaP/PEI nanoparticles (C). Red: Actin; Blue: Nucleus; Green: EGFP. Scale bar 20  $\mu$ m.

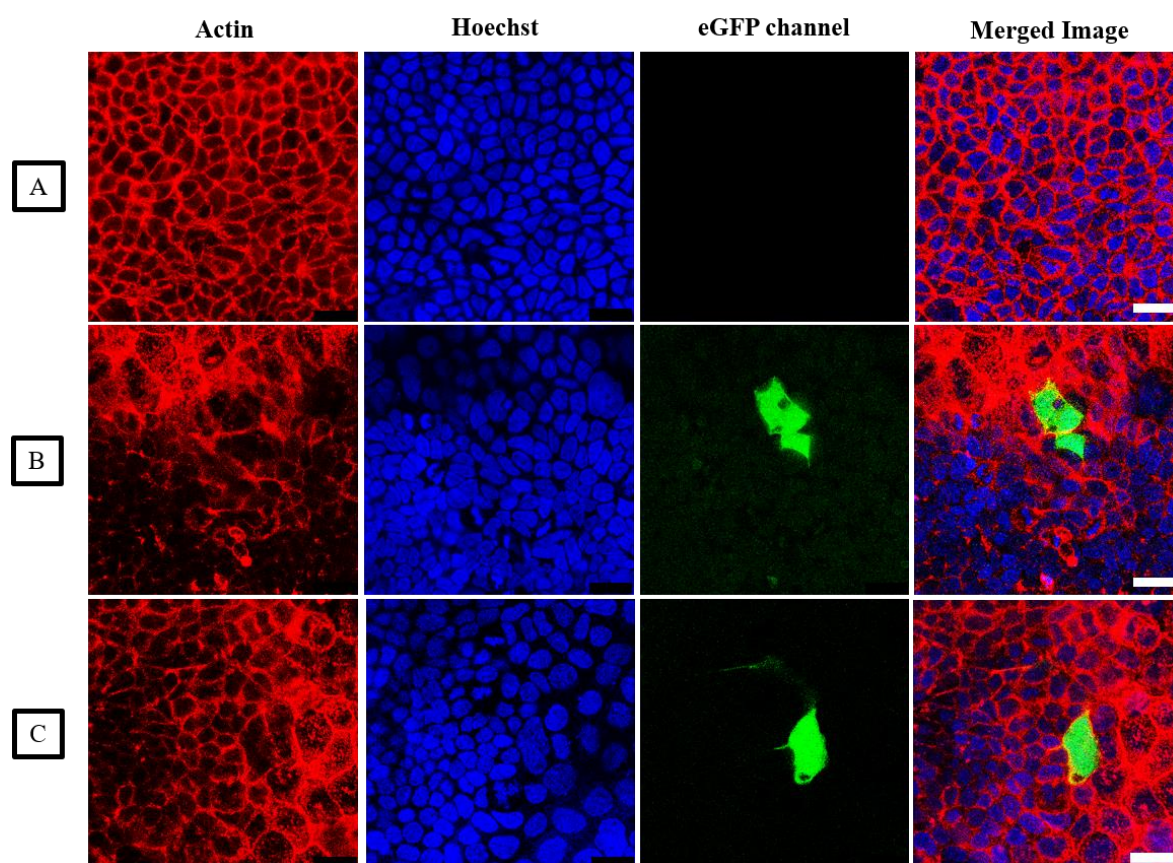


Figure 21: Confocal laser scanning microscopy images of Caco-2 cells after transfection for 72 h. Untreated cells (A); Lipofectamine control (B); and dispersed CaP/PEI/cEGFP-DNA/CaP/PEI nanoparticles (C). Red: Actin; Blue: Nucleus; Green: EGFP. Scale bar 20  $\mu\text{m}$ .

The obtained results prove a successful transfection and uptake by HeLa and Caco-2 cells with the synthesized calcium phosphate nanoparticles. Furthermore calcium phosphate nanoparticles are non-cytotoxic, biocompatible and easily applied *in vitro* and *in vivo* [251]. Therefore, these nanoparticles are suitable for further application in this work.

#### 5.1.4 Characterization of calcium phosphate nanoparticles for gene silencing

CaP/PEI/siRNA-EGFP/CaP/PEI nanoparticles were synthesized and characterized by SEM, DLS, UV/Vis spectrometry and AAS. Therefore, the colloidal properties, the size and morphology of the particles, the content of nucleic acids and the number of particles in the dispersion could be determined. Figure 22 shows representative SEM images and DLS data of the nanoparticles. SEM of the CaP/PEI/siRNA-EGFP/CaP/PEI nanoparticles showed spherical nanoparticles with a diameter of about 64 nm with a narrow size distribution. Dynamic light scattering showed colloidal stable nanoparticle dispersion with a polydispersity index (PDI) of 0.43, an average particle size of 200 nm (hydrodynamic

diameter) and a positive zeta potential of +16 mV. The specifications of particles are summarized in Table 2.

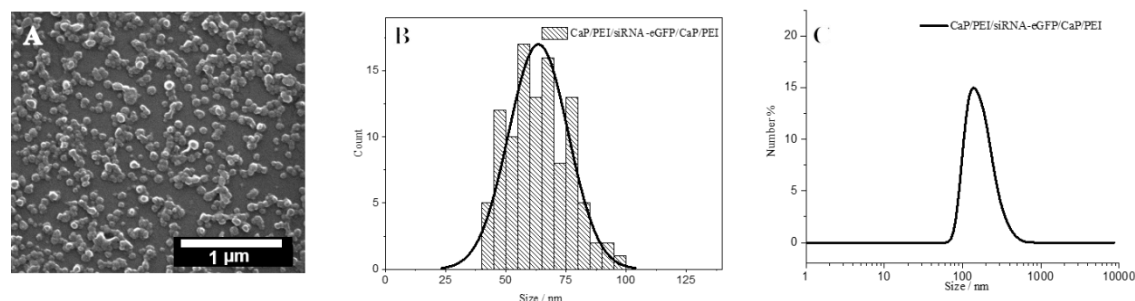


Figure 22. Scanning electron micrograph of CaP/PEI/siRNA-EGFP/CaP/PEI nanoparticles (A), particle size distribution (B), and dynamic light scattering of calcium phosphate nanoparticles (C).

The nanoparticles were then lyophilized with trehalose as a cryoprotectant in the ratio of 1:10. The content of nucleic acid was measured with UV/Vis. Concentration of siRNA was measured from the supernatants after centrifugation and the remaining mass of siRNA on the particles was determined. With the content of calcium measured by AAS, the amount of trehalose used for drying the particles and the content of Nucleic acid from UV/Vis, content of calcium phosphate, calcium, and nucleic acid in the whole dried sample could be calculated. All results were measured, collected and sum up in Table 2.

Table 2: Summary of the characterization of the functionalized calcium phosphate nanoparticles. ( $\pm$  Standard deviation)

Particle type	CaP/PEI/EGFP-siRNA/CaP/PEI
Diameter by SEM / nm	$64 \pm 12$
Diameter by DLS / nm	200
PDI by DLS	0.40
Zeta potential by DLS / mV	$16 \pm 3$
Ca content by AAS / wt %	0.38
CaP content / wt %	0.94
Nucleic acid content / wt %	0.15
Mass ratio CaP : nucleic acid	1 : 0.16

### 5.1.4 Silencing the EGFP in HeLa EGFP cells

Calcium phosphate nanoparticles can be prepared to direct the materials for a specific application like biomedicine. Due to its properties, calcium phosphate nanoparticles are an ideal siRNA carrier for gene transferring [252]. Here, a direct application of calcium phosphate nanoparticles loaded with siRNA-EGFP is described and evaluated in vitro.

The first step in gene silencing was to test the efficiency of the various particles used to silence specific genes on HeLa-EGFP cells. These cells expressed the green fluorescent protein EGFP, so that they could be visualized by using a fluorescence microscope. By comparing light and fluorescence microscopic images, the proportion of fluorescent cells could be determined. If the cellular synthesis of EGFP is prevented by means of siRNA, the proportion of fluorescent cells should decrease. For this purpose, approximately 1 mg of CaP/PEI/siRNA-EGFP/CaP/PEI and therefore 2.25  $\mu\text{g}$  of siRNA per well were added to the cells. The microscopic images after incubation with the different types of nanoparticles are shown in Figure 23. Gene silencing by the nanoparticles was compared in each case with an untreated control and with the muting efficiency of Lipofectamine. Figure 23 shows that nanoparticles dramatically reduced the expression of EGFP. The quantitative evaluation of the microscopic images or gene silencing percentage is summarized in Figure 24. In addition to the microscopic images, gene expression was also examined using confocal microscopy in Figure 25. In confocal microscopy, it is obvious that the calcium phosphate nanoparticles can reduce the expression of EGFP.

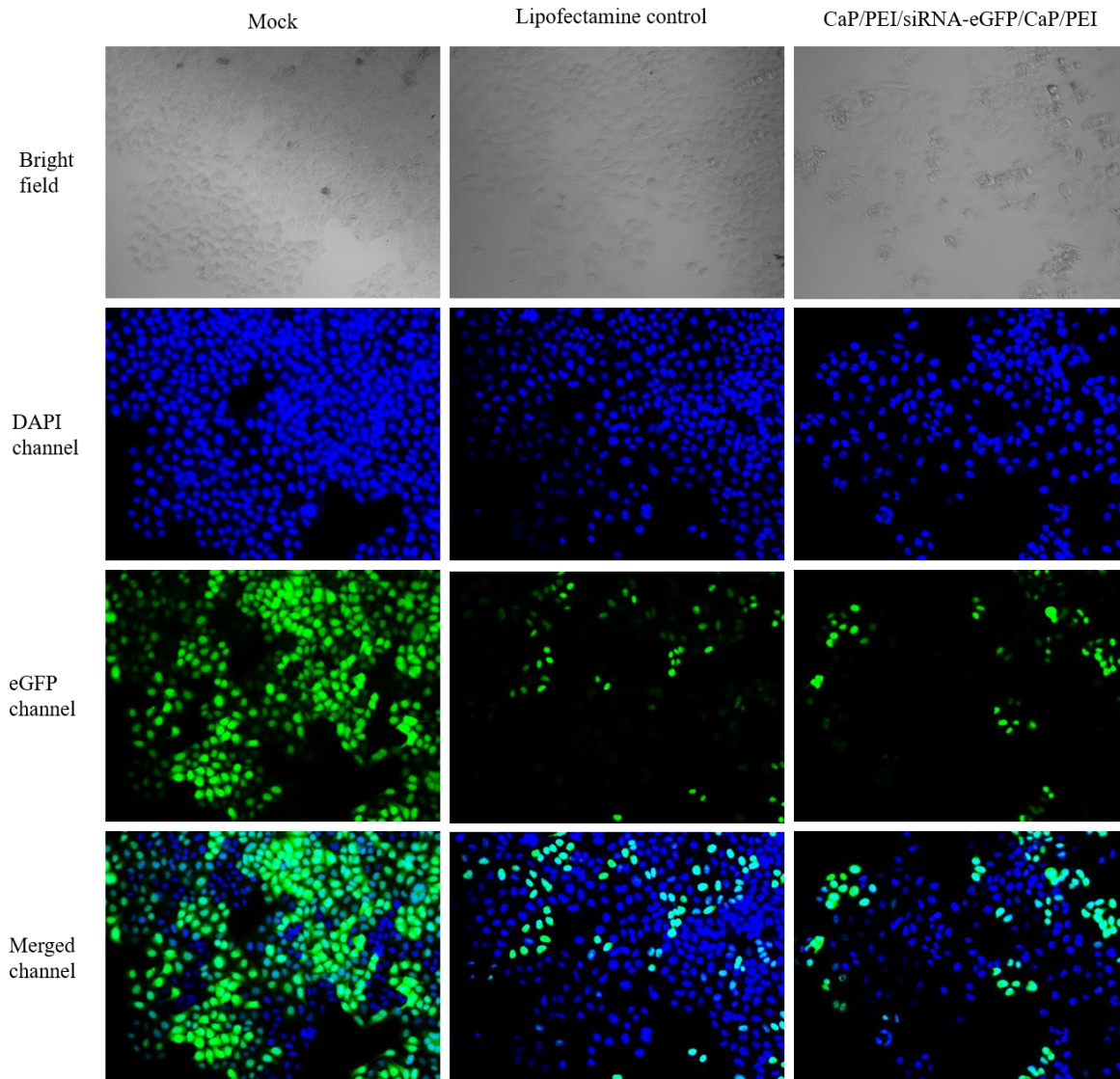


Figure 23: Microscopic images (Keyence) of HeLa-EGFP cells after incubation for 24 h with CaP/PEI/siRNA-EGFP/CaP/PEI particles. Magnification: 20x.

The gene silencing efficiency of nanoparticles carrying siRNA was studied. For this purpose, EGFP-expressing HeLa cells were used. The green fluorescence of EGFP was silenced by the corresponding siRNA (Figure 23). Expression of green fluorescent protein EGFP was dramatically decreased after 24 h incubation of the cells with bioactive calcium phosphate nanoparticles. This reduction in EGFP expression is comparable to the lipofectamine control indicating the good performance of nanoparticles in gene silencing.

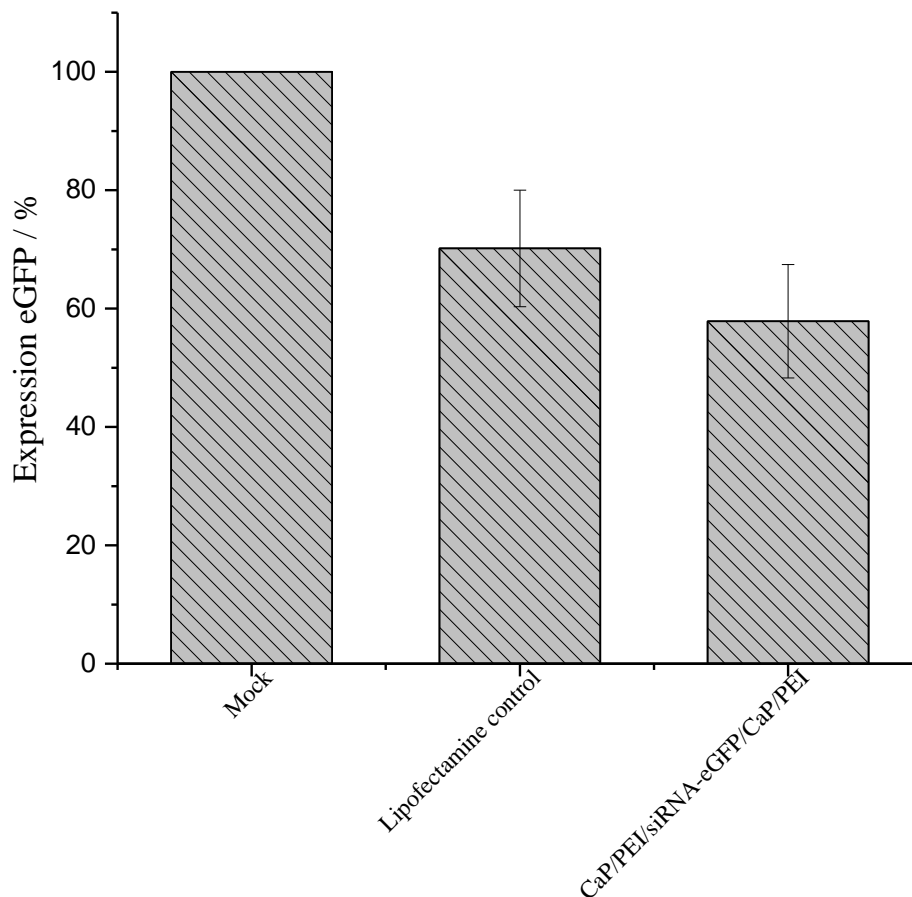


Figure 24: Expression of EGFP in HeLa-EGFP cells after silencing EGFP using CaP/PEI/siRNA-EGFP/CaP/PEI and Lipofectamine. The expression of EGFP in the control was defined as 100 %. The expression of EGFP after the muting was normalized to the control in order to indicate the percentage of expression.

Silencing efficiency is expected to vary between different cell lines [253, 254]. Some cells such as macrophages are more resistant to transfection and gene silencing because of releasing enzymes that can degrade nucleic acids after phagocytosis [255]. Here, as mentioned, HeLa-EGFP cell line is used and delivery of the nucleic acid (siRNA) into the cytosol is required [113]. Figure 24 showed the silencing efficiency of HeLa-EGFP cells with bioactive calcium phosphate nanoparticles. Gene silencing efficiency was obtained from the formula mentioned in section 4.4.5. In this formula and according to the digital microscope images (Figure 23), first the number of non-fluorescing cells in Mock is subtracted from the total number of non-fluorescing cells in the sample and the result is divided by the total number of fluorescing cells in the section. Silencing efficiency of the cells without treatment was considered as 100 %. The gene silencing efficiency was quantified by counting about 200–1000 cells per image and determination of the percentage of green-fluorescent cells. Figure 24 shows the results of gene silencing after evaluation of

gene silencing percentage. In this experiment, a successful gene silencing leads to a suppression of the green fluorescence. The efficiency of gene silencing by the lipofectamine control was 70 % and by the original nanoparticles was 58 %, which is only slightly less than the lipofectamine control. This result indicates that the functionalized calcium phosphate nanoparticles can be effective in gene silencing. This result shows that calcium phosphate nanoparticles can be applied as siRNA carriers for siRNA loading and *in vitro* transfection.

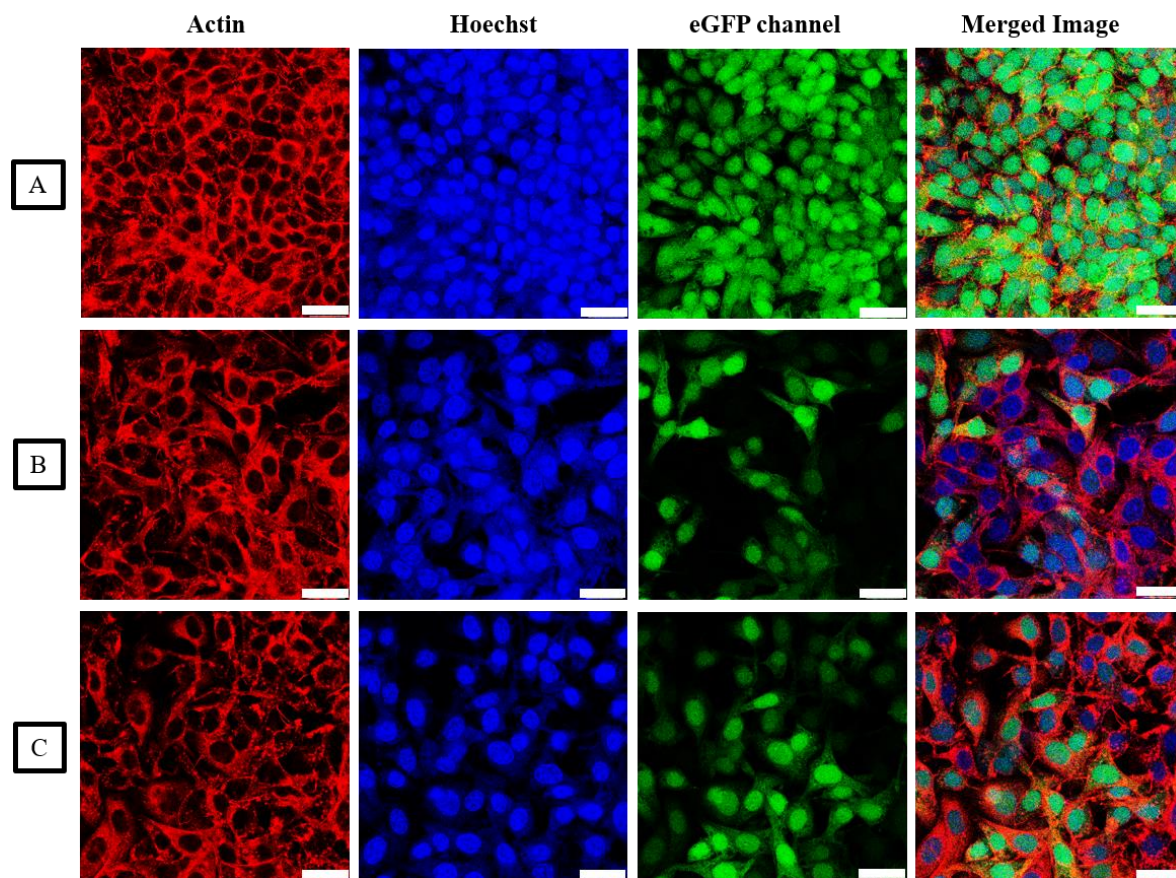


Figure 25: Confocal images of HeLa-EGFP cells after the EGFP was silenced with CaP/PEI/siRNA-EGFP/CaP/PEI nanoparticles. Untreated cells (Mock, A), and cells after 24 h incubating with Lipofectamine (B) and CaP/PEI/siRNA-EGFP/CaP/PEI nanoparticles (C). In the sample 2.25  $\mu\text{g}$  siRNA were used per well. Red:Actin cytoskeleton (stained with Alexa Fluor660-phalloidin); Blue: Cell nuclei (stained with Hoechst33342); Green: EGFP. The scale corresponds to 20  $\mu\text{m}$ .

To be more precise about the gene silencing with the functionalized calcium phosphate nanoparticles, confocal microscopy was performed (Figure 25). Again, HeLa EGFP cells and about 2.25  $\mu\text{g}$  siRNA per well were used and the cells were incubated for 24 h with the particles and lipofectamine. Untreated cells (Mock) and lipofectamine as a positive control

were used. According to the confocal images, gene silencing of the particles is successful and the particles are able to reduce the expression of EGFP in HeLa-EGFP cells. These results correspond with the digital microscope, the green fluorescent cells were reduced significantly in confocal images (Figure 25 C) showing that the bioactive calcium phosphate nanoparticles can silent the EGFP.

### 5.2 Transport of nanoparticles into the intestine

The particles can be transported into the intestine in two routes. The method that is more comfortable for the patient is certainly the oral ingestion of the particles. Before the particles can reach the intestine to be effective for treatment, they must first pass through the stomach. In the acidic environment of the stomach, however, calcium phosphate particles dissolve and the functionalization will be destroyed. To prevent this, freeze-dried functionalized calcium phosphate nanoparticles were placed in a soft gelatin capsule. The capsule was then coated with different pH-sensitive polymers such as Eudragit L100, CAP, HPMC, and polymer combinations. These polymers are insoluble in water at acidic pH values and therefore protect the particles from gastric acid. At pH values above 6, the polymers are water-soluble. Thus, they dissolve in the intestine, and after the gelatin capsule has dissolved, the particles can be released and deliver the drug for the treatment.

Alternatively, the particles can enter the intestine via rectal administration. For this purpose, a suppository was developed that also contained previously freeze-dried, functionalized calcium phosphate nanoparticles. The suppository consisted of adeps solidus (hard fat). The melting point of the hard fat is 35 °C. In the first step, the nanoparticles could be dispersed in the melted fat. In a suitable form, the fat solidified again at room temperature. At body temperature, the fat melts again to release the particles in the intestine. This part of the thesis describes the experimental characterizations, properties and in vitro tests of the transport vehicles loaded with functionalized calcium phosphate nanoparticles. MTT test, uptake, transfection and gene silencing studies were performed for the capsules and suppositories. For the cell uptake CaP/PEI-FITC, and for the transfection triple-shell functionalized (CaP/PEI/cEGFP-DNA/CaP/PEI) were used. In gene silencing, the green fluorescent protein EGFP was silenced in HeLa-EGFP cells. For this purpose, triple-shell functionalized calcium phosphate nanoparticles (CaP/PEI/siRNA-EGFP/CaP/PEI) were used.

### **5.2.1 Characterization of the transport vehicle (capsules)**

In order to be able to transport the particles into the intestine via oral administration, freeze-dried calcium phosphate nanoparticles were first filled into size M gelatin capsules. According to the manufacturer (Torpac Inc.), the capsules have a diameter of 1.27 mm and a length of 8.4 mm and are therefore suitable for transport into the intestines of mice after coating [256].

To obtain an enteric gelatin capsule, capsules had to be coated with enteric polymers. Among the commercially available polymers for colon-specific drug delivery are Eudragit L100, cellulose acetate phthalate (CAP), and hydroxypropyl methylcellulose (HPMC) [257]. Eudragit L100 and Eudragit S100 are anionic copolymers based on methacrylic acid and methyl methacrylate that are insoluble at low pH and soluble at pH 7 [258]. Cellulose acetate phthalate is a frequently used tablet-coating material employed to produce enteric films [259]. Hydroxypropyl methylcellulose which is a synthetic modification of the natural polymer cellulose is frequently applied as controlled drug release polymer [260]. It belongs to the family of hydrophilic polymers which swell and take on a gel form if in contact with water or organic solvents. The drug release rate can be controlled by changing the thickness of the layer and by adding chitosan to Eudragit L100 [261]. Polyvinyl alcohol (PVA) has been studied for use in drug release because it can fine-tune the release kinetics [262]. Therefore, two-layered HPMC/PVA Eudragit L100 coatings were also prepared. In that case, HPMC/PVA is applied as inner layer and Eudragit L100 is applied as outer enteric coating layer to prevent the dissolution in the dissolving of drugs in the acidic stomach medium [263]. Except chitosan, all polymers are water-soluble above a pH of 5–6. According to Pharmacopoeia Europaea (Ph. Eur.), enteric-coated drug forms must remain stable for at least 2 h in a simulated acidic stomach environment (0.1M HCl; pH 1) [142].

In the intestine, however, the pH value is between pH 6 and 8, depending on the section of the intestine. Thus, the polymers should prevent the capsules from degrading in the stomach. The rise in the pH value in the intestine would cause the polymer to dissolve, as a result of that capsules would also dissolve and release the nanoparticles.

The use of the coated gelatin capsule for the transport of nanoparticles was tested in vitro for the functionalized calcium phosphate nanoparticles as well as dye-labeled calcium phosphate nanoparticles. The characterization of the particles was described in Section 5.1.1 and 5.1.4. The characterization of the capsule filled with functionalized calcium phosphate nanoparticles and coated with enteric coating polymers is summarized in Table 3 for all types of particles.

Table 3. Characterization of nanoparticle-filled and polymer-coated capsules (mean  $\pm$  standard deviation). All numbers correspond to one capsule; the standard deviations illustrate the variation between the individually filled capsules. The capsule weight and the loading were recorded individually for each capsule and used to compute the loading of each capsule. The loading of nanoparticles with nucleic acids was determined spectrophotometrically. The ratio of nanoparticles/nucleic acid to trehalose was given by the lyophilization conditions.

Empty gelatin capsule weight/mg	2.3 $\pm$ 0.5
Loading with particles + trehalose/mg	2.8 $\pm$ 1.1
Content of Ca (CaP/PEI/cEGFP-DNA/CaP/PEI)/ $\mu$ g	5.9 $\pm$ 2.3
Content of CaP (CaP/PEI/cEGFP-DNA/CaP/PEI)/ $\mu$ g	14.8 $\pm$ 5.8
Content of Ca (CaP/PEI/siRNA-EGFP/CaP/PEI)/ $\mu$ g	10.6 $\pm$ 4.2
Content of CaP (CaP/PEI/siRNA-EGFP/CaP/PEI)/ $\mu$ g	26.3 $\pm$ 10.3
Content of Ca (CaP/PEI-FITC)/ $\mu$ g	10.4 $\pm$ 4.1
Content of CaP (CaP/PEI-FITC)/ $\mu$ g	26.0 $\pm$ 10.2
Content of cEGFP-DNA (CaP/PEI/cEGFP-DNA/CaP/PEI)/ $\mu$ g	2.0 $\pm$ 0.8
Content of siRNA (CaP/PEI/siRNA-EGFP/CaP/PEI)/ $\mu$ g	4.2 $\pm$ 1.7
Content of FITC (CaP/PEI-FITC)/ $\mu$ g	4.2 $\pm$ 1.7
Enteric coating layer/mg	3.0 $\pm$ 1.0

In oral delivery of protein and peptide drugs, delivering the medicinal agents selectively in the intestine needs suitable devices. It is essential that the drug-loaded carrier systems should be protected from the harsh environment of the stomach and deliver the cargo in the large intestine where drug action or absorption is desired. To do this, enteric-coatings are studied and among these polymers Eudragit L100 and CAP are chosen for this work. These polymer-coated capsules are not destroyed in acidic medium of stomach (pH 1-2) however, by reaching into the large intestine (pH 7-8), these polymers dissolve in intestine and nanoparticles are released [264]. Moreover, in order to achieve site and time specific drug delivery, combination of enteric polymers is used. In this method, gelatin capsules are coated with two polymers-coatings which the inner polymer-coating is water-soluble and the outer layer is pH resistant polymer.

Here, gelatin capsules were coated with various enteric coatings and different methods were used to deliver the bioactive calcium phosphate nanoparticles into intestine. Eudragit L100 and CAP were used to protect the capsules from being destroyed in stomach due to their well-known performance in different pH values. As shown schematically in figure 26 B, coated capsules are supposed to be protected by Eudragit L100 or CAP in stomach medium.

For site and time specific drug delivery system, Eudragit L100 were mixed with chitosan powder and coated the capsules. In this system, the chitosan powder in Eudragit L100 is considered to accelerate the release process.

Gelatin capsules were correspondingly coated first with HPMC or HPMC/PVA as an inner capsule-coating-polymers and then they coated with Eudragit L100 as an outer polymer-coating which gave the most promising result in protecting the capsules from being destroyed in stomach medium [265, 266].

In order to test the capsules in acidic medium similar to the stomach and in intestine like medium, simulations of these two media were carried out. The capsules were first inserted in 1.5 mL Eppendorf tubes containing simulated acidic medium of stomach (0.1 M HCL, pH 1) for 2 h. To simulate the temperature of human body, the Eppendorf tube was inserted in a beaker filled with water with the temperature of 37 °C. After 2 h, the capsules were taken out of the medium and let to be dried in room temperature. The capsules were then prepared for SEM characterization. Almost the same process was also done for the simulated intestine medium, as the capsules were inserted in the Eppendorf tube containing MOPS buffer, 0.15 M, pH 7.1, in the beaker with 37 °C water. After every 30 min the capsules taken out and dried in the room temperature and prepared for SEM. Figure 26 A shows the simulation process of the stomach and intestine, and Figure 27 shows the SEM images of the capsules.

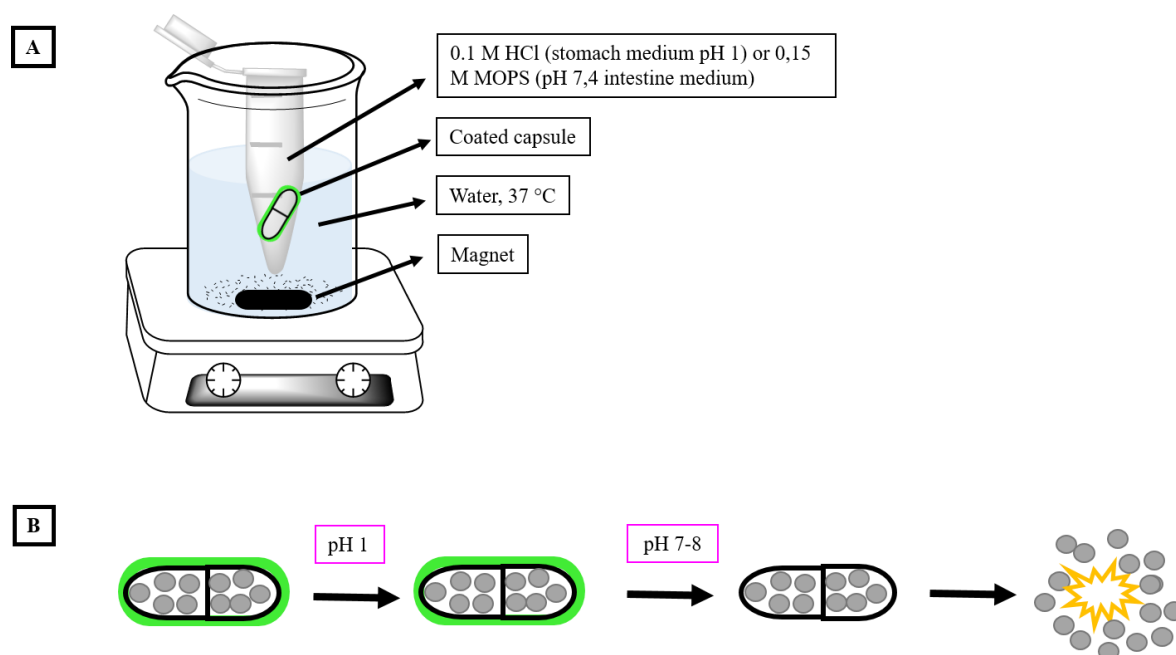


Figure 26: Schematic of the simulation of stomach or intestine process (A), schematic of capsule function in the stomach and intestine (B).

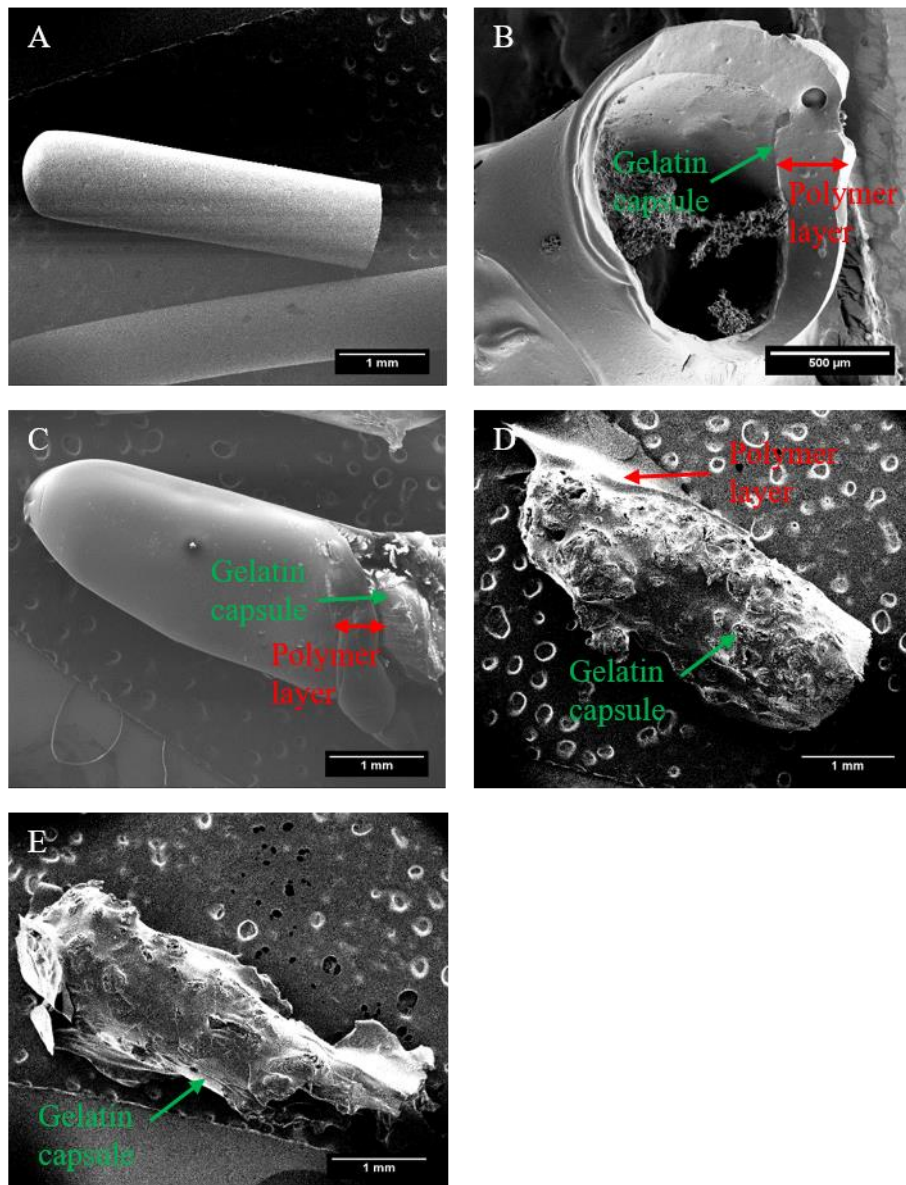


Figure 27: SEM images of soft gelatin capsule (A), Eudragit-coated gelatin capsule after being 2 h in acidic medium pH 1 (B), Eudragit-coated capsule after being in MOPS buffer with pH 7.1 for 30 min, (C), 60 min (D) and 90 min (E).

In order to check the physical changes of capsules after being in simulating stomach medium and intestine medium, SEM was used. Here, Eudragit L100 as an enteric-coating-polymer was used. A capsule was filled with calcium phosphate nanoparticles and this capsule was then coated with Eudragit L100 as an enteric coated polymer. This capsule was then inserted in acidic medium of stomach mentioned in figure 26 A and after 2 h, capsule was removed from the acidic medium of stomach, cut up and was given for SEM examinations. Figure 27 shows the SEM of soft gelatin capsule (A) and physical changes of the enteric coated

capsules in the acidic medium (B) and the intestine medium (C-E). SEM image of Eudragit-coated capsule (Figure 27, B) is the cross section SEM image to find out if the polymer has survived in acidic medium after 2 h and protected the capsule. A soft gelatin capsule as a control was also used (Figure 27, A). As it shown in Figure 27, the enteric coated capsule remained with minimal changes after being 2 h in the acidic condition so that the cargo was still in the coated capsule. Moreover, in SEM image (B) the layer of Eudragit around the gelatin capsule was seen which showed that this polymer survived in acidic medium of stomach and could protect the gelatin capsule and nanoparticles from releasing and dissolving in acidic medium. SEM image of the capsule showed that the capsule was stayed with negligible changes after being 2 h in acidic medium of stomach which correlated to the expectations [267].

On the other hand, in the intestine medium, the capsules should be able to release the cargo within 90 min. According to SEM image (C) the polymer coatings tend to be destroyed after 30 min leading to dissolved gelatin capsules and release of the nanoparticles. Nevertheless, the polymer-coated layer was still remained, and it was noticeable in SEM images. It was supposed that in this step the polymer layer became thinner than before and tended to dissolve gradually in intestine medium. After 60 min and 90 min of being in intestine medium (D and E), the polymer coating layer was damaged by phosphate buffer with pH 7.1. The coating dissolution process revealed by SEM fits the desired theoretical evaluations.

### **5.2.2 Release rate of the nanoparticle filled capsules after being in stomach and intestine simulation medium**

The capsules were filled either with calcium phosphate/trehalose or with solid methylene blue as model compound to analyze the release. The release of particles was then followed by determining the  $\text{Ca}^{2+}$  content in the immersion medium by AAS. The release of methylene blue was followed by UV/Vis spectroscopy. Two different pH values were applied: Simulated stomach medium (0.1 M HCl, pH 1) and simulated intestine conditions (MOPS buffer, 0.15 M, pH 7.1). Aliquots were taken every 15 min. In the case of uncoated capsules, a rapid release was observed at pH 1, while coated capsules released a maximum of 10 %, depending on the enteric coating polymer used. At pH 7.1, coated capsules showed rapid release of the particles within two hours. All enteric coatings had similar release times for calcium phosphate nanoparticles and methylene blue (Figure 28). There was no significant difference between calcium phosphate nanoparticles and methylene blue, indicating a release of both compounds by diffusion out of the degrading capsule at neutral pH. As the passage

of material from the stomach into the colon needs a few hours, [145, 268-270] this release rate is well suited to target the colon. Furthermore, calcium phosphate nanoparticles that are released earlier will be transported further to exert their biological function during their presence in the colon. The intended gene therapy will also require a couple of hours which is well correlated to the residence time in the colon.

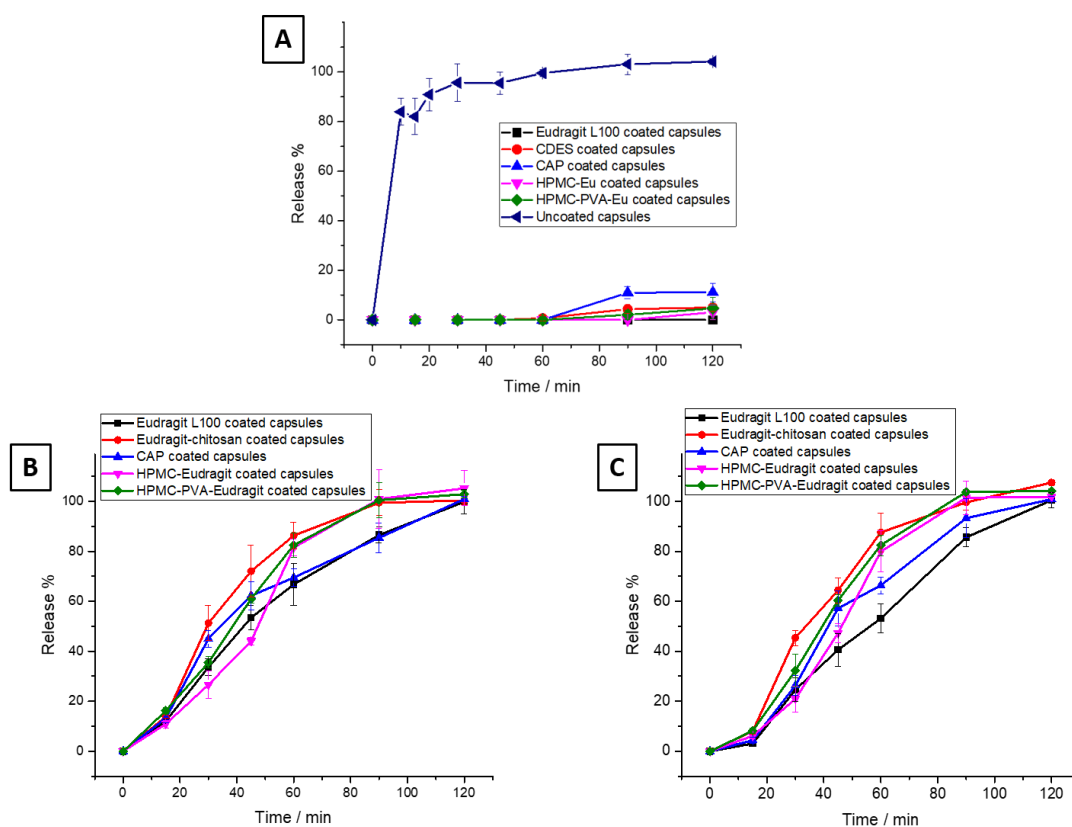


Figure 28. Atomic absorption spectroscopic (AAS) results of the release of calcium phosphate nanoparticles from polymer-coated capsules A: Under simulated stomach conditions (0.1 M HCl, pH 1 and B: Under simulated intestinal conditions, i.e. MOPS buffer (0.15 M, pH 7.1). C: The release of methylene blue (by UV spectroscopy) from the polymer-coated capsules in MOPS buffer (0.15 M, pH 7.1) was measured as control. Each experiment was performed in quadruplicate, and error bars indicate the standard deviation of the mean [124].

### 5.2.3 Colloid-chemical analysis of the particle release from the gelatin capsule

In order to prove the protection of the particles by the coated capsule, the release of the particles from the capsule should first be detected. The release of the particles should be characterized by DLS measurements (Figure 29). In this part, the released particles from the Eudragit L100 and Eudragit-chitosan coated capsules were studied. After releasing from the capsule, the particles were characterized by means of DLS. For comparison, the particles

were also characterized by means of DLS immediately after the synthesis. The results of the DLS measurements are shown in Figure 29.

First, a coated capsule filled with nanoparticles was dissolved in MOPS buffer (0.15 M, pH 7.1). The capsule was not previously incubated in HCl. Both the number and the mean size distribution (z-average) of the detected particles differed significantly from the original size distribution of the particles, which were measured directly after the synthesis. The software also rated the quality of the measurement as poor. Furthermore, the zeta potential changed from +16 mV to -11 mV. This suggested that undissolved components of the capsule or the Eudragit L100 influenced the DLS measurement. The measured signal could therefore not be correctly assigned to the particles (Figure 29).

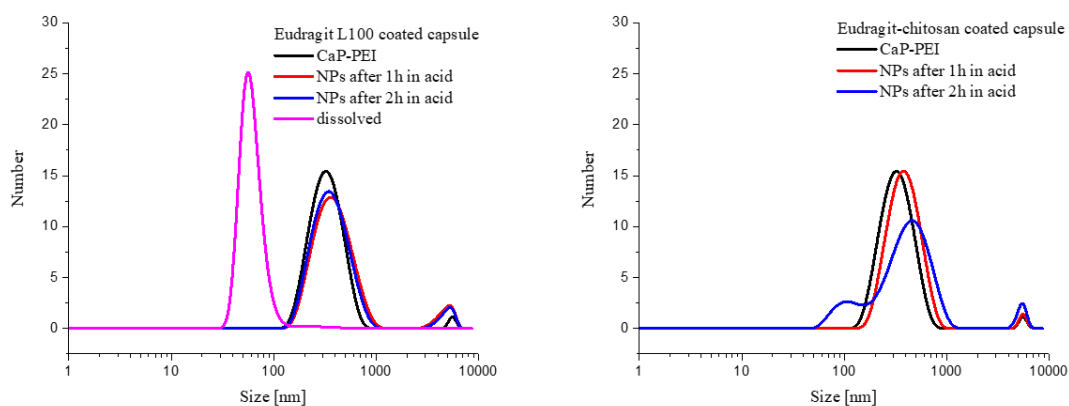


Figure 29: DLS measurements of calcium phosphate nanoparticles released from a gelatin capsule. Particle size distribution after synthesis; a capsule filled with particles was coated and cut after 1 h and 2 h incubation in HCl. The particles were taken up in water and measured in the DLS; dissolved: the capsule was dissolved in MOPS buffer (0.15 M, pH 7.1) after incubation in HCL for 0 h and measured by means of DLS. Right graph: Eudragit-coated capsule and the Left graph: Eudragit-chitosan-coated capsule.

The capsules were also studied with DLS after being in HCl for 1 and 2 h and then dried, cut and the particles were taken up in water after filtration of rest of the capsules and polymer before the measurement. The capsule did not dissolve in water and the pieces could be separated from the dispersion by brief centrifugation or filtration.

The measurements after incubation for 1 h and 2 h in HCl each showed a signal that was comparable to the measurement after the synthesis, both in terms of the intensity of the scattered light and in the position of the peak. The same process was achieved with the dispersed chitosan in Eudragit coated capsules. The measurements after incubation for 1 h

in HCl showed a signal that was comparable to the measurement after the synthesis. However, after 2 h of incubation in HCl, the DLS measurement showed 3 peaks. The software again assessed the measurement results as inadequate due to the poor cumulative fit. The mean particle size distribution (z-average), on the other hand, was again in the same size range as the comparison measurement.

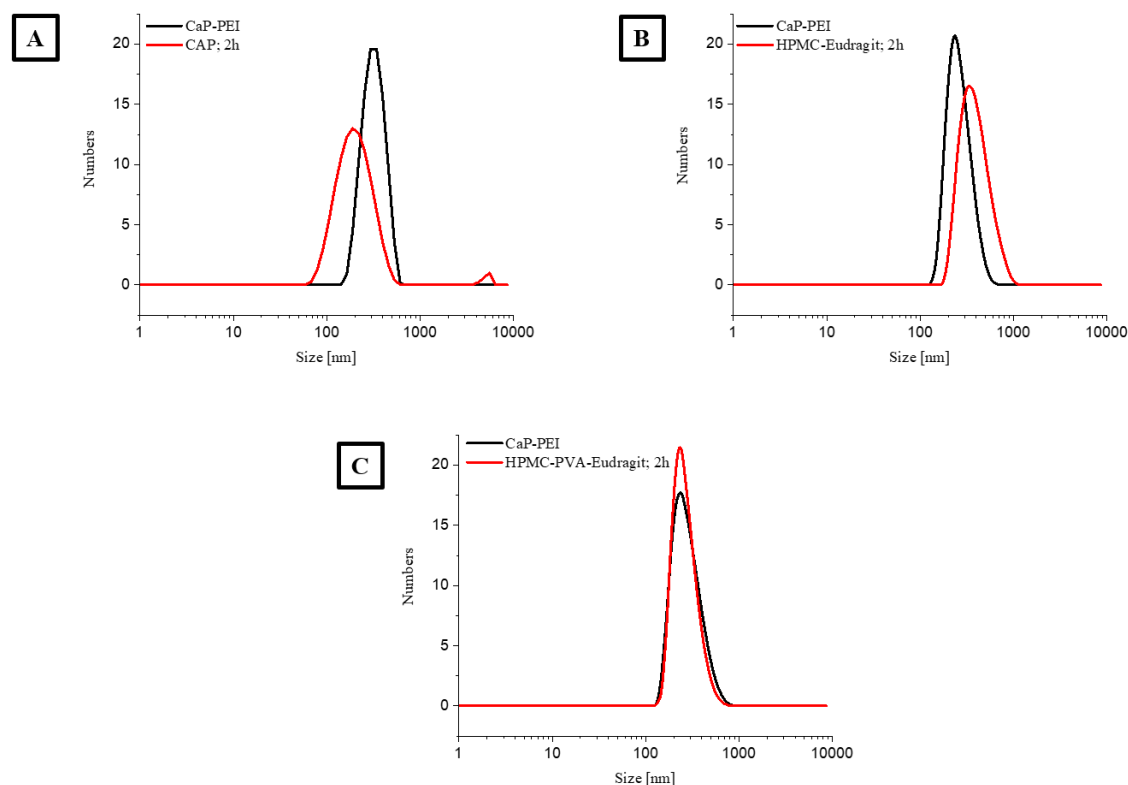


Figure 30: DLS measurements of calcium phosphate nanoparticles released from a gelatin capsule. Particle size distribution after synthesis (CaP-PEI) and after being in CAP-coated capsule (A), HPMC-Eudragit-coated capsule (B), and HPMC-PVA-Eudragit-coated capsule (C) in acidic medium (pH 1, 2 h).

To study also about the protection of the particles by other enteric coating polymers, release of nanoparticles from the coated capsules after 2 h was investigated and compared to the synthesized calcium phosphate nanoparticles. Release of the particles should be characterized by DLS measurements. The capsule was incubated in HCl for 2 h and then dried at room temperature. The capsules were then cut into two pieces with a sharp cutter and these two pieces of capsules were put in an Eppendorf tube containing water and mixed. Dispersion of calcium phosphate nanoparticles in water was achieved after filtration of mixture and separating the rest of enteric coated capsule. The nanoparticles were then

characterized by DLS (Figure 30) and compared to the calcium phosphate nanoparticles which dissolved directly after synthesis of particles. In Addition, the Eudragit coated capsules DLS studies about the nanoparticles released from CAP, HPMC-Eudragit and HPMC-PVA-Eudragit coated capsules after 2 h in acidic medium were performed (Figure 30).

All the released nanoparticles indicated a signal that was comparable to the measurement after the synthesis, both in terms of the intensity of the scattered light and in the position of the peak. These results show that nanoparticles stayed with insignificant changes after being in the coated-capsules in acidic medium of stomach for 2 h.

### 5.2.4 In vitro investigations of the transport vehicles

#### 5.2.4.1 MTT

After studying the quality of calcium phosphate nanoparticles which released from the coated-capsules and after making sure that the nanoparticles are well protected by the polymer coated capsules in acidic medium, the particles will be studied *in vitro* by cell cultures. For a clinical application, the combination of enteric coating, gelatin, trehalose, and nanoparticles must not be toxic. Therefore, extensive cytotoxicity tests on all components with HeLa and Caco-2 cells by MTT assay (Figure 31, 32) was performed. As an alternative for the capsules and oral delivery, suppositories as promising transporting agents in rectal administration were developed. The comprehensive process of making the suppositories containing nanoparticles was explained in section 4.5.2. In addition, to study further about the uptake, transfection, and gene silencing of the released nanoparticles from capsules and suppositories, different bioactive calcium phosphate nanoparticles (CaP/PEI-FITC, CaP/PEI/cEGFP-DNA/CaP/PEI, CaP/PEI/siRNA-EGFP/CaP/PEI) were synthesized and characterized and the results were gathered in the following sections.

In order to study about toxicity of nanoparticles after releasing from the capsules and suppositories, HeLa and Caco-2 cells were used. HeLa is a cervical cancer cell line that is widely used and has evolved into a standard cell line to test the biological compounds and nanoparticles. A well differentiated human intestinal epithelial cell line, Caco-2, were also used as a model to study passive drug absorption across the intestinal epithelium [271]. The Caco-2 cell line (Cancer coli-2) was established from human colorectal adenocarcinoma. [272] Because of its similarity to the small intestinal epithelium, Caco-2 cells are a well-suited *in vitro* model to evaluate the passing of nanoparticles across epithelial barriers [273].

In this study, cell viability of bioactive calcium phosphate nanoparticles, all the used enteric-polymers, coated-capsules, and suppositories were investigated, calculated and displayed in Figure 31.

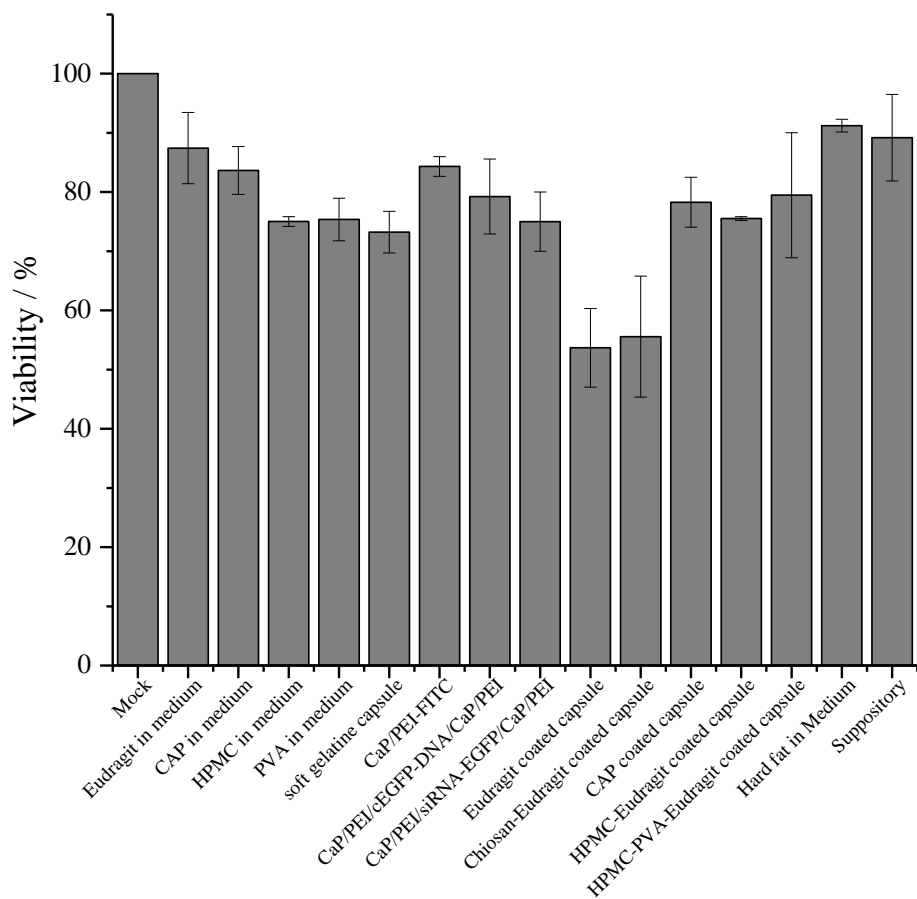


Figure 31: Viability of HeLa cells by the MTT assay after incubating the cells for 24 h with nanoparticles, polymers, coated-capsules and suppositories (mean  $\pm$ standard deviation; N = 3 for each experiment). For the pure polymers, the concentrations were 6 mg mL<sup>-1</sup>.

To test the cytotoxicity of the particles, the cells were incubated with the particles for 24 h with HeLa cells (Figure 31) and Caco-2 cells (Figure 32). All the nanoparticles as well as polymers, hard fat, polymer coated capsules and suppositories were used. After the end of the incubation, the cells were incubated with a MTT reagent and the absorption at 570 nm was measured in triplets. The intensity was calculated in relation to a sample of untreated cells. Three wells per particle type and six wells as a Mock group were used. The results of the investigations using MTT are shown in Figure 31 for the HeLa cells. A high cell viability was measured after 24 h. For all particle types, capsules (except for Eudragit L100 and Eudragit-chitosan coated capsule) and suppositories, the viability was over 80 %, so that the

particles in the concentration used can be regarded as non-toxic. Only Eudragit L100 and Eudragit-chitosan coated capsules after an incubation time of 24 h showed a viability of < 60 %. That could be caused by high concentrations of Eudragit used in the capsules. As HPMC-Eudragit and HPMC-PVA-Eudragit coated capsules also had Eudragit in the system, showed acceptable viability (around 70 %) and these capsules had a smaller amount of Eudragit as protecting polymer for the capsules.

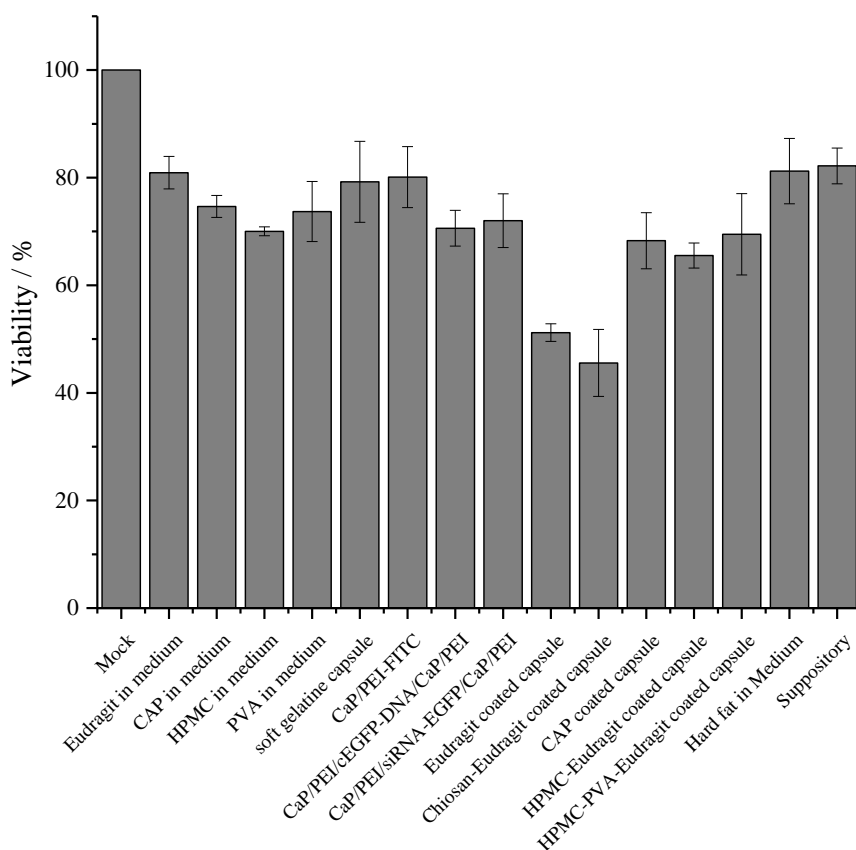


Figure 32: Viability of Caco-2 cells by the MTT assay after incubating the cells for 24 h with nanoparticles, polymers, coated-capsules and suppositories (mean  $\pm$  standard deviation; N = 3 for each experiment). For the pure polymers, the concentrations were 6 mg mL<sup>-1</sup>.

Figure 32 showed the toxicity test in the Caco-2 cells. All the nanoparticles, polymers, hard-fat, capsules and suppositories were given to the Caco-2 cells. After 24 h incubation time, the cells were incubated with the MTT reagent and the absorption at 570 nm was measured in triplets. The results were the same as viability examined previous with HeLa cells. According to the results, Caco-2 cells showed also proper viability for all nanoparticles, polymers, hard-fat, capsules and suppositories except for the Eudragit and Eudragit-chitosan-coated capsule.

### 5.2.4.2 Uptake and transfection with uncoated-capsules

In order to estimate the interaction between the soft gelatin capsules and calcium phosphate nanoparticles with the HeLa cells, uptake and transfection of the calcium phosphate nanoparticles released from the uncoated soft gelatin capsules were studied.

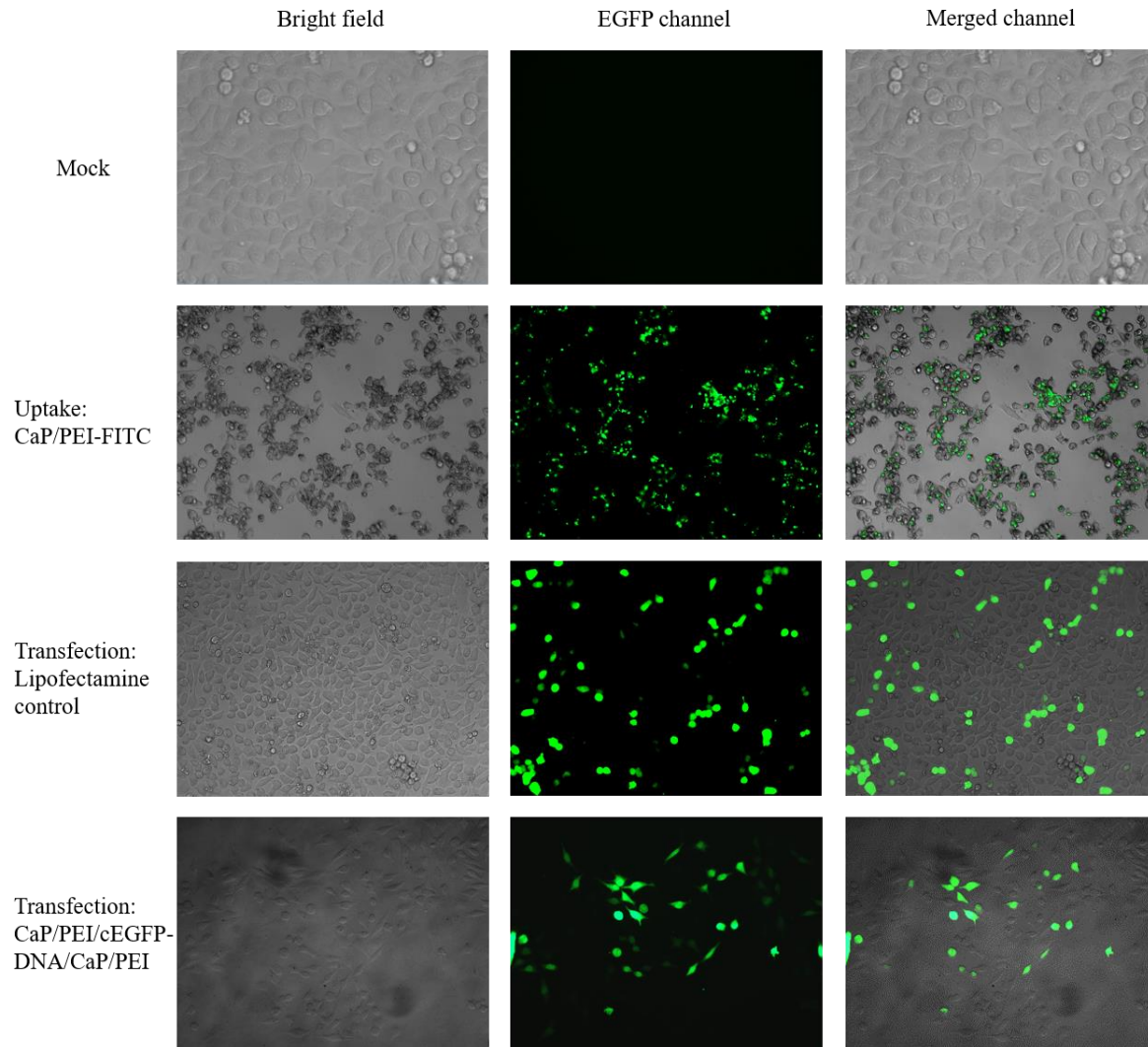


Figure 33: Light and fluorescence microscopic images of HeLa cells 24 h after incubation with CaP/PEI-FITC nanoparticles released from the uncoated gelatin capsule (uptake); Lipofectamine as positive control (Transfection) and CaP/PEI/cEGFP-DNA/CaP/PEI nanoparticles released from the uncoated gelatin capsule (Transfection). Untreated control (Mock); Magnification 20x.

To test the uptake of the released nanoparticles from gelatin capsule, cells were incubated with the released CaP/PEI-FITC nanoparticles for 24 h with HeLa cells (Figure 33). The gelatin capsule contained about 3 mg of dried calcium phosphate nanoparticles with trehalose and were first dissolved in the cell medium, filtered and given to the HeLa cells. After the incubation, the cells were fixated and prepared for light and fluorescent microscopy.

In order to study more efficiently about the nanoparticles released from coated-capsules, transfection study was also performed. Gene therapy is a technology transferring exogenous gene such as plasmid DNA or small interfering RNA (siRNA) into the target cells to treat gene-mediated diseases [274]. Therefore, Transfection and gene silencing by nanoparticles were performed. For transfection, the cells were incubated with the released triple-shell CaP/PEI/cEFG-DNA/CaP/PEI nanoparticles, fixated and prepared for microscopy. In Figure 33 uptake and transfection are shown and the images prove that released nanoparticles can be easily absorbed by the HeLa cells and transfection can take place. It can be also assumed that soft gelatin capsule had no effect in changing the quality of the nanoparticles.

### **5.2.4.3 Uptake with enteric-coated-capsules and suppositories**

In section 5.2.4.2, uptake and transfection of calcium phosphate nanoparticles released from uncoated capsules were studied to guarantee that soft-gelatin-capsule did not have a negative impact on calcium phosphate nanoparticles. Successful uptake and transfection results in study about the nanoparticles and uncoated capsule showed that released calcium phosphate nanoparticles had their functionalized quality. For this reason, as a next step, the performance of the released nanoparticles from enteric-coated capsules and suppositories is discussed in this section.

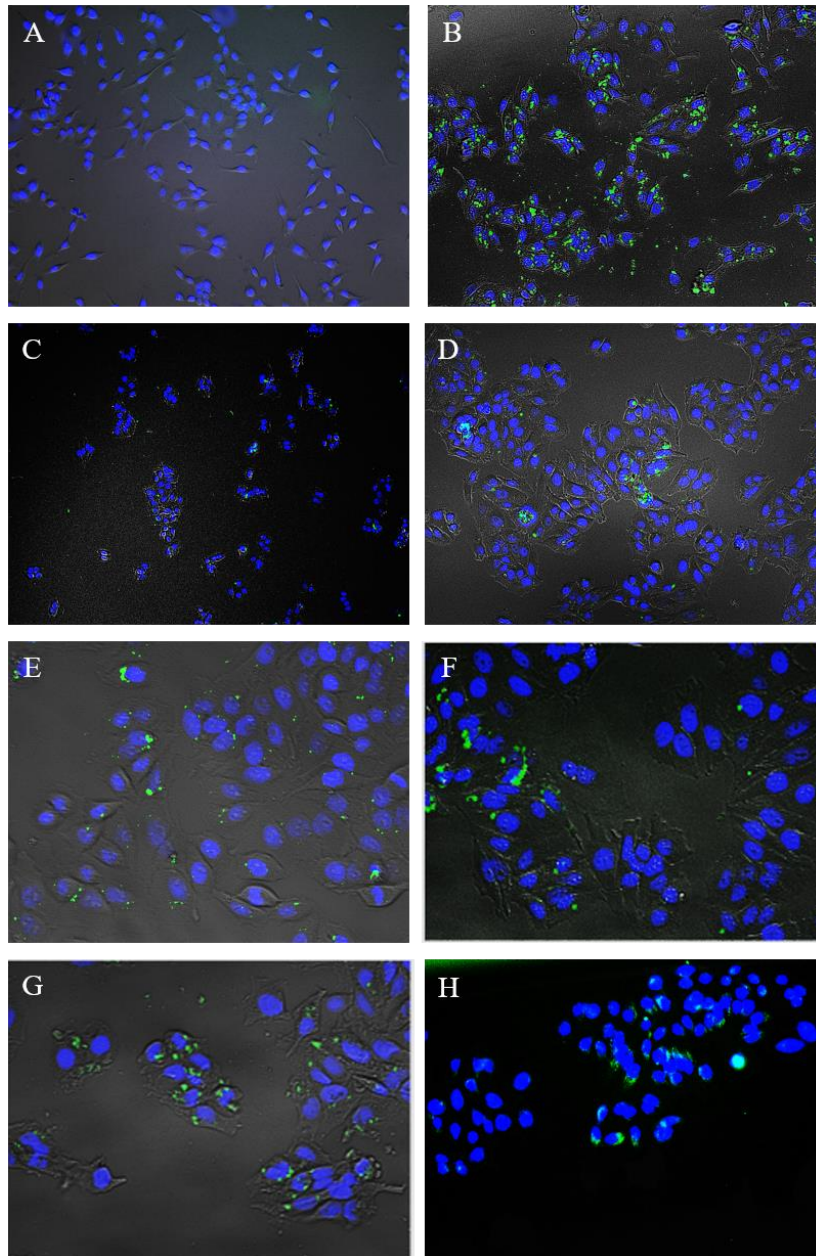


Figure 34: Fluorescence microscopic images of HeLa cells incubated for 24 h with untreated cells (A), dispersed CaP/PEI-FITC nanoparticles (B) and with CaP/PEI-FITC nanoparticles after release from polymer-coated capsules, coated with cellulose acetate phthalate (CAP; C), Eudragit L100 (D), Eudragit L100-chitosan (E), hydroxypropylmethylcellulose-Eudragit L100 (HPMC-Eudragit; F), or hydroxypropylmethylcellulose-polyvinylalcohol-Eudragit L100 (HPMC-PVA-Eudragit; G), and suppository (H). Red: Actin; Blue: Nucleus; Green: CaP/PEI-FITC nanoparticles. Scale bars 20  $\mu\text{m}$ .

In order to test the capsules and suppositories *in vitro*, after performing MTT test, uptake with the bioactive calcium phosphate nanoparticles were considered. As a control, freeze-dried particles were re-dispersed in the cell medium and incubated with cells. To begin with uptake, the cells were treated with the re-dispersed particles, polymer coated capsules and suppository. After 24 h of incubation, the particles showed the expected uptake into the cells

(Figure 34). In this experiment, uptake of the released CaP/PEI-FITC nanoparticles from the coated capsules and suppository could be easily detected, which indicated that the enteric coating polymers were not preventing the uptake of the particles. It can therefore be assumed that particles released from a coated capsule were already absorbed by the cells. Nevertheless, for being certain about the uptake step and absorbing the particles into the cells, confocal microscopy was also performed.

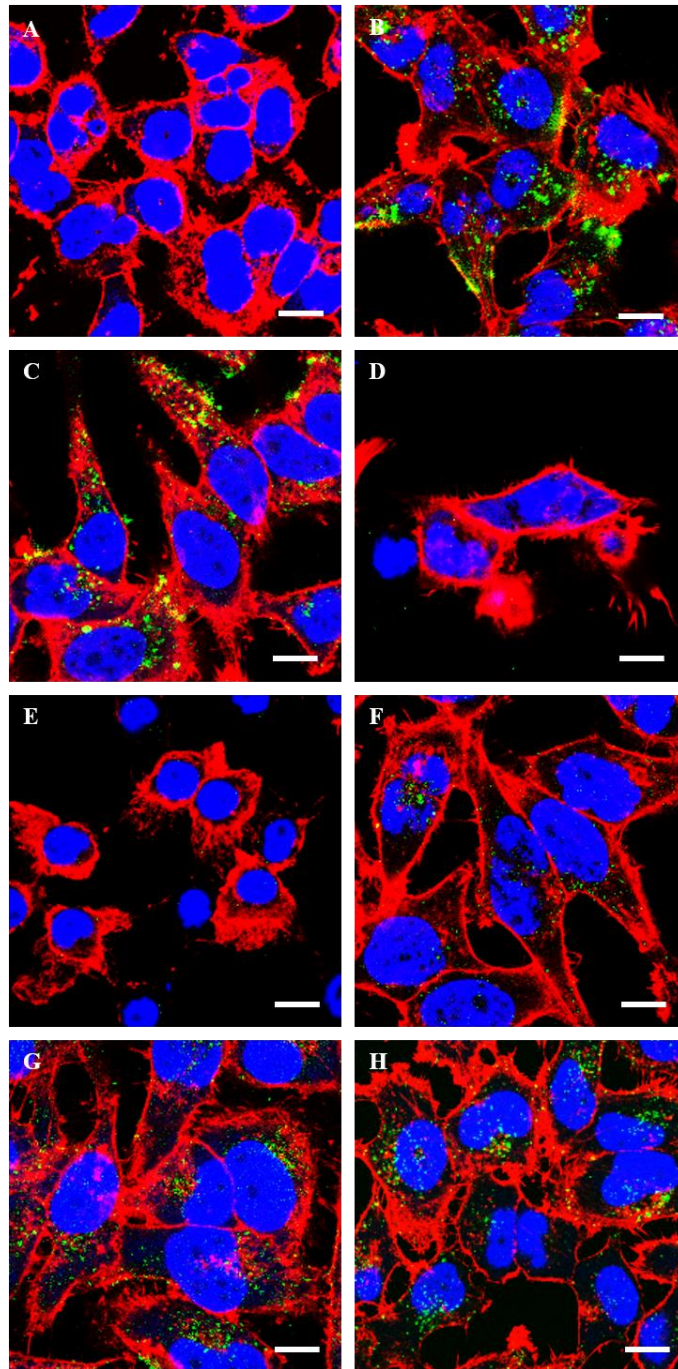


Figure 35: Confocal laser scanning microscopy images of HeLa cells incubated for 24 h with Mock (A), dispersed CaP/PEI-FITC nanoparticles (B) and with CaP/PEI-FITC nanoparticles after release from polymer-coated capsules, coated with cellulose acetate phthalate (CAP; C), Eudragit L100 (D), Eudragit L100-chitosan (E), hydroxypropylmethylcellulose-Eudragit L100 (HPMC-Eudragit; F), or hydroxypropylmethylcellulose-polyvinylalcohol-Eudragit L100 (HPMC-PVA-Eudragit; G), and suppository (H). Red: Actin; Blue: Nucleus; Green: CaP/PEI-FITC nanoparticles. Scale bars 20  $\mu\text{m}$ .

Uptake of calcium phosphate nanoparticles that were released from enteric-coated capsules after dissolution was studied on HeLa cells and Caco-2 cells. Fluorescent CaP/PEI-FITC nanoparticles alone (in dispersion) and released from polymer-coated capsules were given to HeLa cells (Figure 35) and Caco-2 cells (Figure 36). It has been demonstrated earlier that the PEI-FITC label remains on calcium phosphate nanoparticles in cell culture [275].

All particles were taken up by the cells, except in the cases of Eudragit and Eudragit-chitosan. The particles which had been enclosed in capsules coated by the other enteric polymers were efficiently taken up by the cells. In the case of using suppositories, the melting of the suppository at 37°C in aqueous cell culture medium leads to a two-phase system (water and oil) where the drug-loaded nanoparticles are probably distributed between both phases. However, a major part is well dispersed in water as shown by cell culture experiments described below. Uptake studies on HeLa cells and caco-2 cells with CaP/PEI-FITC nanoparticles and CaP/PEI-FITC nanoparticles released from suppositories showed that calcium phosphate nanoparticles which had been enclosed in suppositories were efficiently taken up by HeLa cells.

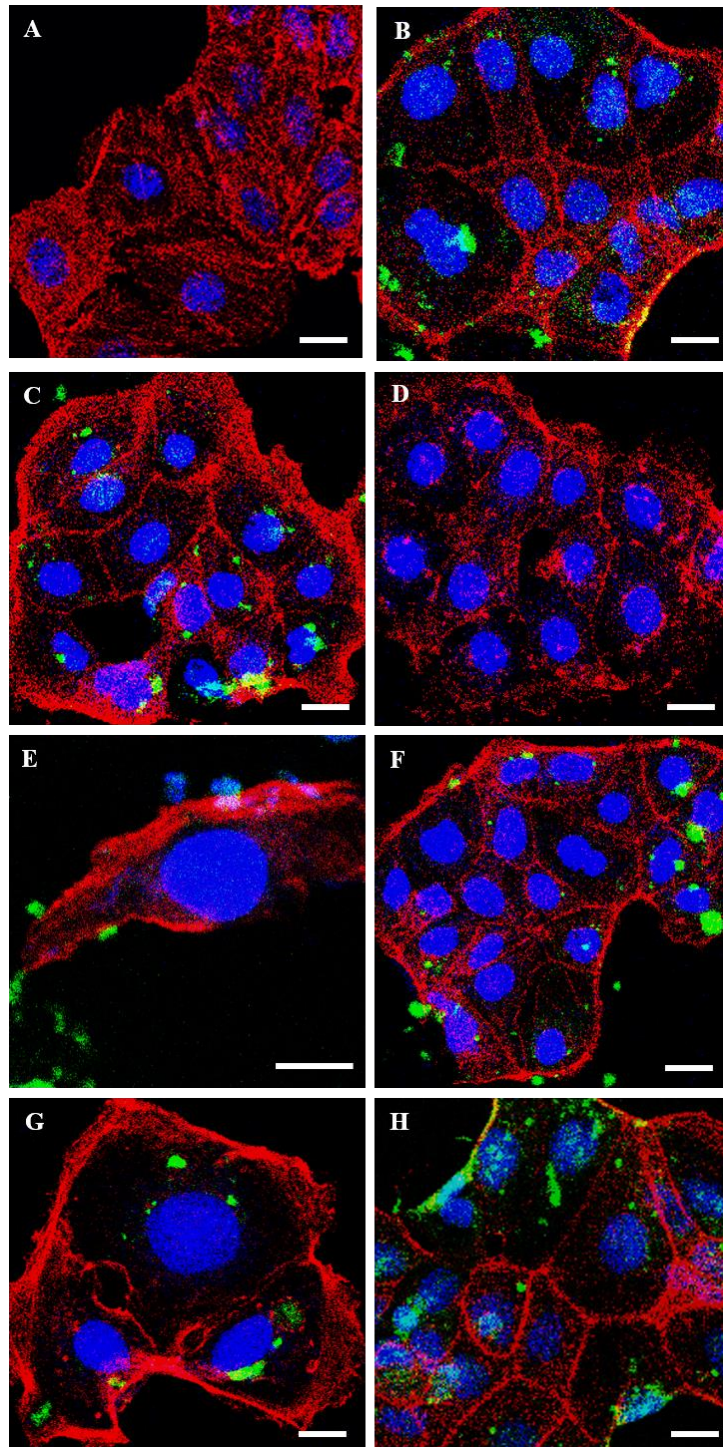


Figure 36: Confocal laser scanning microscopy images of Caco-2 cells incubated for 24 h with untreated cells (A), dispersed CaP/PEI-FITC nanoparticles (B) and with CaP/PEI-FITC nanoparticles after release from polymer-coated capsules, coated with cellulose acetate phthalate (CAP; C), Eudragit L100 (D), Eudragit L100-chitosan (E), hydroxypropylmethylcellulose-Eudragit L100 (HPMC-Eudragit; F), or hydroxypropylmethylcellulose-polyvinylalcohol-Eudragit L100 (HPMC-PVA-Eudragit; G), and suppository (H). Red: Actin; Blue: Nucleus; Green: CaP/PEI-FITC nanoparticles. Scale bars 20 μm.

The results so far have shown that Eudragit and Eudragit-chitosan interact with the positively charged calcium phosphate nanoparticles and inhibit uptake. In all experiments, all the coated capsules were always dissolved in cell culture medium to simulate the dissolving of the capsules in intestinal environment. However, the high concentration of proteins in the medium did not inhibit the interaction between nanoparticles and Eudragit. There are of course several other substances in the intestine that could possibly inhibit the interaction. Nevertheless, in the *in vitro* experiments, it was shown that two-layered-coated-capsules such as HPMC-Eudragit, and HPMC-PVA-Eudragit coated capsules had essentially reliable viability and uptake. Moreover, since nanoparticles were packed into the soft gelatin capsules, presence of the uncoated capsule would also be a reason for dropping cell viability or lack of proper result in uptake studies. It could be that the uncoated capsule would dissolve too slowly and the interaction between gelatin capsule, particles and Eudragit might occur.

#### **5.2.4.4 Transfection with enteric-coated-capsules and suppositories**

As mentioned in the previous section, particle uptake does not necessarily lead to transfection of the cells. After the DNA has left the lysosomes, it must still be transported across the nuclear membrane. The intact plasmid then must be transcribed in the core so that proteins can be expressed. After successful results in transfection studies with released calcium phosphate nanoparticles from uncoated-capsules, transfection with released calcium phosphate nanoparticles from enteric-coated-capsules and suppositories should be investigated. In order to perform transfection with released nanoparticles from polymer-coated-capsules and suppositories, CaP/PEI/cEGFP-DNA/CaP/PEI nanoparticles were used. CaP/PEI/cEGFP-DNA/CaP/PEI nanoparticles were synthesized as mentioned in section 4.1.3. Bioactive calcium phosphate nanoparticles were filled into soft-gelatin-capsules and these gelatin capsules were covered with different pH-dependent-polymers. Suppositories were prepared according to the process explained in section 4.5.2. In this study, HeLa and Caco-2 cells were employed. Equal amount of DNA per well was applied to both cell types. Lipofectamine was used according to the manufacturer's recommendations as a positive control. Using fluorescence microscopy and confocal microscopy, transfected and non-transfected cells can be distinguished from one another. Fluorescence microscopic images of cells transfected by CaP/PEI/cEGFP-DNA/CaP/PEI nanoparticles are shown in Figure 37 and the confocal images are shown in Figure 38 (for the HeLa cells) and Figure 39 (for Caco-

2 cells). The transfection efficiency was calculated according to the light and fluorescence microscopic images.

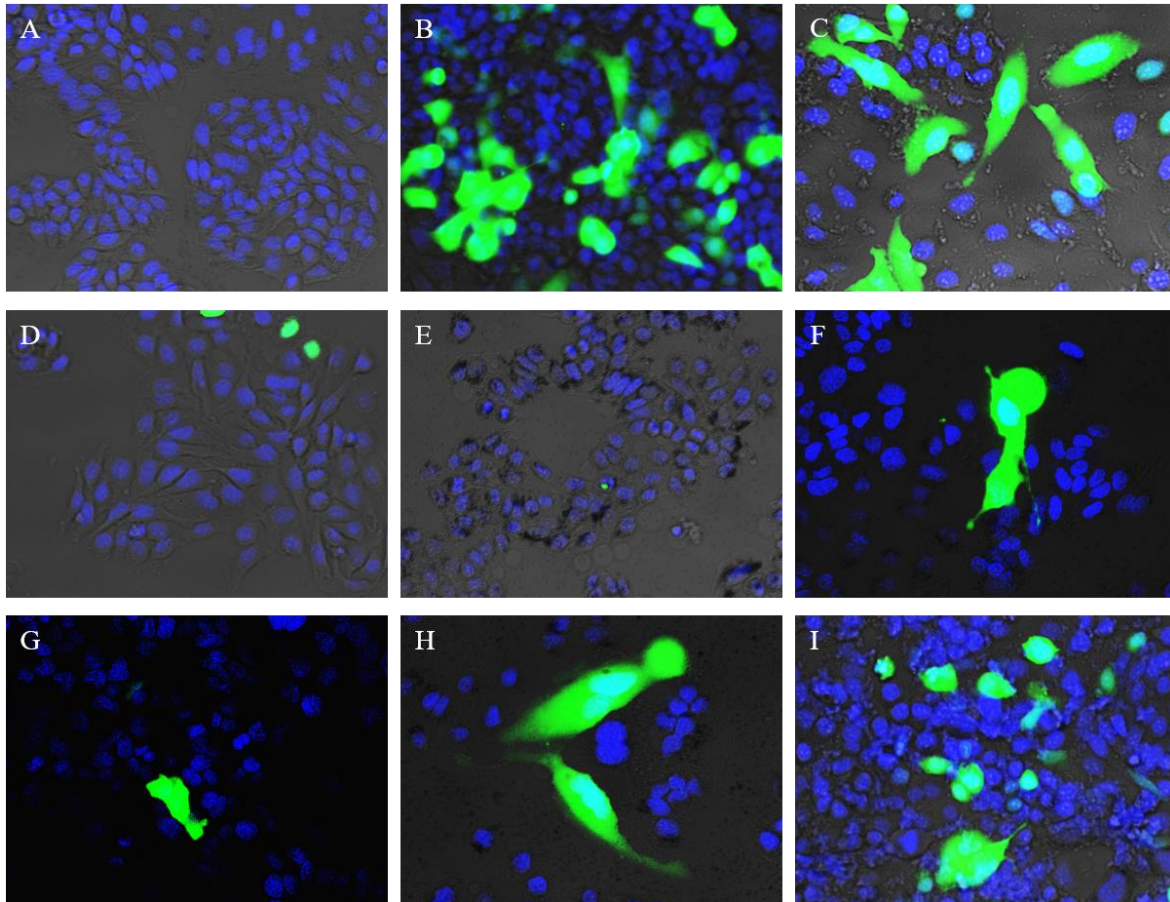


Figure 37: Microscopic images of untreated HeLa cells (A), cells after transfection with lipofectamine as a positive control (B), CaP/PEI/cEGFP-DNA/CaP/PEI particles (C), and CaP/PEI/cEGFP-DNA/CaP/PEI particles release from the capsules coated with Eudragit L100 (D), Eudragit-chitosan (E), CAP (F), HPMC-Eudragit (G), HPMC-PVA-Eudragit (H), and the same particles release from the suppository (I). Magnification: 20x.

The transfection of nanoparticles, all the enteric-coated capsules, and suppositories were shown in Figure 37. Cells were treated with the re-dispersed particles, polymer coated capsules and suppository as well as the lipofectamine as a positive control. After 24 h of incubation, the particles were washed out and the cells were incubated for another 48 h. After incubation, the cells were washed, fixated, dye-labeled and prepared for the microscopy step. The images showed the expected transfection with the HeLa cells (Figure 37). In this experiment, transfection of the released CaP/PEI/cEGFP-DNA/CaP/PEI nanoparticles from the CAP, HPMC-Eudragit, and HPMC-PVA-Eudragit coated capsules and suppository was acceptable, which is in agreement with the previous data for the uptake studies. Nevertheless,

in the case of Eudragit-coated capsule, transfection was not detected and in the case of Eudragit-chitosan coated capsule, no transfection with the HeLa cells was found.

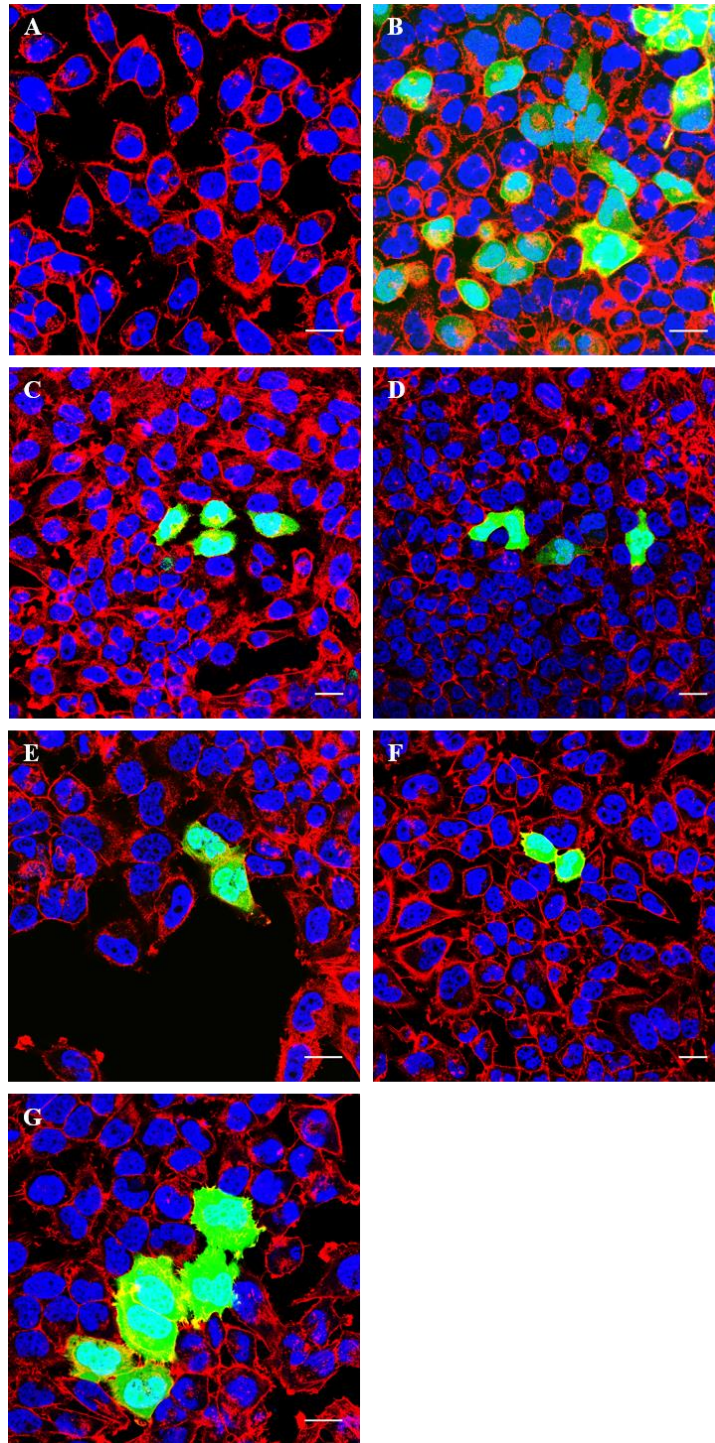


Figure 38: Confocal laser scanning microscopy images of HeLa cells after transfection for 72 h. Untreated cells (A; 0 %); Lipofectamine™ control (B; 22 %); dispersed CaP/PEI/cEGFP-DNA/CaP/PEI nanoparticles (C; 15 %); and CaP/PEI/cEGFP-DNA/CaP/PEI nanoparticles from dissolved capsules, coated with cellulose acetate phthalate (CAP; D; 13 %), hydroxypropylmethylcellulose-Eudragit L100 (HPMC-Eudragit) (E; 5 %), or hydroxypropylmethylcellulose-polyvinylalcohol-Eudragit L100 (HPMC-PVA-Eudragit) (F; 6 %), and Suppository (G; 13 %). Red: Actin; Blue: Nucleus; Green: EGFP. Scale bar 20  $\mu\text{m}$ .

The nanoparticle-mediated transfection efficiency was then determined for nanoparticles carrying cEGFP-DNA, both dispersed and released from polymer-coated capsules, with HeLa cells (Figure 38) and Caco-2 cells (Figure 39). Transfection with the fluorescent protein EGFP was not observed in cells incubated with nanoparticles released from capsules coated with Eudragit and Eudragit-chitosan. This is probably due to an insufficient uptake in these cases as shown before. As there was almost no uptake of particles from Eudragit- and Eudragit-chitosan-coated capsules, together with an increased cytotoxicity, these coatings were not studied further. As positive control, the commercial transfection agent Lipofectamine was used. The transfection efficiency was quantified by counting about 200–2000 cells per image and determination of the percentage of green-fluorescent cells (light and fluorescence microscopic images). For both cell lines, the transfection efficiency of Lipofectamine was the highest, and that of the dispersed nanoparticles about 75 % of Lipofectamine. The nanoparticles that had been released from the capsule still had about half of the efficiency of the dispersed nanoparticles, i. e. about 30 to 40 % of the Lipofectamine value. This loss in transfection is in line with earlier results [276] and could be due to some irreversible agglomeration after re-dispersion. Again, it was not possible to apply particle size characterization methods like DLS to the particles from dissolved capsules (not even after filtration) because there was too much particulate matter in the sample, probably due to an insufficient dissolution of the capsule. However, it can be concluded that the particles are released from the capsules in their bioactive state, with the DNA being still intact.

The transfection of the released nanoparticles from the suppositories, showed that the suppositories could also be as effective as the pure nanoparticles.

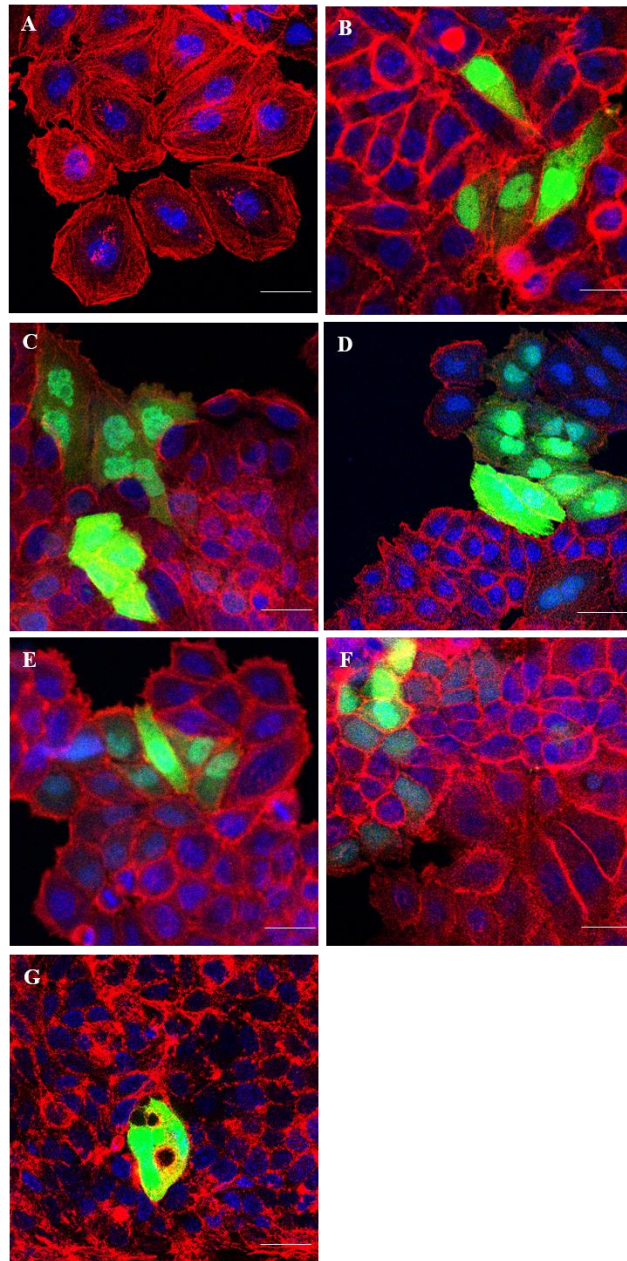


Figure 39: Confocal laser scanning microscopy images of Caco-2 cells after transfection for 72 h. Untreated cells (A; 0 %); Lipofectamine<sup>TM</sup> control (B; 10 %); dispersed CaP/PEI/cEGFP-DNA/CaP/PEI nanoparticles (C; 8 %); and CaP/PEI/cEGFP-DNA/CaP/PEI nanoparticles from dissolved capsules, coated with cellulose acetate phthalate (CAP; D; 4 %), hydroxypropylmethylcellulose-Eudragit L100 (HPMC-Eudragit) (E; 5%), or hydroxypropylmethylcellulose-polyvinylalcohol-Eudragit L100 (HPMC-PVA-Eudragit) (F; 7 %), and suppository (G; 4 %). Red: Actin; Blue: Nucleus; Green: EGFP. Scale bar 20  $\mu$ m.

Transfection studies with Caco-2 cells also showed the same expected transfection results as the HeLa cells. Therefore, it can be concluded that the released nanoparticles from the polymer-coated capsules and suppositories will be absorbed appropriately by the HeLa and Caco-2 cells.

#### **5.2.4.5 Gene silencing**

To analyze the biological effect of the redispersed nanoparticles and the nanoparticles released from the transport vehicles (coated capsules and suppositories), the expression of EGFP in cells treated with nanoparticles was compared with an untreated control and positive lipofectamine control. To begin with, CaP/PEI/siRNA-EGFP/CaP/PEI nanoparticles were synthesized as mentioned in section 4.1.4. These nanoparticles were packed into soft-gelatin capsules and the capsules were coated with enteric-polymers. Suppositories were also prepared with these nanoparticles. Before cell experiments, the capsules were dissolved in cell culture medium using a water bath for 2 h. After dissolving the capsules in cell culture medium, this solution was filtered to remove extra capsule-coatings and gelatin-capsule. Due to the small size of the nanoparticles, they pass through the filter and remain in the solution.

Figure 40 qualitatively shows the gene silencing by the CaP/PEI/siRNA-EGFP/CaP/PEI nanoparticles after the release. In addition to the untreated control, only the results after the release from the coated capsules and from the suppository are shown here. Qualitative differences in the EGFP expression after the release of particles from the transport vehicles and the untreated control were evident from the images.

In order to test the efficiency of the particles and particles released from the capsules and suppositories, HeLa-EGFP cells were used. These cells expressed the green fluorescent protein EGFP, so that they could be visualized using a fluorescence microscope. By comparing light and fluorescence microscopic images, the proportion of fluorescent cells could be determined. If the cellular synthesis of EGFP is prevented by means of siRNA, the proportion of fluorescent cells should decrease. Efficiency of gene silencing can be determined in each case according to the microscopic images.

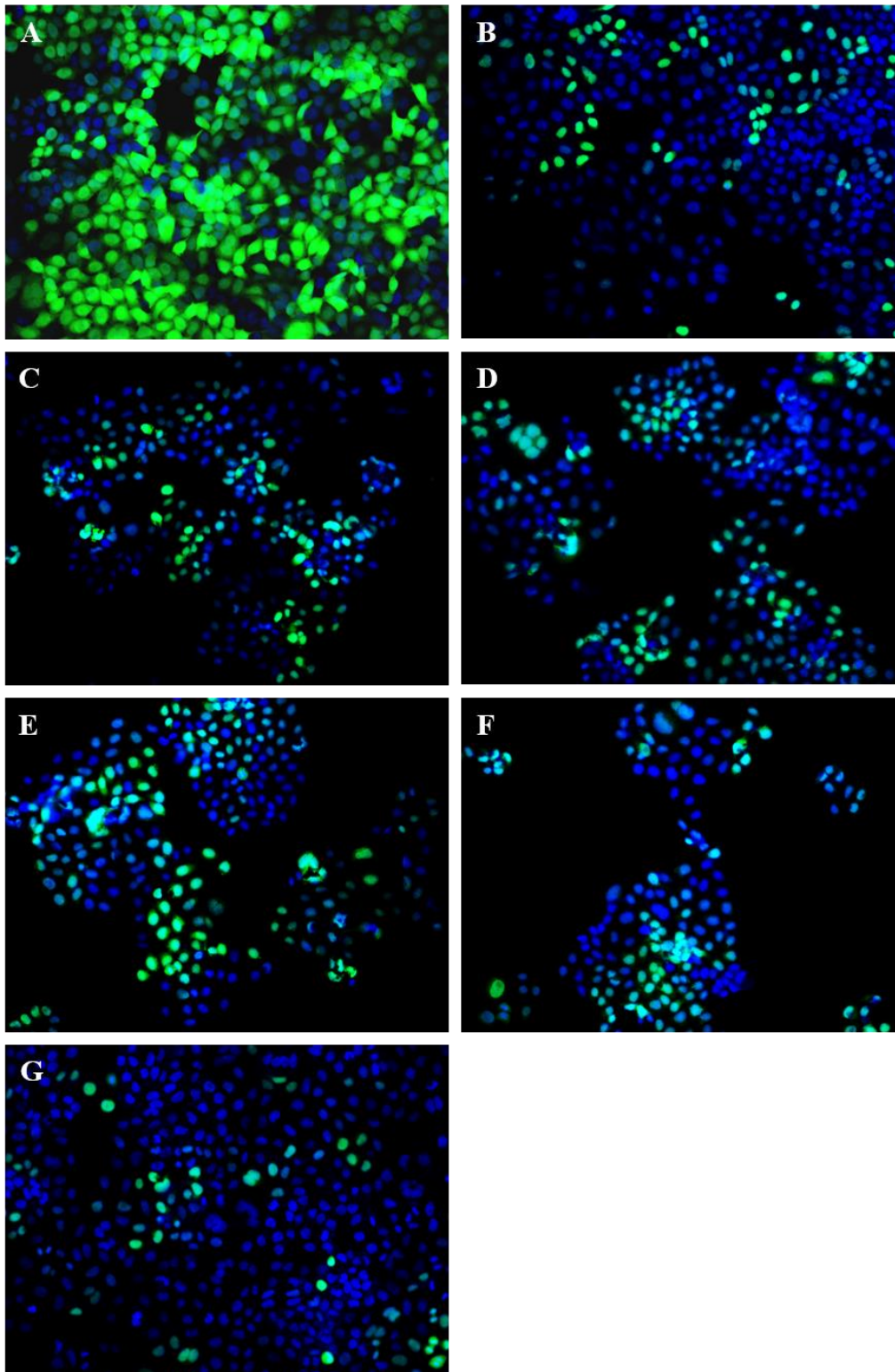


Figure 40: Microscopic images of untreated HeLa-EGFP cells (Mock) (A), cells 24 h after silencing with lipofectamine as a positive control (B), CaP/PEI/siRNA-EGFP/CaP/PEI particles (C), and CaP/PEI/siRNA-EGFP/CaP/PEI particle release from the capsules coated with CAP (D), HPMC-Eudragit (E), HPMC-PVA-Eudragit (F), and the same particle release from the suppository (G). Magnification: 20x.

The gene silencing of bioactive calcium phosphate nanoparticles, all of the enteric coated capsules, and suppositories is shown in Figure 40. HeLa-EGFP cells were used in this study. HeLa-EGFP cells were seeded and incubated for 24 h, then lipofectamine and released nanoparticles from the capsules and suppositories were added to the cells. Every capsule containing nanoparticles was dissolved in the cell medium, filtered and given to the HeLa-EGFP cells. The suppository was also inserted into the cell medium, melted in 37 °C and given to the cells. The cells were incubated 24 h with the nanoparticles. After incubation, the cells were washed to get rid of the excess nanoparticles and incubated for 48 h. Then, the cells were washed, fixated, dyed and prepared for the microscopy. The microscopic images with the redispersed nanoparticles, lipofectamine, different types of enteric coating capsules and suppository are shown in Figure 40. The silencing by the nanoparticles and released nanoparticles from the transporting systems was compared in each case with an untreated control and with the silencing efficiency of Lipofectamine. Figure 40 shows that released nanoparticle from all types of enteric coated capsules and suppository reduced the expression of EGFP.

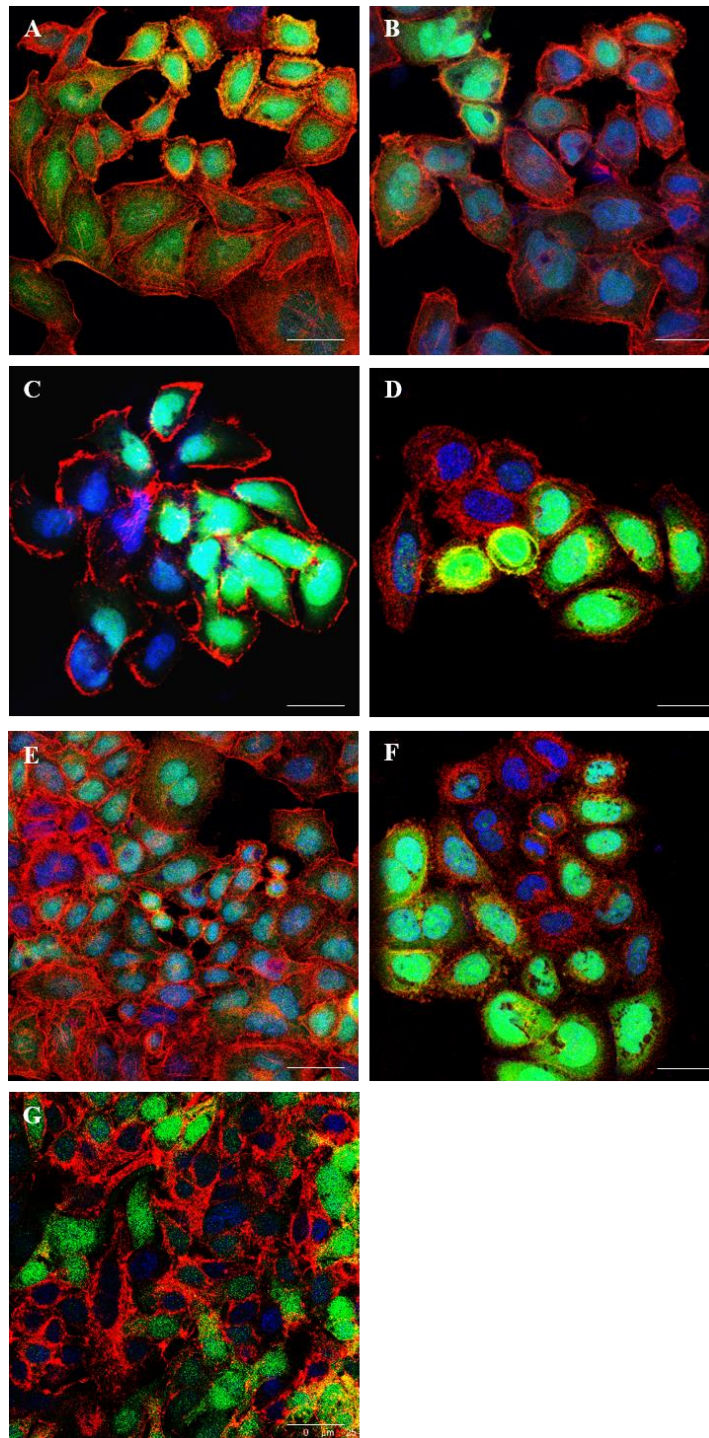


Figure 41: Confocal laser scanning microscopy images of HeLa-EGFP cells after gene silencing for 72 h. Untreated cells (A); Lipofectamine control (B; 60 %); dispersed CaP/PEI/siRNA-EGFP/CaP/PEI nanoparticles (C; 58 %); and CaP/PEI/siRNA-EGFP/CaP/PEI nanoparticles from dissolved capsules, coated with cellulose acetate phthalate (CAP; D; 21 %), hydroxypropylmethylcellulose-Eudragit L100 (HPMC-Eudragit) (E; 43 %), or hydroxypropylmethylcellulose-polyvinyl alcohol-Eudragit L100 (HPMC-PVA-Eudragit) (F; 28 %), and suppository (G; 50 %). Red: Actin; Blue: Nucleus; Green: EGFP. Scale bar 20  $\mu\text{m}$ .

The gene silencing study of nanoparticles carrying siRNA was also studied with confocal microscopy. This is an especially crucial experiment because siRNA is prone to rapid degradation by RNAses [277] which could occur during freeze-drying and dissolution. For this purpose, EGFP-expressing HeLa cells were used. The green fluorescence of EGFP was to be silenced by the corresponding siRNA (Figure 41). As mentioned in section 4.4.5, the amount of gene silencing in percent can be calculated from the ratio of the still fluorescing cells to the total number of cells according to the digital microscope images (Figure 40). This method depends on the absolute number of cells within each image. The typical percentage of green fluorescing cells in the control was 80-90 %. The gene silencing efficiency was about half of the dispersed control particles and still very substantial. The transfection efficiency was quantified by counting about 200–2000 cells per image and determination of the percentage of green-fluorescent cells. The gene silencing efficiency was determined with the help of digital microscopy, calculated and summarized below the Figure 41.

The efficiency of gene silencing using the triple-shell nanoparticles (CaP/PEI/siRNA-EGFP/CaP/PEI) was 58 % which was slightly less than the efficiency of gene silencing using lipofectamine (60 %). Released nanoparticles from Eudragit- and Eudragit-chitosan-coated capsules did not show statistically significant differences in the efficiency of gene silencing. In contrast, the triple-shell nanoparticles released from CAP-, HPMC-Eudragit-, and HPMC-PVA-Eudragit-coated capsules showed much more efficient, giving an efficiency of gene silencing of 21 %, 43 %, and 28 % respectively. As it is appearing in the confocal images, CAP, HPMC-Eudragit, and HPMC-PVA-Eudragit and suppository showed proper cytocompatibility and successful gene silencing. Additionally, released nanoparticles from the suppositories showed the greatest gene efficiency with 50 %.

As mentioned in section 2.5, endocytic uptake pathways are considered as an essential process for further understanding of the mechanism of gene delivery [96, 278]. Occasionally, endocytic pathways responsible for the uptake of nanomaterials are the receptor-mediated endocytosis, the receptor-independent pathway and micropinocytosis [279-281]. The receptor-mediated endocytosis is usually known as clathrin-mediated endocytosis. The receptor-independent pathway can be further subdivided into caveolin-mediated endocytosis, clathrin-independent endocytosis, clathrin- and caveolin-independent endocytosis. It is important to know the endocytosis pathway during the gene delivery process [282]. Calcium phosphate nanoparticles have been proven to be a powerful agents of gene delivery. Olton et al. showed that endocytosis of calcium phosphate nanoparticles

was both clathrin- and caveolae-dependent, and they also suggested that the caveolae mechanism was the major contributor [283].

### 5.2.4.6 Conclusion

Due to the background of inflammatory bowel disease, strategies were sought in this section to bring functionalized calcium phosphate nanoparticles undamaged and effective into the intestine. In the present study we showed how to prepare calcium phosphate nanoparticles and calcium phosphate nanoparticles functionalized with DNA-cEGFP and siRNA-EGFP as delivery system for transfection and efficient gene silencing. The particles had a size around 100 nm with spherical morphology. For oral purpose, particles were filled into a gelatin capsule and coated with five different pH-sensitive polymers such as Eudragit L100, chitosan dispersed in Eudragit L100 (Eudragit-chitosan), CAP and two-layer coating systems such as HPMC-Eudragit, and HPMC-PVA-Eudragit system. In vitro tests have shown that the Eudragit and Eudragit-chitosan polymers have a negative effect on the transfection and silencing efficiency of the particles. However, the other enteric polymers namely CAP, HPMC-Eudragit, and HPMC-PVA-Eudragit do not have negative effect on the nanoparticles and they show appropriate uptake, transfection and gene silencing efficiency in the cells. These polymers can be assumed to protect the nanoparticles in the way through the stomach and they can release their cargo without damage in the intestine. As an alternative for the oral drug delivery with the capsules, suppositories were also developed for rectal administration of the particles. The suppositories show proper cell viability in in vitro studies as well as very acceptable uptake, transfection and gene silencing by the cells.

### 5.3 Calcium phosphate PLGA nanoparticles for drug delivery

Poly (lactide-co-glycolide) (PLGA) is a biocompatible and biodegradable polymer based on polylactic acid and polyglycolic acid. PLGA as a polymer degrades into lactic acid and glycolic acid which are the PLGA monomers [284]. PLGA nanoparticles can be synthesized using various methods. However, the most commonly used method is the oil-in-water emulsion, with the PLGA contains hydrophobic active ingredients [285, 286]. These emulsions include the polymer and the active ingredient in an organic solvent such as dichloromethane (DCM). This organic phase will then be transferred into an aqueous phase, mostly with surfactants such as polyvinyl alcohol (PVA). The emulsification, which is a production of fine oil droplets in the aqueous phase, carried out by using ultrasound treatment or homogenization methods. After removing the organic solvent, the polymer stabilizes the

nanoparticles and encapsulates the hydrophobic active ingredients in the polymer matrix. For the encapsulation of hydrophilic active ingredients such as peptides, proteins and nucleic acids develop mostly water-in-oil-in-water emulsions (W/O/W).

In this chapter, calcium phosphate nanoparticles as the hydrophilic active ingredients dissolved first in water and PLGA dissolved in DCM. After that, dispersed calcium phosphate nanoparticles in water were dispersed in DCM contains PLGA as an organic phase. After emulsifying the mixture with ultrasound, a primary water-in-oil Emulsion is created. This primary water in oil emulsion was then added to another aqueous phase which was dissolved PVA in water and emulsified again. This process resulted in a water-in-oil-in-water emulsion (W/O/W), in which the hydrophilic active ingredients were in the inner (primary) aqueous phase and surrounded with the organic solvent containing dissolved polymer.

The objective of the present work was to study *in vitro* about the encapsulated bioactive calcium phosphate nanoparticles in PLGA. In the following, first the colloid chemical characterization of calcium phosphate-PLGA nanoparticles will be discussed and then the biological effectiveness of calcium phosphate-PLGA nanoparticles in cell culture experiments will be investigated.

### 5.3.1 Characterization of the nanoparticles

In order to determine the morphology and size of the nanoparticles, scanning electron microscopy (SEM) was performed. Dynamic light scattering was also acquired to obtain the hydrodynamic size of the nanoparticles. The scanning electron microscope images, associated histogram, and the DLS diagrams of the different calcium phosphate nanoparticles were assembled in figure 42.

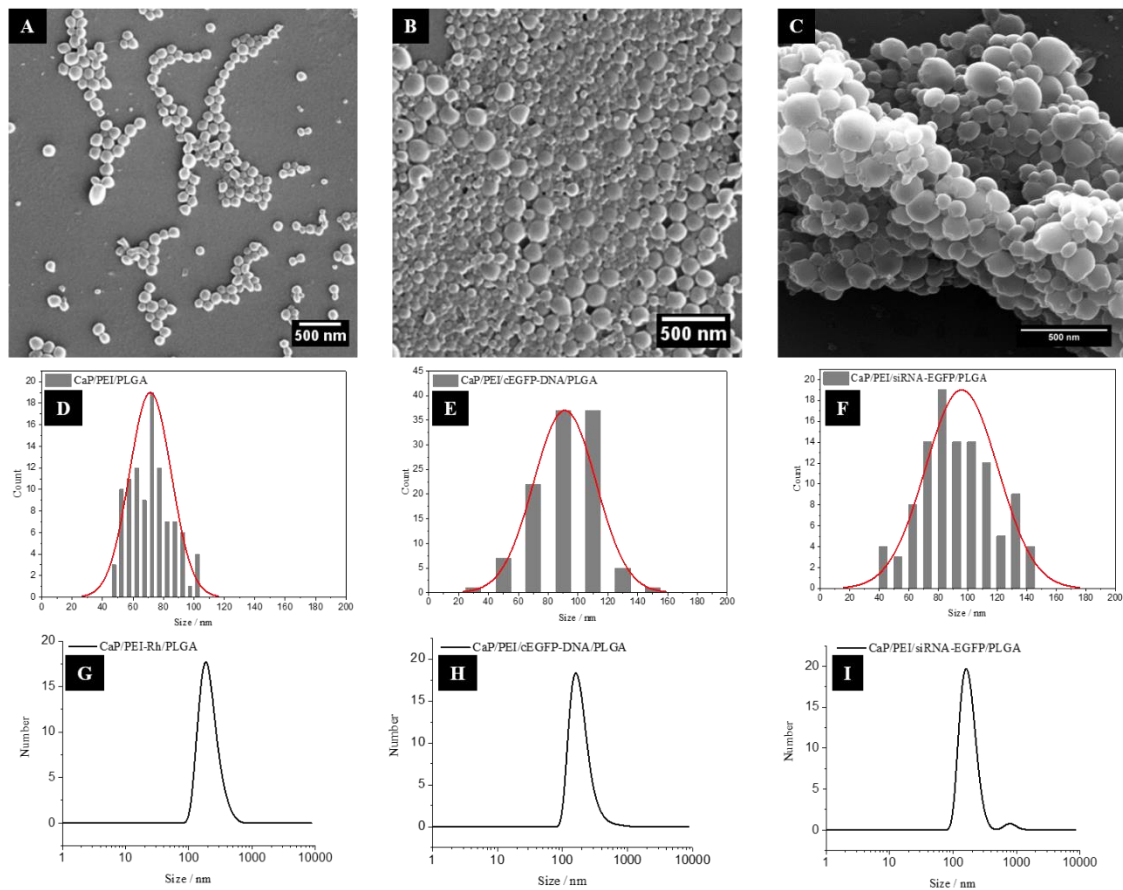


Figure 42: Scanning electron microscope images (A, B, and C), the size distribution (D, E, and F), as well as DLS graphs (G, H, and I) of CaP/PEI-Rhodamine/PLGA, CaP/PEI/cEGFP-DNA/PLGA, and CaP/PEI/siRNA-EGFP/PLGA respectively.

Figure 42 shows that the calcium phosphate-PLGA nanoparticles were monodisperse spherical nanoparticles. According to its histogram, the calcium phosphate-PLGA nanoparticles were in the size range of  $75 \pm 29$  nm. Calcium phosphate-PLGA nanoparticles did not show any agglomeration according to the SEM images. The bioactive calcium phosphate nanoparticles were also analyzed by SEM and DLS. The calcium phosphate-DNA-PLGA nanoparticles showed a spherical morphology. The histogram obtained from the SEM images reveal an average size of 95 nm for the particles. According to the DLS data, these nanoparticles have an average size of 110 nm which is in good agreement with the size obtained by SEM. Calcium phosphate-siRNA-PLGA nanoparticles indicated the average particle size of 100 nm by SEM and 105 nm by DLS. Calcium phosphate-DNA-PLGA and calcium phosphate-siRNA-PLGA nanoparticles showed bigger nanoparticle size in comparison to the calcium phosphate-PLGA nanoparticles. These results of the colloid chemical characterization of the calcium phosphate nanoparticles and bioactive calcium phosphate nanoparticles showed that with the water-in-oil-in-water emulsion technique, the

nanoparticles were achieved in a size range of approx. 100 nm. These nanoparticles are suitable for uptake studies as well as the transfection and gene silencing [287, 288].

### 5.3.2 MTT test

To determine the cytotoxicity of the calcium phosphate-PLGA nanoparticles and calcium phosphate-nucleic acid-PLGA nanoparticles, the viability of the HeLa cells after 24 h incubation with the nanoparticles was determined by MTT test. Figure 43 shows the viability of the HeLa cells 24 h after incubation with calcium phosphate-PLGA and calcium phosphate-nucleic acid-PLGA nanoparticles. For MTT, a 24-well plate with 50000 cells per well, were used. The nanoparticles were first dried with trehalose in the ratio of 1:10. The redispersed nanoparticles in cell culture medium (DMEM) were given to the cells. In this study 2 mg and 5 mg of each type of nanoparticles were redispersed in 1 mL DMEM, 500  $\mu$ L of this solution were given to the HeLa cells.

After the end of the incubation, the cells were incubated with MTT reagent and the absorbance at 570 nm was measured in triplets. The intensity was calculated in relation to a sample of untreated cells. Three wells per particle type and six wells as a Mock group were used. The results of the investigations using MTT are shown in Figure 43.

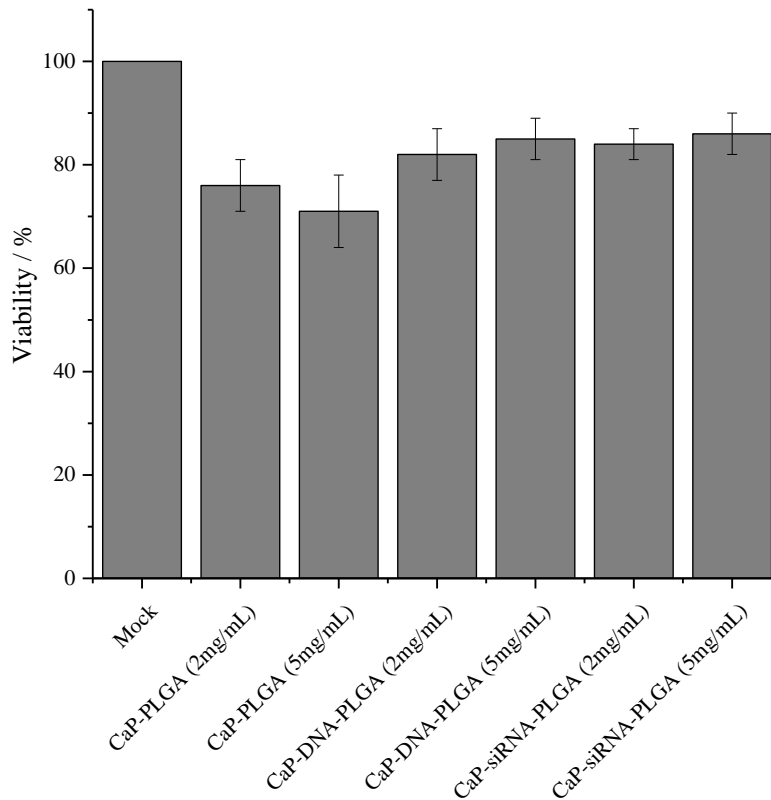


Figure 43, viability of the HeLa cells 24 h after incubation with calcium phosphate PLGA nanoparticles in two different concentration ( $2 \text{ mg mL}^{-1}$  and  $5 \text{ mg mL}^{-1}$ ) is shown. The vitality of the cells after incubation with CaP-PLGA nanoparticles was more than 65 % for both concentrations. Bioactive calcium phosphate nanoparticles showed better cell viability with more than 80 % cell viability after 24 h incubation for both concentrations. However, all of the calcium phosphate-PLGA-Nanoparticles represented promising cell viability by the HeLa cells after 24 h of incubation.

### 5.3.3 Uptake of nanoparticles in HeLa cells

Uptake studies were carried out to check which particles can be absorbed by the cells. For this purpose, the cells were seeded in 8-well  $\mu$ -slides with 20000 cells per well and, after adhesion, incubated with fluorescence-labeled nanoparticles for 24 h. Figure 44 shows the confocal laser microscope images of the cells. A sample of untreated cells (Mock) is considered as a control. The freeze-dried nanoparticles were dissolved in DMEM and given to the cells in three different concentrations. No fluorescence in the wavelength range for rhodamine could be found in the Mock group. For CaP/PEI-Rhodamine/PLGA, signals for rhodamine were detected in the cells for all concentrations of particles.

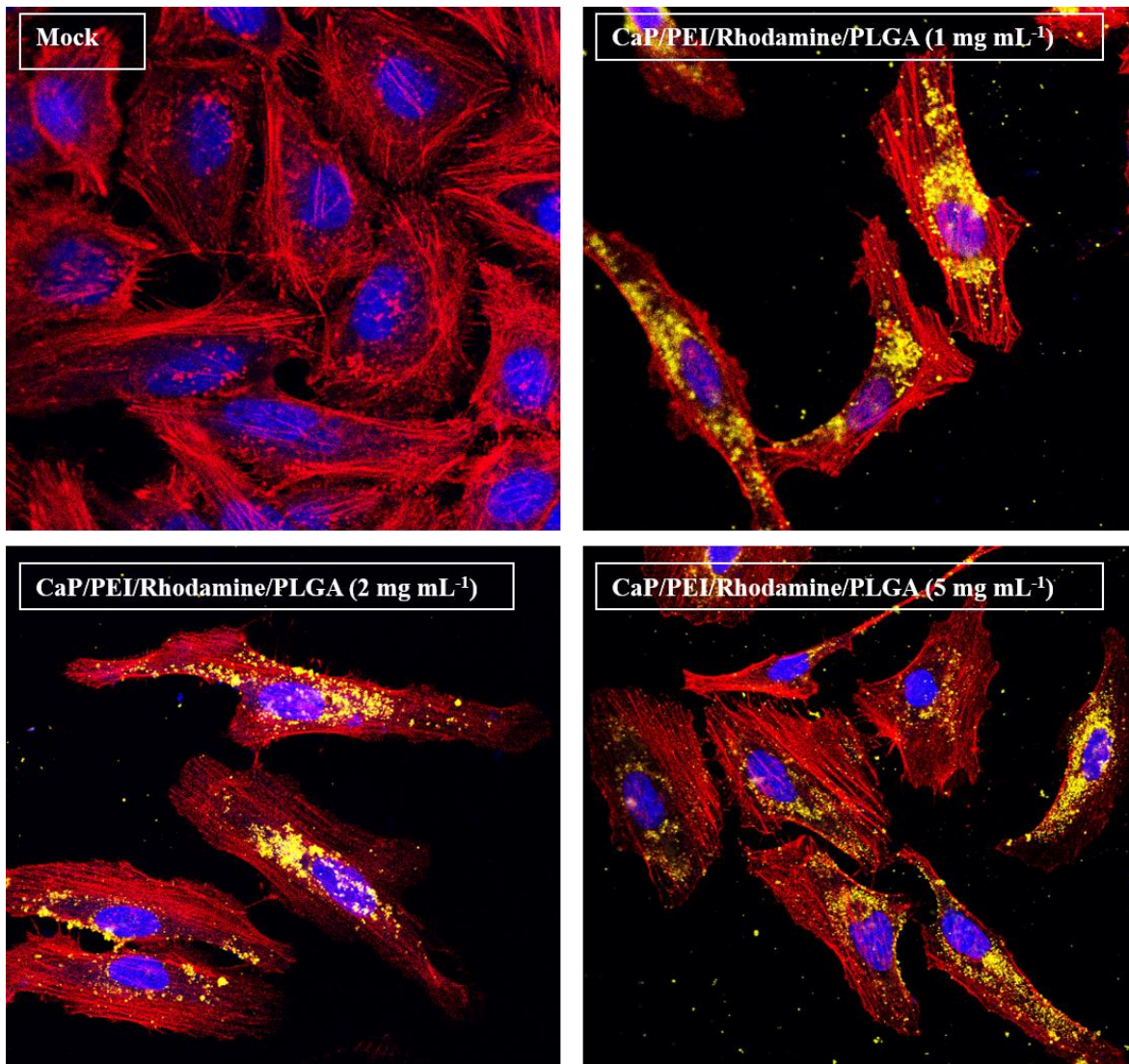


Figure 44: CLSM images of HeLa cells 24 h after the incubation with calcium phosphate/PEI-Rhodamine/PLGA nanoparticles in concentration of 1, 2, and 5 mg mL<sup>-1</sup>. Mock indicates the untreated cells. The scale corresponds to 20  $\mu$ m in each case.

The confocal laser scanning microscopy images (Figure 44) showed that CaP/PEI-rhodamine/PLGA nanoparticles were efficiently taken up from the HeLa cells. The finely distributed, diffuse fluorescence in the cytosol indicated that the nanoparticles can get in the cytoplasm of the cells. The particles did not show any agglomeration for all concentrations. The uptake with the endocytosis mechanisms, depends on the cell line and the surface charge of nanoparticles. Two important steps in transport of active ingredients using nanoparticles, are the entry of active ingredient carrier into the cell and release of the active ingredient from the endo- and lysosomes into the cytosol of the cell [16]. According to the results of CLSM and uptake study, it can be concluded that the nanoparticles could be carried effectively with the encapsulated system and because of their small size, could get into the HeLa cells.

### 5.3.4 Transfection of nanoparticles in HeLa cells

The CaP/PEI/cEGFP-DNA/PLGA nanoparticles were synthesized for transfection experiments. This plasmid DNA is responsible for the green fluorescent protein and encoded (pcDNA3-EGFP). If the transfection of HeLa cells with pcDNA3-EGFP occurs, EGFP present in the cells expresses so that the cells show a green fluorescence.

In Figure 45, HeLa cells were transfected with EGFP plasmid DNA. For this purpose, the cells were incubated for 24 h with CaP/PEI/cEGFP-DNA/PLGA nanoparticles. The non-absorbed nanoparticles were then removed from the culture by washing the cells three times with PBS. The cells were incubated for a further 48 h, fixated, dyed and examined by CLSM. A group of untreated cells (Mock) and a group of cells incubated with Lipofectamine and EGFP plasmid DNA served as controls.

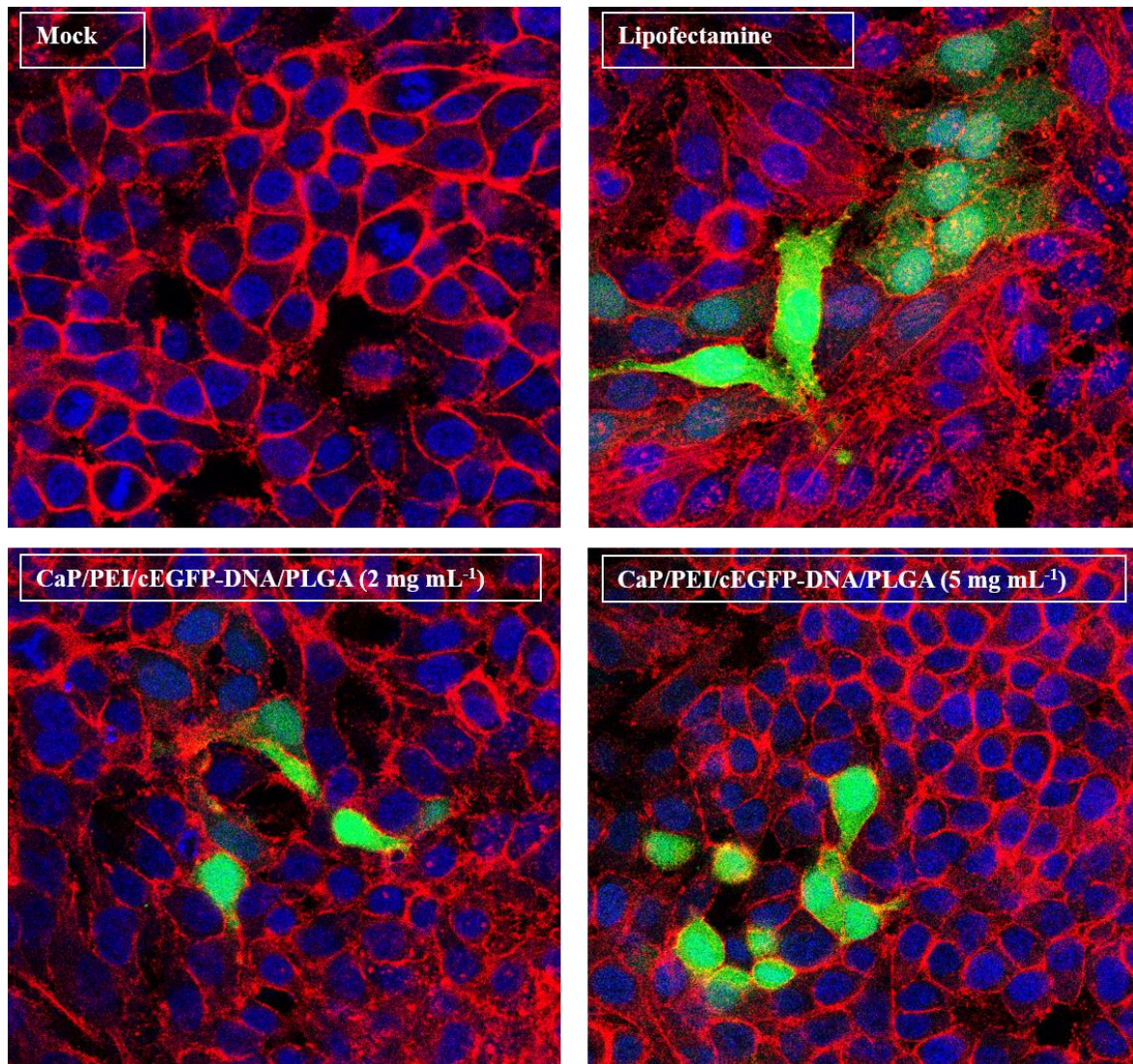


Figure 45: CLSM transfection images of HeLa cells 24 h after the incubation with Lipofectamine and calcium phosphate/PEI/cEGFP-DNA/PLGA nanoparticles in concentration of 2, and 5 mg mL<sup>-1</sup>. Mock indicates the untreated cells. The scale corresponds to 20  $\mu$ m in each case.

Figure 45 shows the results of the transfection tests of dispersed nanoparticles. No emissions in the wavelength range for EGFP could be measured in the Mock group. The Lipofectamine control shows a high transfection efficiency. The cells that were incubated with functionalized nanoparticles also showed adequate fluorescent cells. The transfection efficiency determined by light and fluorescence microscopy and the calculated results are gathered here. According to the calculated transfection efficiency, Lipofectamine presented 31 % transfection efficiency, and the nanoparticles showed 14 % and 20 % transfection efficiency respectively for 2 mg mL<sup>-1</sup> and 5 mg mL<sup>-1</sup> freeze-dried nanoparticles with trehalose. Due to the different amount of polymers in the system, accurate calculation of DNA percentage in whole system was challenging. However, the approximate amount of

DNA used in this study was 6  $\mu\text{g}$  per well in case of 2  $\text{mg mL}^{-1}$  dried nanoparticles and 9  $\mu\text{g}$  per well for 5  $\text{mg mL}^{-1}$  dried nanoparticles.

### 5.3.5 Gene silencing of nanoparticles in HeLa cells

For gene silencing investigations, HeLa-EGFP cells were used which steadily expressed the green fluorescent protein [246, 276, 289]. HeLa-EGFP cell line fluoresces green because of continuous EGFP expression. These green fluorescent HeLa cells are transfected with a siRNA that is directed against the sequence of the gene coding for EGFP. As a result, the green fluorescence of the HeLa-EGFP will be reduced. With comparing the non-fluorescent cells with the fluorescent cells, the gene silencing efficiency can be determined.[246]

The HeLa-EGFP cells were incubated for 24 h with CaP/PEI/siRNA-EGFP/PLGA nanoparticles. The non-absorbed nanoparticles were then removed from the culture by washing the cells three times with PBS. The cells were incubated for a further 48 h, fixated, dyed and examined on the CLSM. A group of untreated cells (Mock) and a group of cells incubated with Lipofectamine and EGFP plasmid DNA served as controls.

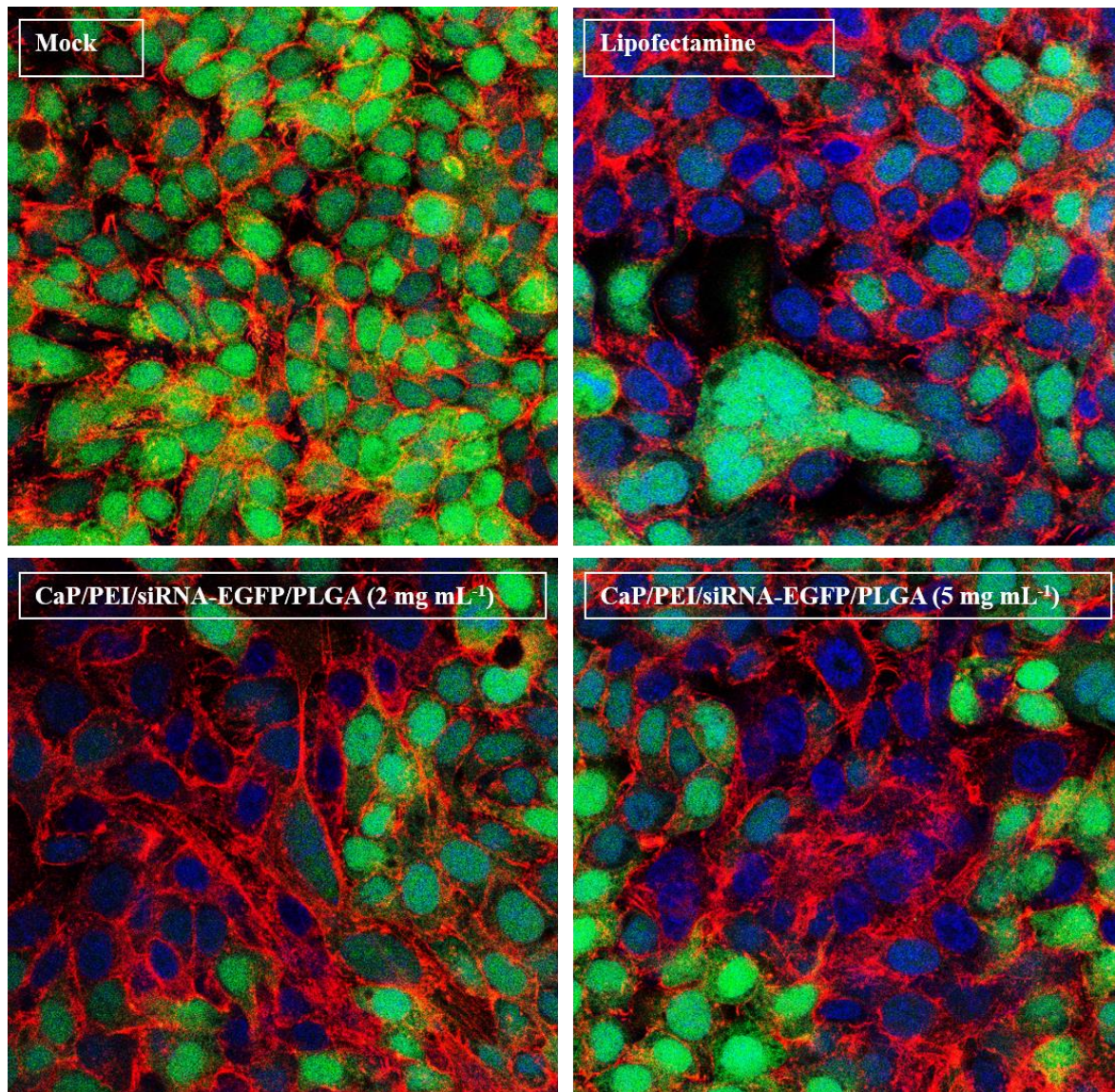


Figure 46: CLSM gene silencing images of HeLa cells 24 h after the incubation with Lipofectamine and calcium phosphate/PEI/siRNA-EGFP/PLGA nanoparticles in concentration of 1, 2, and 5 mg mL<sup>-1</sup>. The scale corresponds to 20 μm in each case.

In Figure 46 gene silencing can be seen in the confocal images. The intensity of the green fluorescence after adding CaP/PEI/siRNA-EGFP/PLGA nanoparticles in comparison to untreated HeLa-EGFP cells (Mock) was prominently reduced. Lipofectamine showed a significant decrease of green fluorescence in the cells. Two concentrations of the siRNA-loaded nanoparticles showed also very appropriate gene silencing. The gene silencing efficiency was determined in every case according to the fluorescent microscopy. Gene silencing efficiency for Lipofectamine was 56 % and for the nanoparticles showed 26 % and 29 % respectively for 2 mg mL<sup>-1</sup> and 5 mg mL<sup>-1</sup> freeze-dried nanoparticles with trehalose.

The approximate amount of siRNA used in gene silencing study was 9  $\mu\text{g}$  per well in case of 2  $\text{mg mL}^{-1}$  dried nanoparticles and 22.5  $\mu\text{g}$  per well for 5  $\text{mg mL}^{-1}$  dried nanoparticles.

### 5.3.6 Conclusion

In this section of the work the synthesis of polylactide encapsulated nanoparticles was described with a water-in-oil-in-water emulsion technique. The nanoparticles indicated the size of approximately 100 nm and spherical morphology. The nanoparticles were then tested in *in vitro* studies. All kinds of nanoparticles demonstrated proper cell viability by the HeLa cells, very suitable uptake by the cells without changing in quality of the nanoparticles or agglomerations, appropriate transfection efficiency and gene silencing. Calcium phosphate–PLGA nanoparticles and calcium phosphate-nucleotide-PLGA nanoparticles showed promising cell biological properties that make it suitable for use for transporting the nucleic acids or proteins.

### 5.4 Strontium and magnesium-doped calcium phosphate nanoparticles

Bone is an inorganic–bioorganic composite material consisting mainly of collagen proteins and calcium phosphates. Its structure, surface roughness, chemistry, and mechanical properties of biomaterials are fascinating for the researchers [9, 50].

Moreover, calcium phosphate nanoparticles which are in the form of amorphous calcium phosphate (ACP) as well as hydroxyapatite in the body, are known as inorganic phase of bones and teeth [50, 290-295]. Calcium phosphate nanoparticles are used extensively for therapeutic delivery applications, due to their biocompatibility and controllable biodegradability [55, 296-300]. Bone defects resulting from tumour resection, osteomyelitis, and trauma have been intensified the attentions of employing the bioactive materials for the repair of bone in recent decades [301-304].

Recent studies have been shown that even small substitution changes have considerable consequences on the thermal stability, solubility, and *in vitro* osteoclastic and osteoblastic responses as well as *in vivo* degradation and bone regeneration. Moreover, some more specific studies on magnesium-doped calcium phosphates have reported an increase in solubility, which shows improvements in biocompatibility [187, 196, 305, 306].

Biological apatite is an inorganic calcium phosphate salt in apatite form and nano-size with a biological derivation. It is the main inorganic component of biological hard tissues such as bones and teeth. Therefore, biological apatite has a wide application in dentistry and

orthopedics by using as dental fillers and bone substitutes for bone reconstruction and regeneration. Furthermore, biological apatite has been employed with restructuring of bone defect in oral implantology, periodontology, bone substitutes surgery as well as orthopaedics, thanks to its resemblance in chemical compositions and structure, together with its outstanding bioactivity and biocompatibility [14, 307-310].

Magnesium ions are the fourth most abundant cations in mammals after sodium, potassium, and calcium. Also, magnesium is the second most prevalent intracellular cation [311, 312]. Inside mammalian cells magnesium plays multiple essential roles including: regulation of calcium and sodium ion channels, stabilizing DNA, being a cofactor and catalyser for many enzymes, and stimulating cell growth and proliferation [313, 314].

The main ion replacing calcium in biological apatite is magnesium which plays also an essential role in bone metabolism, while it influences the bone augmentation by involving osteoblast and osteoclast activities which prevents the possible risk factors for osteoporosis in humans [305].

Strontium (Sr), which also exists in the mineral segment of the bone is a natural bone-seeking element integrating into the bone at the same rate as Ca [295, 315, 316]. Strontium enhances both bone mass and strength due to its performance in stimulating formation of bone as well as inhibiting bone resorption [317-319].

Strontium has been demonstrated to promote osteoblast function and inhibit osteoclast performance in *in-vitro* studies. Studies showed that cellular mechanisms directing this response to involve the calcium sensing receptor (CaSR), which is a g-protein-coupled receptor (GPCR) located in the bone cells and affected bone remodelling [320].

In this study, calcium phosphate nanoparticles were doped with different ratios of magnesium and strontium. The objective of this study was to compare magnesium-doped calcium phosphate nanoparticles with strontium-doped calcium phosphate nanoparticles in different cell lines.

### 5.4.1 Characterization of strontium-doped calcium phosphate nanoparticles

Five different types of nanoparticles were synthesized here. The nanoparticles were based on calcium phosphate, but with differed percentage of strontium. Calcium phosphate nanoparticles were also used as a control. All types of nanoparticles were stabilized and dye-labeled with PEI-Rhodamine to be able to be followed in *in vitro* studies. All the nanoparticles were characterized in detail using SEM, DLS, and AAS. In this way, the colloidal properties, the size and morphology of the particles in the dispersion could be determined. Figure 47 shows DLS measurement curves of all types of particles.

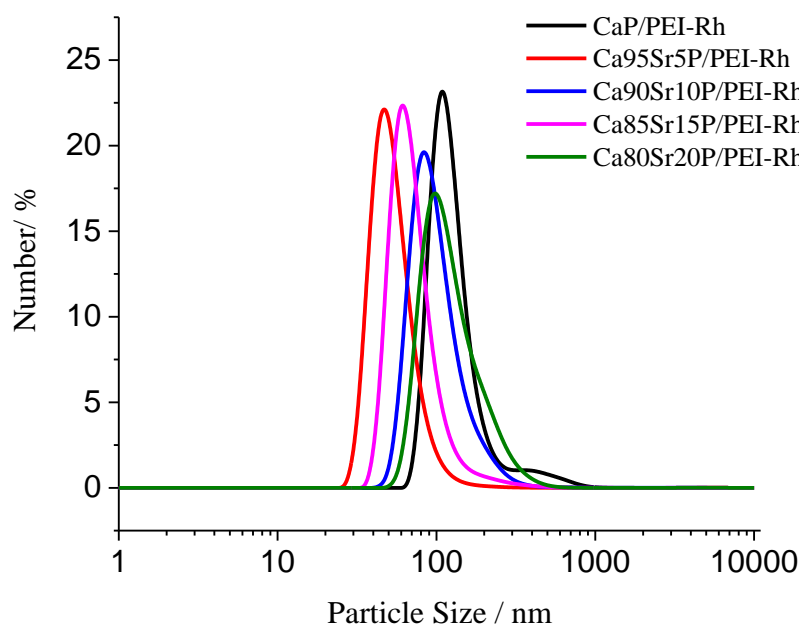


Figure 47: DLS measurements of calcium phosphate nanoparticles and strontium-doped calcium phosphate nanoparticles stabilized and dye-labeled with PEI-Rhodamine (PEI<sup>Rh</sup>).

The DLS measurement curves showed narrow size distributions for all nanoparticle types. Nevertheless, they were slightly different between the calcium phosphate nanoparticles and strontium-doped calcium phosphate nanoparticles. Strontium-doped calcium phosphate nanoparticles showed also smaller size rather than the pure calcium phosphate nanoparticles. The PDI values of the measurements were in the same range as the values of calcium phosphate nanoparticles.

Table 4: AAS measurements of strontium-doped calcium phosphate nanoparticles stabilized and dyed with PEI-Rhodamine (PEI<sup>Rh</sup>).

Sample	Calcium content / mol %	Strontium content / mol %
Sr5Ca95P/PEI <sup>Rh</sup>	91	9
Sr10Ca90P/PEI <sup>Rh</sup>	85	15
Sr15Ca85P/PEI <sup>Rh</sup>	84	16
Sr20Ca80P/PEI <sup>Rh</sup>	81	19

Table 4 shows the AAS values of the strontium-doped calcium phosphate nanoparticles. The synthesized particles should have 5 %, 10 %, 15 %, and 20 % strontium. AAS results indicates that the experimental amount of strontium in doped nanoparticles is slightly different to the theoretical values which was completely acceptable.

SEM images of the doped calcium phosphate nanoparticles with strontium are shown in Figure 48. All types of particles had the typical morphology. Mainly spherical particles were present. Associated histograms of the particles size were also provided by randomly counting the size of around 100 to 200 particles in SEM images. According to the histograms, the strontium-doped calcium phosphate nanoparticles have average size of 40 nm. Like DLS, SEM shows that the pure calcium phosphate nanoparticles have bigger size of the nanoparticles. As shown in the SEM image and histogram of pure calcium phosphate nanoparticles, the average size of the particles is 50 nm which is slightly bigger than the strontium-doped calcium phosphate nanoparticles.

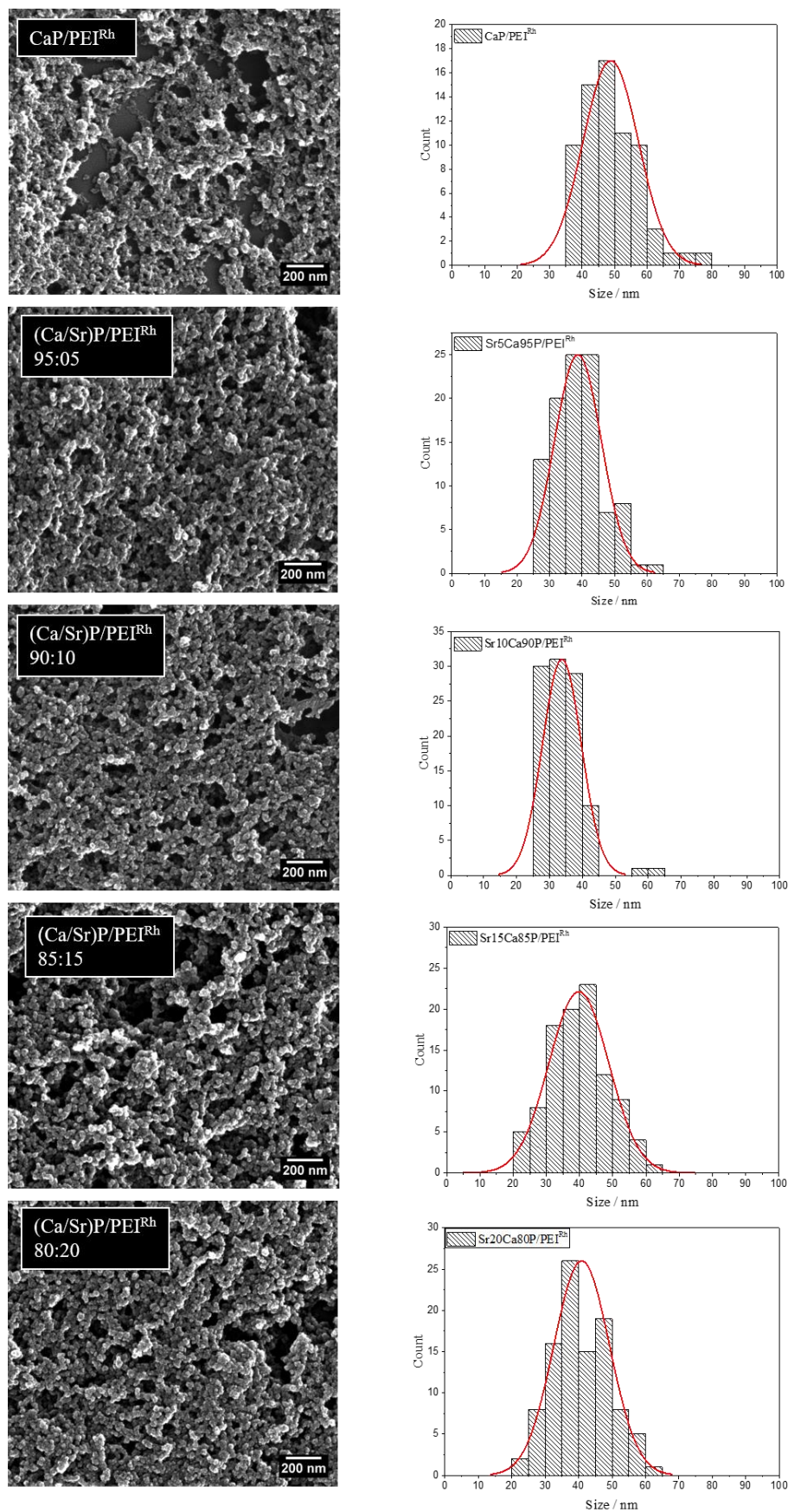


Figure 48: SEM images and relative histogram of calcium phosphate nanoparticles and strontium-doped calcium phosphate nanoparticles stabilized and dyed with PEI-Rhodamine (PEI<sup>Rh</sup>).

Hydroxyapatite ( $\text{Ca}_{10}(\text{PO}_4)_6(\text{OH})_2$ ) or as the abbreviation form HA is capable of keeping its crystal structure after ionic substitution. Most of the cations usually exchange with calcium ions, and anions replace the hydroxy groups or phosphate groups of the HA crystal. Both kinds of substitution cause contraction or expansion of the lattice parameter. Maintenance of charge neutrality is an essential parameter for any bulk material [321]. The replacement of calcium ions with bivalent cations such as strontium ions does not cause any charge imbalance in the crystal lattice.

Table 5: DLS measurements of strontium-doped calcium phosphate nanoparticles stabilized and dyed with PEI-Rhodamine ( $\text{PEI}^{\text{Rh}}$ )

Name	Size (DLS) / nm	PDI	Zeta potential / mV	Size (SEM) / nm
CaP/ $\text{PEI}^{\text{Rh}}$	105	0.3	$9 \pm 3$	50
Sr5Ca95P/ $\text{PEI}^{\text{Rh}}$	70	0.3	$8 \pm 3$	40
Sr10Ca90P/ $\text{PEI}^{\text{Rh}}$	95	0.3	$10 \pm 4$	35
Sr15Ca85P/ $\text{PEI}^{\text{Rh}}$	85	0.3	$11 \pm 3$	40
Sr20Ca80P/ $\text{PEI}^{\text{Rh}}$	100	0.3	$10 \pm 4$	45

DLS, zetapotential and SEM measurements of all samples were collected in Table 5. DLS showed aggregates however, the small nanoparticles with a size of 50-120 nm were present in each sample. The zeta potential of all particles was always positive with a value of around +10 mV. To check the DLS data we performed scanning electron microscopy of the particles. It showed a much smaller particle size than that obtained by DLS. Partially it is due to the fact that DLS measurements show the hydrodynamic radius of the particles whereas electron microscopy shows the inorganic core. Strontium-doped calcium phosphate nanoparticles had a spherical morphology with particle size around 40 nm, showing a reduction of particle size with an addition of strontium.

#### **5.4.2 Cell-biological characterization of strontium-doped nanoparticles in different cells**

In order to characterize the strontium-doped calcium phosphate nanoparticles in cells, the nanoparticles were first freeze-dried with trehalose with a ratio of 1:10 to 1:20. Then the

particles were stored in the refrigerator to prevent any changes of the particles. 3 mg of the dried nanoparticles with trehalose were dissolved in either 500  $\mu$ L cell medium (for reaching cell cytotoxicity test) or 250  $\mu$ L cell medium (for uptake studies). The results of cytotoxicity test and uptake with three different cell lines are shown in this section.

#### 5.4.2.1 MTT test

In order to determine the cytotoxicity of the strontium-doped calcium phosphate nanoparticles, the vitality of the HeLa cells 24 h after incubation with the nanoparticles studied in MTT test. Figure 49 shows the vitality of the HeLa cells 24 h after incubation with strontium-doped nanoparticles and pure calcium phosphate nanoparticles dispersed in DMEM as a cell medium. After the end of the incubation, the cells were incubated with MTT reagent and the absorbance at 570 nm was measured in triplets. The intensity was calculated in relation to a sample of untreated cells. Three wells per particle type and six wells as a Mock group were used. The results of the investigations using MTT are shown in Figure 49.

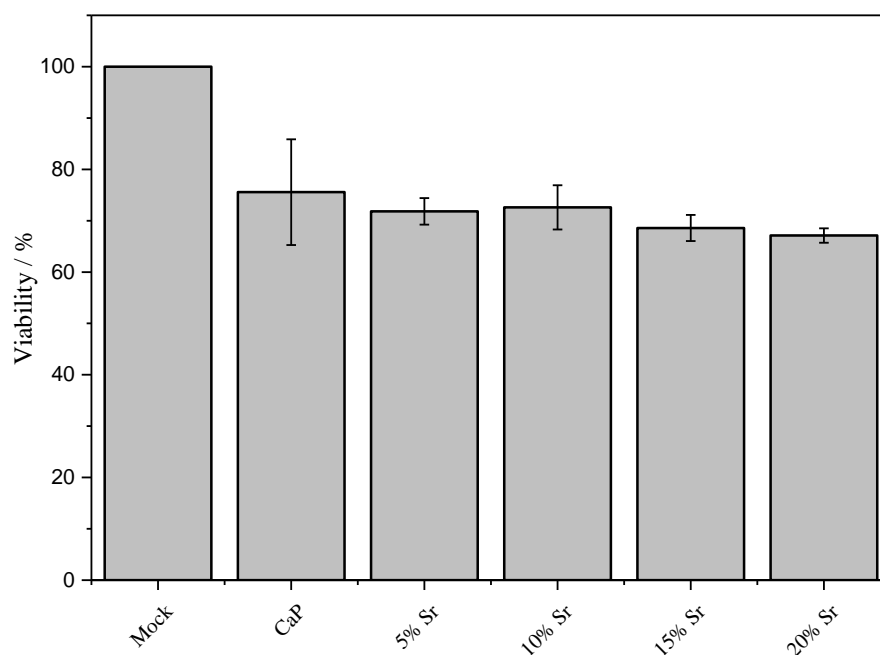


Figure 49: Diagram of the MTT results for the incubation of HeLa cells after 24 h with strontium-doped nanoparticles, pure calcium phosphate nanoparticles dispersed in cell medium and a group of untreated cells as a comparison (Mock).

All the nanoparticles showed a high cell viability measured after 24 h. For all particle types after 24 hours, the viability was over 70 %, so that the particles in the applied concentrations

were non-toxic. The differences in cytotoxicity found for the different types of particles were not significant.

### 5.4.2.2 Uptake

As major part of the cell biological investigations, uptake studies were initially carried out to check which particles can be absorbed by the cells. For this purpose, three different cell lines were used. HeLa cells, MG63 cells, and MC3T3 cells were developed. In this study, cells from the human osteosarcoma cell line MG-63 were used which is osteoblast-like cell and has been well reported to represent the appropriate human osteoblast model [322]. MC3T3 was the other cell line which derived from newborn murine calvarias or the top part of the skull. MC3T3 cell line has been widely reported to present osteoblast-like behavior. In order to research the uptake of the nanoparticles by cells, cells were seeded in 8-well  $\mu$ -slides and, after adhesion, incubated with fluorescence-labeled nanoparticles for 24 h.

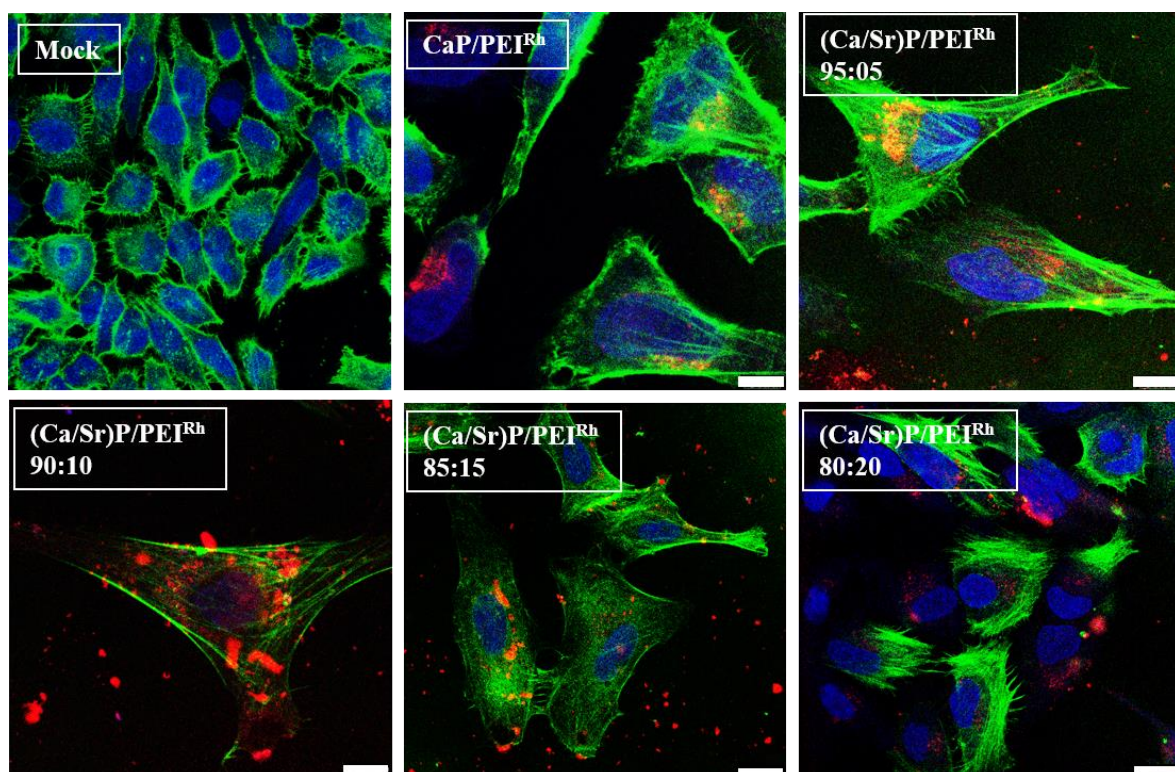


Figure 50: Uptake studies of HeLa cells with untreated cells (Mock), and after incubation for 24 h with calcium phosphate/PEI-rhodamine ( $\text{CaP/PEI}^{\text{Rh}}$ ), 5 %, 10 %, 15 %, and 20 % strontium-doped calcium phosphate nanoparticles. Red: actin; blue: nucleus; red: nanoparticles contained rhodamine. Scale: 10 $\mu\text{m}$ .

Figure 50 shows the confocal laser microscope images of the HeLa cells after completing the incubation. A sample of untreated cells (Mock) as a control is also considered. No fluorescence in the wavelength range for rhodamine could be found in the Mock group. The fluorescence in this area came exclusively from the labeled nanoparticles. For CaP/PEI<sup>Rh</sup>, and all the strontium-doped calcium phosphate nanoparticles colored with rhodamine, a signal for rhodamine was detected in the cells for all types of particles. In the case of 10 % and 15 % strontium-doped calcium phosphate nanoparticles, agglomeration could be detected. Nevertheless, there were also smaller particles which were absorbed by the HeLa cells.

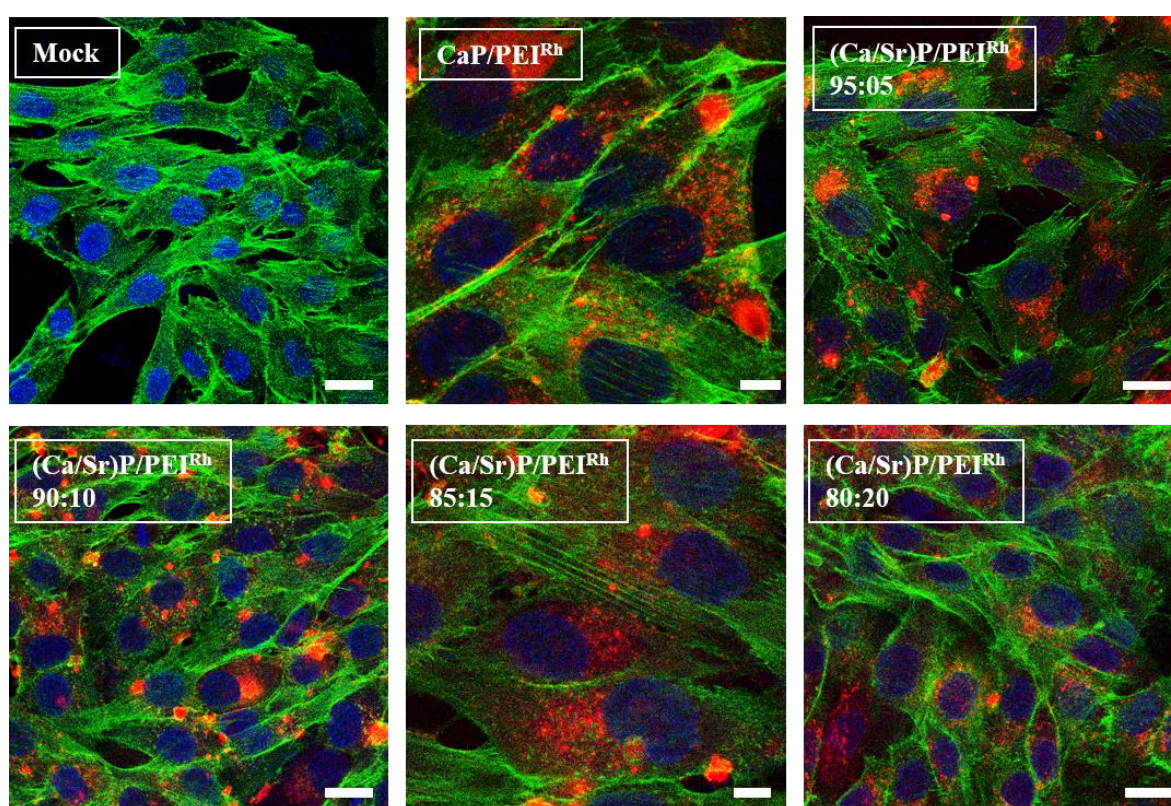


Figure 51: Uptake studies of MG-63 cells with untreated cells (Mock), and after 24 h incubation time with calcium phosphate/PEI-rhodamine (CaP/PEI<sup>Rh</sup>), and 5 %, 10 %, 15 %, and 20 % strontium-doped calcium phosphate nanoparticles. Red: actin; blue: nucleus; red: nanoparticles. Scale: 10  $\mu$ m.

Figure 51 shows the confocal laser microscope images of the MG-63 cells after 24 h of incubation. Untreated cells (Mock) were considered as a control. No fluorescence in the wavelength range for rhodamine could be found in the Mock group. As it is shown in the confocal images, all the strontium-doped calcium phosphate nanoparticles were taken up by the MG-63 cells as well as the pure calcium phosphate nanoparticles. No difference between

the uptakes of the various types of nanoparticles were seen in these pictures. As a result, all types of nanoparticles can be taken up equally by MG-63 cells.

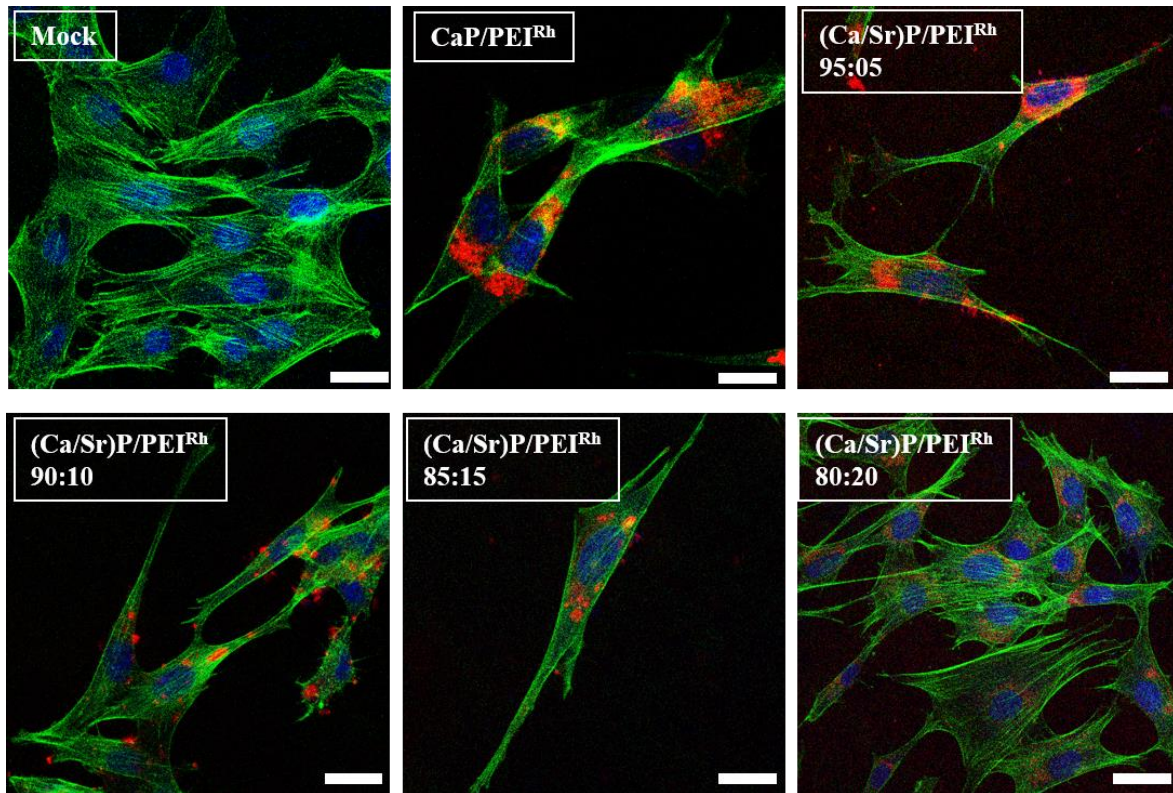


Figure 52: Uptake studies of MC3T3 cells with untreated cells (Mock), and after incubating for 24 h with calcium phosphate/PEI-rhodamine (CaP/PEI<sup>Rh</sup>), and 5 %, 10 %, 15 %, and 20 % strontium-doped calcium phosphate nanoparticles. Red: actin; blue: nucleus; red: nanoparticles contained rhodamine. Scale: 20  $\mu$ m.

Figure 52 shows the confocal microscope images of the MC3T3 cells after 24 h of incubation, fixating and dyeing the cells. A sample of untreated cells (Mock) as usual was considered as a control. No fluorescence in the wavelength range for rhodamine could be found in the Mock group. According to the confocal images, pure calcium phosphate nanoparticles in the MC3T3 showed agglomeration, however, a large amount of the nanoparticles were taken up by the MC3T3 cells. The same result in uptake of 5 % strontium-doped nanoparticles was discovered. Overall, it is obvious that all of the nanoparticle types were taken up by the cells.

### 5.4.3 Characterization of magnesium-doped calcium phosphate nanoparticles

In this section, two different types of magnesium-doped calcium phosphate nanoparticles were synthesized. Positive-charged nanoparticles were synthesized with PEI-rhodamine and Negative-charged nanoparticles were prepared with CMC-FITC. Stabilization with PEI results in positive zeta potentials, and with CMC negative zeta potentials. Both PEI-stabilized and CMC-stabilized nanoparticles are used to understand the differences between the positive and negative magnesium-doped nanoparticles *in vitro*. All nanoparticles were characterized with AAS, EDX, DLS, and SEM as well as the *in vitro* studies.

#### 5.4.3.1 Negatively-charged nanoparticles

Here five different magnesium-doped calcium phosphate nanoparticles stabilized and dye-labeled with CMC-FITC ( $\text{CMC}^{\text{FITC}}$ ) were synthesized and characterized. The doped nanoparticles have 5 %, 10 %, 15 %, or 20 % magnesium as a doping percentage. Pure calcium phosphate nanoparticles were also stabilized and dye-labeled with CMC-FITC to act as a control for the doping system.

Figure 64 shows the DLS diagram of the magnesium-doped calcium phosphate nanoparticles which are stabilized and dye-labeled with CMC-FITC.

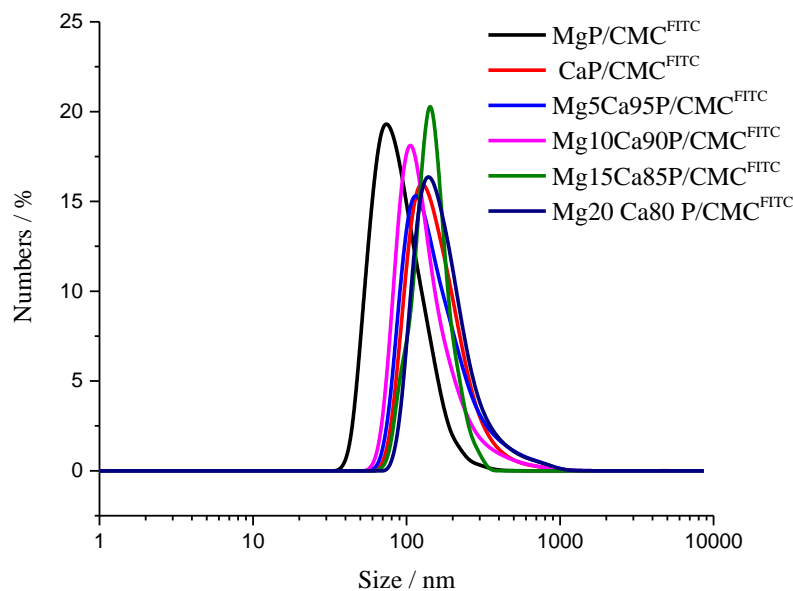


Figure 53: DLS measurements of calcium phosphate nanoparticles and magnesium-doped calcium phosphate nanoparticles stabilized and dye-labeled with CMC-FITC ( $\text{CMC}^{\text{FITC}}$ )

The DLS measurement curves in Figure 53 showed narrow size distributions for the nanoparticle types. Nevertheless, there were slight differences between the magnesium-doped calcium phosphate nanoparticles and pure calcium phosphate nanoparticles. The dynamic light scattering showed in the number distribution for all particle systems monodisperse systems with a PDI <0.3. According to the DLS all the nanoparticles showed an average size of 100 to 140 nm.

The 5 % magnesium-doped calcium phosphate nanoparticles (Mg5Ca95P/CMC<sup>FITC</sup>) had, according to number distribution, a particle size of 115 nm and a zeta potential of  $-13 \pm 3$  mV with a PDI of 0.3. For 10 % magnesium-doped calcium phosphate nanoparticles (Mg10Ca90P/CMC<sup>FITC</sup>), the mean particle diameter was 105 nm with a zeta potential of  $-19 \pm 4$  mV and a PDI of 0.3. Both synthesized systems showed smaller size than the pure calcium phosphate nanoparticles with a particle size of 125 nm and a zeta potential of  $-17 \pm 5$  mV with a PDI of 0.3.

The 15 % magnesium-doped calcium phosphate nanoparticles (Mg15Ca85P/CMC<sup>FITC</sup>) had, according to number distribution, a particle size of 140 nm and a zeta potential of  $-20 \pm 5$  mV with a PDI of 0.4. For 20 % magnesium-doped calcium phosphate nanoparticles (Mg20Ca80P/CMC<sup>FITC</sup>), the mean particle diameter was also 140 nm with a zeta potential of  $-18 \pm 7$  mV and a PDI of 0.3. The particle size indicated greater agglomeration than the first two doped systems.

All the systems gave monodisperse particle size distributions, slight agglomeration and negative zeta potential.

Table 6: AAS and EDX measurements of magnesium-doped calcium phosphate nanoparticles stabilized and stained with CMC-FITC (CMC<sup>FITC</sup>)

Sample	AAS Ca/ mol %	AAS Mg/ mol %	EDX Ca / mol %	EDX Mg / mol %
CaP/CMC <sup>FITC</sup>	100	0	100	0
Mg5Ca95P/CMC <sup>FITC</sup>	92	8	97	3
Mg10Ca90P/CMC <sup>FITC</sup>	93	7	89	11
Mg15Ca85P/CMC <sup>FITC</sup>	89	11	83	17
Mg20Ca80P/CMC <sup>FITC</sup>	86	14	79	21

Table 6 shows the AAS and EDX values of the magnesium-doped calcium phosphate nanoparticles. Synthesized magnesium-doped calcium phosphate nanoparticles should have 5 %, 10 %, 15 %, and 20 % magnesium. AAS results indicates that the experimental amount of strontium in doped nanoparticles is slightly different to the theoretical values which was completely acceptable.

The magnesium-doped calcium phosphate nanoparticles were then characterized with SEM to check the morphology and size of the nanoparticles. SEM images of magnesium-doped calcium phosphate nanoparticles are shown in Figure 54. DLS, zeta potential, PDI, and SEM information of magnesium-doped calcium phosphate nanoparticles are also summarized in Table 7.

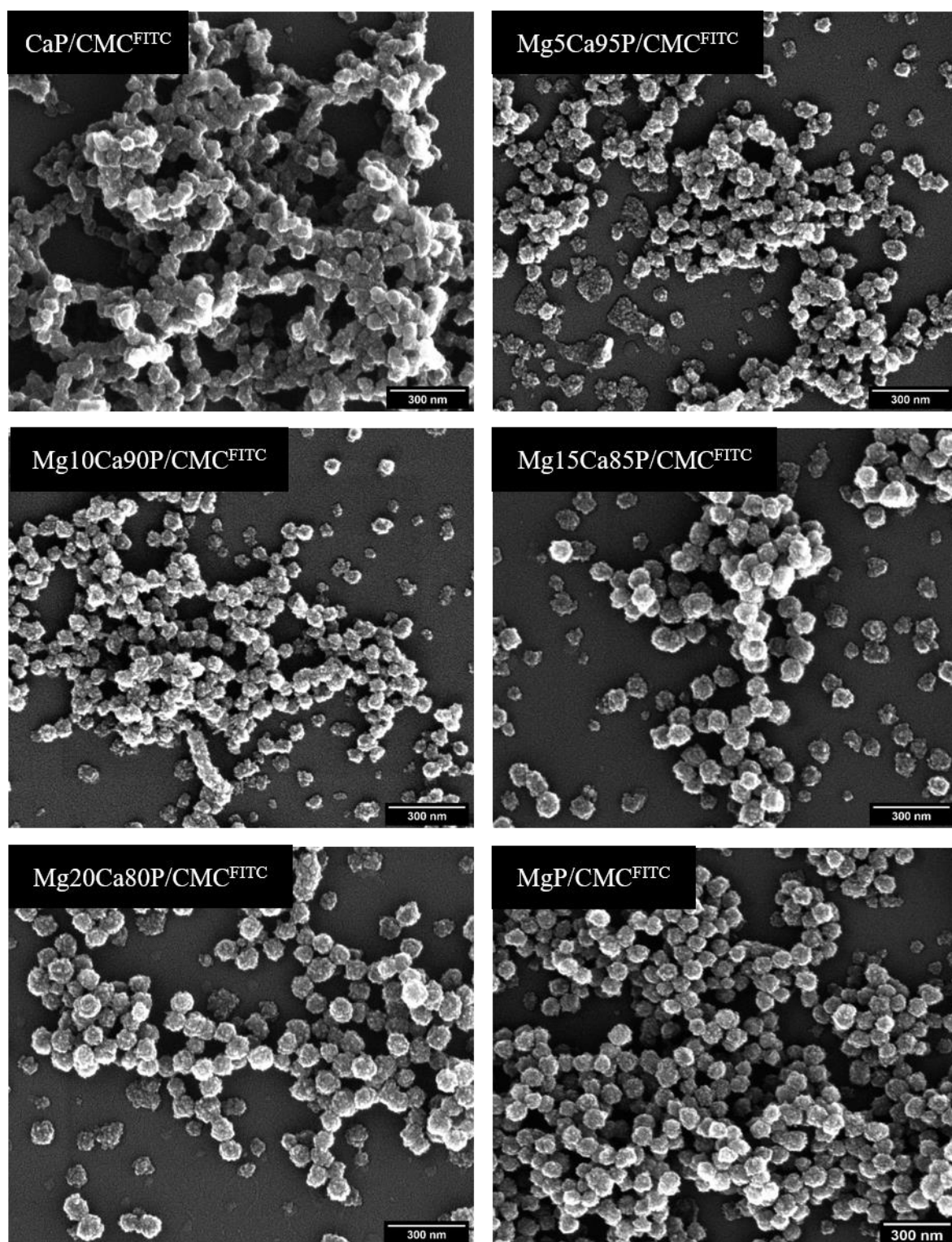


Figure 54: SEM images of calcium phosphate nanoparticles and magnesium-doped calcium phosphate nanoparticles stabilized and stained with CMC-FITC (<sup>FITC</sup>).

SEM images of the magnesium-doped calcium phosphate nanoparticles, calcium phosphate nanoparticles and magnesium phosphate nanoparticles are shown in Figure 54. For all particle systems, monodisperse particle size distributions with a spherical morphology could

be found. In the case of pure CMC-FITC-stabilized calcium phosphate nanoparticles (CaP/CMC<sup>FITC</sup>), the particles have a spherical morphology with a slight agglomeration. The average particle size in all the CMC-stabilized magnesium-doped nanoparticles were about 40 to 50 nm.

According to the SEM images of the nanoparticles the spherical morphology of the calcium phosphate nanoparticles was maintained after the addition of magnesium. The monodispersity in the magnesium-doped calcium phosphate nanoparticles was improved. As it is clear in the images, there were no significant agglomeration detected by the images.

Table 7: DLS measurements of Magnesium-doped calcium phosphate nanoparticles stabilized and stained with CMC-FITC (CMC<sup>FITC</sup>)

Name	Size (DLS) / nm	PDI	Zeta potential / mV	Size (SEM) / nm
CaP/CMC <sup>FITC</sup>	125	0.3	-17 ± 5	80
Mg5Ca95P/CMC <sup>FITC</sup>	115	0.3	-13 ± 3	50
Mg10Ca90P/CMC <sup>FITC</sup>	105	0.3	-19 ± 4	55
Mg15Ca85P/CMC <sup>FITC</sup>	140	0.4	-20 ± 5	80
Mg20Ca80P/CMC <sup>FITC</sup>	140	0.3	-18 ± 7	85

All magnesium-doped calcium phosphate nanoparticle data are summarized in Table 7. All particles were freshly prepared before the experiments and did not show any changes in their properties (e.g. particle size and shape) during the time of the experiments (i.e. a few days). DLS measurements showed that magnesium-doped calcium phosphate nanoparticles had sizes around 100-140 nm, negative zeta potential around -13 to -20 mV and a PDI of 0.3 whereas calcium phosphate nanoparticles had a diameter of 105 nm with a zeta potential of -17 mV. DLS measurements showed aggregates which is due to the fact that DLS measurements show the hydrodynamic radius of the particles. On the other hand, SEM images showed that magnesium-doped calcium phosphate nanoparticles had a spherical morphology with particle size around 50-85 nm. In the case of 5 % and 10 % magnesium-doped calcium phosphate nanoparticles, the average size of the nanoparticles were slightly smaller than the other doping systems which is in agreement with the previous DLS data.

The difference in the particle size between the size determination using DLS and SEM indicates the level of agglomeration of the particles.

### 5.4.3.2 Positively-charged nanoparticles

In this section, magnesium-doped calcium phosphate nanoparticles in percentages of 5 %, 10 %, 15 %, and 20 % were synthesized. These magnesium-doped calcium phosphate nanoparticles were with the PEI<sup>Rh</sup> stabilized and stained. Pure calcium phosphate nanoparticles was also developed as a control. All the nanoparticles were characterized with AAS, DLS, EDX, and SEM as well as *in vitro* studies with different cell lines.

Figure 66 shows the DLS diagrams of the magnesium-doped calcium phosphate nanoparticles as well as the two pure calcium phosphate and magnesium phosphate nanoparticles as control.

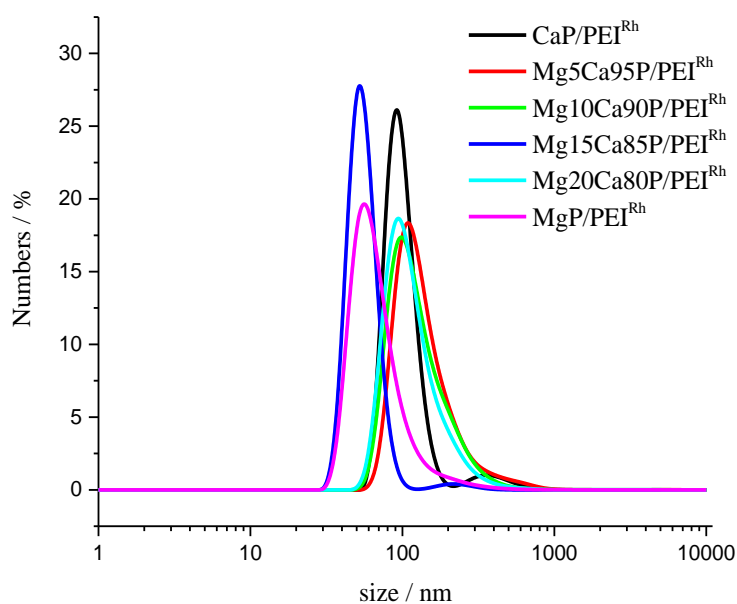


Figure 55: DLS measurements of calcium phosphate nanoparticles and magnesium-doped calcium phosphate nanoparticles stabilized and dyed with PEI-Rhodamine (PEI<sup>Rh</sup>).

The DLS results in Figure 55 show that the synthesized magnesium-doped calcium phosphate nanoparticles with a hydrodynamic diameter of approx. 90 to 110 nm are very well in the typical size range for calcium phosphate nanoparticles. The pure magnesium phosphate nanoparticles showed the average size of 70 nm which is smaller than the average size of the pure calcium phosphate nanoparticles and most of the magnesium-doped calcium

phosphate nanoparticles. 15 % magnesium-doped calcium phosphate nanoparticles presented also smaller average size by 65 nm in DLS. Moreover, all particles showed monomodal particle size distribution by DLS. Pure calcium phosphate nanoparticles (CaP/PEI<sup>Rh</sup>) presented a DLS average size of 90 nm, positive zeta potential about  $7 \pm 3$  mV and the DLS peak showed a monomodal particle size distribution. Pure magnesium phosphate nanoparticles (MgP/PEI<sup>Rh</sup>) showed a smaller size by 70 nm, positive zeta potential about  $10 \pm 4$  mV and also a monodisperse particle size distribution. All of the nanoparticles had a PDI of 0.3 which was another proof for the monomodality of the nanoparticles.

The 5 % magnesium-doped calcium phosphate nanoparticles (Mg5Ca95P/PEI<sup>Rh</sup>) had according to number distribution a particle size of 105 nm and a zeta potential of  $5 \pm 3$  mV. The particle size indicated greater agglomeration in this system. For 10% magnesium-doped calcium phosphate nanoparticles (Mg10Ca90P/ PEI<sup>Rh</sup>), the mean particle diameter was 95 nm with a zeta potential of  $8 \pm 4$  mV. For 20% magnesium-doped calcium phosphate nanoparticles (Mg20Ca80P/ PEI<sup>Rh</sup>), the mean particle diameter was also 90 nm with a zeta potential of  $15 \pm 7$  mV. All the 5 %, 10 %, and 20 % magnesium-doped calcium phosphate nanoparticles showed same average size by DLS.

The 15 % magnesium-doped calcium phosphate nanoparticles (Mg15Ca85P/ PEI<sup>Rh</sup>) had, according to number distribution, a particle size of 65 nm and a zeta potential of  $8 \pm 3$  mV. All the systems gave monodisperse particle size distributions. The size ranges indicated a slight agglomeration of the particles and all of the nanoparticles showed positive zeta potential.

Table 8 shows the AAS and EDX values of the magnesium-doped calcium phosphate nanoparticles. The synthesized magnesium-doped calcium phosphate nanoparticles should have 5 %, 10 %, 15 %, and 20 % magnesium. AAS and EDX data of these magnesium-doped calcium phosphate nanoparticles are summarized in Table 8. According to AAS and EDX data, magnesium-doped calcium phosphate nanoparticles showed slightly different ratios than the expected values.

Table 8: AAS and EDX measurements of magnesium-doped calcium phosphate nanoparticles stabilized and stained with PEI-Rhodamine (PEI<sup>Rh</sup>).

Sample	AAS Ca / mol%	AAS Mg / mol%	EDX Ca / mol%	EDX Mg / mol%
CaP/PEI <sup>Rh</sup>	100	0	100	0
Mg5Ca95P/PEI <sup>Rh</sup>	91	9	93	7
Mg10Ca90P/PEI <sup>Rh</sup>	85	15	87	13
Mg15Ca85P/PEI <sup>Rh</sup>	84	16	83	17
Mg20Ca80P/PEI <sup>Rh</sup>	81	19	82	18
MgP/PEI <sup>Rh</sup>	0	100	0	100

Positively-charged nanoparticles were characterized by SEM to check their morphology and size. Figure 56 shows representative SEM images and associated histogram for the magnesium-doped calcium phosphate nanoparticles. Histograms from Figure 56 determined average size of the magnesium-doped calcium phosphate nanoparticles.

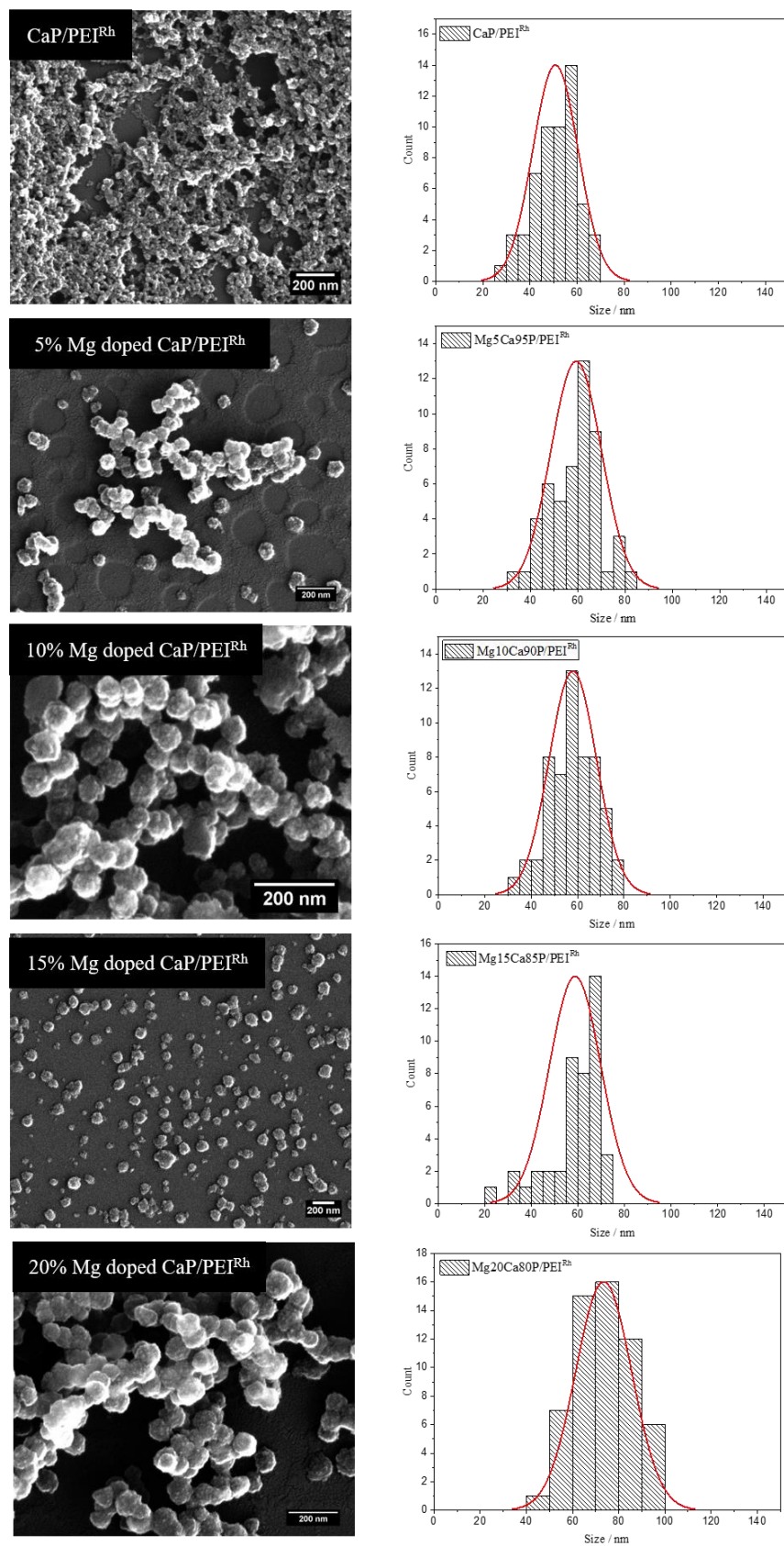


Figure 56: SEM images and relative histogram of calcium phosphate nanoparticles and magnesium-doped calcium phosphate nanoparticles stabilized and dyed with PEI-Rhodamine (PEI<sup>Rh</sup>).

SEM images of the magnesium-doped calcium phosphate nanoparticle and pure calcium phosphate nanoparticles are shown in Figure 56. With the Image J software, the diameters of approx. 100 particles were measured manually and the measured values were evaluated. For all particle systems, monodisperse particle size distributions with a spherical morphology could be found. All the nanoparticles had average particles size between 60 to 70 nm. Pure calcium phosphate nanoparticles showed the average size of 55 nm by SEM. SEM data of magnesium-doped calcium phosphate nanoparticles together with PDI, zetapotential and DLS average size of the nanoparticles are summarized in Table 9.

Table 9: DLS measurements of magnesium-doped calcium phosphate nanoparticles stabilized and stained with PEI<sup>Rh</sup>.

Name	Size (DLS) / nm	PDI	Zeta potential / mV	Size (SEM) / nm
CaP/PEI <sup>Rh</sup>	90	0.3	7 ± 3	55
Mg5Ca95P/PEI <sup>Rh</sup>	105	0.3	5 ± 3	60
Mg10Ca90P/PEI <sup>Rh</sup>	95	0.3	8 ± 4	60
Mg15Ca85P/PEI <sup>Rh</sup>	65	0.3	8 ± 3	55
Mg20Ca80P/PEI <sup>Rh</sup>	90	0.3	15 ± 4	75

### 5.4.3.3 Cell biological characterization of magnesium-doped nanoparticles in different cells

#### 5.4.3.3.1 MTT test

The viability of HeLa cells after 24 h of incubation with negatively and positively charged magnesium-doped calcium phosphate nanoparticles were determined with MTT test (Figure 57). The vitality of the HeLa cells 24 h after incubation with magnesium-doped nanoparticles and pure calcium phosphate nanoparticles dispersed in DMEM was performed. After the end of the incubation, the cells were incubated with MTT reagent and the absorbance at 570 nm was measured in triplets. The intensity was calculated in relation to a sample of untreated cells. Three wells per particle type and six wells as a Mock group were used. The results of the investigations using MTT are shown in Figure 57.

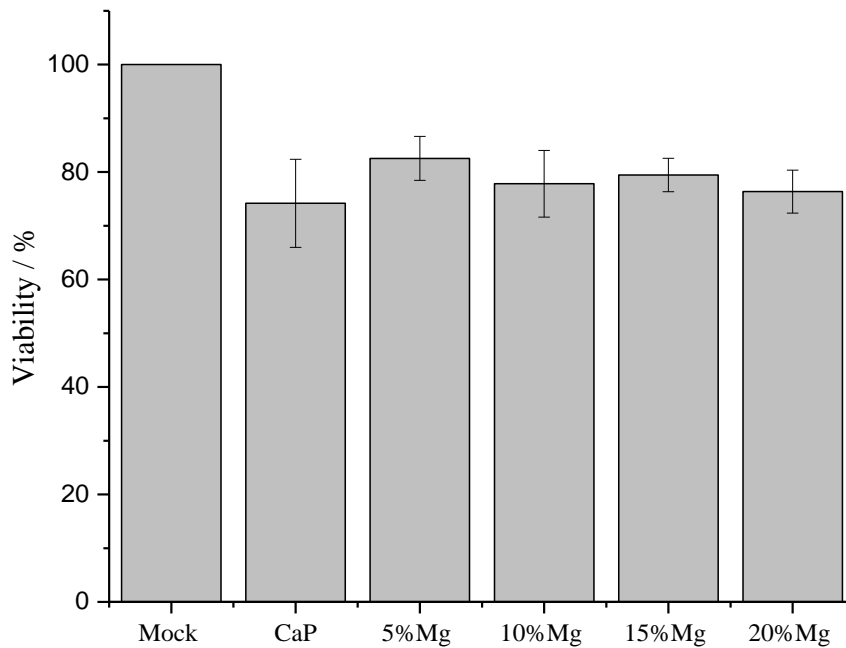


Figure 57: Diagram of the MTT results for the incubation of HeLa cells with magnesium-doped nanoparticles and pure calcium phosphate nanoparticles dispersed in cell medium, and a group of untreated cells as a comparison (Mock). All of the nanoparticles were stabilized and stained with CMC-FITC (CMC<sup>FITC</sup>).

Figure 57 showed the viability of HeLa cells after incubation with the CMC<sup>FITC</sup> stabilized magnesium-doped calcium phosphate nanoparticles and pure calcium phosphate nanoparticles. The evaluated toxicity test of the negatively charged magnesium-doped calcium phosphate nanoparticles and pure calcium phosphate nanoparticles showed almost no reduction of cell viability after incubation of the cells with magnesium-doped calcium phosphate nanoparticles in comparison to pure calcium phosphate nanoparticles. All the magnesium-doped calcium phosphate nanoparticles indicated more cell viability rather than the pure calcium phosphate nanoparticles. The viability of the cells in all of the magnesium-doped calcium phosphate nanoparticles is about 80 %.

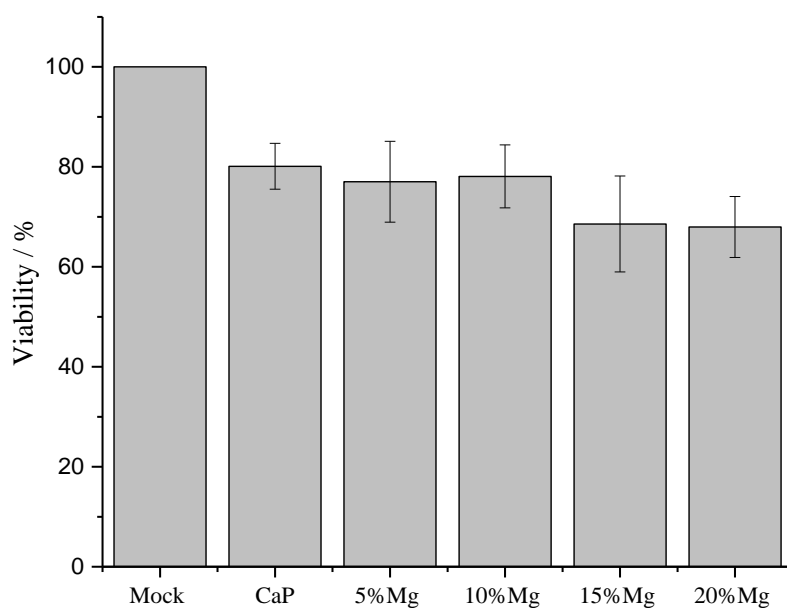


Figure 58: Diagram of the MTT results for the incubation of HeLa cells with magnesium-doped nanoparticles, pure calcium phosphate nanoparticles dispersed in cell medium and a group of untreated cells as a comparison (Mock). All of the nanoparticles were stabilized and stained with PEI-Rhodamine (PEI<sup>Rh</sup>).

Figure 58 showed the viability of HeLa cells after incubation with the positively-charged magnesium-doped calcium phosphate nanoparticles and pure calcium phosphate nanoparticles. The calculated viability results of the positively-charged magnesium-doped calcium phosphate nanoparticles and pure calcium phosphate nanoparticles showed that viability of positively-charged magnesium-doped calcium phosphate nanoparticles were more than 70 %. Pure calcium phosphate nanoparticles presented more cell viability than the other nanoparticles by the cell viability around 80 %. 5 % and 10 % magnesium-doped calcium phosphate nanoparticles showed also the appropriate cell viability around 76 % and 78 %. Nevertheless, in the cases of 15 % and 20 % magnesium-doped calcium phosphate nanoparticles, the cell viability decreased to 66 %. This could be because of the agglomeration of the nanoparticles or more amount of magnesium in the medium of the cells.

### 5.4.3.3.2 Uptake studies of magnesium-doped calcium phosphate nanoparticles

Here, the uptake of negatively-charged nanoparticles and positively-charged nanoparticles is discussed. A previous study about the mechanism of uptake of the negatively charged calcium phosphate nanoparticles and positively charged calcium phosphate nanoparticles suggested that negatively charged calcium phosphate nanoparticles enter the cell by macropinocytosis [101, 323, 324]. For positively charged calcium phosphate nanoparticles, the mechanism of uptake into the cells occurs clathrin- or caveolin-mediated endocytosis [325, 326]. Nevertheless, a study about uptake of calcium phosphate nanoparticles showed that uptake mechanism of calcium phosphate nanoparticles into HeLa cells occurred by macropinocytosis rather than by clathrin- or caveolin-mediated endocytosis [101].

Three different cell lines named: HeLa, MG-63, and MC3T3 cells were used for microscopic examinations of the uptake of the negatively charged and positively charged magnesium-doped calcium phosphate nanoparticles as well as pure calcium phosphate nanoparticles as control. The cells were trypsinized 24 h before the uptake experiments and seeded in the 8-well  $\mu$ -slide plate with a cell density of  $10 \cdot 10^3$  cells per well. For cell uptake, 2-3 mg of the dried magnesium-doped calcium phosphate nanoparticles and pure calcium phosphate nanoparticles were dispersed in 1 mL of the cell culture medium. 200  $\mu$ L of the dispersion were added to the cell line. The cells were incubated for 24 h at 37 °C under a 5 % CO<sub>2</sub> atmosphere. After the incubation, the cells were washed three times with PBS and fixated and stained to be prepare for the confocal microscopy.

#### 5.4.3.3.2.2 Uptake studies of negatively charged magnesium-doped calcium phosphate nanoparticles

The CMC<sup>FITC</sup> stabilized magnesium-doped calcium phosphate nanoparticles were synthesized as mentioned in experimental section, characterized and used here. In order to study *in vitro* about these negatively-charged magnesium-doped calcium phosphate nanoparticles, three different cell lines were also used. In this section, uptake studies with negatively-charged magnesium-doped calcium phosphate nanoparticles by HeLa, MG-63, and MC3T3 cells are shown.

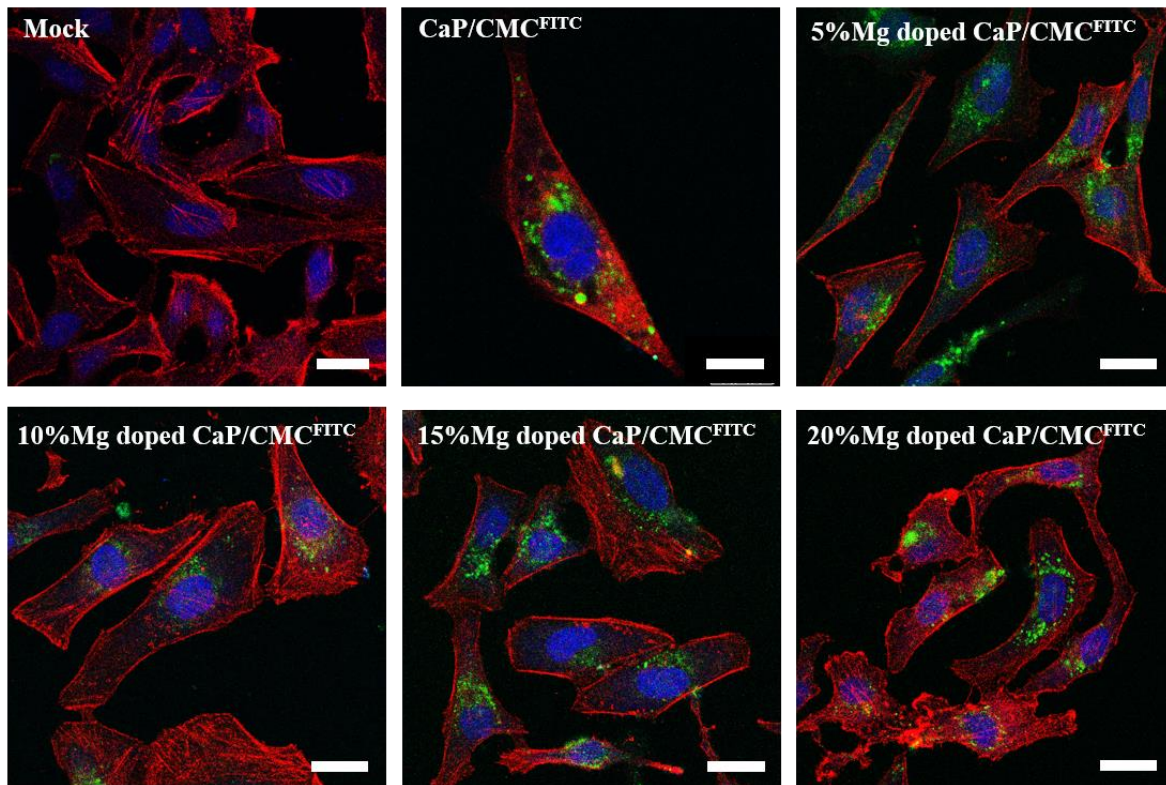


Figure 59: Uptake studies of HeLa cells with untreated cells (Mock), and after incubation for 24 h with calcium phosphate/CMC-FITC ( $\text{CaP}/\text{CMC}^{\text{FITC}}$ ), and 5 %, 10 %, 15 %, and 20 % magnesium-doped calcium phosphate nanoparticles. Red: actin; blue: nucleus; green: nanoparticles contained FITC. Scale: 20  $\mu\text{m}$ .

Figure 59 shows the confocal microscope images of the HeLa cells after 24 h incubation with either calcium phosphate or magnesium-doped calcium phosphate nanoparticles which were stabilized and stained with  $\text{CMC}^{\text{FITC}}$ . A sample of untreated cells (Mock) as a control is also considered. The nanoparticles are shown in green color and can be identified inside the cell. No fluorescence in the wavelength range for FITC could be found in the Mock group. The fluorescence in these images came exclusively from the labeled nanoparticles. The nanoparticles could be clearly identified inside the cell volume and it confirmed the uptake of the prepared nanoparticles. CLSM z-stacking confirmed that the nanoparticles were inside the cell and not over it.

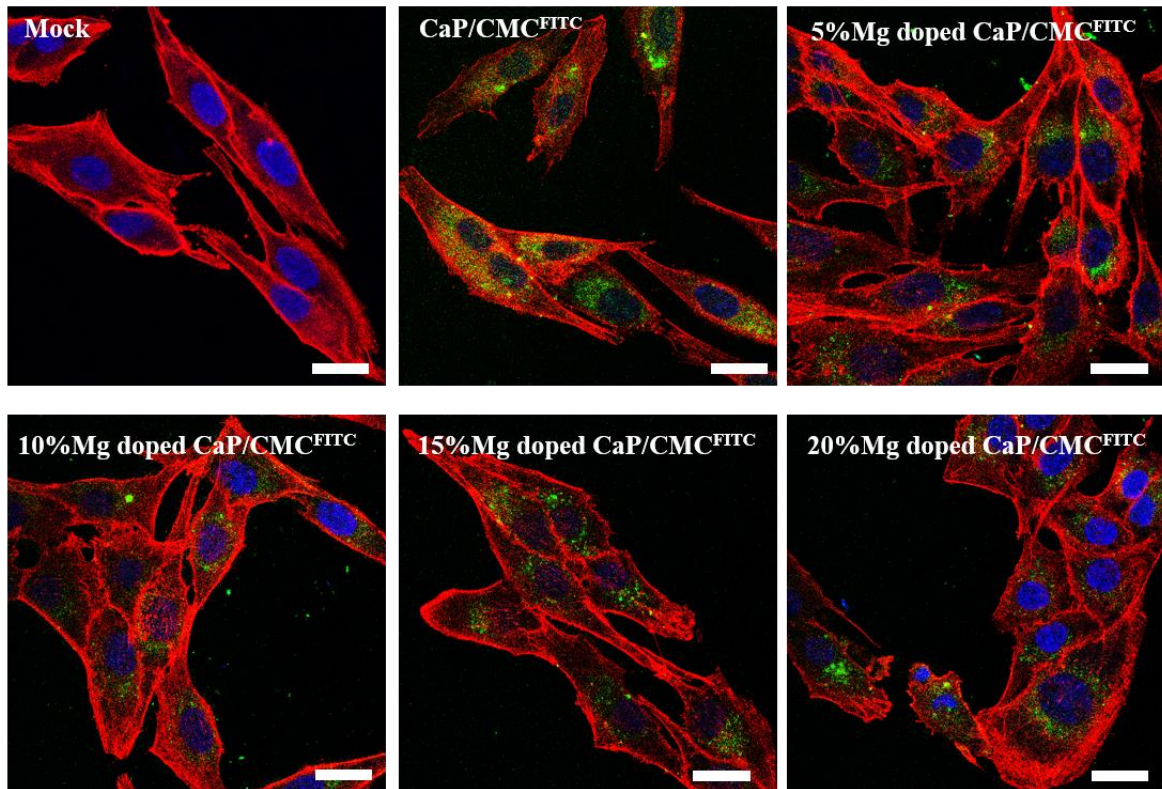


Figure 60: Uptake studies of MG-63 cells with untreated cells (Mock), and after incubation for 24 h with calcium phosphate/CMC-FITC ( $\text{CaP/CMC}^{\text{FITC}}$ ), and 5%, 10%, 15%, and 20% magnesium-doped calcium phosphate nanoparticles. Red: actin; blue: nucleus; green: nanoparticles contained FITC. Scale: 20  $\mu\text{m}$ .

Figure 60 shows the confocal microscope images of the MG-63 cells after treating with the calcium phosphate and magnesium-doped calcium phosphate nanoparticles which stabilized and dyed with  $\text{CMC}^{\text{FITC}}$ . In these images, similarly to the images by HeLa cells, the nanoparticles were perfectly taken up by the MG-63 cells. There is no significant variance between cell uptake of magnesium-doped calcium phosphate nanoparticles and pure calcium phosphate nanoparticles.

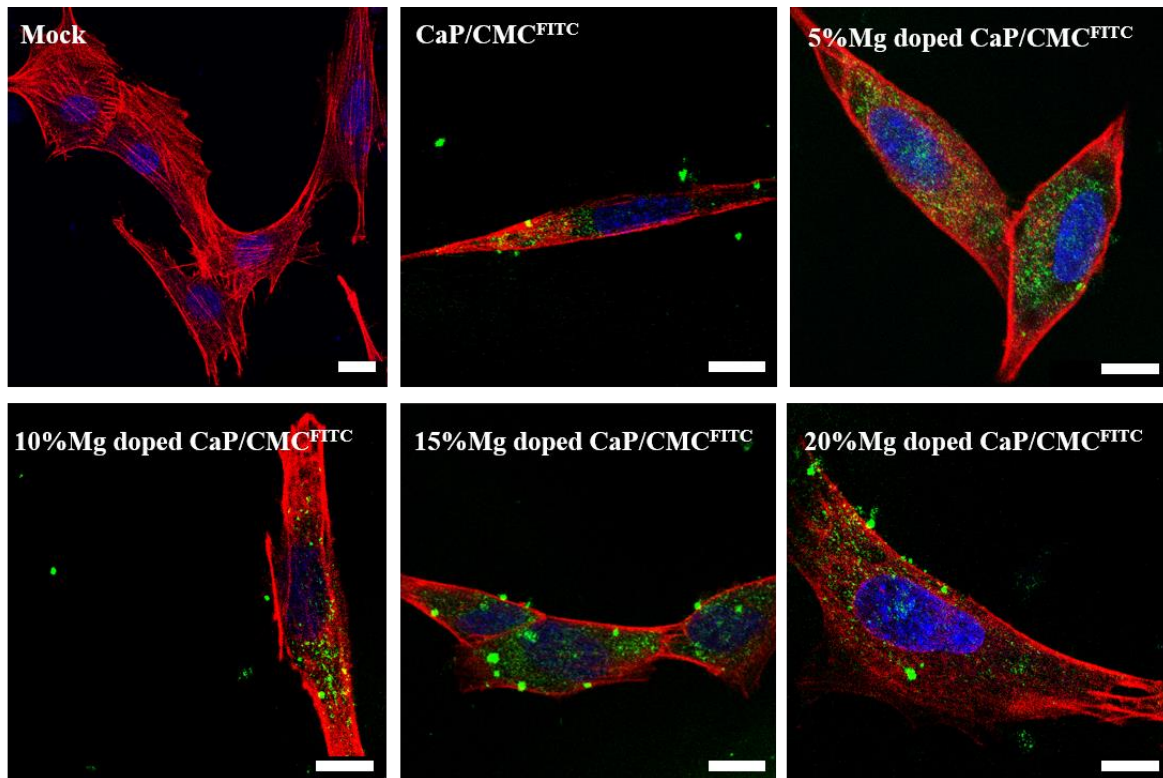


Figure 61: Uptake studies of MC3T3 cells with untreated cells (Mock), and after incubation for 24 h with calcium phosphate/CMC-FITC ( $\text{CaP/CMC}^{\text{FITC}}$ ), and 5 %, 10 %, 15 %, and 20 % magnesium-doped calcium phosphate nanoparticles. Red: actin; blue: nucleus; green: nanoparticles contained FITC. Scale: 10  $\mu\text{m}$ .

Figure 61 shows the confocal microscope images of the MC3T3 cells after incubation with the calcium phosphate and magnesium-doped calcium phosphate nanoparticles which stabilized and dyed with  $\text{CMC}^{\text{FITC}}$ . According to the confocal images, Mock did not show any fluorescence in the wavelength range for FITC. The fluorescence in the wavelength range for FITC were observed in all of the MC3T3 cells which were treated with the nanoparticles. Pure calcium phosphate nanoparticles showed smaller amount of particles inside the cells than the magnesium-doped calcium phosphate nanoparticles. Agglomerates of the nanoparticles were seen in the images, nevertheless, all kind of the nanoparticles showed were taken up by MC3T3 cells.

#### 5.4.3.3.2 Uptake studies of positively charged magnesium-doped calcium phosphate nanoparticles

Uptake studies were initially carried out to check which particles can be absorbed by the cells. For this purpose, three different cell lines were used. HeLa cells, MG63 cells, and

MC3T3 cells were studied. MG-63 and MC3T3 cells have been widely reported to present osteoblast-like behavior.

In order to study *in vitro* about uptake of nanoparticles by cells, cells were seeded in 8-well  $\mu$ -slides and, after adhesion, incubated with positively-charged magnesium-doped calcium phosphate nanoparticles for 24 h. after the incubation, cytoskeleton and nucleolus of cells were colored and studied with confocal microscope.

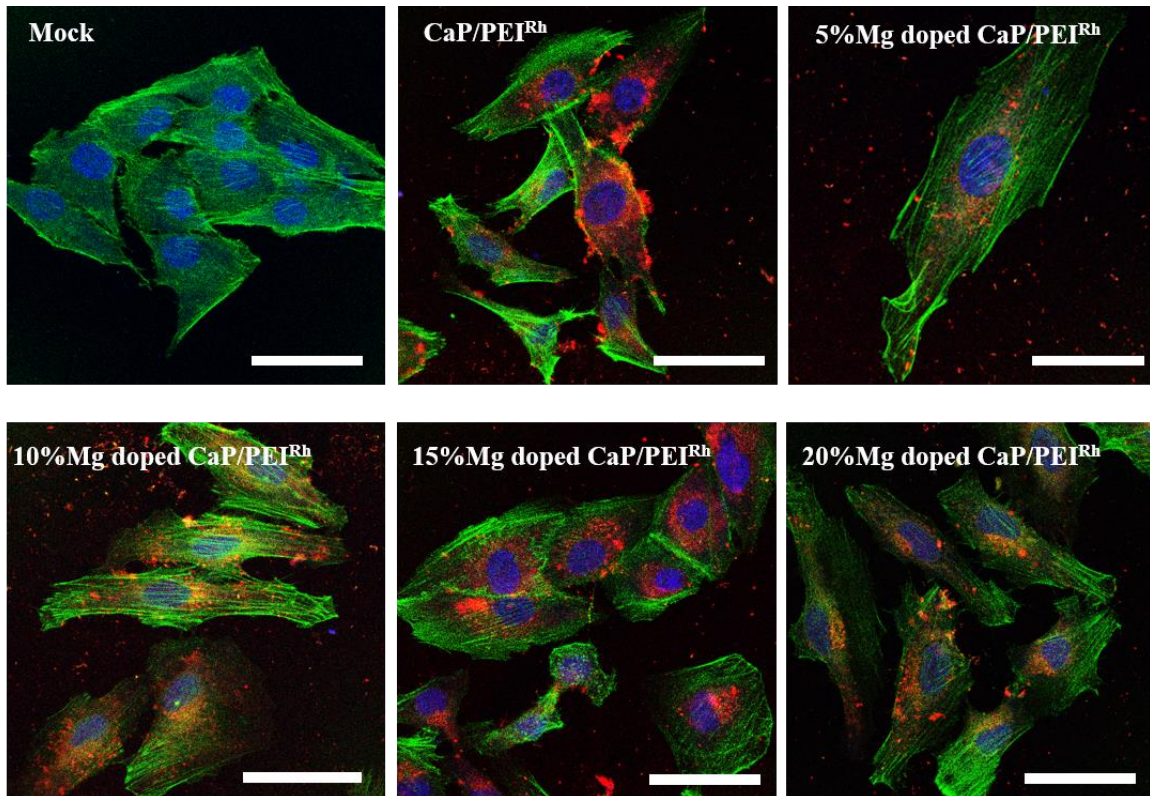


Figure 62: Uptake studies of HeLa cells with untreated cells (Mock), and after incubation for 24 h with calcium phosphate/PEI-Rhodamine (CaP/PEI<sup>Rh</sup>), and 5 %, 10 %, 15 %, and 20 % magnesium-doped calcium phosphate nanoparticles. Red: actin; blue: nucleus; red: nanoparticles contained rhodamine. Scale: 50  $\mu$ m.

Figure 62 shows the confocal microscope images of HeLa cells after incubating with the positively charged calcium phosphate and magnesium-doped calcium phosphate nanoparticles. As it is obvious in every image, the PEI<sup>Rh</sup>-stained magnesium-doped calcium phosphate nanoparticles could be taken up by HeLa cells.

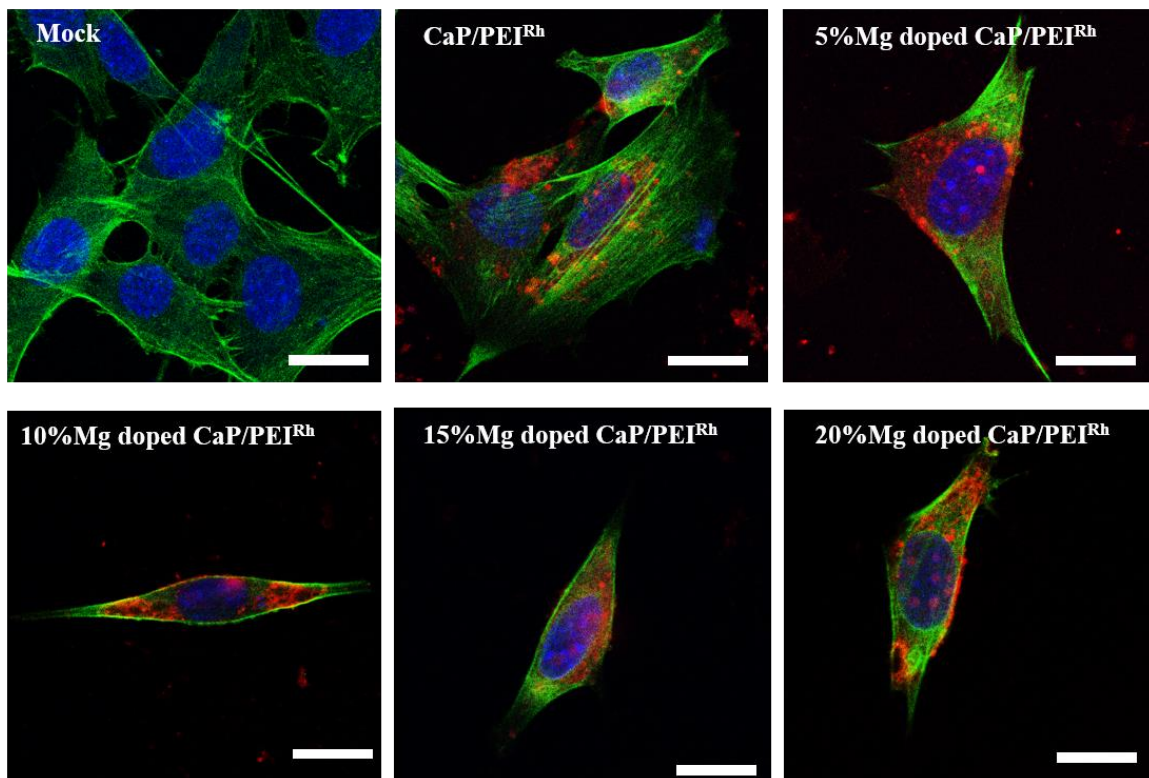


Figure 63: Uptake studies of MG-63 cells with untreated cells (Mock), and after incubation for 24 h with calcium phosphate/PEI-Rhodamine (CaP/PEI<sup>Rh</sup>), and 5 %, 10 %, 15 %, and 20 % magnesium-doped calcium phosphate nanoparticles. Red: actin; blue: nucleus; red: nanoparticles contained rhodamine. Scale: 10  $\mu$ m.

Uptake studies of the positively-charged magnesium-doped calcium phosphate nanoparticles were also performed on the MG-63 cell line and the confocal images were shown in figure 63. Here, the *in vitro* studies with MG-63 cell line showed a good cellular uptake with positively-charged magnesium-doped calcium phosphate nanoparticles. These magnesium-doped calcium phosphate nanoparticles could be absorbed by the MG-63 cells.

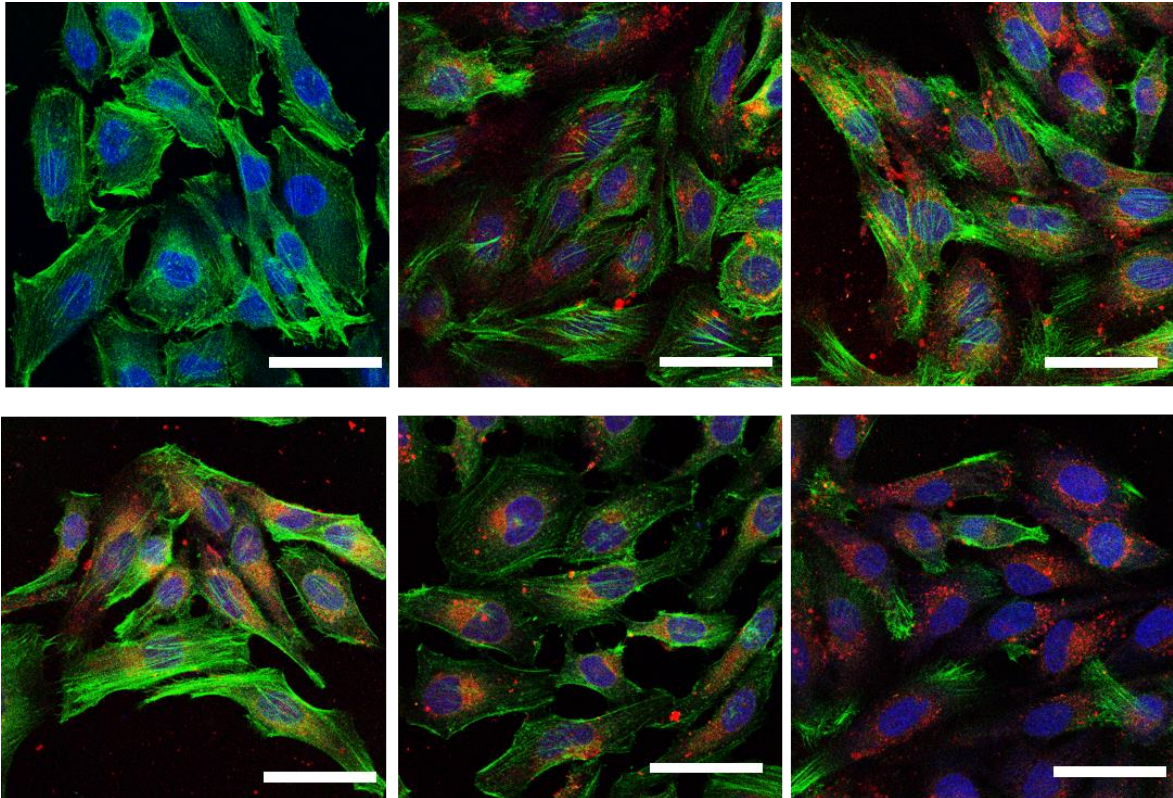


Figure 64: Uptake studies of MC3T3 cells with untreated cells (Mock), and after incubation for 24 h with calcium phosphate/PEI-Rhodamine (CaP/PEI<sup>Rh</sup>), and 5 %, 10 %, 15 %, and 20 % magnesium-doped calcium phosphate nanoparticles. Red: actin; blue: nucleus; red: nanoparticles contained rhodamine. Scale: 50  $\mu$ m.

By studying with MC3T3 cell line, uptake studies of the positively charged magnesium-doped calcium phosphate nanoparticles were also examined in this cells and shown in figure 64. In these confocal images there was no detectable fluorescence in the wavelength range for rhodamine. However, according to the images, positively charged magnesium-doped calcium phosphate nanoparticles were taken up by Mc3T3 cells. There is a small amount of agglomerates noticeable in the images. Nevertheless, nanoparticles were clearly taken up by the cells with actually no reduction in the number of live cells.

### 5.4.3.3.3 ALP studies

In order to study about ALP activities of nanoparticles, HeLa cells were used and prepared as mentioned in section 4.4.7. All experiments were performed in triplicates and repeated independently three times. The results represent the average values of triplicates. Error bars indicate the standard deviation (SD) of triplicates unless otherwise indicated. Figure 65 showed the ALP activity graphs of the strontium- and magnesium-doped calcium phosphate nanoparticles after 7, 14, and 21 days of incubation with HeLa cells.

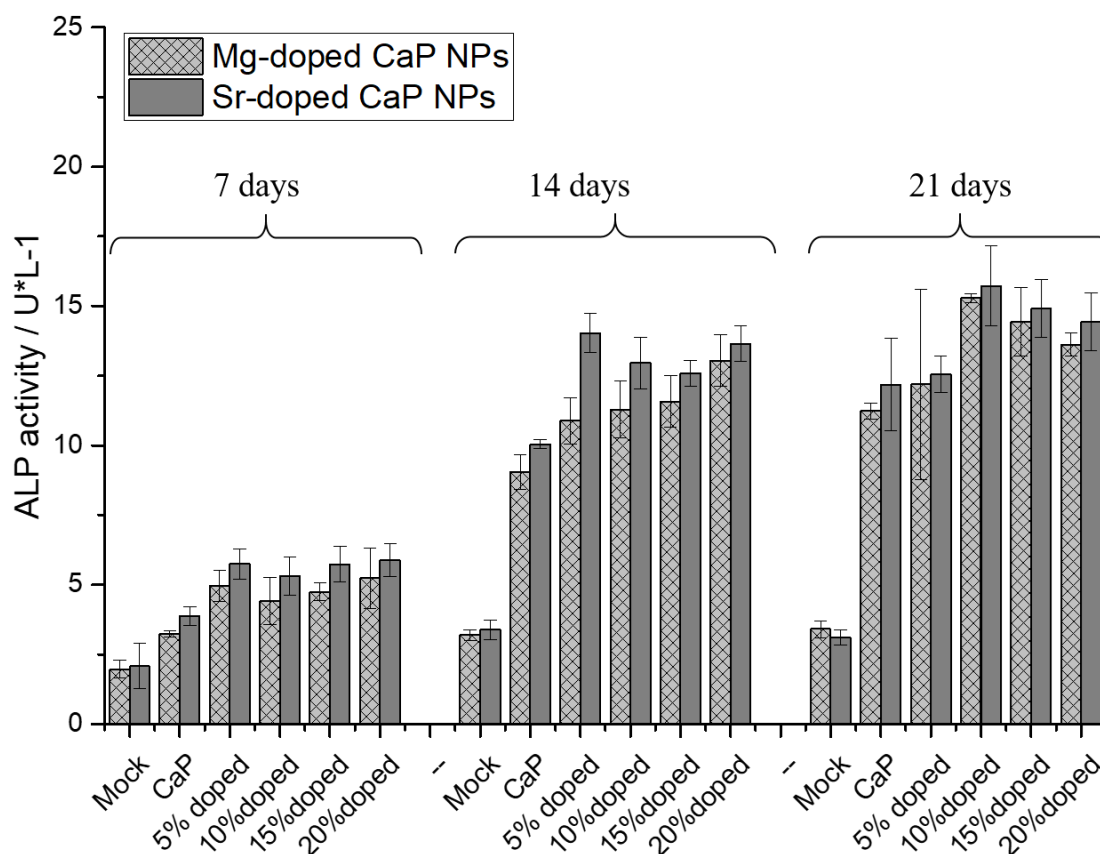


Figure 65: Alkaline phosphatase (ALP) activity in the HeLa cells treated with strontium- and magnesium-doped calcium phosphate nanoparticles was measured using the p-nitrophenyl phosphate assay and normalized to protein content after incubation for 7, 14, and 21 days.

Calcium phosphate nanoparticles without strontium and magnesium was used as a control. This pure calcium phosphate nanoparticles showed ALP activity more than the Mock group which was the cells without any nanoparticles. Nevertheless, the ALP activity of calcium phosphate nanoparticles showed the smaller amount of ALP activity rather than the strontium and magnesium-doped calcium phosphate nanoparticles. There were no significant differences between the ALP activities of sample groups with various concentrations of

strontium and magnesium. In all the cases, strontium-doped calcium phosphate nanoparticles showed more ALP activity than the magnesium-doped calcium phosphate nanoparticles.

After culturing the cells and nanoparticles for 14 days, changes in the ALP activity trend between sample groups was observed. Pure calcium phosphate nanoparticles presented less amount of ALP activity in comparison to the strontium and magnesium-doped calcium phosphate nanoparticles and strontium-doped calcium phosphate nanoparticles had more ALP activity than the magnesium-doped calcium phosphate nanoparticles. Strontium-doped calcium phosphate nanoparticles showed different changing trend than the same after 7 days. 5 % strontium-doped calcium phosphate nanoparticles showed more ALP activity than the other strontium-doped calcium phosphate nanoparticles. On the other hand, magnesium-doped calcium phosphate nanoparticles showed slight changes of ALP trend in comparison to the ALP activities after 7 days. Magnesium-doped calcium phosphate nanoparticles showed more ALP activities with increasing in doping percentages of the magnesium in nanoparticles.

According to ALP graphs (Figure 65), the ALP activities were higher as compared to the 7 days culture time and the data showed that strontium and magnesium-doped calcium phosphate nanoparticles can enhance the positive effect of the calcium phosphate nanoparticles and activity in HeLa cells. Previous studies prove that strontium replacement for calcium into hydroxyapatite have a beneficial effect on the osteointegration and bone regeneration of MG63 osteoblast-like cells and prevents unwanted bone resorption [295, 327, 328].

As mentioned before, magnesium is one of the most useful trace elements. A study on magnesium-doped hydroxyapatite was reported an increase in osteoblast activity and reduction in osteoclast activity [198].

Changes in ALP activities after 21 days were also increased in comparison to the ALP activities after 14 days. As ALP activities of pure calcium phosphate nanoparticles were increased from  $8 \text{ U L}^{-1}$  (ALP activities after 14 days) to  $12 \text{ U L}^{-1}$  (ALP activities after 21 days). In addition it was obvious that ALP activities were improved by increasing percentage of the strontium or magnesium in doped-nanoparticles. ALP activities of 10 % strontium- and 10 % magnesium-doped calcium phosphate nanoparticles showed that this ratio of doping nanoparticles had maximum alkaline phosphatase activities among other ratios after 21 days.

### 5.4.3.3.4 Conclusion

In this part of the work, a synthesis method for preparing highly uniform and spherical strontium or magnesium-doped calcium phosphate nanoparticles was developed. The composition of the strontium or magnesium-doped calcium phosphate nanoparticles can be tuned by proper choice of mineralizing solutions. The nanoparticles showed separate spherical nanoparticles in SEM. Uptake studies showed that the nanoparticles could easily be taken up by three different cell line such as HeLa, MG-63, and MC3T3.

All of the results together showed that strontium-doped calcium phosphate nanoparticles have great potential for being employed in biomedicine or medicine. In the studies with magnesium-doped calcium phosphate nanoparticles, negatively and positively charged nanoparticles were developed which both showed also successful uptake by the cell lines. ALP activity is considered an important parameter for the mineralization of bone and a useful biochemical marker of bone formation. In this work, the effect of both strontium- and magnesium-doped calcium phosphate nanoparticles on the production of alkaline phosphatase by HeLa cells after 7, 14, and 21 days of culture were shown. After culturing for 7 days, the relative ALP activities of HeLa cells were higher on the sample groups treated with nanoparticles as compared with controls. After 14, and 21 days, the relative ALP activities of HeLa cells were three times and four times higher on the sample groups treated with nanoparticles as compared with controls.

## 5.5 Incorporation of ultra-small gold nanoparticles and gold nanoclusters in capsules and suppositories

As mentioned before, metal nanoparticles have been the subject of many studies in drug delivery and tumor therapy because of their versatile properties [329-334]. Among them, gold nanoparticles are especially prominent because of their low toxicity, their good uptake by cells, and their comparatively easy synthesis and functionalization [335-337]. In the last decade, ultrasmall gold nanoparticles (approximately 2 nm) have gained increasing interest due to their small size which lies between molecules and proteins [338-341]. Unlike larger (plasmonic) nanoparticles, they show a distinct autofluorescence, which is promising for imaging and theragnostic [342, 343]. It has been shown that a decreasing size of nanoparticles can improve the delivery efficiency in tumor tissue [344, 345]. Ultrasmall gold nanoparticles can also cross the blood-brain barrier [346]. Gold nanoclusters are even smaller (<1 nm). They have an intense autofluorescence due to molecule-like electronic transitions [347]. Thus, they have been proposed for biolabeling and bioimaging [348]. Bovine serum

albumin (BSA) has been used in the synthesis of gold nanoclusters as both reducing and stabilizing agent [249]. It represents an excellent model protein to study the protein transport together with nanoparticles as such nanoclusters have a low cytotoxicity. Generally, nanocarriers can transport drugs into cells for a therapeutic action, e.g. nucleic acids, peptides and proteins, or small molecules [124, 127, 349-352]. Therefore, the ultra-small gold nanoparticles and nanoclusters were decided to use in this study and survey the possibility of transporting them with the capsules and suppositories into the colon or intestine [353].

### 5.5.1 Characterization of ultra-small gold nanoparticles

Glutathione-coated gold nanoparticles (Au-GSH) and BSA-functionalized gold nanoclusters (Au-BSA) were used as model compounds for the delivery of nanoparticles into the colon. Glutathione (GSH) is a tripeptide consisting of the three amino acids glutamic acid, cysteine and glycine. It can bind to gold by the thiol group of the central cysteine. The Au-GSH nanoparticles were characterized with respect to size and composition. HRTEM provided information about size and morphology of the nanoparticles (Figure 66). Au-GSH particles are shown in the TEM image with an average core diameter of  $1.7 \pm 0.5$  nm. This was in good agreement with the DCS results that gave the hydrodynamic diameter of water-dispersed nanoparticles (Figure 67). This confirms well-dispersed nanoparticle without significant agglomeration.

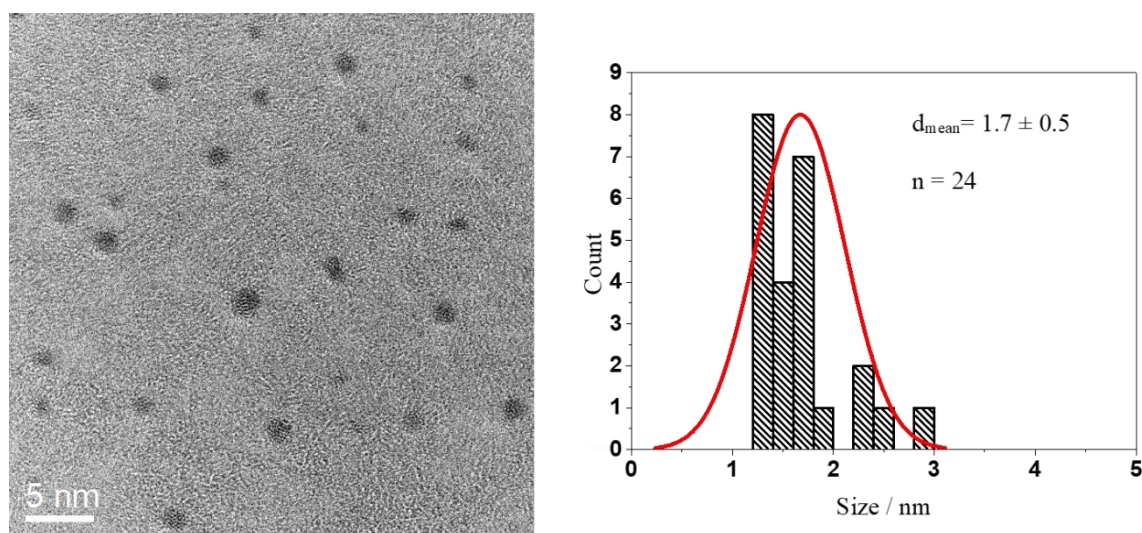


Figure 66: HRTEM image of Au-GSH nanoparticles (left) and particle size distribution (right). Measurement and Analysis were carried out by Dr. Kateryna Loza under the supervision of Dr. Mark Heggen in the Ernst Ruska-Center, Forschungszentrum Jülich GmbH, Germany.

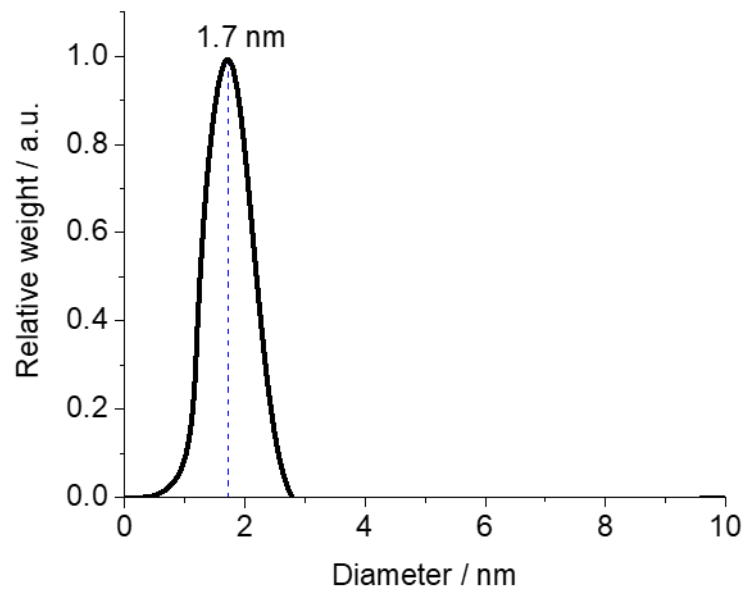


Figure 67: Disc centrifugal sedimentation data (DCS) of Au-GSH nanoparticles.

UV/Vis spectroscopy showed no surface plasmon resonance peak which would be caused by larger gold nanoparticles, confirming the absence of bigger (plasmonic) gold particles. To follow the nanoparticles inside cells, we labelled them with the dye FITC. In turn, the UV/Vis absorption spectrum of Au-GSH-FITC nanoparticles showed the presence of FITC with two typical absorption maxima at 450 and 490 (Figure 68).

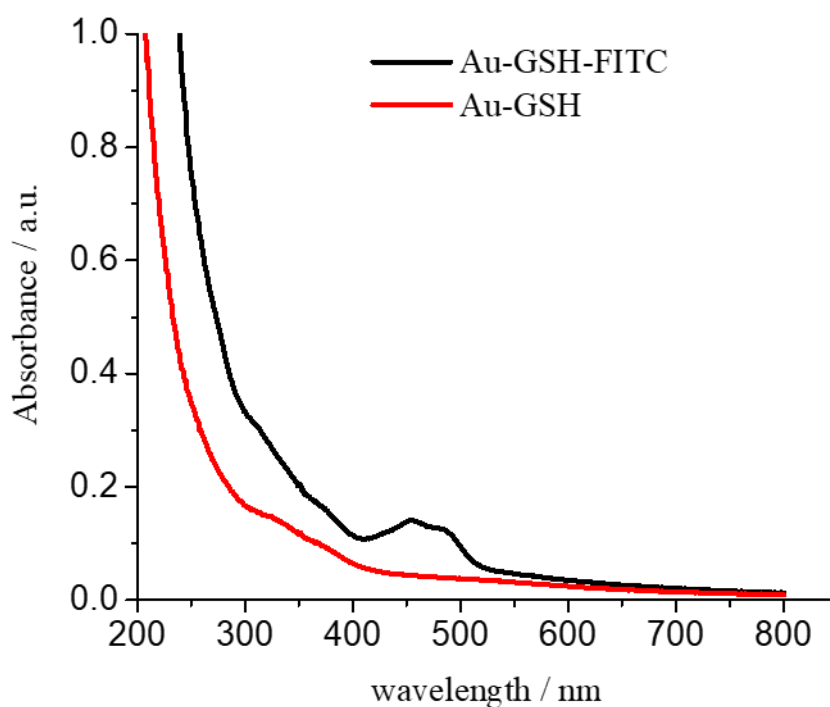


Figure 68: UV/Vis spectra of Au-GSH nanoparticles before (black) and after labelling with NHS fluorescein (FITC) (red).

The ligand structure is accessible by NMR spectroscopy as the nanoparticles are ultrasmall. The  $^1\text{H}$ -NMR spectra of pure GSH in  $\text{D}_2\text{O}$  at pH 4 and 8.5 showed all expected peaks with a notable pH-dependency of the chemical shift. The spectrum of Au-GSH nanoparticles showed broadened downfield-shifted signals. This NMR peak broadening is a well-known phenomenon that is caused by the presence of the metallic nanoparticle [68-72]. It depends on the distance between magnetic nucleus and metal particle. Therefore, the signal of the (alpha) protons of the cysteine was shifted most and decreased in intensity. The NMR spectrum of the particles was measured with water suppression, which also suppressed the signal of the H2 proton due to its close proximity to the water signal. The absence of sharp NMR signals in the spectrum of the Au-GSH nanoparticles confirmed that there were no residual or detached ligands in the dispersion (Figure 69).

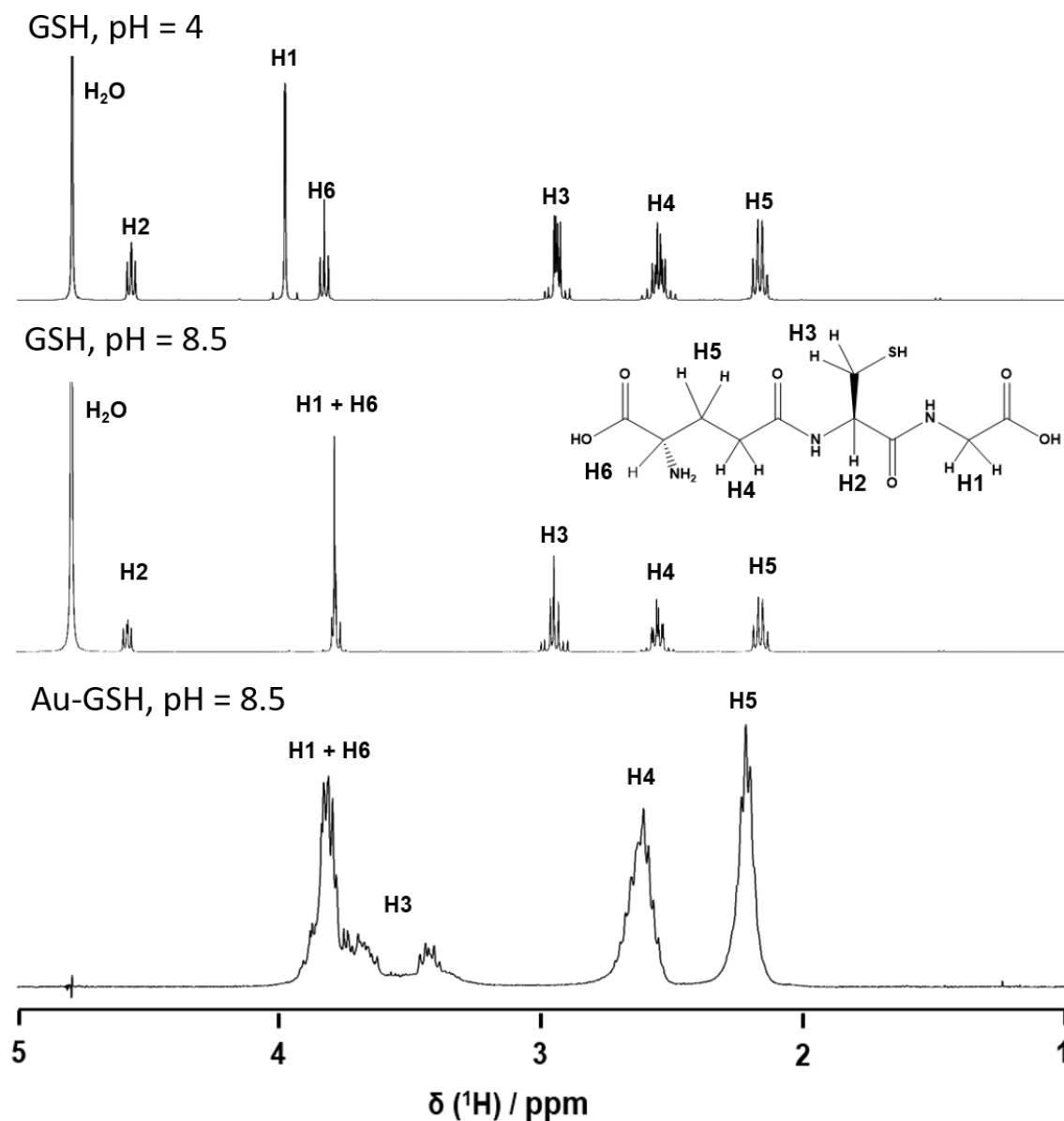


Figure 69: <sup>1</sup>H-NMR spectra of dissolved glutathione (GSH; pH 4.0 and pH 8.5) and of glutathione-functionalized ultrasmall gold nanoparticles (Au-GSH; pH 8.5).

Gold clusters can also be stabilized by proteins. In this respect, BSA is a model protein which also has the advantage to render the gold cluster autofluorescent [347, 354]. To probe the integrity of the gold-BSA cluster complex, we additionally labelled BSA with AlexaFluor555. Thus, we could follow both the gold core and the fluorescent protein shell. Figure 70 shows the fluorescence spectra of Au-BSA and of Au-BSA-Alexa555 nanoclusters. The gold core gives rise to a broad emission peak with maxima at 664 and 680 nm. The AF555 dye leads to a sharp emission maximum at 567 nm. The molar ratio of gold to BSA was determined by AAS (Au) and by UV spectroscopy (BSA-AF555). We obtained

a molar ratio Au: BSA of 4: 1 after the purification of nanoclusters, in accordance with earlier studies [354-358].

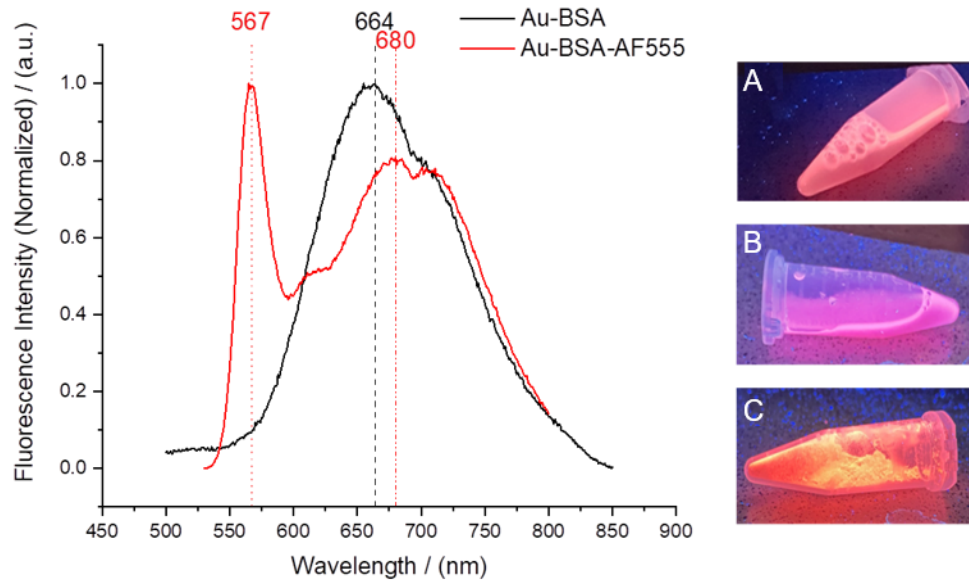


Figure 70: Left: Fluorescence spectra of Au-BSA and Au-BSA-AF555 nanoclusters. Right: Images of fluorescing nanoclusters under UV irradiation: Au-BSA dispersion (A), Au-BSA-AF555 dispersion (B), and solid Au-BSA-AF555 freeze-dried with trehalose (C).

### 5.5.2 Capsule and suppository loading

For colon delivery, capsules and suppositories were loaded with freeze-dried Au-GSH nanoparticles and Au-BSA nanoclusters. Table 10 and 11 give the full characterization data for nanoparticle-loaded capsules and suppositories.

Table 10: Characterization of gelatin capsules, loaded with either Au-GSH nanoparticles or Au-BSA nanoclusters. Given are weight percentages with respect to the total weight of nanocarriers including trehalose ( $\pm$  indicates the standard deviation).

Empty capsule weight / mg	$2.2 \pm 0.5$
Capsule content of Au-GSH-FITC + trehalose / mg	$3.3 \pm 0.5$ (100 %)
Capsule content of Au / $\mu\text{g}$	$34 \pm 5$ (1.05 %)
Capsule content of FITC / $\mu\text{g}$	$4.0 \pm 0.6$ (0.12 %)
Capsule content of Au-BSA-AF555 + trehalose / mg	$3.3 \pm 0.5$ (100 %)
Capsule content of Au / $\mu\text{g}$	$6.3 \pm 0.9$ (0.19 %)
Capsule content of AF555 / $\mu\text{g}$	$0.2 \pm 0.05$ (0.007 %)
Capsule content of BSA / mg	$0.5 \pm 0.1$ (14.6 %)

Table 11: Characterization of hard-fat suppositories, loaded with either Au-GSH nanoparticles or Au-BSA nanoclusters. Given are weight percentages with respect to the total weight of a suppository ( $\pm$  indicates the standard deviation).

Total suppository weight / mg	$60 \pm 2$ (100 %)
Suppository content of hard fat / mg	$48 \pm 2$ (80.3 %)
Suppository content of Au-GSH-FITC + trehalose / mg	$11.8 \pm 0.5$ (19.7 %)
Suppository content of Au / $\mu\text{g}$	$124 \pm 5$ (0.2 %)
Suppository content of FITC / $\mu\text{g}$	$14.2 \pm 0.6$ (0.02 %)
Suppository content of Au-BSA-AF555 + trehalose / mg	$11.8 \pm 0.5$ (19.7 %)
Suppository content of Au / $\mu\text{g}$	$22.5 \pm 1.0$ (0.04 %)
Suppository content of AF555/ $\mu\text{g}$	$0.9 \pm 0.05$ (0.002 %)
Suppository content of BSA / mg	$1.7 \pm 0.1$ (2.8 %)

### 5.5.3 Particle release from capsules and suppositories

Nanocarrier-filled coated capsules were immersed in simulated stomach medium (0.1 M HCl, pH 1) and simulated intestinal medium (MOPS buffer, 0.15 M, pH 7.1) to assess the nanoparticle release rate. The release of particles was followed by measuring the gold concentration in the immersion medium. The filled capsules were immersed in 600  $\mu\text{L}$  of simulated stomach medium or 500  $\mu\text{L}$  of MOPS buffer, respectively, and aliquots of 100  $\mu\text{L}$  were taken every 15 to 30 min. 100  $\mu\text{L}$  *aqua regia* was added to each sample to dissolve the

gold nanocarriers, then it was diluted with water to 3 mL, and analyzed by AAS (Figure 71 and 72).

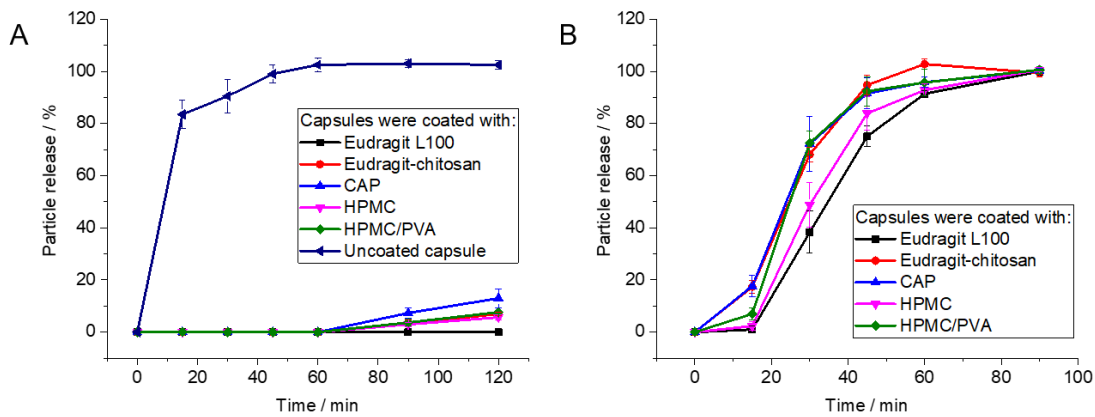


Figure 71: Atomic absorption spectroscopic (AAS) results of the release of Au-GSH from polymer-coated capsules: A: Simulated stomach conditions (pH 1) and B: Simulated intestinal conditions (pH 7.1). Error bars indicate the standard deviation of the mean ( $N=4$ ).

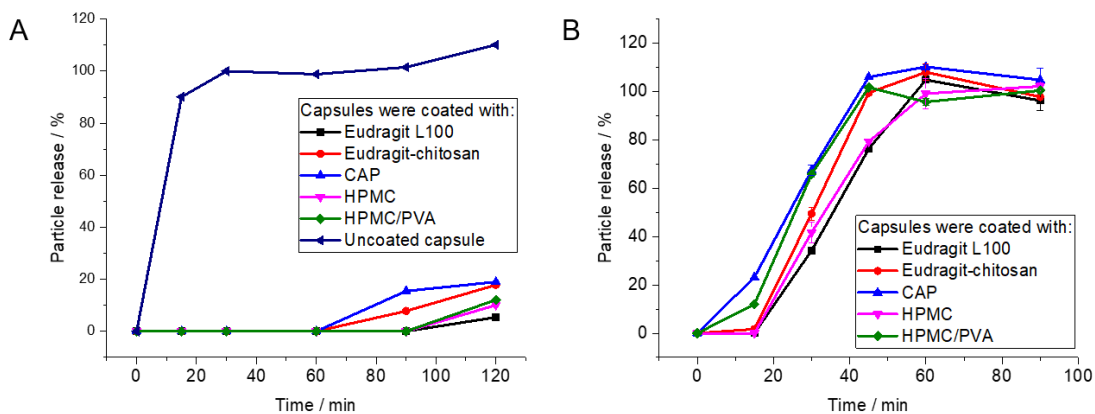


Figure 72: Atomic absorption spectroscopic (AAS) results of the release of Au-BSA nanoclusters from polymer-coated capsules: A: Simulated stomach conditions (pH 1) and B: Simulated intestinal conditions (pH 7.1).

For uncoated gelatin capsules (Figure 71 and 72), a rapid particle release was observed at pH 1 as the capsules were easily dissolved. The enteric-coated capsules released 12 % at most after 2 h, depending on the enteric coating polymer. In contrast, the coated capsules showed a rapid release of the particles within 90 min at pH 7.1, i.e. at the neutral conditions in the colon. As the passage time from the stomach into the colon is of the order of hours [359-363], this release rate is well suited to transport particles to the colon.

### 5.5.4 In vitro studies of the transport vehicles contain ultra-small gold nanoparticles

After characterizing the capsules in simulation stomach and intestine medium, for any biomedical application, the delivery system and its cargo must be non-toxic. Therefore, the cytotoxicity of gold nanoparticles, gold nanoclusters, capsules and suppositories were assessed with HeLa cells by the MTT assay (Figure 73). For this purpose, a capsule was dissolved in 500  $\mu$ L DMEM, filtered, and 250  $\mu$ L was added to the cell culture (about 16  $\mu$ g gold per well). A half suppository was molten in 1 mL DMEM at 37  $^{\circ}$ C, and 250  $\mu$ L of this solution was given to the cell culture (15.5  $\mu$ g gold per well). As control, 35  $\mu$ g gold nanocarrier was given to the cell culture. Except for Eudragit and Eudragit-chitosan in combination with the gelatin capsules, all components were highly cytocompatible. The cytotoxicity appears to be a synergetic effect of Eudragit L100 and gelatin as found earlier [363].

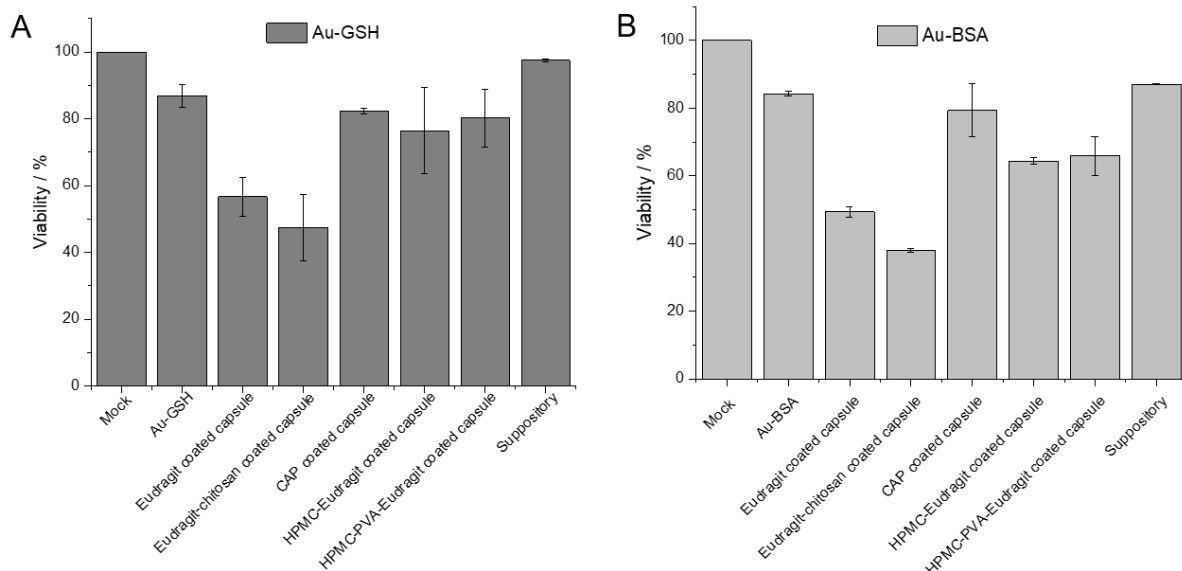


Figure 73: Viability of HeLa cells by the MTT assay in the presence of the components of dissolved enteric-coated capsules and suppositories, previously loaded with Au-GSH nanoparticles and Au-BSA nanoclusters (mean  $\pm$  standard deviation;  $N=3$ )

### 5.5.5 Uptake of particle released from capsules and suppositories by cells

The nanoparticles and nanoclusters were well redispersed after dissolution of the capsule or the suppository and easily taken up by cells, underscoring their ability to act as drug delivery vehicles. Figure 74 shows cell uptake experiments of as-prepared and of released Au-GSH nanoparticles with HeLa cells. Confocal laser scanning microscopy showed a strong green fluorescence of FITC in the cytosol. The nanoparticles were released from the enteric-coated capsules and suppositories and taken up by HeLa cells, except for Eudragit-chitosan-coated capsules. In that case, a possible interaction between the two polymers, the dissolved gelatine capsule, and the particles may have led to agglomeration (the cells were washed before imaging, removing most extracellular particles). Similar results were also obtained for capsules and suppositories containing drug-loaded calcium phosphate nanoparticles that were also successfully taken up by the HeLa cells after dissolution of capsules [363] or suppositories [364].

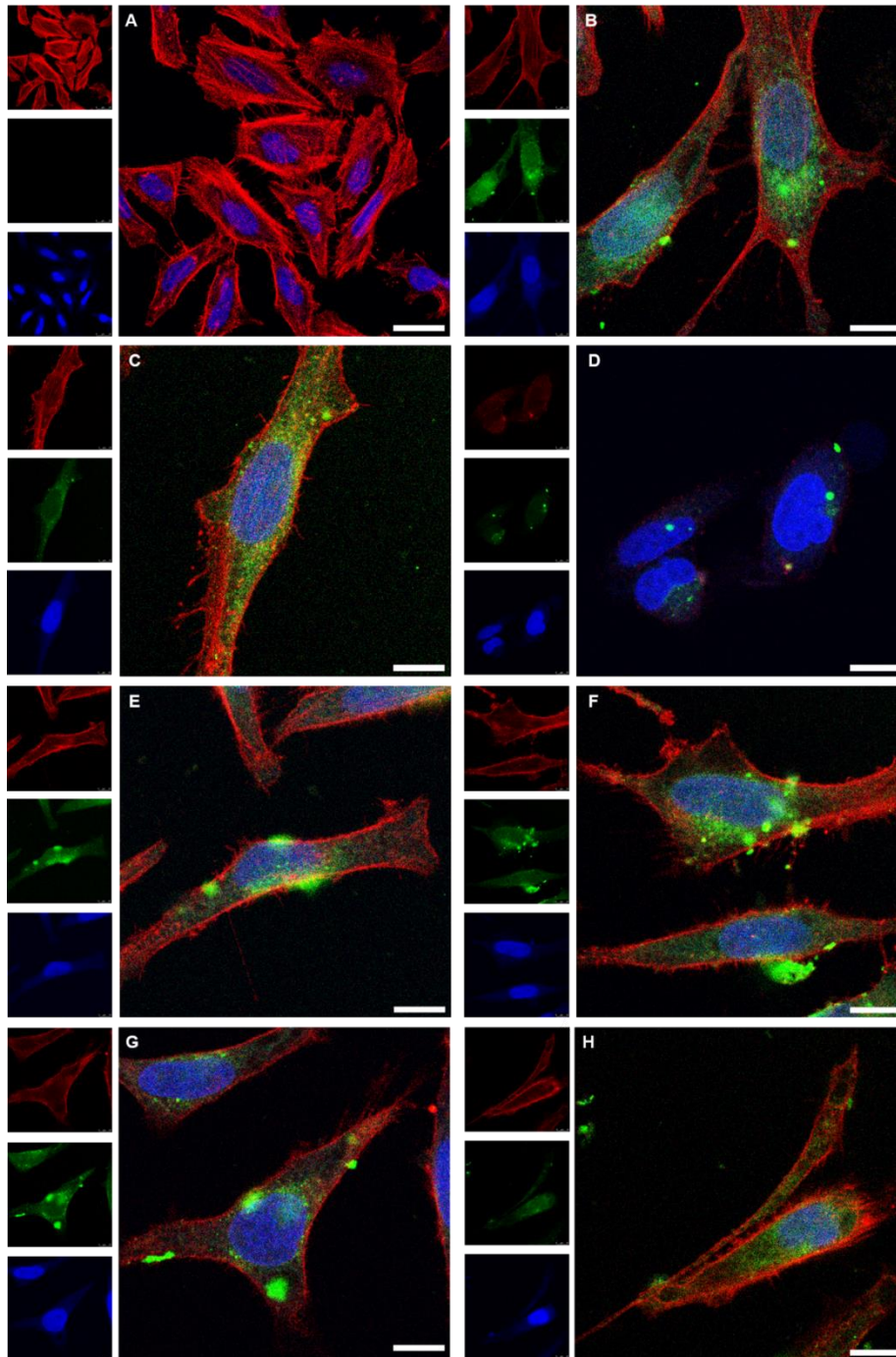


Figure 74: Confocal laser scanning microscopy images of HeLa cells after 24 h cultivation (control; A), and after incubation for 24 h with dispersed Au-GSH-FITC nanoparticles ( $70 \mu\text{g mL}^{-1}$ ) (B). The uptake of Au-GSH-FITC nanoparticles from coated gelatin capsules after dissolution is shown in (C) for Eudragit ( $88 \mu\text{g mL}^{-1}$ ), (D) for Eudragit-chitosan ( $65 \mu\text{g mL}^{-1}$ ), (E) for cellulose acetate phthalate (CAP;  $60 \mu\text{g mL}^{-1}$ ), (F) for hydroxypropylmethylcellulose-Eudragit (HPMC-Eudragit;  $60 \mu\text{g mL}^{-1}$ ), and (G) for hydroxypropylmethylcellulose-polyvinylalcohol-Eudragit (HPMC-PVA-Eudragit;  $72 \mu\text{g mL}^{-1}$ ). (H) shows the uptake of Au-GSH-FITC nanoparticles after release from a hard-fat suppository ( $62 \mu\text{g mL}^{-1}$ ). Red: Actin (cytoskeleton); Blue: Cell nucleus; Green: Au-GSH-FITC nanoparticles. Scale bar  $10 \mu\text{m}$ . All given concentrations refer to gold in the cell culture well.

The results were comparable for Au-BSA-Alexa555 nanoclusters (Figure 75). Confocal laser scanning microscopy showed the green autofluorescence of gold nanoclusters that easily penetrated the cell membrane due to their small size. The nanoclusters were released from the enteric coated capsules and suppositories, obviously in well-dispersed form, and taken up by the HeLa cells.

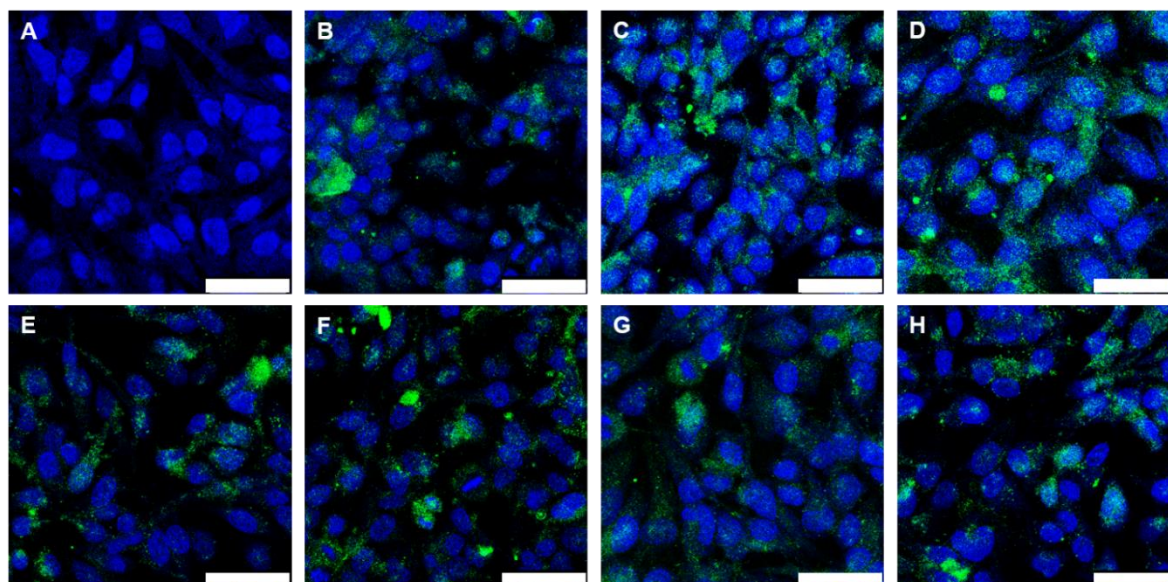


Figure 75: Fluorescence microscopy images of HeLa cells after 24 h cultivation (control; A) and after 24 h incubation with Au-BSA nanoclusters ( $43 \mu\text{g mL}^{-1}$  Au) (B). The uptake of Au-BSA nanoclusters from dissolved capsules is shown in (C) for Eudragit ( $42 \mu\text{g mL}^{-1}$  Au), (D) for Eudragit-chitosan ( $42 \mu\text{g mL}^{-1}$  Au), (E) for CAP ( $45 \mu\text{g mL}^{-1}$  Au), (F) for HPMC-Eudragit ( $50 \mu\text{g mL}^{-1}$  Au), and (G) for HPMC-PVA-Eudragit ( $47 \mu\text{g mL}^{-1}$  Au) (H) shows the uptake of Au-BSA nanoclusters after release from a suppository ( $52 \mu\text{g mL}^{-1}$  Au). Blue: Nucleus; Green: Au-BSA nanocluster autofluorescence. Scale bar  $50 \mu\text{m}$ . All given concentrations refer to gold in the cell culture well.

Protein-coated gold nanoclusters can be used to transport proteins into cells [365]. To monitor the transport of the protein BSA with the ultrasmall gold nanoclusters, cell uptake studies were performed with HeLa cells and Au-BSA-AF555 nanoclusters (Figure 76). Confocal microscopy showed that the gold autofluorescence and the BSA-AF555 fluorescence were mostly co-localized, i.e. gold nanocluster and protein were taken up together.

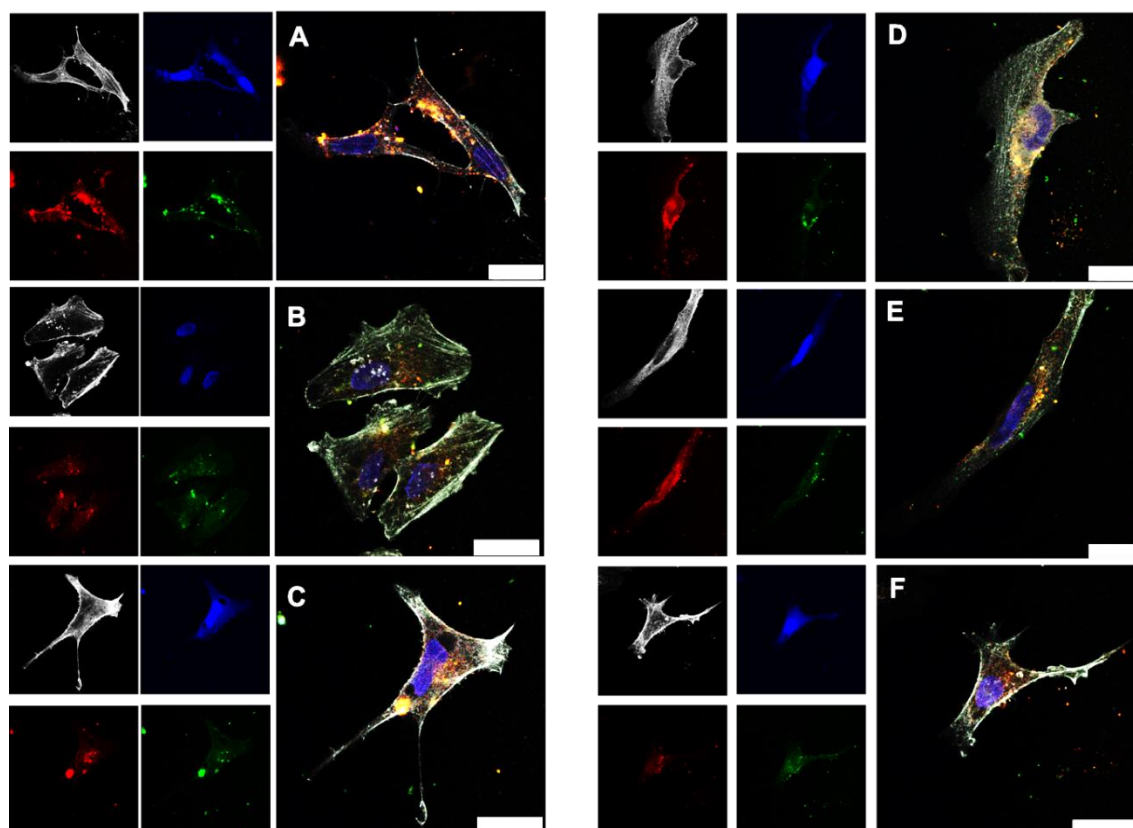


Figure 76: Confocal laser scanning microscopy images of HeLa cells incubated for 24 h with dispersed Au-BSA-AF555 nanoclusters ( $13.3 \mu\text{g mL}^{-1} \text{ Au}$ ) (A). The uptake of Au-BSA-AF555 nanoclusters from dissolved capsules is shown in (B) for Eudragit ( $14.5 \mu\text{g mL}^{-1} \text{ Au}$ ), in (C) for CAP ( $15.4 \mu\text{g mL}^{-1} \text{ Au}$ ), in (D) for HPMC-Eudragit ( $17.0 \mu\text{g mL}^{-1} \text{ Au}$ ), and in (E) for HPMC-PVA-Eudragit ( $16.5 \mu\text{g mL}^{-1} \text{ Au}$ ) (F) shows the uptake of Au-BSA-AF555 nanoclusters after release from a suppository ( $22 \mu\text{g mL}^{-1} \text{ Au}$ ). Grey: Actin; Blue: Nucleus; Green: Au-BSA autofluorescence; Red: Au-BSA-AF555 fluorescence from AF555. Scale bar  $25 \mu\text{m}$ .

### 5.5.6 Conclusions

The strategies for the oral and rectal transport of ultrasmall gold nanoparticles and gold nanoclusters into the intestine were studied in this chapter. In order to deliver theranostic nanoparticles and nanoclusters to the intestine by oral intake, and protecting them from the gastric acid, they can be freeze-dried gold and filled into a gelatin capsule that is coated with different enteric coating polymers. The enteric coated capsules are stable under the acidic conditions of the stomach (pH 1). The nanoparticles and nanoclusters are well redispersible in cell culture medium (DMEM) after dissolution of capsule or suppository and taken up by HeLa cells. Although Eudragit L100-chitosan as one of our enteric coating options was efficient for protection against acids, an uptake of the nanoparticles into cells did not occur, and it was significantly cytotoxic. In contrast, capsules coated with Eudragit L100, cellulose acetate phthalate, hydroxypropylmethyl cellulose-Eudragit, or

hydroxypropylmethyl/cellulose-polyvinylalcohol-Eudragit are well suited for an efficient particle uptake by cells. Thus, enteric coated capsules and suppositories are efficient carriers of drug-loaded gold nanoparticles and gold-protein nanoclusters for a potential biomedical application, both for local and systemic drug delivery, including proteins.

### 6. Summary and conclusions

In the first part of this work calcium phosphate nanoparticles were synthesized and functionalized with different nucleic acids and dyes to be appropriate for tracking in cells. Strategies for the transport of the synthesized nanoparticles into the intestine were developed with gelatin soft capsules and suppositories. If the nanoparticles are to reach the intestine via oral intake, they must be protected from gastric acid. For this purpose, freeze-dried nanoparticles were filled into a gelatin capsule and coated with different enteric polymers such as Eudragit L 100, a combination of Eudragit L 100 and chitosan, CAP, HPMC-Eudragit L 100, and HPMC-PVA-Eudragit L 100. Different enteric coatings were developed to make the release of nanoparticles more site and time specific. The Protection of the nanoparticles in enteric coated gelatin capsules against gastric acid was researched in simulation experiments. The time specific release rate of the nanoparticles in acidic medium simulating the gastric environment and in basic medium simulating the intestine environment was tracked by AAS and UV/Vis. All the polymer coated capsules showed proper protection of the nanoparticles in acidic medium. The Release rate of the nanoparticles varied for the different enteric coating systems. Eudragit L 100 coated capsule showed delayed release in comparison to the other coated capsules. Nevertheless, if a capsule is coated with a combination of Eudragit L 100 and chitosan, the release rate increases drastically. Another capsule coating system benefits of two layers of polymers. The first layer is a water-soluble polymer and the second layer acts as a protective layer like Eudragit L 100. HPMC-Eudragit L 100 and HPMC-PVA-Eudragit L 100 coated gelatin capsules showed faster release rate than only Eudragit L 100 coated capsule and slower release rate than the Eudragit L 100-chitosan coated capsules.

The released nanoparticles from the capsule were studied in *in vitro* by MTT test, uptake, and transfection in HeLa and Caco-2 cell lines. Cell viability of nanoparticles released from Eudragit L 100 coated capsules and Eudragit® L 100-chitosan coated capsules showed around 40 % viability by both HeLa and Caco-2 cells indicating improper interaction between Eudragit L 100, soft gelatin capsule and nanoparticles. The polymer layer protected the nanoparticles from degradation in gastric acid, but after dissolution at neutral pH values, the polymer interacted with the positively charged nanoparticles, so that they were no longer functional in the cell culture. Uptake and transfection studies also showed that the released nanoparticles from Eudragit L 100 coated capsule and Eudragit L 100-chitosan coated capsule were not appropriate in cell studies. Other coated capsules showed suitable cell viability around 85 % in both HeLa and Caco-2 cells. The released nanoparticles from CAP,

HPMC-Eudragit L 100, and HPMC-PVA-Eudragit L 100 coated capsules could easily be taken up and transfected by both cell lines. Gene silencing was studied by using HeLa-EGFP cells. All released nanoparticles except for the particles released from Eudragit L 100 and Eudragit L 100-chitosan coated capsules showed high gene silencing efficiency which proved functionality of the particles after the release. Alternatively, a suppository was developed that could release the nanoparticles in the intestine after rectal application. In *in vitro* tests it was found that the particles, after being released from a suppository, had very suitable cell viability, cell uptake and transfection efficiency as well as muting efficiencies. In the second part of this work Ultra-small gold nanoparticles (about 1.8 nm) and nanoclusters were synthesized, characterized and studied *in vitro*. Nanoparticles and nanoclusters showed very well cell uptake and viability by HeLa cells. These nanoparticles and nanoclusters then were filled in the previously developed capsules and suppositories. Ultra-small gold nanoclusters were coated with dyed BSA and the nanoparticles functionalized with a FITC dye to be pursuable in *in vitro* studies. Gold nanoparticles and nanoclusters released from coated capsules showed impeccable cell viability and cell uptake by HeLa cells. BSA-dye coated nanoclusters proved that the gold nanoclusters were able to carry BSA in the HeLa cells.

In the next part of this present work, the use of composite materials made of calcium phosphate and biodegradable polymers based on polylactide for the transport of active substances was investigated. Calcium phosphate PLGA nanoparticles were developed as an active substance carrier system for anionic, hydrophilic active substances such as nucleic acids. Water-in-oil-in-water emulsion techniques proved to be optimal synthesis routes and delivered spherical calcium phosphate PLGA nanoparticles with a core diameter of approx. 100 nm. Cell uptake and transfection studies using confocal laser scanning microscopy showed that the nanoparticles were absorbed and transfected very well by HeLa cells. Gene silencing studies with the nanoparticles showed also that these nanoparticles had ideal muting efficiency by HeLa-EGFP cells.

In the last part of this work, strontium- and magnesium-doped calcium phosphate nanoparticles were synthesized for bone regeneration properties. These nanoparticles were doped with concentrations of 5 %, 10 %, 15 %, and 20 % strontium and magnesium, respectively. These nanoparticles were characterized and studied *in vitro*. Spherical nanoparticles with comparable sizes at about 50-70 nm for all compositions were achieved. Cell viability and cell uptake of the nanoparticles were studied with HeLa, MG-63, and MC3T3 cell lines. All the strontium and magnesium doped calcium phosphate nanoparticles

showed promising cell viability by more than 70 % and very proper uptake by these three different cell lines. These doped nanoparticles showed very slight variances in comparison to each other, and a better uptake compared to pure calcium phosphate nanoparticles. In this work, the effect of both strontium- and magnesium-doped calcium phosphate nanoparticles on the production of alkaline phosphatase by HeLa cells after 7, 14, and 21 days of culture were shown. After culturing for 7 days, the relative ALP activities of HeLa cells were higher on the sample groups treated with nanoparticles as compared with controls. After 14, and 21 days, the relative ALP activities of HeLa cells were three times and four times higher on the sample groups treated with nanoparticles as compared with controls.

In summary, it can be stated that in the present work materials and particles based on calcium phosphate were successfully developed both for the transport of active substances in nanomedicine and for the generative production of bone substitute materials.

### 7. Zusammenfassung

Im ersten Teil dieser Arbeit wurden Calciumphosphat-Nanopartikel synthetisiert und mit verschiedenen Nukleinsäuren und Farbstoffen funktionalisiert, um sie für das Tracking in Zellen geeignet zu machen. Strategien für den Transport der synthetisierten Nanopartikel in den Darm wurden mit Gelatine-Weichkapseln und Zäpfchen entwickelt. Sollen die Nanopartikel über die orale Aufnahme in den Darm gelangen, müssen sie vor der Magensäure geschützt werden. Dazu wurden gefriergetrocknete Nanopartikel in eine Weichkapsel gefüllt und mit verschiedenen magensaftresistenten Polymeren wie Eudragit L 100, einer Kombination aus Eudragit L 100 und Chitosan, CAP, HPMC-Eudragit L 100 und HPMC-PVA beschichtet -Eudragit L 100. Verschiedene magensaftresistente Beschichtungen wurden entwickelt, um die Freisetzung von Nanopartikeln orts- und zeitspezifisch zu gestalten. Der Schutz der Nanopartikel in magensaftresistenten Weichkapseln gegen Magensäure wurde in Simulationsexperimenten untersucht. Die zeitspezifische Freisetzungsrates der Nanopartikel in saurem Medium, das die Magen Umgebung simuliert, und in basischem Medium, das die Darm Umgebung simuliert, wurde mit AAS und UV-Vis verfolgt. Alle mit Polymer beschichteten Kapseln zeigten einen angemessenen Schutz der Nanopartikel in saurem Medium, wobei die Freisetzungsrates der Nanopartikel für die verschiedenen magensaftresistenten Beschichtungssysteme variierte. Die mit Eudragit L 100 beschichtete Kapsel zeigte im Vergleich zu den anderen beschichteten Kapseln eine verzögerte Freisetzung. Wird eine Kapsel dennoch mit einer Kombination aus Eudragit® L 100 und Chitosan beschichtet, erhöht sich die Freisetzungsrates drastisch. Ein weiteres Kapselbeschichtungssystem profitiert von zwei Polymerschichten. Die erste Schicht ist ein wasserlösliches Polymer und die zweite Schicht fungiert als Schutzschicht. Die Eudragit L 100, HPMC-Eudragit L 100 und HPMC-PVA-Eudragit L 100 beschichteten Kapseln zeigten eine schnellere Freisetzungsrates als nur Eudragit L 100-beschichtete Kapseln und eine langsamere Freisetzungsrates als die Eudragit L 100-Chitosan-beschichteten Kapseln. Die freigesetzten Nanopartikel aus der Kapsel wurden in vitro durch MTT-Test, Zell-Aufnahme und Transfektion in HeLa- und Caco-2-Zelllinien untersucht. Die Zellviabilität von HeLa und Caco-2-Zellen zeigte für Nanopartikel, die aus Eudragit L 100- und Eudragit L 100-Chitosan-beschichteten Kapseln freigesetzt wurden, Werte von etwa 40 %, was auf eine schädliche Wechselwirkung zwischen Eudragit L 100, Weichgelatine Kapsel und Nanopartikeln hindeutet. Die Polymerschicht schützte die Nanopartikel vor der Auflösung in der Magensäure, aber nach Auflösung bei neutralen pH-Werten wechselwirkte das Polymer mit den positiv geladenen

Nanopartikeln, so dass diese in der Zellkultur nicht mehr funktionsfähig waren. Aufnahme- und Transfektionsstudien zeigten auch, dass die freigesetzten Nanopartikel aus Eudragit L 100-beschichteten Kapseln und Eudragit L 100-Chitosan-beschichteten Kapseln für Zellstudien nicht geeignet waren. Andere beschichtete Kapseln zeigten eine geeignete Zellviabilität von etwa 85 % sowohl in den HeLa- als auch in den Caco-2-Zellen. Die freigesetzten Nanopartikel aus CAP, HPMC-Eudragit L 100 und HPMC-PVA-Eudragit L 100 beschichteten Kapseln konnten problemlos von beiden Zelllinien aufgenommen und transfiziert werden. Gen-Stummschaltung wurde durch die Verwendung von HeLa-EGFP-Zellen untersucht. Alle freigesetzten Nanopartikel mit Ausnahme der Partikel, die von Eudragit L 100 und Eudragit L 100-Chitosan-beschichteten Kapseln freigesetzt wurden, zeigten eine hohe Gen-Stummschaltungs-Effizienz, was die Funktionalität der Partikel nach der Freisetzung bewies. Alternativ wurde ein Zäpfchen entwickelt, das die Nanopartikel nach rektaler Applikation im Darm freisetzen könnte. In In-vitro-Tests wurde festgestellt, dass die Partikel, nachdem sie aus einem Zäpfchen freigesetzt wurden, eine sehr geeignete Zellviabilität, Zellaufnahme- und Transfektionseffizienz sowie Stummschaltungs-Effizienz aufwiesen. Im zweiten Teil dieser Arbeit wurden ultrakleine Goldnanopartikel (ca. 1,8 nm) und Nanocluster synthetisiert, charakterisiert und in vitro untersucht. Nanopartikel und Nanocluster zeigten eine sehr gute Zellaufnahme und Viabilität bei HeLa-Zellen. Diese Nanopartikel und Nanocluster wurden dann in die zuvor entwickelten Kapseln und Zäpfchen gefüllt. Ultrakleine Goldnanocluster wurden mit gelabeltem BSA beschichtet und die Nanopartikel mit einem FITC-Farbstoff funktionalisiert, um in *in-vitro*-Studien verfolgt werden zu können. Aus beschichteten Kapseln freigesetzte Goldnanopartikel und Nanocluster zeigten eine einwandfreie Zellviabilität und Zellaufnahme durch HeLa-Zellen. BSA-farbstoffbeschichtete Nanocluster bewiesen, dass die Gold-Nanocluster BSA in die HeLa-Zellen tragen können.

Im nächsten Teil der vorliegenden Arbeit wurde der Einsatz von Verbundmaterialien aus Calciumphosphat und biologisch abbaubaren Polymeren auf Basis von Polylactid für den Wirkstofftransport untersucht. Als Wirkstoffträgersystem für anionische, hydrophile Wirkstoffe wie Nukleinsäuren wurden Calciumphosphat-PLGA-Nanopartikel entwickelt. Wasser-in-Öl-in-Wasser-Emulsionstechniken erwiesen sich als optimale Syntheserouten und lieferten sphärische Calciumphosphat-PLGA-Nanopartikel mit einem Kerndurchmesser von ca. 100 nm. Zellaufnahme- und Transfektionsstudien mit konfokaler Laser-Scanning-Mikroskopie zeigten, dass die Nanopartikel sehr gut von HeLa-Zellen absorbiert und transfiziert wurden. Gen-Stummschaltungs-Studien mit den Nanopartikeln zeigten auch,

dass diese Nanopartikel eine ideale Stummschaltungseffizienz-Effizienz bei HeLa-EGFP-Zellen aufweisen. Im letzten Teil dieser Arbeit wurden Strontium- und Magnesium-dotierte Calciumphosphat-Nanopartikel für Knochenregenerationseigenschaften synthetisiert. Diese Nanopartikel wurden mit Konzentrationen von 5 %, 10 %, 15 % bzw. 20 % Strontium und Magnesium dotiert. Diese Nanopartikel wurden *in-vitro* charakterisiert und untersucht. Es wurden sphärische Nanopartikel mit vergleichbaren Größen bei etwa 50-70 nm für alle Zusammensetzungen erzielt. Die Viabilität der Zellen und die Zellaufnahme der Nanopartikel wurden mit HeLa-, MG-63- und MC3T3-Zelllinien untersucht. Alle mit Strontium und Magnesium dotierten Calciumphosphat-Nanopartikel zeigten eine vielversprechende Zellviabilität von mehr als 70 % und eine sehr gute Aufnahme durch diese drei verschiedenen Zelllinien. Diese dotierten Nanopartikel zeigten im Vergleich zueinander sehr geringe Abweichungen und eine bessere Aufnahme im Vergleich zu reinen Calciumphosphat-Nanopartikeln. In dieser Arbeit wurde die Wirkung von sowohl Strontium- als auch Magnesium-dotierten Calciumphosphat-Nanopartikeln auf die Produktion von alkalischer Phosphatase durch HeLa-Zellen nach 7, 14 und 21 Tagen Kultivierung gezeigt. Nach 7-tägiger Kultivierung waren die relativen ALP-Aktivitäten der HeLa-Zellen bei den mit Nanopartikeln behandelten Proben Gruppen im Vergleich zu den Kontrollen höher. Nach 14 und 21 Tagen waren die relativen ALP-Aktivitäten der HeLa-Zellen bei den mit Nanopartikeln behandelten Proben Gruppen im Vergleich zu den Kontrollen dreimal beziehungsweise viermal höher. Zusammenfassend kann festgehalten werden, dass in der vorliegenden Arbeit sowohl für den Wirkstofftransport in der Nanomedizin als auch für die generative Herstellung von Knochenersatzmaterialien erfolgreich Materialien und Partikel auf Basis von Calciumphosphat entwickelt wurden.

---

## 8. References

1. Agüero, L., et al., *Alginate microparticles as oral colon drug delivery device: A review*. Carbohydrate polymers, 2017. **168**: p. 32-43.
2. Amidon, S., J.E. Brown, and V.S. Dave, *Colon-targeted oral drug delivery systems: design trends and approaches*. Aaps Pharmscitech, 2015. **16**(4): p. 731-741.
3. Zhang, F., *Melt-extruded Eudragit® FS-based granules for colonic drug delivery*. Aaps Pharmscitech, 2016. **17**(1): p. 56-67.
4. Moghimipour, E., et al., *In vivo evaluation of pH and time-dependent polymers as coating agent for colonic delivery using central composite design*. Journal of Drug Delivery Science and Technology, 2018. **43**: p. 50-56.
5. Liu, F., et al., *A novel concept in enteric coating: a double-coating system providing rapid drug release in the proximal small intestine*. Journal of Controlled Release, 2009. **133**(2): p. 119-124.
6. Pastille, E., et al., *Intestinal helminth infection drives carcinogenesis in colitis-associated colon cancer*. PLoS pathogens, 2017. **13**(9): p. e1006649.
7. Neuhaus, B., *Funktionalisierte Calciumphosphat-Nanopartikel als Instrument zum Eingriff in die Proteinbiosynthese und deren therapeutische Anwendung*. 2015: Duisburg, Essen.
8. Epple, M., et al., *Application of calcium phosphate nanoparticles in biomedicine*. Journal of Materials Chemistry, 2010. **20**(1): p. 18-23.
9. Dorozhkin, S.V., *Calcium orthophosphates in nature, biology and medicine*. Materials, 2009. **2**(2): p. 399-498.
10. Uskoković, V. and D.P. Uskoković, *Nanosized hydroxyapatite and other calcium phosphates: chemistry of formation and application as drug and gene delivery agents*. Journal of biomedical materials research Part B: Applied biomaterials, 2011. **96**(1): p. 152-191.
11. Cai, Y. and R. Tang, *Calcium phosphate nanoparticles in biomineralization and biomaterials*. Journal of Materials Chemistry, 2008. **18**(32): p. 3775-3787.
12. Xu, H. and K.S. Suslick, *Water-Soluble fluorescent silver nanoclusters*. Advanced Materials, 2010. **22**(10): p. 1078-1082.
13. Qi, W. and M. Wang, *Size and shape dependent lattice parameters of metallic nanoparticles*. Journal of Nanoparticle Research, 2005. **7**(1): p. 51-57.
14. Liu, Q., et al., *Insight into biological apatite: physiochemical properties and preparation approaches*. BioMed research international, 2013. **2013**.
15. Dykxhoorn, D.M. and J. Lieberman, *The silent revolution: RNA interference as basic biology, research tool, and therapeutic*. Annu. Rev. Med., 2005. **56**: p. 401-423.
16. Sahay, G., D.Y. Alakhova, and A.V. Kabanov, *Endocytosis of nanomedicines*. Journal of controlled release, 2010. **145**(3): p. 182-195.
17. Sokolova, V., et al., *Ultrasmall gold nanoparticles (2 nm) can penetrate and enter cell nuclei in an in vitro 3D brain spheroid model*. Acta biomaterialia, 2020. **111**: p. 349-362.
18. Goesmann, H. and C. Feldmann, *Nanoparticulate functional materials*. Angewandte Chemie International Edition, 2010. **49**(8): p. 1362-1395.
19. Schmid, G., *Nanoparticles: from theory to application*. 2011: John Wiley & Sons.
20. El-Sayed, M.A., *Some interesting properties of metals confined in time and nanometer space of different shapes*. Accounts of chemical research, 2001. **34**(4): p. 257-264.
21. Mie, G., *Contributions to the optics of turbid media, particularly of colloidal metal solutions*. Contributions to the optics of turbid media, 1976. **25**(3): p. 377-445.
22. Lewis, L.N., *Chemical catalysis by colloids and clusters*. Chemical Reviews, 1993. **93**(8): p. 2693-2730.
23. Somorjai, G.A., *Modern surface science and surface technologies: an introduction*. Chemical reviews, 1996. **96**(4): p. 1223-1236.

24. Frey, N.A., et al., *Magnetic nanoparticles: synthesis, functionalization, and applications in bioimaging and magnetic energy storage*. Chemical Society Reviews, 2009. **38**(9): p. 2532-2542.
25. Rawat, R. *Dense plasma focus-from alternative fusion source to versatile high energy density plasma source for plasma nanotechnology*. in *Journal of Physics: Conference Series*. 2015. IOP Publishing.
26. Verma, S., R. Gokhale, and D.J. Burgess, *A comparative study of top-down and bottom-up approaches for the preparation of micro/nanosuspensions*. International journal of pharmaceutics, 2009. **380**(1-2): p. 216-222.
27. Teo, B.K. and X. Sun, *From top-down to bottom-up to hybrid nanotechnologies: road to nanodevices*. Journal of cluster science, 2006. **17**(4): p. 529-540.
28. O'Dwyer, C., et al., *Bottom-up growth of fully transparent contact layers of indium tin oxide nanowires for light-emitting devices*. Nature nanotechnology, 2009. **4**(4): p. 239-244.
29. Iqbal, P., J.A. Preece, and P.M. Mendes, *Nanotechnology: The "Top-Down" and "Bottom-Up" Approaches*. Supramolecular chemistry: from molecules to nanomaterials, 2012.
30. Salata, O.V., *Applications of nanoparticles in biology and medicine*. Journal of nanobiotechnology, 2004. **2**(1): p. 1-6.
31. Morawski, A.M., et al., *Targeted nanoparticles for quantitative imaging of sparse molecular epitopes with MRI*. Magnetic Resonance in Medicine: An Official Journal of the International Society for Magnetic Resonance in Medicine, 2004. **51**(3): p. 480-486.
32. Nahrendorf, M., et al., *Nanoparticle PET-CT imaging of macrophages in inflammatory atherosclerosis*. Circulation, 2008. **117**(3): p. 379.
33. Cho, K., et al., *Therapeutic nanoparticles for drug delivery in cancer*. Clinical cancer research, 2008. **14**(5): p. 1310-1316.
34. Veiseh, O., et al., *Optical and MRI multifunctional nanoprobe for targeting gliomas*. Nano letters, 2005. **5**(6): p. 1003-1008.
35. Duncan, R. and L. Izzo, *Dendrimer biocompatibility and toxicity*. Advanced drug delivery reviews, 2005. **57**(15): p. 2215-2237.
36. Jaiswal, J.K. and S.M. Simon, *Imaging single events at the cell membrane*. Nature chemical biology, 2007. **3**(2): p. 92-98.
37. Michalet, X., et al., *S Doose, JLL; Sundaresan, G.; Wu, AM; Gambhir, SS; Weiss, S. Quantum Dots for Live Cells. Vivo Imaging, and Diagnostics*. Science, 2005. **307**: p. 538-544.
38. Cao, Y.C., R. Jin, and C.A. Mirkin, *Nanoparticles with Raman spectroscopic fingerprints for DNA and RNA detection*. Science, 2002. **297**(5586): p. 1536-1540.
39. Jin, R., et al., *Controlling anisotropic nanoparticle growth through plasmon excitation*. Nature, 2003. **425**(6957): p. 487-490.
40. Elghanian, R., et al., *Selective colorimetric detection of polynucleotides based on the distance-dependent optical properties of gold nanoparticles*. Science, 1997. **277**(5329): p. 1078-1081.
41. Bergmann, C.P. and A. Stumpf, *Dental ceramics*. Biomaterials, 2013: p. 9-13.
42. Epple, M., *Biomaterialien und Biomineralisation: Eine Einführung für Naturwissenschaftler, Mediziner und Ingenieure*. 2013: Springer-Verlag.
43. Bulmus, V., et al., *A new pH-responsive and glutathione-reactive, endosomal membrane-disruptive polymeric carrier for intracellular delivery of biomolecular drugs*. Journal of Controlled Release, 2003. **93**(2): p. 105-120.
44. Kim, B., K. La Flamme, and N.A. Peppas, *Dynamic swelling behavior of pH-sensitive anionic hydrogels used for protein delivery*. Journal of Applied Polymer Science, 2003. **89**(6): p. 1606-1613.
45. Jeong, B., S.W. Kim, and Y.H. Bae, *Thermosensitive sol-gel reversible hydrogels*. Advanced drug delivery reviews, 2012. **64**: p. 154-162.
46. Chilkoti, A., M.R. Dreher, and D.E. Meyer, *Design of thermally responsive, recombinant polypeptide carriers for targeted drug delivery*. Advanced drug delivery reviews, 2002. **54**(8): p. 1093-1111.

47. Shimoboji, T., et al., *Photoresponsive polymer–enzyme switches*. Proceedings of the National Academy of Sciences, 2002. **99**(26): p. 16592-16596.
48. Shimoboji, T., et al., *Temperature-induced switching of enzyme activity with smart polymer–enzyme conjugates*. Bioconjugate chemistry, 2003. **14**(3): p. 517-525.
49. Ratner, B.D. and S.J. Bryant, *Biomaterials: where we have been and where we are going*. Annu. Rev. Biomed. Eng., 2004. **6**: p. 41-75.
50. Dorozhkin, S.V. and M. Epple, *Biological and medical significance of calcium phosphates*. Angewandte Chemie International Edition, 2002. **41**(17): p. 3130-3146.
51. Gómez-Morales, J., et al., *Progress on the preparation of nanocrystalline apatites and surface characterization: Overview of fundamental and applied aspects*. Progress in Crystal Growth and Characterization of Materials, 2013. **59**(1): p. 1-46.
52. Sokolova, V. and M. Epple, *Inorganic nanoparticles as carriers of nucleic acids into cells*. Angewandte chemie international edition, 2008. **47**(8): p. 1382-1395.
53. Chen, F., et al., *Nanostructured Calcium Phosphates: Preparation and Their Application in Biomedicine*. Nano Biomedicine & Engineering, 2012. **4**(1).
54. Mostaghaci, B., et al., *One-step synthesis of nanosized and stable amino-functionalized calcium phosphate particles for DNA transfection*. Chemistry of Materials, 2013. **25**(18): p. 3667-3674.
55. Mostaghaci, B., B. Loretz, and C.-M. Lehr, *Calcium phosphate system for gene delivery: historical background and emerging opportunities*. Current pharmaceutical design, 2016. **22**(11): p. 1529-1533.
56. Zhang, M. and K. Kataoka, *Nano-structured composites based on calcium phosphate for cellular delivery of therapeutic and diagnostic agents*. Nano Today, 2009. **4**(6): p. 508-517.
57. Pascaud, P., et al., *Adsorption on apatitic calcium phosphates for drug delivery: interaction with bisphosphonate molecules*. Journal of Materials Science: Materials in Medicine, 2014. **25**(10): p. 2373-2381.
58. Bisht, S., et al., *pDNA loaded calcium phosphate nanoparticles: highly efficient non-viral vector for gene delivery*. International journal of pharmaceutics, 2005. **288**(1): p. 157-168.
59. Boix, T., et al., *Adsorption of recombinant human bone morphogenetic protein rhBMP-2m onto hydroxyapatite*. Journal of inorganic biochemistry, 2005. **99**(5): p. 1043-1050.
60. Sokolova, V., et al., *Quantitative determination of the composition of multi-shell calcium phosphate–oligonucleotide nanoparticles and their application for the activation of dendritic cells*. Acta biomaterialia, 2011. **7**(11): p. 4029-4036.
61. Sokolova, V., et al., *Calcium phosphate nanoparticles as versatile carrier for small and large molecules across cell membranes*. Journal of Nanoparticle Research, 2012. **14**(6): p. 1-10.
62. Welzel, T., et al., *Transfection of cells with custom-made calcium phosphate nanoparticles coated with DNA*. Journal of Materials Chemistry, 2004. **14**(14): p. 2213-2217.
63. Sokolova, V., et al., *An outer shell of positively charged poly (ethyleneimine) strongly increases the transfection efficiency of calcium phosphate/DNA nanoparticles*. Journal of materials science, 2010. **45**(18): p. 4952-4957.
64. Devarasu, T., et al., *Potent calcium phosphate nanoparticle surface coating for in vitro and in vivo siRNA delivery: a step toward multifunctional nanovectors*. Journal of Materials Chemistry B, 2013. **1**(36): p. 4692-4700.
65. Kozlova, D., et al., *Cell targeting by antibody-functionalized calcium phosphate nanoparticles*. Journal of Materials Chemistry, 2012. **22**(2): p. 396-404.
66. Haedicke, K., et al., *Multifunctional calcium phosphate nanoparticles for combining near-infrared fluorescence imaging and photodynamic therapy*. Acta biomaterialia, 2015. **14**: p. 197-207.
67. Mukherjee, S., R.N. Ghosh, and F.R. Maxfield, *Endocytosis*. Physiological reviews, 1997.
68. Panariti, A., G. Miserocchi, and I. Rivolta, *The effect of nanoparticle uptake on cellular behavior: disrupting or enabling functions?* Nanotechnology, science and applications, 2012. **5**: p. 87.

69. Richards, D.M. and R.G. Endres, *How cells engulf: a review of theoretical approaches to phagocytosis*. Reports on Progress in Physics, 2017. **80**(12): p. 126601.
70. Underhill, D.M. and A. Ozinsky, *Phagocytosis of microbes: complexity in action*. Annual review of immunology, 2002. **20**(1): p. 825-852.
71. Swanson, J.A., *Shaping cups into phagosomes and macropinosomes*. Nature reviews Molecular cell biology, 2008. **9**(8): p. 639-649.
72. Machta, B.B., et al., *Parameter space compression underlies emergent theories and predictive models*. Science, 2013. **342**(6158): p. 604-607.
73. Dou, H., et al., *Development of a macrophage-based nanoparticle platform for antiretroviral drug delivery*. Blood, 2006. **108**(8): p. 2827-2835.
74. Singh, J., et al., *Advances in nanotechnology-based carrier systems for targeted delivery of bioactive drug molecules with special emphasis on immunotherapy in drug resistant tuberculosis—a critical review*. Drug delivery, 2016. **23**(5): p. 1676-1698.
75. Sun, T., et al., *Engineered nanoparticles for drug delivery in cancer therapy*. Angewandte Chemie International Edition, 2014. **53**(46): p. 12320-12364.
76. Praetorius, N.P. and T.K. Mandal, *Engineered nanoparticles in cancer therapy*. Recent Patents on Drug Delivery & Formulation, 2007. **1**(1): p. 37-51.
77. Kohane, D.S., *Microparticles and nanoparticles for drug delivery*. Biotechnology and bioengineering, 2007. **96**(2): p. 203-209.
78. Parveen, S., R. Misra, and S.K. Sahoo, *Nanoparticles: a boon to drug delivery, therapeutics, diagnostics and imaging*. Nanomedicine: Nanotechnology, Biology and Medicine, 2012. **8**(2): p. 147-166.
79. Pang, L., et al., *A novel strategy to achieve effective drug delivery: exploit cells as carrier combined with nanoparticles*. Drug delivery, 2017. **24**(1): p. 83-91.
80. Lin, S.-Y., et al., *Novel geometry type of nanocarriers mitigated the phagocytosis for drug delivery*. Journal of controlled release, 2011. **154**(1): p. 84-92.
81. De Jong, W.H. and P.J. Borm, *Drug delivery and nanoparticles: applications and hazards*. International journal of nanomedicine, 2008. **3**(2): p. 133.
82. Rustad, R.C., *Pinocytosis*. Scientific American, 1961. **204**(4): p. 120-133.
83. Silverstein, S.C., R.M. Steinman, and Z.A. Cohn, *Endocytosis*. Annual review of biochemistry, 1977. **46**(1): p. 669-722.
84. Iversen, T.-G., T. Skotland, and K. Sandvig, *Endocytosis and intracellular transport of nanoparticles: Present knowledge and need for future studies*. Nano today, 2011. **6**(2): p. 176-185.
85. Conner, S.D. and S.L. Schmid, *Regulated portals of entry into the cell*. Nature, 2003. **422**(6927): p. 37-44.
86. Mettlen, M., et al., *Regulation of clathrin-mediated endocytosis*. Annual review of biochemistry, 2018. **87**: p. 871-896.
87. Kaksonen, M. and A. Roux, *Mechanisms of clathrin-mediated endocytosis*. Nature reviews Molecular cell biology, 2018. **19**(5): p. 313.
88. Panyam, J. and V. Labhsetwar, *Biodegradable nanoparticles for drug and gene delivery to cells and tissue*. Advanced drug delivery reviews, 2003. **55**(3): p. 329-347.
89. Chithrani, B.D. and W.C. Chan, *Elucidating the mechanism of cellular uptake and removal of protein-coated gold nanoparticles of different sizes and shapes*. Nano letters, 2007. **7**(6): p. 1542-1550.
90. Nan, A., et al., *Cellular uptake and cytotoxicity of silica nanotubes*. Nano letters, 2008. **8**(8): p. 2150-2154.
91. Watts, C. and M. Marsh, *Endocytosis: what goes in and how?* Journal of cell science, 1992. **103**(1): p. 1-8.
92. Marsh, M. and A. Helenius, *Adsorptive endocytosis of Semliki Forest virus*. Journal of molecular biology, 1980. **142**(3): p. 439-454.
93. Griffiths, G., R. Back, and M. Marsh, *A quantitative analysis of the endocytic pathway in baby hamster kidney cells*. The Journal of cell biology, 1989. **109**(6): p. 2703-2720.

94. Lamaze, C. and S.L. Schmid, *The emergence of clathrin-independent pinocytic pathways*. Current opinion in cell biology, 1995. **7**(4): p. 573-580.
95. Zhang, S., et al., *Size-dependent endocytosis of nanoparticles*. Advanced materials, 2009. **21**(4): p. 419-424.
96. Doherty, G.J. and H.T. McMahon, *Mechanisms of endocytosis*. Annual review of biochemistry, 2009. **78**: p. 857-902.
97. Lim, J.P. and P.A. Gleeson, *Macropinocytosis: an endocytic pathway for internalising large gulps*. Immunology and cell biology, 2011. **89**(8): p. 836-843.
98. Sandvig, K., et al., *Clathrin-independent endocytosis: mechanisms and function*. Current opinion in cell biology, 2011. **23**(4): p. 413-420.
99. Wieffer, M., T. Maritzen, and V. Haucke, *SnapShot: endocytic trafficking*. Cell, 2009. **137**(2): p. 382. e1-382. e3.
100. Kumari, S., M. Swetha, and S. Mayor, *Endocytosis unplugged: multiple ways to enter the cell*. Cell research, 2010. **20**(3): p. 256-275.
101. Sokolova, V., et al., *Mechanism of the uptake of cationic and anionic calcium phosphate nanoparticles by cells*. Acta biomaterialia, 2013. **9**(7): p. 7527-7535.
102. Gao, H., W. Shi, and L.B. Freund, *Mechanics of receptor-mediated endocytosis*. Proceedings of the National Academy of Sciences, 2005. **102**(27): p. 9469-9474.
103. Glover, D.J., H.J. Lipps, and D.A. Jans, *Towards safe, non-viral therapeutic gene expression in humans*. Nature Reviews Genetics, 2005. **6**(4): p. 299-310.
104. Hamilton, A.J. and D.C. Baulcombe, *A species of small antisense RNA in posttranscriptional gene silencing in plants*. Science, 1999. **286**(5441): p. 950-952.
105. Wurm, F.M., *Production of recombinant protein therapeutics in cultivated mammalian cells*. Nature biotechnology, 2004. **22**(11): p. 1393-1398.
106. Recillas-Targa, F., *Multiple strategies for gene transfer, expression, knockdown, and chromatin influence in mammalian cell lines and transgenic animals*. Molecular biotechnology, 2006. **34**(3): p. 337-354.
107. Pfeifer, A. and I.M. Verma, *Gene therapy: promises and problems*. Annual review of genomics and human genetics, 2001. **2**(1): p. 177-211.
108. Schenborn, E.T. and V. Goiffon, *DEAE-dextran transfection of mammalian cultured cells*. Transcription Factor Protocols, 2000: p. 147-153.
109. Holmen, S.L., et al., *Efficient lipid-mediated transfection of DNA into primary rat hepatocytes*. In Vitro Cellular & Developmental Biology-Animal, 1995. **31**(5): p. 347-351.
110. Washbourne, P. and A.K. McAllister, *Techniques for gene transfer into neurons*. Current opinion in neurobiology, 2002. **12**(5): p. 566-573.
111. Hacein-Bey-Abina, S., et al., *Sustained correction of X-linked severe combined immunodeficiency by ex vivo gene therapy*. New England Journal of Medicine, 2002. **346**(16): p. 1185-1193.
112. Roesler, J., et al., *Third-generation, self-inactivating gp91phoxlentivector corrects the oxidase defect in NOD/SCID mouse—repopulating peripheral blood—mobilized CD34+ cells from patients with X-linked chronic granulomatous disease*. Blood, The Journal of the American Society of Hematology, 2002. **100**(13): p. 4381-4390.
113. Kim, T.K. and J.H. Eberwine, *Mammalian cell transfection: the present and the future*. Analytical and bioanalytical chemistry, 2010. **397**(8): p. 3173-3178.
114. Mehier-Humbert, S. and R.H. Guy, *Physical methods for gene transfer: improving the kinetics of gene delivery into cells*. Advanced drug delivery reviews, 2005. **57**(5): p. 733-753.
115. Chen, X., et al., *Chemical modification of gene silencing oligonucleotides for drug discovery and development*. Drug Discovery Today, 2005. **10**(8): p. 587-593.
116. Dorsett, Y. and T. Tuschl, *siRNAs: applications in functional genomics and potential as therapeutics*. Nature reviews Drug discovery, 2004. **3**(4): p. 318-329.
117. Sashital, D.G. and J.A. Doudna, *Structural insights into RNA interference*. Current opinion in structural biology, 2010. **20**(1): p. 90-97.

118. Kim, D.H. and J.J. Rossi, *Strategies for silencing human disease using RNA interference*. Nature Reviews Genetics, 2007. **8**(3): p. 173-184.
119. Pecot, C.V., et al., *RNA interference in the clinic: challenges and future directions*. Nature Reviews Cancer, 2011. **11**(1): p. 59-67.
120. Reischl, D. and A. Zimmer, *Drug delivery of siRNA therapeutics: potentials and limits of nanosystems*. Nanomedicine: Nanotechnology, Biology and Medicine, 2009. **5**(1): p. 8-20.
121. He, Q., et al., *Calcium phosphate nanoparticle adjuvant*. Clinical and diagnostic laboratory immunology, 2000. **7**(6): p. 899-903.
122. Cui, Z. and R.J. Mumper, *Microparticles and nanoparticles as delivery systems for DNA vaccines*. Critical Reviews™ in Therapeutic Drug Carrier Systems, 2003. **20**(2&3).
123. Sokolova, V., et al., *Functionalisation of calcium phosphate nanoparticles by oligonucleotides and their application for gene silencing*. Journal of Materials Chemistry, 2007. **17**(8): p. 721-727.
124. Hosseini, S., K. Wey, and M. Epple, *Enteric Coating Systems for the Oral Administration of Bioactive Calcium Phosphate Nanoparticles Carrying Nucleic Acids into the Colon*. ChemistrySelect, 2020. **5**(31): p. 9720-9729.
125. Lee, V., *Changing needs in drug delivery in the era of peptide and protein drugs*. Peptide and protein drug delivery, 1991.
126. Ikesue, K., P. Kopeckova, and J. Kopecek. *Degradation of proteins by enzymes of the gastrointestinal tract*. in *Proceedings of the International Symposium of Controlled Release of Bioactive Materials*. 1991.
127. Hosseini, S. and M. Epple, *Suppositories with bioactive calcium phosphate nanoparticles for intestinal transfection and gene silencing*. Nano Select, 2021. **2**(3): p. 561-572.
128. Wood, E., C.G. Wilson, and J.G. Hardy, *The spreading of foam and solution enemas*. International journal of pharmaceutics, 1985. **25**(2): p. 191-197.
129. Chowdary Vadlamudi, H., et al., *Anatomical, biochemical and physiological considerations of the colon in design and development of novel drug delivery systems*. Current drug delivery, 2012. **9**(6): p. 556-565.
130. Jay, M., et al., *Disposition of radiolabelled suppositories in humans*. Journal of pharmacy and pharmacology, 1985. **37**(4): p. 266-268.
131. Hardy, J., *Colonic transit and drug delivery*. Drug delivery to the gastrointestinal tract, 1989: p. 75-81.
132. Nugent, S., et al., *Intestinal luminal pH in inflammatory bowel disease: possible determinants and implications for therapy with aminosalicylates and other drugs*. Gut, 2001. **48**(4): p. 571-577.
133. Slabaugh, G., et al., *A robust and fast system for ctc computer-aided detection of colorectal lesions*. Algorithms, 2010. **3**(1): p. 21-43.
134. Davis, S., J. Hardy, and J. Fara, *Transit of pharmaceutical dosage forms through the small intestine*. Gut, 1986. **27**(8): p. 886-892.
135. Hofmann, A.F., et al., *Controlled entry of orally administered drugs: physiological considerations*. Drug Development and Industrial Pharmacy, 1983. **9**(7): p. 1077-1109.
136. Ghube, K., P. Khade, and A. Bhosale, *A Review on Enteric Coating*. Journal of Current Pharma Research, 2020. **10**(4): p. 3848-3862.
137. Brogmann, B. and T.E. Beckert, *Enteric targeting through enteric coating*. Drugs and the Pharmaceutical Sciences, 2001. **115**: p. 1-30.
138. Maroni, A., et al., *Enteric coatings for colonic drug delivery: State of the art*. Expert opinion on drug delivery, 2017. **14**(9): p. 1027-1029.
139. Hussan, S.D., et al., *A review on recent advances of enteric coating*. IOSR J Pharm, 2012. **2**(6): p. 05-11.
140. Lehmann, K., *Magensaftresistente und retardierende Arzneimittelüberzüge aus wässrigen Acrylharzdispersionen*. Acta Pharm. Technol., 1975. **21**: p. 255-260.
141. Thakral, S., N.K. Thakral, and D.K. Majumdar, *Eudragit®: a technology evaluation*. Expert opinion on drug delivery, 2013. **10**(1): p. 131-149.

142. Ashford, M., et al., *An evaluation of pectin as a carrier for drug targeting to the colon*. Journal of Controlled Release, 1993. **26**(3): p. 213-220.
143. Ashford, M., et al., *An in vitro investigation into the suitability of pH-dependent polymers for colonic targeting*. International journal of pharmaceutics, 1993. **91**(2-3): p. 241-245.
144. Goto, T., et al., *Pharmaceutical design of a novel colon-targeted delivery system using two-layer-coated tablets of three different pharmaceutical formulations, supported by clinical evidence in humans*. Journal of controlled release, 2004. **97**(1): p. 31-42.
145. Cheng, G., et al., *Time-and pH-dependent colon-specific drug delivery for orally administered diclofenac sodium and 5-aminosalicylic acid*. World Journal of Gastroenterology: WJG, 2004. **10**(12): p. 1769.
146. Rodríguez, M., J.L. Vila-Jato, and D. Torres, *Design of a new multiparticulate system for potential site-specific and controlled drug delivery to the colonic region*. Journal of controlled release, 1998. **55**(1): p. 67-77.
147. Krogars, K., et al., *Extrusion-spheronization of pH-sensitive polymeric matrix pellets for possible colonic drug delivery*. International Journal of Pharmaceutics, 2000. **199**(2): p. 187-194.
148. Zambito, Y., et al., *Matrices for site-specific controlled-delivery of 5-fluorouracil to descending colon*. Journal of controlled release, 2005. **102**(3): p. 669-677.
149. Hua, Z., et al., *Technology to obtain sustained release characteristics of drugs after delivered to the colon*. Journal of drug targeting, 1999. **6**(6): p. 439-448.
150. Chourasia, M. and S. Jain, *Design and development of multiparticulate system for targeted drug delivery to colon*. Drug delivery, 2004. **11**(3): p. 201-207.
151. Lamprecht, A., et al., *Design of pH-sensitive microspheres for the colonic delivery of the immunosuppressive drug tacrolimus*. European Journal of Pharmaceutics and Biopharmaceutics, 2004. **58**(1): p. 37-43.
152. Nykänen, P., et al., *Organic acids as excipients in matrix granules for colon-specific drug delivery*. International journal of pharmaceutics, 1999. **184**(2): p. 251-261.
153. Nykänen, P., et al., *Citric acid as excipient in multiple-unit enteric-coated tablets for targeting drugs on the colon*. International journal of pharmaceutics, 2001. **229**(1-2): p. 155-162.
154. Verbeke, K., et al., *In vivo evaluation of a colonic delivery system using isotope techniques*. Alimentary pharmacology & therapeutics, 2005. **21**(2): p. 187-194.
155. Missaghi, S., et al., *Delayed release film coating applications on oral solid dosage forms of proton pump inhibitors: case studies*. Drug development and industrial pharmacy, 2010. **36**(2): p. 180-189.
156. Ali, S.F.B., et al., *Blend of cellulose ester and enteric polymers for delayed and enteric coating of core tablets of hydrophilic and hydrophobic drugs*. International journal of pharmaceutics, 2019. **567**: p. 118462.
157. Arjun, N., et al., *Development, evaluation, and influence of formulation and process variables on in vitro performance of oral elementary osmotic device of atenolol*. International journal of pharmaceutical investigation, 2016. **6**(4): p. 238.
158. HODGE, H.C., H.H. FORSYTH, and G.H. RAMSEY, *Clinical tests of cellulose acetate phthalate as an enteric coating*. Journal of Pharmacology and Experimental Therapeutics, 1944. **80**(3): p. 241-249.
159. Park, H.-S., et al., *Colon delivery of prednisolone based on chitosan coated polysaccharide tablets*. Archives of pharmacal research, 2002. **25**(6): p. 964-968.
160. Cole, E.T., et al., *Enteric coated HPMC capsules designed to achieve intestinal targeting*. International journal of pharmaceutics, 2002. **231**(1): p. 83-95.
161. Ogura, T., *HPMC capsules: an alternative to gelatin*. Pharm. Tech. Europe, 1998. **10**.
162. Wilding, I., A. Coupe, and S. Davis, *The role of  $\gamma$ -scintigraphy in oral drug delivery*. Advanced drug delivery reviews, 2001. **46**(1-3): p. 103-124.
163. Wilding, I. and S. Newman, *Saving time in the drug development process using gamma scintigraphy*. Pharm. Tech. Eur. Feb, 1998. **10**: p. 26-31.

164. Wilding, I.R., *Site-specific drug delivery in the gastrointestinal tract*. Critical Reviews™ in Therapeutic Drug Carrier Systems, 2000. **17**(6).
165. Ofori-Kwakye, K. and J.T. Fell, *Leaching of pectin from mixed films containing pectin, chitosan and HPMC intended for biphasic drug delivery*. International journal of pharmaceuticals, 2003. **250**(1): p. 251-257.
166. Turner-Warwick, M., *Epidemiology of nocturnal asthma*. The American journal of medicine, 1988. **85**(1): p. 6-8.
167. Willich, S.N., et al., *Increased onset of sudden cardiac death in the first three hours after awakening*. The American journal of cardiology, 1992. **70**(1): p. 65-68.
168. Maggi, L., et al., *Formulation of biphasic release tablets containing slightly soluble drugs*. European journal of pharmaceuticals and biopharmaceuticals, 1999. **48**(1): p. 37-42.
169. Bodmeier, R. and O. Paeratakul, *Constant potassium chloride release from microporous membrane-coated tablets prepared with aqueous colloidal polymer dispersions*. Pharmaceutical research, 1991. **8**(3): p. 355-359.
170. Guo, J.-H., *An investigation into the formation of plasticizer channels in plasticized polymer films*. Drug Development and Industrial Pharmacy, 1994. **20**(11): p. 1883-1893.
171. Gazzaniga, A., et al., *Time-dependent oral delivery systems for colon targeting*. 1995.
172. Gazzaniga, A., et al., *Oral delayed-release system for colonic specific delivery*. International journal of pharmaceuticals, 1994. **108**(1): p. 77-83.
173. Gazzaniga, A., et al., *Time-controlled oral delivery systems for colon targeting*. Expert Opinion on Drug Delivery, 2006. **3**(5): p. 583-597.
174. Purohit, T.J., S.M. Hanning, and Z. Wu, *Advances in rectal drug delivery systems*. Pharmaceutical development and technology, 2018. **23**(10): p. 942-952.
175. Shah, S.M., A.H. Sultan, and R. Thakar, *The history and evolution of pessaries for pelvic organ prolapse*. International Urogynecology Journal, 2006. **17**(2): p. 170-175.
176. Ham, A.S. and R.W. Buckheit Jr, *Designing and developing suppository formulations for anti-HIV drug delivery*. Therapeutic delivery, 2017. **8**(9): p. 805-817.
177. Cheymol, G. *Drug administration through the rectum: reliability, tolerance*. in *Annales de gastroenterologie et d'hepatologie*. 1987.
178. Moolenaar, F. and D. Breimer, *Rectal drug administration: clinical pharmacokinetic considerations*. Clinical pharmacokinetics, 1982. **7**(4): p. 285-311.
179. De Boer, A., L. De Leede, and D. Breimer, *Drug absorption by sublingual and rectal routes*. British journal of anaesthesia, 1984. **56**(1): p. 69-82.
180. Kavazos, K., et al., *Dietary supplementation with omega-3 polyunsaturated fatty acids modulate matrix metalloproteinase immunoreactivity in a mouse model of pre-abdominal aortic aneurysm*. Heart, Lung and Circulation, 2015. **24**(4): p. 377-385.
181. Jirapinyo, P., N. Kumar, and C.C. Thompson, *Patients with Roux-en-Y gastric bypass require increased sedation during upper endoscopy*. Clinical Gastroenterology and Hepatology, 2015. **13**(8): p. 1432-1436.
182. Bolme, P., et al., *Pharmacokinetics of theophylline in young children with asthma: Comparison of rectal enema and suppositories*. European journal of clinical pharmacology, 1979. **16**(2): p. 133-139.
183. Li, B., et al., *Shape of vaginal suppositories affects willingness-to-try and preference*. Antiviral research, 2013. **97**(3): p. 280-284.
184. Saladin, K.S. and C. Porth, *Nervous tissue*. Anatomy and physiology: the unity of form and function. WCB/McGraw-Hill co, New York, 1998: p. 430-445.
185. Elliott, J., *Hydroxyapatite and nonstoichiometric apatites*. Structure and chemistry of the apatites and other calcium orthophosphates, 1994. **18**: p. 111-189.
186. LeGeros, R.Z., *Calcium phosphates in oral biology and medicine*. Monographs in oral sciences, 1991. **15**: p. 109-111.
187. Shepherd, J.H., D.V. Shepherd, and S.M. Best, *Substituted hydroxyapatites for bone repair*. Journal of Materials Science: Materials in Medicine, 2012. **23**(10): p. 2335-2347.

188. Worth, A., et al., *The evaluation of processed cancellous bovine bone as a bone graft substitute*. Clinical oral implants research, 2005. **16**(3): p. 379-386.
189. Knowles, J., S. Talal, and J. Santos, *Sintering effects in a glass reinforced hydroxyapatite*. Biomaterials, 1996. **17**(14): p. 1437-1442.
190. Kim, H.W., et al., *Sol-Gel Preparation and Properties of Fluoride-Substituted Hydroxyapatite Powders*. Journal of the American Ceramic Society, 2004. **87**(10): p. 1939-1944.
191. Saranya, K., M. Kowshik, and S.R. Ramanan, *Synthesis of hydroxyapatite nanopowders by sol-gel emulsion technique*. Bulletin of Materials Science, 2011. **34**(7): p. 1749-1753.
192. Shepherd, D. and S.M. Best, *Production of zinc substituted hydroxyapatite using various precipitation routes*. Biomedical Materials, 2013. **8**(2): p. 025003.
193. Fathi, M., A. Hanifi, and V. Mortazavi, *Preparation and bioactivity evaluation of bone-like hydroxyapatite nanopowder*. Journal of materials processing technology, 2008. **202**(1-3): p. 536-542.
194. Barakat, N.A., et al., *Extraction of pure natural hydroxyapatite from the bovine bones bio waste by three different methods*. Journal of materials processing technology, 2009. **209**(7): p. 3408-3415.
195. Ren, F., et al., *Synthesis, characterization and ab initio simulation of magnesium-substituted hydroxyapatite*. Acta Biomaterialia, 2010. **6**(7): p. 2787-2796.
196. Landi, E., et al., *Biomimetic Mg-substituted hydroxyapatite: from synthesis to in vivo behaviour*. Journal of Materials Science: Materials in Medicine, 2008. **19**(1): p. 239-247.
197. Rude, R.K., F.R. Singer, and H.E. Gruber, *Skeletal and hormonal effects of magnesium deficiency*. Journal of the American College of Nutrition, 2009. **28**(2): p. 131-141.
198. Bigi, A., et al., *The role of magnesium on the structure of biological apatites*. Calcified tissue international, 1992. **50**(5): p. 439-444.
199. Tampieri, A., et al. *Magnesium doped hydroxyapatite: synthesis and characterization*. in *Key Engineering Materials*. 2004. Trans Tech Publ.
200. Sprio, S., et al., *Raman and cathodoluminescence spectroscopies of magnesium-substituted hydroxyapatite powders*. Journal of materials research, 2005. **20**(4): p. 1009-1016.
201. Laurencin, D., N. Almora-Barrios, and H. Nora, de Leeuw, *Christel Gervais, Christian Bonhomme, Francesco Mauri, Wojciech Chrzanowski, Jonathan C. Knowles, Robert J. Newport, Alan Wong, Zhehong Gan, Mark E. Smith, Magnesium incorporation into hydroxyapatite*. Biomaterials, 2011. **32**(7): p. 1826-1837.
202. Bigi, A., et al., *Strontium-substituted hydroxyapatite nanocrystals*. Inorganica Chimica Acta, 2007. **360**(3): p. 1009-1016.
203. Gerstenfeld, S., et al., *Effect of strontium on bone metabolism in hemodialysis patients*. Nefrologia: publicacion oficial de la Sociedad Espanola Nefrologia, 2003. **23**: p. 52-56.
204. Ravi, N.D., R. Balu, and T. Sampath Kumar, *Strontium-substituted calcium deficient hydroxyapatite nanoparticles: synthesis, characterization, and antibacterial properties*. Journal of the American Ceramic Society, 2012. **95**(9): p. 2700-2708.
205. Li, Z., et al., *Chemical composition, crystal size and lattice structural changes after incorporation of strontium into biomimetic apatite*. Biomaterials, 2007. **28**(7): p. 1452-1460.
206. Curran, D.J., et al., *Mechanical parameters of strontium doped hydroxyapatite sintered using microwave and conventional methods*. Journal of the Mechanical Behavior of Biomedical Materials, 2011. **4**(8): p. 2063-2073.
207. Instruments, M., *Zetasizer Nano Series User Manual-MAN0317 Issue 1.0*. Malvern Instruments Ltd., England, 2003.
208. Zetasizer, N., *Zetasizer nano series user manual*. England: Malvern Instruments Ltd, 2003: p. 314-323.
209. Hassan, P.A., S. Rana, and G. Verma, *Making sense of Brownian motion: colloid characterization by dynamic light scattering*. Langmuir, 2015. **31**(1): p. 3-12.
210. Berne, B.J. and R. Pecora, *Dynamic light scattering: with applications to chemistry, biology, and physics*. 2000: Courier Corporation.

211. Hassellöv, M., et al., *Nanoparticle analysis and characterization methodologies in environmental risk assessment of engineered nanoparticles*. *Ecotoxicology*, 2008. **17**(5): p. 344-361.
212. Ring, E.A. and N. De Jonge, *Microfluidic system for transmission electron microscopy*. *Microscopy and Microanalysis*, 2010. **16**(5): p. 622.
213. JOSEPH, G., *SCANNING ELECTRON MICROSCOPY AND X-RAY MICROANALYSIS; A TEXT FOR BIOLOGISTS, MATERIALS SCIENTISTS, AND GEOLOGISTS*. 1981.
214. Augsten, K., J. Ohnsorge und R. Holm, *Rasterelektronenmikroskopie—Eine Einführung für Mediziner und Biologen (2. überarbeitete u. erweiterte Auflage)*. XI+ 155 S., 143 Abb. Stuttgart 1978. Georg Thieme-Verlag. DM 64, 00. 1980, Wiley Online Library.
215. Aziz, Z., et al., *Analytical ultracentrifugation: techniques and methods*. 2007: Royal Society of Chemistry.
216. Van der Meer, S.B., *Oberflächenfunktionalisierung von ultrakleinen Goldnanopartikeln für die selektive Proteinadressierung*. 2020: Universitaet Duisburg-Essen (Germany).
217. Goodhew, P., *General introduction to transmission electron microscopy (TEM)*. *Aberration-Corrected Analytical Transmission Electron Microscopy*, 2011: p. 1-19.
218. Fultz, B. and J.M. Howe, *Inelastic electron scattering and spectroscopy*. *Transmission Electron Microscopy and Diffractometry of Materials*, 2008: p. 163-221.
219. Günther, H., *NMR spectroscopy: basic principles, concepts and applications in chemistry*. 2013: John Wiley & Sons.
220. Gunther, H. and H. Gunther, *NMR spectroscopy: basic principles, concepts, and applications in chemistry*. 1994: John Wiley & Sons Chichester, UK.
221. Abraham, R.J., J. Fisher, and P. Loftus, *Introduction to NMR spectroscopy*. Vol. 2. 1998: Wiley New York.
222. Sanders, J.K. and B.K. Hunter, *Modern NMR spectroscopy: a guide for chemists*. 1988.
223. Duer, M.J., *Introduction to solid-state NMR spectroscopy*. 2004: Oxford, UK.
224. Otto, M., *Analytical chemistry. 2. tot. rev. ed.; Analytische Chemie*. 2000.
225. Hesse, M., H. Meier, and B. Zeeh, *Spektroskopische Methoden in der organischen Chemie*. 2005: Georg Thieme Verlag.
226. Steinhäuser, M., *Stabilisierung und Funktionalisierung von Calciumphosphat-Nanopartikeln mit Proteinen und Tetraetherlipiden*. 2009.
227. Schwedt, G., T.C. Schmidt, and O.J. Schmitz, *Analytische Chemie: Grundlagen, Methoden und Praxis*. 2016: John Wiley & Sons.
228. Hauk, A., *Quantifizierung von DNA durch Absorptionsmessung*. *Biologie in unserer Zeit*, 2013. **43**(5): p. 278-278.
229. Bhat, S., et al., *Comparison of methods for accurate quantification of DNA mass concentration with traceability to the international system of units*. *Analytical chemistry*, 2010. **82**(17): p. 7185-7192.
230. Atkins, P.W. and J. De Paula, *Physikalische chemie*. 2013: John Wiley & Sons.
231. Dickmann, T., et al., *Prädiktoren von visuellem Modellverständnis in der Chemie*. Gesellschaft für Didaktik der Chemie und Physik Jahrestagung in Berlin, 2015.
232. Hof, M., R. Hutterer, and V. Fidler, *Fluorescence spectroscopy in biology: advanced methods and their applications to membranes, proteins, DNA, and cells*. Vol. 3. 2004: Springer Science & Business Media.
233. Gey, M.H., *Instrumentelle Analytik und Bioanalytik: Biosubstanzen, Trennmethode, Strukturanalytik, Applikationen*. 2015: Springer-Verlag.
234. Gey, M.H., *Selektive Bioanalytik*. *Instrumentelle Analytik und Bioanalytik: Biosubstanzen, Trennmethode, Strukturanalytik, Applikationen*, 2008: p. 347-372.
235. Abdelwahed, W., et al., *Freeze-drying of nanoparticles: formulation, process and storage considerations*. *Advanced drug delivery reviews*, 2006. **58**(15): p. 1688-1713.
236. Mosmann, T., *Rapid colorimetric assay for cellular growth and survival: application to proliferation and cytotoxicity assays*. *Journal of immunological methods*, 1983. **65**(1-2): p. 55-63.

237. Berridge, M.V. and A.S. Tan, *Characterization of the cellular reduction of 3-(4, 5-dimethylthiazol-2-yl)-2, 5-diphenyltetrazolium bromide (MTT): subcellular localization, substrate dependence, and involvement of mitochondrial electron transport in MTT reduction*. Archives of biochemistry and biophysics, 1993. **303**(2): p. 474-482.
238. Borlinghaus, R.T., *Konfokale Mikroskopie in Weiß: Optische Schnitte in Allen Farben*. 2016: Springer.
239. Harris, H., *The human alkaline phosphatases: what we know and what we don't know*. Clinica chimica acta, 1990. **186**(2): p. 133-150.
240. Sabokbar, A., et al., *A rapid, quantitative assay for measuring alkaline phosphatase activity in osteoblastic cells in vitro*. Bone and mineral, 1994. **27**(1): p. 57-67.
241. Tang, Z., et al., *Assays for alkaline phosphatase activity: progress and prospects*. TrAC Trends in Analytical Chemistry, 2019. **113**: p. 32-43.
242. Chernousova, S., et al., *A genetically active nano-calcium phosphate paste for bone substitution, encoding the formation of BMP-7 and VEGF-A*. RSC advances, 2013. **3**(28): p. 11155-11161.
243. Kovtun, A., R. Heumann, and M. Epple, *Calcium phosphate nanoparticles for the transfection of cells*. Bio-medical materials and engineering, 2009. **19**(2-3): p. 241-247.
244. Frede, A., et al., *Local delivery of siRNA-loaded calcium phosphate nanoparticles abates pulmonary inflammation*. Nanomedicine: Nanotechnology, Biology and Medicine, 2017. **13**(8): p. 2395-2403.
245. Neuhaus, B., et al., *Gene silencing of the pro-inflammatory cytokine TNF- $\alpha$  with siRNA delivered by calcium phosphate nanoparticles, quantified by different methods*. Journal of Materials Chemistry B, 2015. **3**(36): p. 7186-7193.
246. Dördelmann, G., et al., *Calcium phosphate increases the encapsulation efficiency of hydrophilic drugs (proteins, nucleic acids) into poly (d, l-lactide-co-glycolide acid) nanoparticles for intracellular delivery*. Journal of Materials Chemistry B, 2014. **2**(41): p. 7250-7259.
247. Brust, M., et al., *Synthesis of thiol-derivatised gold nanoparticles in a two-phase liquid-liquid system*. Chem. Commun., 1994: p. 801-802.
248. Liz-Marzán, L.M., *Gold nanoparticle research before and after the Brust–Schiffrin method*. Chem. Comm., 2013. **49**: p. 16-18.
249. Xie, J., Y. Zheng, and J.Y. Ying, *Protein-directed synthesis of highly fluorescent gold nanoclusters*. Journal of the American Chemical Society, 2009. **131**(3): p. 888-889.
250. Cardarelli, F., et al., *The intracellular trafficking mechanism of Lipofectamine-based transfection reagents and its implication for gene delivery*. Scientific reports, 2016. **6**(1): p. 1-8.
251. Kollenda, S.A., et al., *In vivo biodistribution of calcium phosphate nanoparticles after intravascular, intramuscular, intratumoral, and soft tissue administration in mice investigated by small animal PET/CT*. Acta biomaterialia, 2020. **109**: p. 244-253.
252. Horiuchi, T., et al., *Transmembrane TNF- $\alpha$ : structure, function and interaction with anti-TNF agents*. Rheumatology, 2010. **49**(7): p. 1215-1228.
253. Smith, N., et al., *An efficient method for gene silencing in human primary plasmacytoid dendritic cells: silencing of the TLR7/IRF-7 pathway as a proof of concept*. Scientific reports, 2016. **6**(1): p. 1-12.
254. Kasai, H., et al., *Efficient siRNA delivery and gene silencing using a lipopolyptide hybrid vector mediated by a caveolae-mediated and temperature-dependent endocytic pathway*. Journal of nanobiotechnology, 2019. **17**(1): p. 1-14.
255. Jensen, K., J.A. Anderson, and E.J. Glass, *Comparison of small interfering RNA (siRNA) delivery into bovine monocyte-derived macrophages by transfection and electroporation*. Veterinary immunology and immunopathology, 2014. **158**(3-4): p. 224-232.
256. McIntosh, I., et al., *Application of Polymer Coatings on Non-banded Size M "Mouse" Capsules Containing Immediate and Extended-Release Formulations*.

- 
257. Pillai, O. and R. Panchagnula, *Polymers in drug delivery*. Current opinion in chemical biology, 2001. **5**(4): p. 447-451.
258. Doerdelmann, G., D. Kozlova, and M. Epple, *A pH-sensitive poly (methyl methacrylate) copolymer for efficient drug and gene delivery across the cell membrane*. Journal of Materials Chemistry B, 2014. **2**(41): p. 7123-7131.
259. Malm, C., J. Emerson, and G. Hiait, *Cellulose acetate phthalate as an enteric coating material*. Journal of the American Pharmaceutical Association (Scientific ed.), 1951. **40**(10): p. 520-525.
260. Karavas, E., E. Georgarakis, and D. Bikiaris, *Application of PVP/HPMC miscible blends with enhanced mucoadhesive properties for adjusting drug release in predictable pulsatile chronotherapeutics*. European Journal of Pharmaceutics and Biopharmaceutics, 2006. **64**(1): p. 115-126.
261. Shimono, N., et al., *Chitosan dispersed system for colon-specific drug delivery*. International journal of pharmaceutics, 2002. **245**(1-2): p. 45-54.
262. Lorenzo-Lamosa, M., et al., *Design of microencapsulated chitosan microspheres for colonic drug delivery*. Journal of controlled release, 1998. **52**(1-2): p. 109-118.
263. Zaki, I., et al., *A comparison of the effect of viscosity on the precorneal residence of solutions in rabbit and man*. Journal of pharmacy and pharmacology, 1986. **38**(6): p. 463-466.
264. Narayani, R. and K. Panduranga Rao, *Polymer-coated gelatin capsules as oral delivery devices and their gastrointestinal tract behaviour in humans*. Journal of Biomaterials Science, Polymer Edition, 1996. **7**(1): p. 39-48.
265. Kerdsakundee, N., et al., *Multifunctional nanotube–mucoadhesive poly (methyl vinyl ether-co-maleic acid)@ hydroxypropyl methylcellulose acetate succinate composite for site-specific oral drug delivery*. Advanced healthcare materials, 2017. **6**(20): p. 1700629.
266. Sangalli, M., et al., *In vitro and in vivo evaluation of an oral system for time and/or site-specific drug delivery*. Journal of Controlled Release, 2001. **73**(1): p. 103-110.
267. Belali, N., N. Wathoni, and M. Muchtaridi, *Advances in orally targeted drug delivery to colon*. Journal of advanced pharmaceutical technology & research, 2019. **10**(3): p. 100.
268. Chourasia, M. and S. Jain, *Pharmaceutical approaches to colon targeted drug delivery systems*. J Pharm Pharm Sci, 2003. **6**(1): p. 33-66.
269. Zhang, T., et al., *Oral nano-delivery systems for colon targeting therapy*. Pharmaceutical nanotechnology, 2017. **5**(2): p. 83-94.
270. Maurer, J.M., et al., *Gastrointestinal pH and transit time profiling in healthy volunteers using the IntelliCap system confirms ileo-colonic release of ColoPulse tablets*. PLoS One, 2015. **10**(7): p. e0129076.
271. Artursson, P. and J. Karlsson, *Correlation between oral drug absorption in humans and apparent drug permeability coefficients in human intestinal epithelial (Caco-2) cells*. Biochemical and biophysical research communications, 1991. **175**(3): p. 880-885.
272. Fogh, J., J.M. Fogh, and T. Orfeo, *One hundred and twenty-seven cultured human tumor cell lines producing tumors in nude mice*. Journal of the National Cancer Institute, 1977. **59**(1): p. 221-226.
273. Hidalgo, I.J., T.J. Raub, and R.T. Borchardt, *Characterization of the human colon carcinoma cell line (Caco-2) as a model system for intestinal epithelial permeability*. Gastroenterology, 1989. **96**(2): p. 736-749.
274. Verma, I.M. and M.D. Weitzman, *Gene therapy: twenty-first century medicine*. Annu. Rev. Biochem., 2005. **74**: p. 711-738.
275. Kollenda, S., et al., *A pH-sensitive fluorescent protein sensor to follow the pathway of calcium phosphate nanoparticles into cells*. Acta Biomaterialia, 2020. **111**: p. 406-417.
276. Klesing, J., S. Chernousova, and M. Epple, *Freeze-dried cationic calcium phosphate nanorods as versatile carriers of nucleic acids (DNA, siRNA)*. Journal of Materials Chemistry, 2012. **22**(1): p. 199-204.
277. Shim, M.S. and Y.J. Kwon, *Efficient and targeted delivery of siRNA in vivo*. The FEBS journal, 2010. **277**(23): p. 4814-4827.

278. Alex, S.M. and C.P. Sharma, *Enhanced intracellular uptake and endocytic pathway selection mediated by hemocompatible ornithine grafted chitosan polycation for gene delivery*. Colloids and Surfaces B: Biointerfaces, 2014. **122**: p. 792-800.
279. Pereira, P., et al., *siRNA inhibition of endocytic pathways to characterize the cellular uptake mechanisms of folate-functionalized glycol chitosan nanogels*. Molecular pharmaceutics, 2015. **12**(6): p. 1970-1979.
280. Sevimli, S., et al., *The endocytic pathway and therapeutic efficiency of doxorubicin conjugated cholesterol-derived polymers*. Biomaterials science, 2015. **3**(2): p. 323-335.
281. Zhang, H., et al., *Arginine conjugation affects the endocytic pathways of chitosan/DNA nanoparticles*. Journal of Biomedical Materials Research Part A, 2011. **98**(2): p. 296-302.
282. Li, A., et al., *The gene transfection and endocytic uptake pathways mediated by PEGylated PEI-entrapped gold nanoparticles*. Arabian Journal of Chemistry, 2020. **13**(1): p. 2558-2567.
283. Olton, D.Y., et al., *Intracellular trafficking pathways involved in the gene transfer of nano-structured calcium phosphate-DNA particles*. Biomaterials, 2011. **32**(30): p. 7662-7670.
284. Danhier, F., et al., *PLGA-based nanoparticles: an overview of biomedical applications*. Journal of controlled release, 2012. **161**(2): p. 505-522.
285. Vauthier, C. and K. Bouchemal, *Methods for the preparation and manufacture of polymeric nanoparticles*. Pharmaceutical research, 2009. **26**(5): p. 1025-1058.
286. Wischke, C. and S.P. Schwendeman, *Principles of encapsulating hydrophobic drugs in PLA/PLGA microparticles*. International Journal of pharmaceutics, 2008. **364**(2): p. 298-327.
287. Adler, A.F. and K.W. Leong, *Emerging links between surface nanotechnology and endocytosis: impact on nonviral gene delivery*. Nano today, 2010. **5**(6): p. 553-569.
288. Jones, A.T., *Macropinocytosis: searching for an endocytic identity and role in the uptake of cell penetrating peptides*. Journal of cellular and molecular medicine, 2007. **11**(4): p. 670-684.
289. Klesing, J., et al., *An injectable paste of calcium phosphate nanorods, functionalized with nucleic acids, for cell transfection and gene silencing*. Journal of Materials Chemistry, 2010. **20**(29): p. 6144-6148.
290. Meyer, F., et al., *Overview of calcium phosphates used in biomimetic oral care*. The open dentistry journal, 2018. **12**: p. 406.
291. Bose, S. and S. Tarafder, *Calcium phosphate ceramic systems in growth factor and drug delivery for bone tissue engineering: a review*. Acta biomaterialia, 2012. **8**(4): p. 1401-1421.
292. Eliaz, N. and N. Metoki, *Calcium phosphate bioceramics: a review of their history, structure, properties, coating technologies and biomedical applications*. Materials, 2017. **10**(4): p. 334.
293. Bienek, D.R. and D. Skrtic, *Utility of amorphous calcium phosphate-based scaffolds in dental/biomedical applications*. Biointerface research in applied chemistry, 2017. **7**(1): p. 1989.
294. Dorozhkin, S.V., *Amorphous calcium (ortho) phosphates*. Acta Biomaterialia, 2010. **6**(12): p. 4457-4475.
295. Khalifehzadeh, R. and H. Arami, *DNA-templated strontium-doped calcium phosphate nanoparticles for gene delivery in bone cells*. ACS biomaterials science & engineering, 2019. **5**(7): p. 3201-3211.
296. Degli Esposti, L., et al., *Calcium phosphate-based nanosystems for advanced targeted nanomedicine*. Drug development and industrial pharmacy, 2018. **44**(8): p. 1223-1238.
297. Habraken, W., et al., *Calcium phosphates in biomedical applications: materials for the future?* Materials Today, 2016. **19**(2): p. 69-87.
298. Szcześ, A., L. Hołysz, and E. Chibowski, *Synthesis of hydroxyapatite for biomedical applications*. Advances in colloid and interface science, 2017. **249**: p. 321-330.
299. Tabaković, A., M. Kester, and J.H. Adair, *Calcium phosphate-based composite nanoparticles in bioimaging and therapeutic delivery applications*. Wiley Interdisciplinary Reviews: Nanomedicine and Nanobiotechnology, 2012. **4**(1): p. 96-112.
300. Liu, C. and H. He, *Developments and applications of calcium phosphate bone cements*. 2018: Springer.

301. Vallet-Regí, M. and E. Ruiz-Hernández, *Bioceramics: from bone regeneration to cancer nanomedicine*. *Advanced Materials*, 2011. **23**(44): p. 5177-5218.
302. Habibovic, P. and J. Barralet, *Bioinorganics and biomaterials: bone repair*. *Acta biomaterialia*, 2011. **7**(8): p. 3013-3026.
303. Dimitriou, R., et al., *Bone regeneration: current concepts and future directions*. *BMC medicine*, 2011. **9**(1): p. 1-10.
304. Goldhahn, J., et al., *Clinical evaluation of medicinal products for acceleration of fracture healing in patients with osteoporosis*. *Bone*, 2008. **43**(2): p. 343-347.
305. Iafisco, M., et al., *Biomimetic magnesium–carbonate-apatite nanocrystals endowed with strontium ions as anti-osteoporotic trigger*. *Materials Science and Engineering: C*, 2014. **35**: p. 212-219.
306. Landi, E., et al., *Densification behaviour and mechanisms of synthetic hydroxyapatites*. *Journal of the European Ceramic Society*, 2000. **20**(14-15): p. 2377-2387.
307. Wenk, H.-R. and F. Heidelbach, *Crystal alignment of carbonated apatite in bone and calcified tendon: results from quantitative texture analysis*. *Bone*, 1999. **24**(4): p. 361-369.
308. Horvath, A.L., *Solubility of structurally complicated materials: II. Bone*. *Journal of Physical and Chemical Reference Data*, 2006. **35**(4): p. 1653-1668.
309. Cannizzaro, G., et al., *Early loading of implants in the atrophic posterior maxilla: lateral sinus lift with autogenous bone and Bio-Oss versus crestal mini sinus lift and 8-mm hydroxyapatite-coated implants. A randomised controlled clinical trial*. *European Journal of Oral Implantology*, 2009. **2**(1).
310. Stavropoulos, A. and T. Karring, *Guided tissue regeneration combined with a deproteinized bovine bone mineral (Bio-Oss®) in the treatment of intrabony periodontal defects: 6-year results from a randomized-controlled clinical trial*. *Journal of clinical periodontology*, 2010. **37**(2): p. 200-210.
311. Weisinger, J.R. and E. Bellorín-Font, *Magnesium and phosphorus*. *The Lancet*, 1998. **352**(9125): p. 391-396.
312. Wolf, F.I. and A. Cittadini, *Chemistry and biochemistry of magnesium*. *Molecular aspects of medicine*, 2003. **24**(1-3): p. 3-9.
313. Maguire, M.E. and J.A. Cowan, *Magnesium chemistry and biochemistry*. *Biometals*, 2002. **15**(3): p. 203-210.
314. Nabiyouni, M., Y. Ren, and S.B. Bhaduri, *Magnesium substitution in the structure of orthopedic nanoparticles: A comparison between amorphous magnesium phosphates, calcium magnesium phosphates, and hydroxyapatites*. *Materials Science and Engineering: C*, 2015. **52**: p. 11-17.
315. Basu, S., et al., *(Fe/Sr) codoped biphasic calcium phosphate with tailored osteoblast cell functionality*. *ACS Biomaterials Science & Engineering*, 2018. **4**(3): p. 857-871.
316. Marie, P., et al., *Mechanisms of action and therapeutic potential of strontium in bone*. *Calcified tissue international*, 2001. **69**(3): p. 121.
317. Marie, P.J., *Strontium ranelate: new insights into its dual mode of action*. *Bone*, 2007. **40**(5): p. S5-S8.
318. Querido, W., A.L. Rossi, and M. Farina, *The effects of strontium on bone mineral: A review on current knowledge and microanalytical approaches*. *Micron*, 2016. **80**: p. 122-134.
319. Lode, A., et al., *Strontium-modified premixed calcium phosphate cements for the therapy of osteoporotic bone defects*. *Acta biomaterialia*, 2018. **65**: p. 475-485.
320. Marx, D., et al., *A review of the latest insights into the mechanism of action of strontium in bone*. *Bone reports*, 2020: p. 100273.
321. Basu, S. and B. Basu, *Doped biphasic calcium phosphate: synthesis and structure*. *Journal of Asian Ceramic Societies*, 2019. **7**(3): p. 265-283.
322. Miclau, T., et al., *Bone toxicity of locally applied aminoglycosides*. *Journal of orthopaedic trauma*, 1995. **9**(5): p. 401-406.
323. Lai, S.K., et al., *Characterization of the intracellular dynamics of a non-degradative pathway accessed by polymer nanoparticles*. *Journal of Controlled Release*, 2008. **125**(2): p. 107-111.

324. Liu, N.Q., et al., *Human immunodeficiency virus type 1 enters brain microvascular endothelia by macropinocytosis dependent on lipid rafts and the mitogen-activated protein kinase signaling pathway*. Journal of virology, 2002. **76**(13): p. 6689-6700.
325. Rejman, J., et al., *Size-dependent internalization of particles via the pathways of clathrin- and caveolae-mediated endocytosis*. Biochemical journal, 2004. **377**(1): p. 159-169.
326. Harush-Frenkel, O., et al., *Targeting of nanoparticles to the clathrin-mediated endocytic pathway*. Biochemical and biophysical research communications, 2007. **353**(1): p. 26-32.
327. Capuccini, C., et al., *Strontium-substituted hydroxyapatite coatings synthesized by pulsed-laser deposition: in vitro osteoblast and osteoclast response*. Acta biomaterialia, 2008. **4**(6): p. 1885-1893.
328. Mihailescu, I.N., et al., *Advanced biomimetic implants based on nanostructured coatings synthesized by pulsed laser technologies*, in *Laser-Surface Interactions for New Materials Production*. 2010, Springer. p. 235-260.
329. Ristig, S., et al., *An easy synthesis of autofluorescent alloyed silver-gold nanoparticles*. Journal of Materials Chemistry B, 2014. **2**(45): p. 7887-7895.
330. Schmid, G., D. Talapin, and E. Shevchenko, *Metal Nanoparticles*. 2004, Wiley-VCH: Weinheim, Germany. p. 328368.
331. Leifert, A., et al., *Molecularly stabilised ultrasmall gold nanoparticles: synthesis, characterization and bioactivity*. Nanoscale, 2013. **5**(14): p. 6224-6242.
332. Dreaden, E.C., et al., *The golden age: gold nanoparticles for biomedicine*. Chemical Society Reviews, 2012. **41**(7): p. 2740-2779.
333. Barcikowski, S. and F. Mafuné, *Trends and current topics in the field of laser ablation and nanoparticle generation in liquids*. 2011, ACS Publications.
334. Voliani, V., et al., *Cancer phototherapy in living cells by multiphoton release of doxorubicin from gold nanospheres*. Journal of Materials Chemistry B, 2013. **1**(34): p. 4225-4230.
335. Huang, X., et al., *Plasmonic photothermal therapy (PPTT) using gold nanoparticles*. Lasers in medical science, 2008. **23**(3): p. 217-228.
336. Paciotti, G.F., et al., *Colloidal gold: a novel nanoparticle vector for tumor directed drug delivery*. Drug delivery, 2004. **11**(3): p. 169-183.
337. Sazgarnia, A., et al., *Therapeutic effects of acoustic cavitation in the presence of gold nanoparticles on a colon tumor model*. Journal of Ultrasound in Medicine, 2013. **32**(3): p. 475-483.
338. Schmid, G., W.G. Kreyling, and U. Simon, *Toxic effects and biodistribution of ultrasmall gold nanoparticles*. Archives of toxicology, 2017. **91**(9): p. 3011-3037.
339. Mathaes, R., et al., *Non-spherical micro- and nanoparticles: fabrication, characterization and drug delivery applications*. Expert opinion on drug delivery, 2015. **12**(3): p. 481-492.
340. van der Meer, S.B., et al., *Click chemistry on the surface of ultrasmall gold nanoparticles (2 nm) for covalent ligand attachment followed by NMR spectroscopy*. Langmuir, 2019. **35**(22): p. 7191-7204.
341. Kopp, M., S. Kollenda, and M. Epple, *Nanoparticle-protein interactions: therapeutic approaches and supramolecular chemistry*. Accounts of chemical research, 2017. **50**(6): p. 1383-1390.
342. Shang, L. and G.U. Nienhaus, *Small fluorescent nanoparticles at the nano-bio interface*. Materials Today, 2013. **16**(3): p. 58-66.
343. Zheng, J., P.R. Nicovich, and R.M. Dickson, *Highly fluorescent noble-metal quantum dots*. Annu. Rev. Phys. Chem., 2007. **58**: p. 409-431.
344. Kim, C., et al., *Recognition-mediated activation of therapeutic gold nanoparticles inside living cells*. Nature chemistry, 2010. **2**(11): p. 962-966.
345. Cabral, H., et al., *Accumulation of sub-100 nm polymeric micelles in poorly permeable tumours depends on size*. Nature nanotechnology, 2011. **6**(12): p. 815-823.
346. Ruks, T., et al., *Solution NMR Spectroscopy with Isotope-Labeled Cysteine (<sup>13</sup>C and <sup>15</sup>N) Reveals the Surface Structure of l-Cysteine-Coated Ultrasmall Gold Nanoparticles (1.8 nm)*. Langmuir, 2018. **35**(3): p. 767-778.

347. Dong, L., et al., *Cytotoxicity of BSA-stabilized gold nanoclusters: In vitro and in vivo study*. *Small*, 2015. **11**(21): p. 2571-2581.
348. Muhammed, M.A.H., et al., *Bright, NIR-emitting Au 23 from Au 25: characterization and applications including biolabeling*. *Chemistry: A European Journal*, 2009. **15**(39): p. 10110-10120.
349. Revia, R.A., Z.R. Stephen, and M. Zhang, *Theranostic nanoparticles for RNA-based cancer treatment*. *Accounts of chemical research*, 2019. **52**(6): p. 1496-1506.
350. Jensen, S.A., et al., *Spherical nucleic acid nanoparticle conjugates as an RNAi-based therapy for glioblastoma*. *Science translational medicine*, 2013. **5**(209): p. 209ra152-209ra152.
351. Mohammadi-Samani, S. and B. Taghipour, *PLGA micro and nanoparticles in delivery of peptides and proteins; problems and approaches*. *Pharmaceutical development and technology*, 2015. **20**(4): p. 385-393.
352. Enea, M., et al., *Study of the intestinal uptake and permeability of gold nanoparticles using both in vitro and in vivo approaches*. *Nanotechnology*, 2020. **31**(19): p. 195102.
353. Hosseini, S., et al., *Pathways for Oral and Rectal Delivery of Gold Nanoparticles (1.7 nm) and Gold Nanoclusters into the Colon: Enteric-Coated Capsules and Suppositories*. *Molecules*, 2021. **26**(16): p. 5069.
354. Xie, J., Y. Zheng, and J.Y. Ying, *Protein-directed synthesis of highly fluorescent gold nanoclusters*. *J. Am. Chem. Soc.*, 2009. **131**: p. 888-889.
355. Zhang, P., et al., *Rapid synthesis of highly luminescent and stable Au 20 nanoclusters for active tumor-targeted imaging in vitro and in vivo*. *Nanoscale*, 2014. **6**: p. 2261-2269.
356. Wen, X., et al., *Structure-correlated dual fluorescent bands in BSA-protected Au25 nanoclusters*. *J. Phys. Chem. C*, 2012. **116**: p. 11830-11836.
357. Chatteraj, S. and K. Bhattacharyya, *Fluorescent gold nanocluster inside a live breast cell: etching and higher uptake in cancer cell*. *J. Phys. Chem. C*, 2014. **118**: p. 22339-22346.
358. Khlebtsov, B., et al., *Multifunctional Au nanoclusters for targeted bioimaging and enhanced photodynamic inactivation of Staphylococcus aureus*. *RSC Adv.*, 2015. **5**: p. 61639-61649.
359. Cheng, H., S. Huang, and G. Huang, *Design and application of oral colon administration system*. *J. Enzyme Inhib. Med. Chem.*, 2019. **34**: p. 1590-1596.
360. Chourasia, M.K. and S.K. Jain, *Pharmaceutical approaches to colon targeted drug delivery systems*. *J. Pharm. Pharm. Sci.*, 2003. **6**: p. 33-66.
361. Zhang, T., et al., *Oral nano-delivery systems for colon targeting therapy*. *Pharm. Nanotechnol.*, 2017. **5**: p. 83-94.
362. Maurer, J.M., et al., *Gastrointestinal pH and transit time profiling in healthy volunteers using the intellicap system confirms ileo-colonic release of colopulse tablets*. *PLoS One*, 2015. **10**: p. e0129076-e0129076.
363. Hosseini, S., K. Wey, and M. Epple, *Enteric coating systems for the oral administration of bioactive calcium phosphate nanoparticles carrying nucleic acids into the colon*. *ChemistrySelect*, 2020. **5**: p. 9720-9729.
364. Hosseini, S. and M. Epple, *Suppositories with bioactive calcium phosphate nanoparticles for intestinal transfection and gene silencing*. *NanoSelect*, 2021. **2**: p. 561-572.
365. Cui, M., Y. Zhao, and Q. Song, *Synthesis, optical properties and applications of ultra-small luminescent gold nanoclusters*. *Trends Anal. Chem.*, 2014. **57**: p. 73-82.

## 9. Appendix

### 9.1 List of abbreviations used

abbreviation	Long name
AAS	Atomic absorption spectroscopy
AF	AlexaFluor®
ALP	Alkaline Phosphatase
BSA	Bovine serum albumin
Caco-2	Colon Carcinoma Cell Line
CaP	Calcium phosphate
CAP	Cellulose acetate phthalate
CLSM	Confocal laser scanning microscopy
CMC	Carboxymethyl cellulose
CS	Chitosan
DAPI	4',6-diamidin-2-phenylindol
DCM	Dichloromethane
DLS	Dynamic light scattering
DMEM	Dulbecco's Modified Eagle Medium
DMSO	Dimethyl sulfoxide
DNA	Deoxyribonucleic acid
DPBS	Dulbecco's phosphate buffered saline
EDX	Energy dispersive X-ray spectroscopy
EGFP or eGFP	Enhanced green fluorescent protein
FITC	Fluorescein isothiocyanate
GS	Gene silencing
HA	Hydroxyapatite
HeLa	Henrietta Lacks cervix carcinoma
HPMC	Hydroxypropyl methylcellulose
IBD	inflammatory bowel diseases
MTT	3-(4,5-dimethylthiazol-2-yl)-2,5-diphenyltetrazolium bromide
MW or Mw	Molecular weight
NPs	Nanoparticles

PDI	Poly dispersity index
pDNA	Plasmid DNA
PEI	Polyethylenimine
PLGA	Poly Lactic-co-Glycolic Acid
pNPP	p-Nitrophenyl phosphate
P/S	Penicillin/Streptomycin
PVA	Poly(vinyl alcohol)
Rh	Rhodamine
RNA	Ribonucleic acid
SEM	Scanning electron microscopy
siRNA	Small interfering RNA
TE	Transfection efficiency
TEM	Transmission electron microscopy
UV/Vis	Ultraviolet-visible
Wt.%	Weight percent

## 9.2 List of devices used

Instrument	Short name	Model	Company
Atomic absorption spectrometer	AAS	M-Series AA	Thermo Electron Corporation
Confocal laser scanning microscope	CLSM	TCS SP8 AOBS	Leica
Dynamic light scattering	DLS	Nano ZS ZEN 3600	Malvern
Fluorescence microscope	-	BZ 9000	Keyence
Fluorescence spectrophotometer	-	Cary Eclipse	Agilent Technologies
Lyophilizer	-	Alpha 2-4 LSC	Christ
Microvolume spectrophotometer	Nanodrop	DS-11 FX+	DeNovix
pH-meter	-	pH340	WTW
Scanning electron microscope	SEM	Apreo S	Thermo Electron Corporation
Sonotrode	Ultrasonic	UP50H	Heilscher
Transmission electron microscope	TEM	JEM-1400+ 120KV TEM with cryo and tomographic goniometer	JEOL
Ultracentrifugation	-	Sorvall WX Ultra Series	Thermo Electron Corporation
Ultraviolet-visible spectrophotometer	UV-Vis	Cary 300 Bio	Varian

## 9.3 List of chemicals used

Reagent	Company	Purity
Aceton	Bernd Kraft	-
Adeps solidus (pharmaceutical hard fat, Witepsol®W25)	Caesar and Loretz GmbH	-
Alexa Fluor™ 488 Phalloidin	Invitrogen	-
Alexa Fluor™ 647 Phalloidin	Invitrogen	-
ALP Kit	abcam	-
Ammonia solution 30%	Carl Roth	p.a.
Bovine serum albumin (BSA)	SERVA Electrophoresis	-
Branched polyethyleneimine (PEI), Mw= 25,000 g/mol	Sigma-Aldrich	-
Calcium lactate pentahydrate	Sigma-Aldrich	p.a.
CAP	Sigma-Aldrich	M = 2.5 kDa
Chitosan (2-amino-2-deoxy-(1,4)-D-glucopyranan, poly-(1,4-D-glucopyranosamine)	Sigma-Aldrich	viscosity > 400 mPa s
Diammonium hydrogenphosphate	VWR Life Science	p.a.
Dichlormethan	Fisher Scientific	-
Dulbecco's modified Eagle's medium (DMEM)	Invitrogen	-
Dulbecco's phosphate-buffered saline (DPBS)	Invitrogen	-
Dimethyl sulfoxide (DMSO)	Carl Roth	≥ 99.5 %
Ethanol (absolute)	Fischer Chemicalr	≥ 99.8%
Eudragit L100	Evonik Industries	Mw=125 000 g mol <sup>-1</sup>
Fetal bovine serum (FBS)	Invitrogen	-
Hoechst	Invitrogen	-
HPMC	Sigma-Aldrich	80–120 cP; Mw = 26 kDa

## Appendix

L-glutathione	Sigma-Aldrich	> 98%,
Lipofectamine 2000	Invitrogen	
Magnesiumnitrat-Hexahydrat	Merck	≥ 99 %
NHS-fluorescein (5/6-carboxyfluorescein succinimidyl ester)	Thermo Scientific	> 90%
Polyvinylalkohol	Sigma-Aldrich	30-70 kDa, 87-90% Hydrolysiert
Poly(vinylalkohol)/PVA	Sigma-Aldrich	87–90% hydrolysed, M = 30–70 kDa
siRNA, 5'-GCCGAUGG-GUUGUACCUUG-3')	Dharmacon	-
Sodium borohydride	Fluka	> 96%
Sodium hydroxide	VWR Prolabo	> 98.6%
Strontiumnitrat	Merck	≥ 99 %
Trehalose	VWR Life Science	≥ 98 %
Triton® X-100	Sigma-Aldrich	-
Trypsin-EDTA	Life Technologies	-
Ultrapure distilled water (DNase/RNase free)	Invitrogen	-
α-MEM	Life Technologies	-
(4,5-dimethylthiazol-2-yl)-2,5diphenyl-tetrazolium bromide (MTT)	Invitrogen	-

## 9.4 List of publications

S. Hosseini, K. Wey, M. Epple, Enteric coating systems for the oral administration of bioactive calcium phosphate nanoparticles into the colon, *ChemistrySelect* **2020**, 5, 9720-9729.

S. Hosseini, and M. Epple, Suppositories with bioactive calcium phosphate nanoparticles for intestinal transfection and gene silencing, *Nano Select* **2021**, 2, 561-572.

O. Wetzel, S. Hosseini, K. Loza, M. Heggen, O. Prymak, P. Bayer, C. Beuck, T. Schaller, F. Niemeyer, C. Weidenthaler, and M. Epple, Metal–Ligand Interface and Internal Structure of Ultrasmall Silver Nanoparticles (2 nm), *The Journal of Physical Chemistry B* **2021**.

S. Hosseini, O. Wetzel, K. Kostka, M. Heggen, K. Loza, and M. Epple, Pathways for Oral and Rectal Delivery of Gold Nanoparticles (1.7 nm) and Gold Nanoclusters into the Colon: Enteric-Coated Capsules and Suppositories, *Molecules* **2021**, 26, 5069.

## 9.5 Contributions to conferences

Annual Meeting of the German Society for Biomaterials (DGBM), Braunschweig 2018. S. Hosseini, and M. Epple, An enteric coating system for the oral administration of functional nanoparticles into the colon. **(Poster contribution)**

2nd CENIDE Conference, Bergisch-Gladbach 2020. S. Hosseini, and M. Epple, In vitro studies of calcium phosphate nanoparticles for drug delivery into the colon by capsules and suppositories. **(Oral contribution)**

11<sup>th</sup> World Biomaterials Congress (WBC), Virtual 2020. S. Hosseini, and M. Epple, In vitro studies of calcium phosphate nanoparticles for drug delivery into the colon by capsules and suppositories. **(Oral contribution)**

31st Annual Conference of European Society for Biomaterials (ESB), Virtual 2021. S. Hosseini, K. Kostka, and M. Epple, In-vitro cell responses to strontium/magnesium-doped calcium phosphate nanoparticles. **(Poster contribution + short talk)**

Annual Meeting of the German Society for Biomaterials (DGBM), Virtual 2021. S. Hosseini, O. Wetzels, K. Kostka, and M. Epple, In vitro studies on the oral and rectal administration of ultrasmall gold nanoparticles for colon gene therapy. **(Oral contribution)**

Annual Meeting of the German Society for Biomaterials (DGBM), Virtual 2021. S. Hosseini, K. Kostka, and M. Epple, Suppositories containing calcium phosphate nanoparticles for local gene therapy in the colon. **(Oral contribution)**

## **9.6 CV**

The Curriculum vitae is not included in the online version for privacy reasons.

Der Lebenslauf ist in der Online-Version aus Gründen des Datenschutzes nicht enthalten.







## 9.7 Eidesstattliche Erklärungen

Hiermit versichere ich, die vorliegende Arbeit mit dem Titel:

“Synthesis, characterisation and in vitro investigation of bioactive nanoparticles”

selbst verfasst und keine außer den angegebenen Hilfsmitteln und Quellen verwendet zu haben.

Zudem erkläre ich, dass ich die Arbeit in dieser oder einer ähnlichen Form bei keiner anderen Fakultät eingereicht habe.

Essen, den

Shabnam Hosseini

## 9.8 Acknowledgments

First, I want to thank Prof. Dr. Matthias Epple for receiving me into his research group and giving me the opportunity to work in an interesting and active research topic, as well as all the provided access to the required facilities and materials. Additionally, I thank him for all his support and motivation during these years.

I would like to express my gratitude to Prof. Dr. Christian Mayer for the assessment of my thesis.

Next, I am thankful to the technical and administrative staff Carola, Sabine K., Ursula, Sabine B., Robin, for all their support during these years.

To all the PhD students in the group I thank them for the pleasant working atmosphere. Specially, I would like to thank Kathrin, Dr. Loza, and Mateusz for their great support and good mood. I would like to thank Benedikt for his very good mood, support and reading and correcting my thesis.

Additionally, I would like to thank Dr. Johannes Koch and Dr. Nina Schulze from the light microscopy imaging facilities (IMCES and ICCE) for their support with the different microscopy techniques.

I will like to thank my family for their great and constant support and motivation that kept me always going forward, as well as to the good friends I made in Essen.

Finally, I truly thank Oliver for his unique support and motivation in these years as well as all his afford to teach me German language. This experience would not have been the same without him.